An electron paramagnetic resonance study of carbon based electronic materials.

by

Michael Peter Collins.

Submitted for the degree of Doctor of Philosophy
to
University of Dublin,
Trinity College.

Physics Department,
Trinity College Dublin.
October 1999

Declaration

I declare that this thesis is entirely my own work and has not been submitted as an exercise for a degree at this or any other university. This thesis may be freely lent or copied.

Michael Peter Collins

Acknowledgements

I wish to acknowledge and thank my supervisors Dr. E. C. Finch and Dr. R. C. Barklie for their great help and support during the execution and writing of this thesis. I would also like to thank everybody in the lab, namely J. Coleman, D. J. Carey C. Hogan and B. Holm. Also thanks to everybody in the physics department: C. Smith, P. Flanagan, T. Burke, J. Kelly and anybody I forgot to mention.

Abstract

Electron paramagnetic resonance (EPR) measurements have been made on films of hydrogenated amorphous carbon (a-C:H) and ion implanted 6H-SiC. We examine several sets of a-C:H films. The first and second sets of films were grown by plasma-enhanced chemical vapour deposition (PECVD) on the ground electrode, which produces polymeric a-C:H, the thickness is varied in the first set of a-C:H films while the nitrogen content is varied in the second. The third set of a-C:H films was grown, on the live electrode and deposited with a range of negative self-bias voltages (V_b), from 50 to 540V. This produced films with structures ranging from diamond-like a-C:H (DLC) to graphite-like a-C:H (GLHC). A fourth set of a-C:H films was produced by magnetically confined PECVD, these films initially had a DLC structure (without nitrogen) and were produced with various nitrogen contents. In the first (polymeric a-C:H) set we find two defects are present, one due to defects from the Si substrate and possibly at the C/Si interface the second defect due to carbon dangling bonds, uniformly distributed through the bulk of the film. Increasing the nitrogen content in the second set of films (polymeric a-C:H,N) had no major effect on the EPR spectra. Increasing V_b from 50 to 540V in the third set of films causes the ΔB_{pp} to fall, the spin concentration to increase from $2\times10^{17}cm^{-3}$ to $\approx2\times10^{20}cm^{-3}$ while g_0 remains constant. Relaxation time measurements (T_1, T_2) reveal that exchange narrowing is taking place in these a-C:H films produced with V_b above 100V. The EPR measurements were made on a fourth set of nitrogenated a-C:H films (V_b=10 and V_b equivalent to ≈100V), containing a range of nitrogen contents (V_b=10V). Increasing the nitrogen content in the second a-C:H,N film (V_b equivalent to ≈100V) from 0 to 15at.% causes the spin concentration to drop sharply, the g-value to increase from 2.0025 to 2.0032 and the linewidth to decrease. We believe that the fall in the spin concentration is due to the recombination of unpaired electrons with electrons supplied by the nitrogen. EPR spectra taken at about 10K failed to reveal any evidence of unpaired spins localised on nitrogen. This indicated that nitrogen was an inefficient donor in a-C:H. The dependence on the anneal temperature, up to about 600°C, of the spin concentration, g-value, linewidth and lineshape has been measured for a-C:H films both with and without nitrogen. Also the dependence of the

relaxation times (T_1, T_2), up to 600°C, has been measured for a a-C:H film (V_b=400V).

Crystalline (0001) wafers of n-type 6H-SiC have been implanted with 200keV Ge^+ ions in the dose range 10^{12} to $10^{15}cm^{-2}$. EPR measurements have been made on these samples both before and after annealing them at temperatures in the range room temperature to 1500°C. The as-implanted samples have an isotropic asymmetric EPR spectrum whose linewidth increases with dose before falling when a continuous buried amorphous SiC layer is produced. This increase is interpreted in terms of the change in the heights of a line with g=2.0028(2), ΔB_{pp}=0.4mT associated primarily with carbon dangling bonds in the a-SiC and a line with g=2.0033-2.0039 of uncertain origin. The variation with anneal temperature of the populations of these defects is reported.

Table of contents

Chapter 1:

Amorphous hydrogenated carbon (a-C:H) : A review of its structure and properties.

Introduction 1.1

In recent years hydrogenated amorphous carbon (a-C:H) and nitrogenated a-C:H, (a-C:H,N), grown by plasma enhanced chemical vapour deposition (PECVD) have been attracting considerable interest. Much of this interest has been concerned with the use of a-C:H as a hard coating (Tsai and Bogy 1987). Also there has been interest in using polymeric a-C:H for the active material in electroluminescent (EL) devices (Kim and Wager 1988; Yoshimi et al. 1992) because it has a high photoluminescence (PL) efficiency (Cernogora 1997) and a wide band gap. Also polymeric a-C:H and a-C:H,N may be used in field-emission displays (Shah 1997).

The bulk of the work in this thesis is concerned with characterising the paramagnetic defects present in hydrogenated amorphous carbon and nitrogenated a-C:H. In this first chapter of the thesis we review the structures of a-C:H and how these structures are related to selected physical properties of amorphous hydrogenated carbon.

1.2 Carbon

We begin by examining the bonding configurations of carbon and the common crystalline allotropes of carbon.

The number of chemical compounds that contain carbon is many times greater than the entire number of compounds which do not contain carbon. This vast number of possible compounds containing carbon is made possible by the fact that carbon can bond with other carbon atoms forming chains, thousands of atoms long, or rings of varying sizes; these chains and rings can have cross-links and branches giving rise to a vast number of possible combinations. To these carbon atoms are normally attached

atoms of other elements predominantly hydrogen but also oxygen, nitrogen, chlorine, sulphur and many others. The formation of chains and rings by carbon is facilitated by the fact that carbon can bond in a number of possible configurations, i.e. carbon atoms can easily hybridise into the sp, sp^2 and sp^3 bonding configurations. This is in contrast with other group IV elements which mainly hybridise to the sp^3 configuration, e.g. Si. Figure 1.1 shows a schematic representation of these three hybridised configurations (taken from Robertson 1986, p. 318).

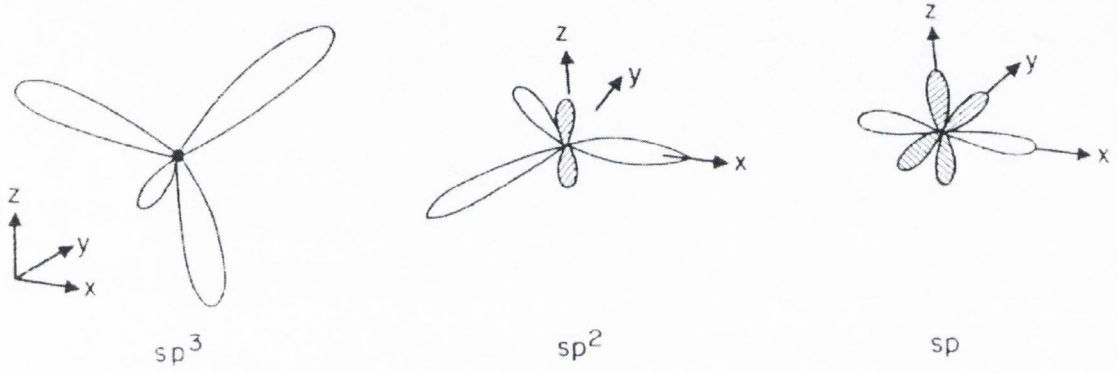

Figure 1.1 : Carbon hybrid bonding configurations.

The two major allotropes of pure carbon are graphite and diamond. These have very different physical and chemical properties due to the differences in their micro-structures.

Graphite is highly conductive, quite soft and chemically active while diamond is a electrical insulator, the hardest substance known and chemically inert (Lee 1991, pp. 407-408) . These differences in the physical properties of crystalline carbon are caused by their differing bonding configurations. Pure crystalline diamond contains carbon with sp^3 hybridised bonds. The crystalline lattice for diamond is shown in figure 1.2 (taken from Russell 1981, p. 597). The strength of the diamond lattice is due to the interlocking 3-dimensional structure composed of sp^3 hybridised sigma (σ) bonds. Each carbon atom is bonded to 4 other carbon atoms though 4 equivalent covalent bonds. The poor conductivity and chemical inertness of diamond originates from the fact that the 4 valance electrons on each carbon atom are involved in these 4 sigma (σ) covalent bonds.

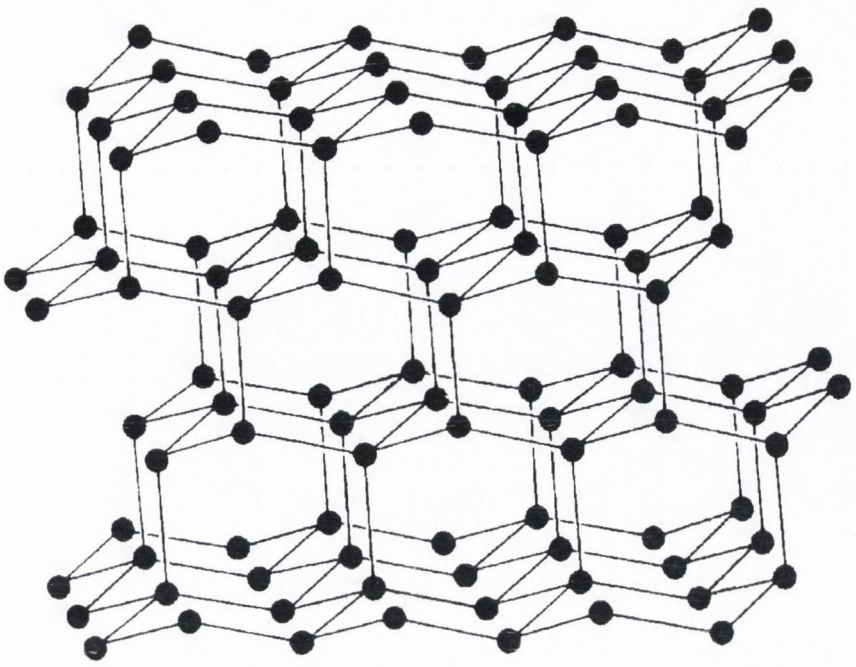

Figure 1.2 : Diamond lattice.

The structure of graphite on the other hand is made up of layers of sp^2 bonded carbon, these layers are held together by relatively weak van der Waals forces (otherwise called London forces) (Lee 1991, p. 408). Figure 1.3 shows the structure of an individual graphite layer and how these layers stack in graphite (taken from Russell 1981, p. 598). The carbon atoms in each layer are bonded to 3 other carbon atoms though 3 sp^2 hybridised, covalent, σ bonds. The remaining π-electrons (originally from the p_z atomic orbitals of the carbon atoms) delocalise over the entire graphite layer (Russell 1981, p. 598), analogous to the delocalisation seen in benzene. These delocalised π-electrons give rise to the high conductivity of graphite and also, since they are not strongly bound, to its chemical reactivity.

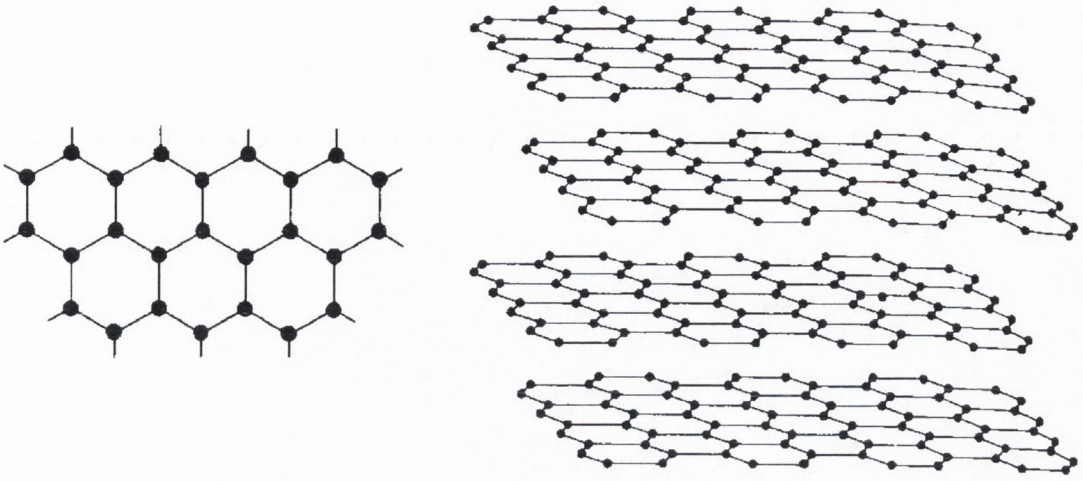

Figure 1.3 : Graphite lattice.

We can see that the presence of either sp^2 or sp^3 bonding has a significant effect on the structure, chemical and physical properties of these two allotropes of carbon. The structures and properties of amorphous carbon (a-C) and amorphous hydrogenated carbon (a-C:H) also depend strongly upon the amount of sp^2 and sp^3 hybridised carbon bonding within them.

In fact, in a-C:H films the ratio of sp^2/sp^3 bonding is one of the major parameters which controls the structure and properties of these films. a-C:H films with low hydrogen content and a high proportion of sp^3 bonded carbon might be expected to have similar physical and chemical properties to diamond. While a-C:H films with low hydrogen content and a high proportion of sp^2 would be expected to have properties similar to graphite. In fact this ratio of sp^2/sp^3 bonding together with the hydrogen content mainly determines the structure of a-C:H.

1.3 The structure of a-C:H

In this section of the chapter we review the possible structures of a-C:H. The two major factors which control the micro-structure of a-C:H are the ratio of sp^2 to sp^3 bonds within the film and the hydrogen content of the film. Unlike diamond and graphite a-C:H films are amorphous, so any comparison between a-C:H and the crystalline structures of diamond or graphite is only an approximation.

Figure 1.4 displays a ternary phase diagram showing how the sp^2/sp^3 ratio and the hydrogen content control the structure of a-C:H films (taken from Robertson 1996a and Giorgis et al. 1998).

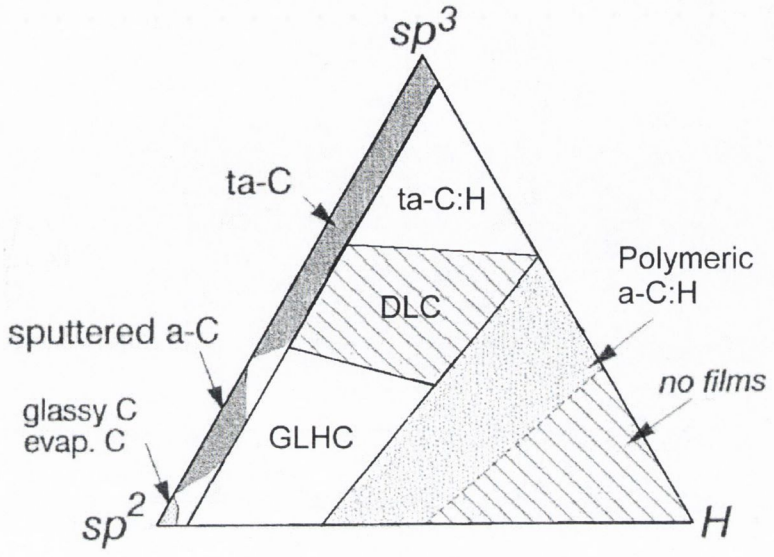

Figure 1.4 : a-C:H ternary phase diagram.

We can see in this phase diagram that depending on the sp^2/sp^3 ratio and the hydrogen content a-C:H can be divided into different types.

Amorphous tetrahedral carbon (ta-C or ta-C:H) which contains very little hydrogen and almost ~80% sp^3 bonded carbon has properties very similar to diamond, i.e. hard, chemically inert and an insulator. The term diamond-like carbon (DLC) is usually is used for a-C:H films containing a slightly lower sp^2/sp^3 ratio.

a-C:H films containing a very low amount of hydrogen and a high proportion of sp^2 bonding are sometimes referred to as graphite-like hydrogenated carbon (GLHC). The physical and chemical properties of this type of film are somewhat similar to those of graphite.

Films containing a high amount of sp^3 bonding and a high hydrogen content (≈50%) have chains of hydrocarbon. Such films have properties akin to organic polymers are thus called polymeric a-C:H or polymer-like a-C:H films.

These three cases are the extremes and in general the hydrogen content and the sp^2/sp^3 produces a-C:H films whose structure and properties are somewhere between these extremes. In fact a whole matrix of possible structures for a-C:H films can be produced by varying the hydrogen and sp^2 bonding content. Of course how close they are to these three extreme cases depends upon these two factors. These 3 terms

(DLC, GLHC and polymeric a-C:H) are only qualitative and are used to describe a-C:H films with a range of sp^2/sp^3 and hydrogen contents.

Robertson and O'Reilly (1987) and Robertson (1986) suggested that a-C:H contains what they term islands or regions of sp^2 bonded carbon. They believe that that in these regions of sp^2 bonding the carbon atoms exist in the form of fused aromatic rings. These aromatic clusters of sp^2 bonded carbon are separated from each other by a matrix of sp^3 bonded carbon. The π bonding energy is believed to be maximised by the formation of these aromatic clusters. The size of these clusters of aromatic rings depended upon the amount of sp^2 bonding present in the a-C:H film. Later Robertson (1996a) modified this model somewhat; he suggested that disorder in the structure of the film limited the size of aromatic clusters to one or two fused six-fold rings. He also suggested that the sp^2 bonded regions contain short olefinic chains of conjugated polymers intermixed with these aromatic rings. Figure 4.7 in chapter 4 shows a general schematic diagram of such a structure (taken from Robertson 1996a). Based upon his general schematic diagram we produced our own two-dimensional schematic structural diagrams for the DLC, GLHC and polymeric a-C:H films. Figure 1.5 shows the diagram for DLC, i.e. a-C:H films with a low hydrogen and sp^2 bonded content.

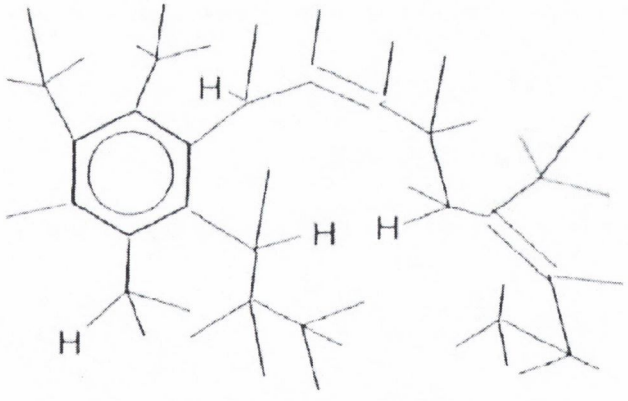

Figure 1.5 : Schmatic diagram for diamond-like a-C:H.

Figure 1.6 shows the diagram for GLHC, i.e. a-C:H films with a low hydrogen content and containing a high amount of sp^2 bonded carbon. Robertson (1996a) expected that the cluster size of fused six-fold aromatic ring to be limited by disorder to only one.

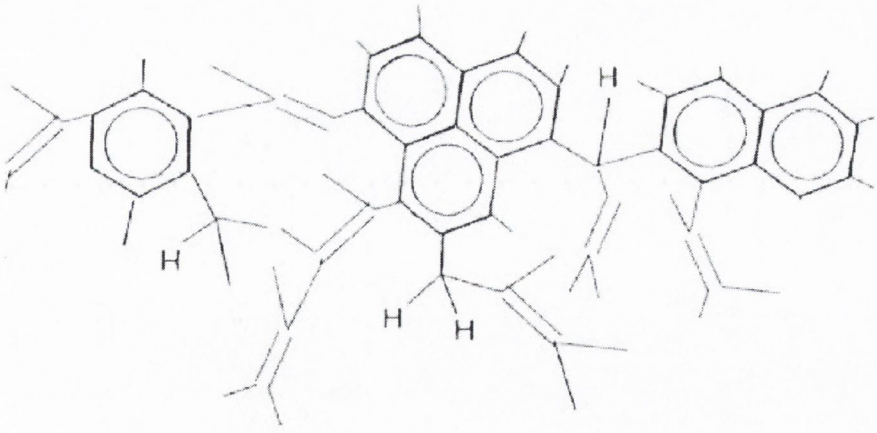

Figure 1.6 : Schmatic diagram for graphite-like a-C:H

And finally figure 1.7 shows the schematic structural diagram for polymeric a-C:H films, which contain a high amount of hygrogen and a low amount of sp^2 bonded carbon.

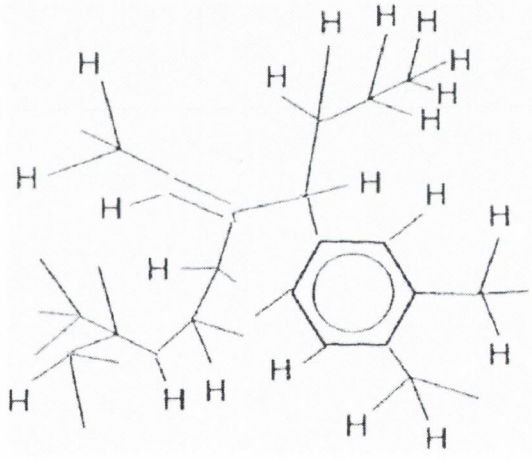

Figure 1.7 : Schmatic diagram for polymeric a-C:H.

All these possible a-C:H film structure may be produced by using different production methods, e.g. plasma enhanced chemical vapour deposition (PECVD), sputtering etc, and by varying conditions used during deposition.

We shall now look at how these structures can explain some of observed physical properties of a-C:H films.

1.4 Physical properties of a-C:H

In this section we consider how the physical properties of a-C:H can be related to the possible structures of the films just described.

1.4.1 Optical band gap of a-C:H

We first examine how the optical band gap of a-C:H is related to its structure. The optical band gaps can be measured in two different manners. The first termed the 'E_{04}' optical gap is measured by taking the photon energy at which the absorption coefficient (α) equals $10^4 cm^{-1}$. The second optical gap call the 'Tauc' gap is calculated from a plot of the square root of α times the energy ($(\alpha E)^{1/2}$) against the photon energy (E), the 'Tauc' gap is energy at which the extrapolated line, from the $(\alpha E)^{1/2}$ data, intercepts the x-axis (the energy axis).

In general a-C:H is a semiconductor as the structure of a-C:H lies between the two extremes of diamond and graphite. The size of the optical band gap in a-C:H films is controlled by the size of the sp^2 clusters which in turn is determined by amount of sp^2 bonded carbon within the film. Robertson (1996a, 1997) and Chhowalla et al. (1997) reported that the optical band gap decreased when the sp^2 content of the a-C:H films increased. Silva et al. (1996) and Rusli et al. (1996) found for their PECVD grown a-C:H films that the optical band gap fell with increasing negative self bias (V_b), as increasing V_b increases the sp^2 content of the films produced. This agrees with the results found by the others mentioned earlier. Also Weiler et al. (1996) found that the Tauc optical gap for ta-C:H decreased with increasing sp^2 content. The energy gap (E_g) depends basically upon the π-bonding present within the a-C:H film and not its hydrogen content (Robertson 1996a; Chhowalla et al. 1997). This idea is supported by the results obtained by Silva et al. (1996) where the hydrogen content remained between 24-20at.% with increasing negative self-bias voltage (V_b), which is proportional to the sp^2 content, while the optical band gap (the Tauc and E_{04} gap) fell by approximately 40%.). A schematic

density of states (DOS) diagram for a-C:H is shown in figure 1.8 (taken from Robertson and O'Reilly 1987).

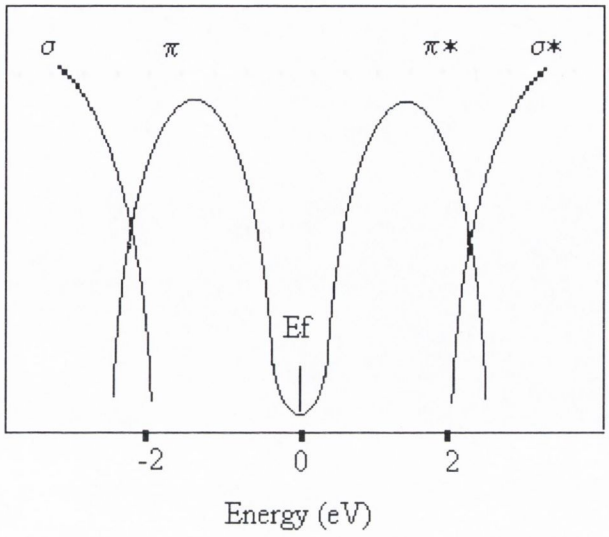

Figure 1.8 : Density of states (DOS) diagram for a-C:H.

The band gap (E_g) for a planar structure of fused six-fold aromatic ring was reported to be given by the following relationship (Robertson 1986),

$$E_g \approx 6 / M^{1/2} \text{ [eV]} \qquad (1.1)$$

Where M is the number of fused six-fold aromatic rings in each cluster.

This would account for the reduction in the optical band gap with increasing sp^2 content because the size of M would also increase and thus reduce E_g. This theory was later modified by Robertson (1996a) to take account of disorder which distorts the sp^2 structure and mixes the π and σ states within the film. This disorder limits the size of the aromatic clusters, i.e. M. So Robertson (1996a) states that E_g is related to the cluster size as follows,

$$E_g \approx 3 / M^{1/2} \text{ [eV]} \qquad (1.2)$$

Robertson (1996a) also found that the Tauc optical band gap (E_{Tauc}) decreases almost linearly with increasing sp^2 content and determined the following empirical relationship,

$$E_g \text{ (Tauc gap)} \approx 3.0 - 0.5z \text{ [eV]} \qquad (1.3)$$

Where z is the faction of sp^2 bonding within the film.

A similar linear relationship between the E_{04} optical gap and the negative self-bias voltage (V_b), which is correlated to the sp^2 content, was also observed by Rusli et al. (1996). The magnitude of the E_{04} gap is usually larger than the Tauc gap which agrees with the data analysed by Rusli et al. (1996) and Robertson (1996a).

As paramagnetic defects arise in a-C:H from unpaired π-electrons there is a relationship between the optical band and the spin concentration. The optical band gap increases as the paramagnetic defect density decreases (Silva et al. 1996; Robertson 1986, p. 366).

Annealing of various a-C:H films also causes a reduction in E_g with increasing annealing temperature. Fink et al. (1984) found that E_g falls from 1.20 to <0.5eV when the annealing temperature is raised from room temperature to 550°C, for one of their a-C:H films grown by plasma decomposition of benzene. Bounouh et al. (1993) found that for one of their a-C:H samples, E_{04} and E_{Tauc} falls from 3.30 and 2.50eV to 1.37 and 1.10eV respectively, after being annealed at 500°C. For the other a-C:H sample they examined, E_{04} and E_{Tauc} falls from 1.28 and 1.03eV to 0.90 and 0.83eV respectively, after being annealed at 500°C. We believe that annealing tends to graphitize the a-C:H films, i.e. increase the sp^2 content and therefore E_g should and does fall.

1.4.2 Electronic conductivity of a-C:H

We now examine how the electrical conductivity of a-C:H depends upon the structure of the film.

Conductivity as a function of temperature in most a-C:H films is found to closely follow a Arrhenius dependence ($\sigma=\sigma_0 exp(-\Delta E/kT)$) (Lin et al. 1991; Weiler et al. 1996; Ilie et al. 1998; Conway et al. 1998). This suggests that conduction is chiefly by thermal activation. The conductivity at a given temperature depends upon the activation energy (ΔE). Weiler et al. (1996) find that this activation energy (ΔE) increases with decreasing sp^2 content for their a-C:H films grown in a magnetically confined PECVD reactor (they term the deposition system a plasma beam source). So the activation energy required to promote electrons into the conduction band in certain a-C:H films is dependant upon the sp^2 content. The fact that Weiler et al. (1996) find $\sigma_0<10^3\Omega^{-1}cm^{-1}$ suggests that conduction, in their films, occurs by hopping between localised states on near-neighbour sites (Robertson 1986, p. 363), i.e. conduction by hopping in the band tails.

Orzeszko et al. (1984) also find that conductivity for their a-C:H films follow the Arrhenius relationship. They find that ΔE decreases with increasing annealing temperature. From EPR studies (Sadki et al. 1996; Austen et al. 1958; Miller and McKenzie 1983) it is believed that the sp^2 content of films increases with increasing annealing temperature. Therefore results of Orzeszko et al. (1984) supports the idea that ΔE increases as the sp^2 content of the film decreases.

This means, as we might expect that the electrical conduction depends upon the structure of the a-C:H films. It is easier to promote electrons into the conduction band in graphite-like a-C:H films than in diamond-like a-C:H films or polymeric a-C:H. This means that films with structures similar to figure 1.6, containing a high sp^2 and a low hydrogen content, have a higher conductivity relative to other a-C:H structures (figures 1.5 and 1.7).

1.4.3 Mechanical properties

Next we examine how the mechanical strength of a-C:H films depends upon the structure. Weiler et al. (1996) find that the Young's modulus and the mechanical hardness of a-C:H increases as the sp^3 content increases and the H content falls, i.e. going from polymeric a-C:H to diamond-like a-C:H. They also find that Young's modulus and the mechanical hardness of a-C:H films increase as the sp^3 content increases while the hydrogen content remains low, i.e. going from graphite-like a-C:H to diamond like a-C:H.

Thus as we expect structures similar to figure 1.5 have the highest mechanical hardness and Young's modulus. This is simply because it contains a high proportion of tetrahedral sp^3 C-C bonds, giving it similar mechanical properties to diamond.

1.4.4 Photoluminescence

Now we examine how the structure of the a-C:H film influences the photoluminescence properties of the film. As seen in figure 1.7 polymeric a-C:H may contain aliphatic chains and $-CH_3$ groups. These may give rise to electronic states with high energy ($\approx$7eV) and such states may act as energy barriers confining electrons to nearby aromatic clusters.

The aromatic clusters as mentioned earlier are separated by sp^3 regions. The clusters form single interacting systems and therefore is it appropriate to treat the films as a conventional amorphous semiconductor. Therefore the film has disorder-induced band tails, mobility edges and extended states (Robertson 1996b). Figure 1.9 shows a schematic diagram of the mechanism of photoluminescence (PL) in a-C:H. We see in this figure that luminescence occurs by photoexcitation and recombination between tail states within a sp^2 cluster. Non-radiative recombination occurs through tunnelling or hopping of the carrier to a defect site. Thus increasing paramagnetic defect concentration decreases the photoluminescence efficiency of the a-C:H films.

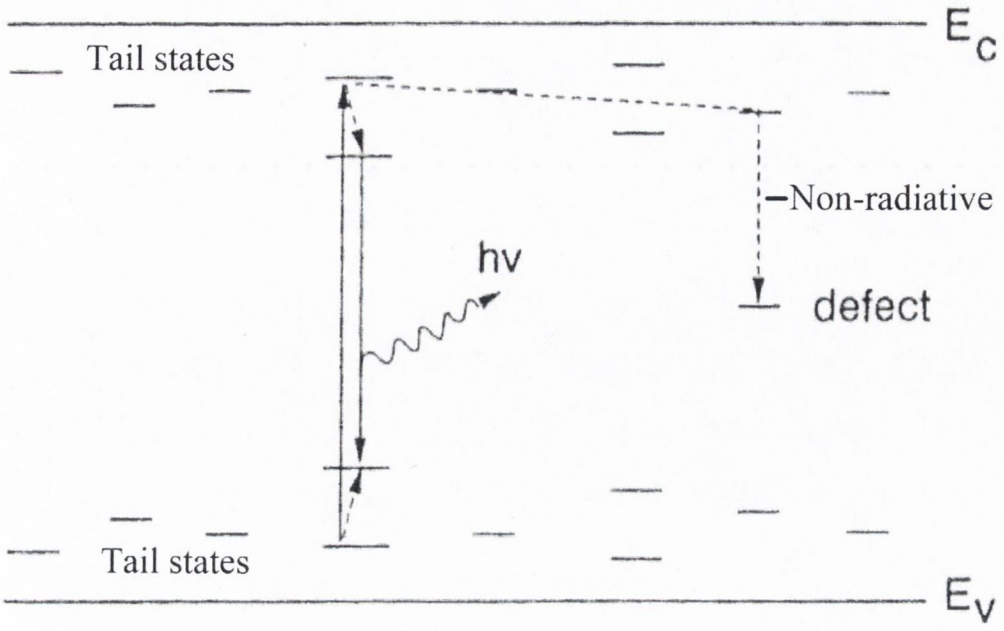

Figure 1.9 : Schematic diagram of the PL mechanism in a-C:H. (Robertson 1996b).

Such a relationship between the paramagnetic spin and the photoluminescence efficiency is reported by González-Hernández et al. (1988). Polymeric a-C:H is found to have the lowest number of paramagnetic defects (chapter 3 and 4), compared to DLC and GLHC and therefore polymeric a-C:H has the highest photoluminescence efficiency.

1.5 Conclusions

We have seen in this chapter that a-C:H has many possible structures which primarily depend upon the sp^2 and hydrogen content of these films. As a result of this three major categories of a-C:H exist. Diamond-like a-C:H (DLC) which contains a low sp^2 and hydrogen content, graphite-like a-C:H (GLHC) containing a high sp^2 and a low hydrogen content and polymeric a-C:H which has a low sp^2 and a high hydrogen content. We also have seen in this chapter that the structure of the a-C:H films has a major effect upon the physical properties of the film, such as electrical conductivity, photoluminescence, mechanical strength and the optical band gap. Paramagnetic defects are seen to have an effect upon the optical band gap and the photoluminescence of these films. Also the number and nature of paramagnetic defects are effected by the sp^2 content of a-C:H films (Weiler et al. 1996; Austen et al.

1958). Therefore electron paramagnetic resonance may be a very useful tool in examining a-C:H films.

1.6 References

Austen, D. E. G., Ingram, D. J. E. and Tapley J. G. (1958).Transactions of the Faraday Society, **54**, 400.

Bounouh, Y., Th⬟ye, M. L., Dehbi-Alaoui, A., Matthews, A., Cernogora, J., Fave, J. L., Colliex, C., Gheorghiu, A. and Sénémaud, C. (1993). Diamond and Related Materials, **2**, 259.

Cernogora, J. (1997). Physica Status Solidi, **201**, 303.

Chhowalla, M., Robertson, J., Chen, C. W., Silva, S. R. P., Davis, C. A. and Amaratunga, G. A. J. (1997). Journal of Applied Physics, **81**, 139.

Conway, N. M. J., Ilie, A., Robertson, J., Milne, W. I. And Tagliaferro, A. (1998). Applied Physics Letters, **73**, 2456

Djordjevi◖, B. R., Thorpe, M. F. and Wooten. F. (1995). Physical Review B, **52**, 5685.

Fink, J., M✧ller-Heinzerling, Th., Pfl✧ger, J., Scheerer, B., Dischler, B., Koidl, P., Bubenzer, A. and Sah, R. E. (1984). Physical Review B, **30**, 4713.

Giorgis, F., Tagliaferro, A. and Fanciulli, M. (1998). In Amorphous Carbon: State Of The Art, (ed. S. R. P. Silva, J. Robertson, W. I. Milne and G. A. J. Amaratunga), p. 143. World scientific, Singapore.

González-Hernández, J., Asomoza, R. and Reyes-Mena, A. (1988). Solid State Communications,

Ilie, A. Conway, N. M. J., Kleinsorge, B., Robertson, J. and Milne, W. I. (1998). Journal of Applied Physics, **84**, 5575.

Kim, S. M. and Wager, J. F. (1998). Applied Physics Letters, **53**, 1880.

Lee, J. D. (1991). Concise Inorganic Chemistry, (4^{th} edn). Chapman and Hall, London.

Lin, S., Noonan, K., Feldman, B. J., Min, D. and Jones, M. T. (1991). Solid State Communications, **80**, 101.

Miller, D. J. and McKenzie, D. R. (1983). Thin Solid Films, **108**, 257.

Orzeszko, S., Bala, W., Fabisiak, K. and Rozploch F. (1984). Physica Status Solidi, **81**, 579.

Robertson, J and O'Reilly, E. P. (1987). Physical Review B, **35**, 2946.

Robertson, J. (1986). Advances in Physics, **35**, 317.

Robertson, J. (1996a). Journal of Non-Crystalline Solids, **198-200**, 615.

Robertson, J. (1996b). Physical Review B, **53**, 16302.

Robertson, J. (1997). Philosophical Magazine B, **76**, 335.

Rusli, G., Amaratunga, G. A. J. and Silva, S. R. P. (1996). Optical Materials, **6**, 93.

Russell, J. B. (1981). General Chemistry, (International edn). McGraw-Hill, Auckland.

Sadki, A., Bounouh, Y., Theye, M. L., Von Bardeleben, J., Cernogora, J. and Fave, J. L. (1996).Diamond and Related Materials, **5**, 439.

Shah, I. (1997). In Physics World, (ed. P. Rogers), p.45. Institute of physics publishing, Bristol.

Silva, S. R. P., Robertson, J., Rusli, Amaratunga, G. A. J. and Schwan, J. (1996). Philosophical Magazine B, **74**, 369.

Tsai, H. and Bogy, D. B. (1987). Journal of Vacuum Science Technology A, **5**, 3287.

Weiler, M., Sattel, Giessen, T. S., Jung, K., Ehrhardt, H., Veerasamy, V. S. and Robertson, J. (1996). Physical Review B, **53,** 1594.

Yoshimi, M., Shimizu, H., Hattori, K., Okamoto, H. and Hamakawa, Y. (1992). Optoelectronic Device Technology, **7**, 69.

Chapter 2:

Introduction to electron paramagnetic resonance.

2.1 Introduction

This chapter outlines certain aspects of electron magnetic resonance. The discussion is limited to isotropic systems only and systems with only one unpaired electron per atom. The only exception is the anisotropic powder pattern which is also described. The electronic interactions giving rise to the standard 'Gaussian' and 'Lorentzian' EPR isotropic lineshapes are considered. The 'Voigt' lineshape is also examined. The dependence on the microwave field of the shape and intensity of a 'Lorentzian' EPR signal is explored. It is shown how from this the spin-lattice (T_1) and spin-spin relaxation times (T_2) can be found. The effect of temperature upon the EPR signal is also considered.

This chapter also describes the experimental methods used to carry out the work presented in this thesis.

Most of the work in this thesis is on hydrogenated amorphous carbon (a-C:H) films grown by plasma enhanced chemical vapour deposition (PECVD). This chapter examines the operation of PECVD reactors and the effects that deposition conditions have upon deposited a-C:H films.

.

2.1 Principles of electron paramagnetic resonance.

2.1.1 Introduction to electron paramagnetic resonance.

In this section of the chapter we will examine the basic principles of electron paramagnetic resonance (EPR).

Electron paramagnetic resonance (EPR) is spectroscopy based upon the resonant absorption of energy from an electromagnetic field when the magnetic dipoles are flipped over in a static magnetic field. In EPR the magnetic dipoles (or moments) usually arise primarily from electron spin angular momentum but there may also be a contribution for electronic orbital angular momentum. The effect by which electronic degenerate energy levels in paramagnetic materials become non-degenerate in the presence of an external magnetic field is called the Zeeman effect.

The energy of a magnetic dipole (moment) in a magnetic field B is given classically below:

$$E = \vec{\mu} \cdot \vec{B} \qquad (2.1)$$

For a quantum mechanical description we replace μ with the appropriate operator (Atherton 1993, p.9) which gives the following for a single electron with spin only angular momentum

$$\vec{H} = g_e \mu_B \vec{S} \cdot \vec{B} \qquad (2.2)$$

Where

B = The static magnetic field vector.

S = The electron spin operator.

μ_B = The Bohr magneton.

g_e = The free electron g-value which is 2.0023

If the static (external) magnetic field is in the z direction then the Hamiltonian becomes:

$$H = g_e \mu_B S_z B_0 \qquad (2.3)$$

Where

B_0 = The magnitude of the static magnetic field along the z-axis.

The eigenvalues of the only remaining operator on the right hand side of the equation, are M_S. The equation above becomes:

$$E = g_e \mu_B B_0 M_S \qquad (2.4)$$

The eigenvalues M_S are –½ and +½ for single unpaired electron and therefore the separation in energy between these two states is:

$$\Delta E = g_e \mu_B B_0 \qquad (2.5)$$

Electron paramagnetic resonance fundamentally involves the excitation of the electrons between these two levels by absorption of electromagnetic radiation though interaction with its magnetic component. This absorption of photons by the unpaired electrons is related to the photon frequency as follows:

$$\Delta E = h\nu = g_e \mu_B B_0 \qquad (2.6)$$

Where

h = Planck constant.

ν = Photon frequency.

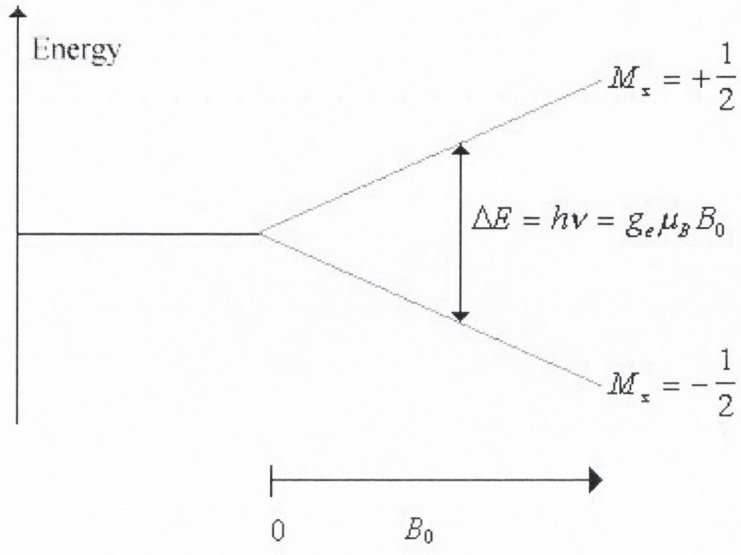

Figure 2.1 : The energy separation as a function of magnetic field.

In practice the angular orbital momentum generally has non-negligible effect on the overall angular momentum. The total angular momentum is a combination of the orbital and spin angular momentum.

$$\vec{J} = \vec{L} + \vec{S} \qquad (2.7)$$

This results in equation (2.2) becoming:

$$\vec{H} = g\mu_B \vec{J} \cdot \vec{B} \qquad (2.8)$$

and equation (2.6) becoming:

$$\Delta E = h\nu = g\mu_B B_0 \qquad (2.9)$$

The effect of a non-zero angular orbital momentum that the value g_e is replaced by the value g which is normally different from the free electron value. This parameter g is called the Landé g-value. This parameter is related to S,L and J by (Atherton 1993, p. 40):

$$g = \frac{3J(J+1) + S(S+1) - L(L+1)}{2J(J+1)} \qquad (2.10)$$

The measured g-value depends upon the atomic and electronic environment which surrounds the unpaired spins. In most solids (Poole 1983, p. 6) electronic orbital angular momentum interacts with the electric fields of the crystal lattice and becomes decoupled from the electronic spin angular momentum. This process is referred to as quenching. The greater this quenching the closer the measured g-value is to free electron value g_e. The difference in g-g_e is in fact a measure of the contribution of orbital angular momentum.

The above equation satisfies the first condition for interaction of magnetic component of electromagnetic with matter mentioned at the start of this chapter i.e. the energy supplied by the photons must equal the energy separation of the electron spin states. The second condition is associated with the polarisation of the magnetic component of the electromagnetic field. Classically a magnetic dipole (or moment) (μ) precesses about the axis of the external field (B_0) at the Larmor frequency ω_0 where

$$\omega_0 = \frac{g\mu_B B_0}{\hbar} \qquad (2.11)$$

Consider that a small magnetic field B_1 ($B_1 << B_0$), rotating about the z-axis, is added to the system. If the frequency ω of B_1 is different from ω_0 then the precessing magnetic moment (μ) is not seriously affected. But if $\omega_0 = \omega$ then B_1 will stay in phase with μ and the whole system will precess about B_1 as well as precessing about the B_0 axis. The frequency of this second precession is:

$$\omega_1 = \frac{g\mu_B B_1}{\hbar} \qquad (2.12)$$

$\omega_1 << \omega_0$ because $B_1 << B_0$ so therefore the magnetic dipole (moment) will relatively slowly oscillate between the extremes of a maximum projection on the +z-axis to a maximum projection on the –z-axis. This B_1 is of course supplied by the electromagnetic radiation. Although this is a classical picture and is not sufficient to explain EPR it does show that the magnetic component of the electromagnetic radiation must be circularly polarised in a plane perpendicular to the static magnetic field in order for a transition to take place. A quantum mechanical treatment can be found in Atherton (1986, p.522). Experimentally, a linear polarised field is used with

B_1 perpendicular to B_0. This component can be thought of as two counter rotating magnetic fields one of which is in phase with the original precession and causing the transition. The other has no effect on the precessing magnetic moment.

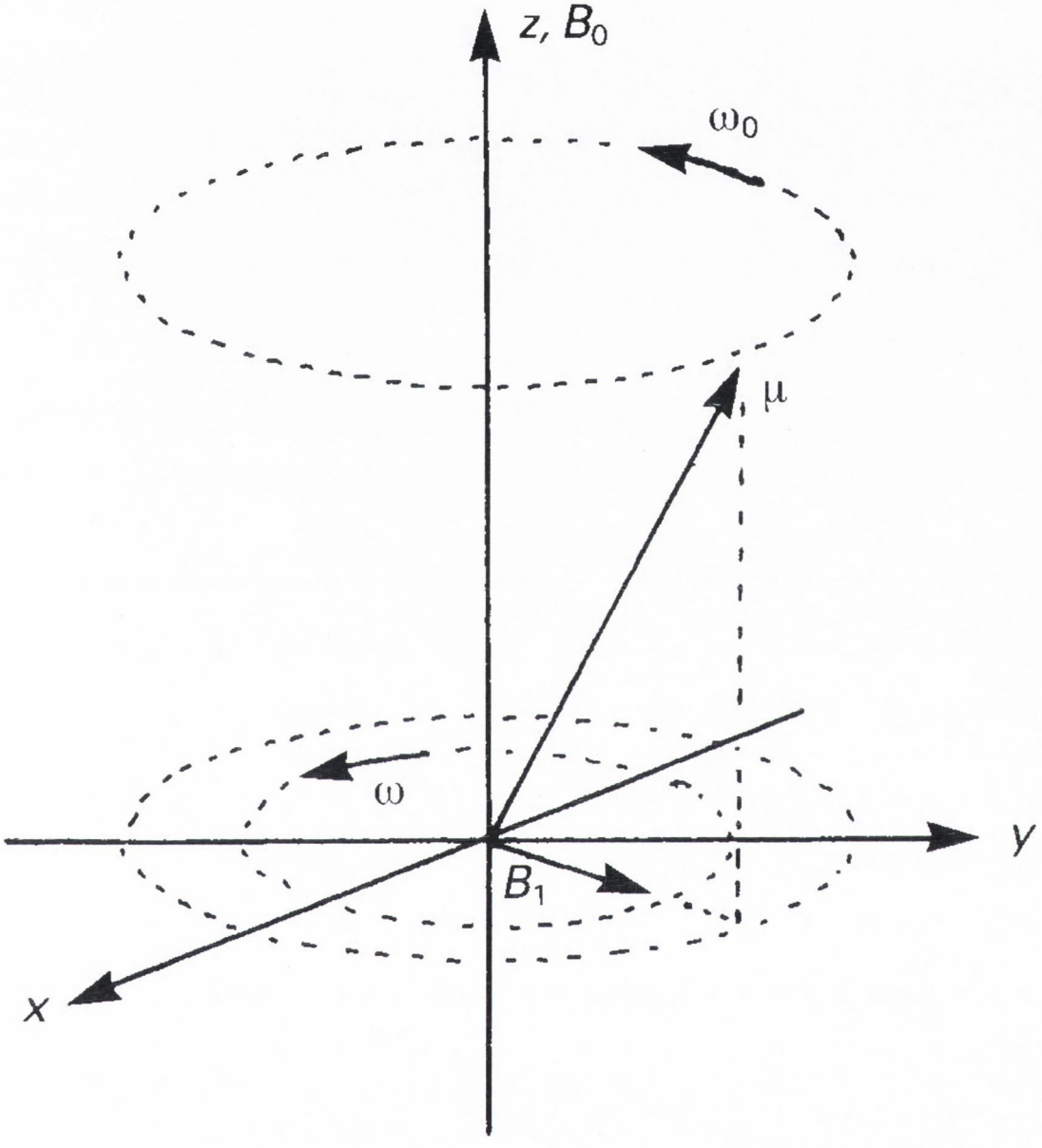

Figure 2.2 : Precession of a spin magnetic moment in an applied magnetic field, B_0. The magnetic moment can interact with a weak magnetic field, B_1, rotating in the xy-plane at a frequency ω if $\omega=\omega_0$. (Atherton 1993, p.13)

2.1.2 EPR lineshapes.

In sections 2.1.2 to 2.1.4 of this chapter we examine common EPR spectral lineshapes produced by paramagnetic defects. This knowledge will aid in our analysis of the experimental EPR spectra in the remaining chapters of this thesis.

During excitation of the electron spins, while carrying out EPR spectrometry, the populations of the spins in the upper and lower energy levels are no longer in thermal equilibrium with their surroundings. The populations continually decay back to thermal equilibrium during resonance and this process is called spin relaxation. The equations describing spin relaxation are described later in this chapter. This means obviously that the state has a finite lifetime. All spectral lines are not infinitely sharp. A state with a finite lifetime blurs its energy levels. This is similar to the Heisenberg uncertainty principle. This blur in energy levels allows EPR absorption above and below the exact magnetic field required for resonance (equation 2.9), giving the resonance line a finite linewidth. Other factors may further broaden the resonance linewidth and are dealt with below.

The two most commonly occurring spectral lineshapes in EPR are the Gaussian and Lorentzian. The two different lines arise from different types of spectral line broadening. The two major types of spectral broadening are homogeneous and inhomogeneous.

Poole (1983, p. 583) lists several causes of homogeneous broadening which are as follows:

1. Dipolar interaction between like spins.
2. Spin-lattice interaction.
3. Interaction with the radiation field.
4. Motion of carries in the microwave field
5. Diffusion of excitation though the sample
6. Motionally narrowed fluctuations in the local field.

Homogeneously broadened lines are Lorentzian in shape.

An inhomogeneously broadened EPR signal is actually a spectral distribution of distinct homogeneously broaden lines combined into a single envelope

(distribution). The case for a Gaussian envelope is shown in figure 2.3. The individual homogeneously broadened lines are all Lorentzian in shape.

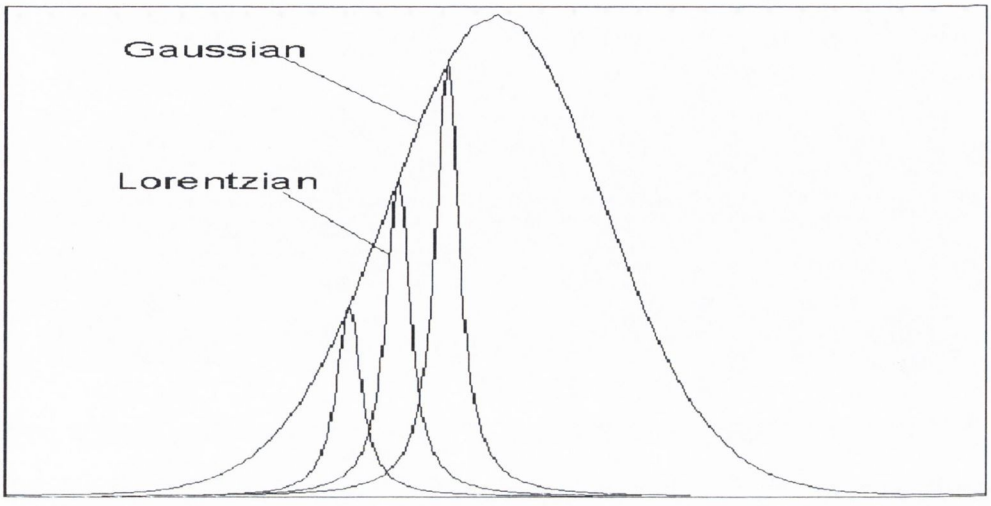

Figure 2.3 : Lorentzian lines in a Gaussian envelope

Poole (1983, p. 583) gives several sources of inhomogeneous broadening:

1. The static magnetic field is inhomogeneous over the volume of the sample being examined. (This is purely an experimental problem).
2. Unresolved fine and hyperfine structure.
3. Dipolar interaction between dissimilar spins. This is basically a conglomeration of spins with distinct g-values.

In general there are three lineshapes which exist due to the mechanisms mentioned above:

1. A Homogeneously broadened line which has a Lorentzian shape.
2. A inhomogeneously broaden line which has a Gaussian shape.
3. A Voigt profile. This is a convolution of the Lorentzian and Gaussian components caused by the presence of both homogeneous and inhomogeneous broadening mechanisms. This type of line is dealt with in section 2.1.3.

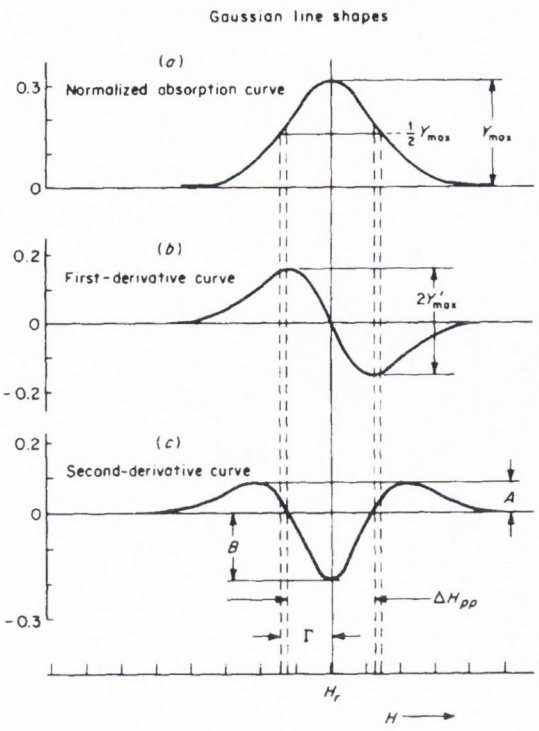

Gaussian line shapes. (*a*) Absorption spectrum. (*b*) First-derivative spectrum. (*c*) Second-derivative spectrum.

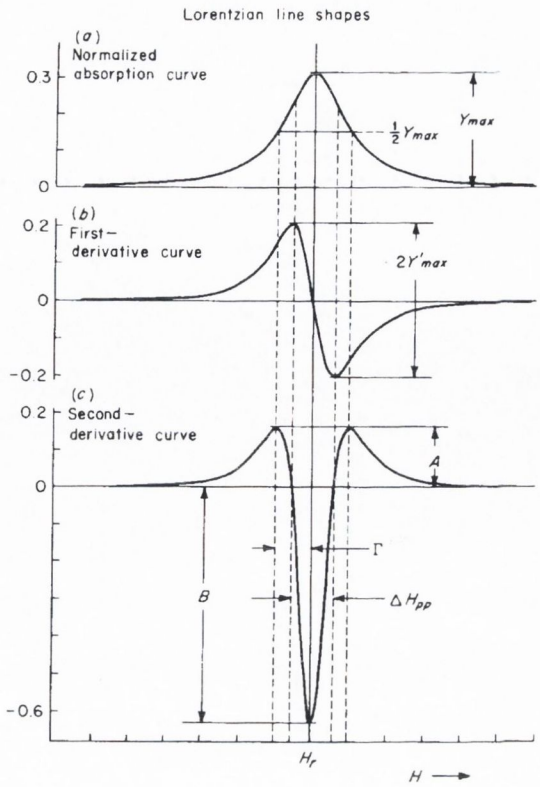

Lorentzian line shapes. (*a*) Absorption spectrum. (*b*) First-derivative spectrum. (*c*) Second-derivative spectrum.

Figure 2.4 : Lorentzian and Gaussian lineshapes (Wertz and Bolton 1986, pp. 34-35).

	Line shape	
	Lorentzian	*Gaussian*
Equation for normalized line	$Y = Y_{max}\frac{\Gamma^2}{\Gamma^2 + (H - H_r)^2}$	$Y = Y_{max}\exp\left[\frac{(-\ln 2)(H - H_r)^2}{\Gamma^2}\right]$
Peak amplitude	$Y_{max} = \frac{1}{\pi\Gamma}$	$Y_{max} = \left(\frac{\ln 2}{\pi}\right)^{\frac{1}{2}}\frac{1}{\Gamma}$
Half-width at half-height	Γ	Γ
Equation for first derivative	$Y' = -Y_{max}\frac{2\Gamma^2(H - H_r)}{[\Gamma^2 + (H - H_r)^2]^2}$	$Y' = -Y_{max}\frac{2(\ln 2)(H - H_r)}{\Gamma^2}\exp\left[\frac{(-\ln 2)(H - H_r)^2}{\Gamma^2}\right]$
Peak-to-peak amplitude	$2Y'_{max} = \frac{3\sqrt{3}}{4\pi}\frac{1}{\Gamma^2}$	$2Y'_{max} = 2\left(\frac{2}{\pi e}\right)^{\frac{1}{2}}\frac{\ln 2}{\Gamma^2}$
Peak-to-peak width	$\Delta H_{pp} = \frac{2}{\sqrt{3}}\Gamma$	$\Delta H_{pp} = \left(\frac{2}{\ln 2}\right)^{\frac{1}{2}}\Gamma$
Equation for second derivative	$Y'' = -Y_{max}2\Gamma^2\left(\frac{\Gamma^2 - 3(H - H_r)^2}{[\Gamma^2 + (H - H_r)^2]^3}\right)$	$Y'' = -Y_{max}\frac{2\ln 2}{\Gamma^4}\{\Gamma^2 - 2(\ln 2)(H - H_r)^2\}\exp\left[\frac{(-\ln 2)(H - H_r)^2}{\Gamma^2}\right]$
Peak amplitude of positive lobe	$A = Y_{max}\left(\frac{1}{2\Gamma^2}\right)$	$A = Y_{max}\frac{4e^{-\frac{3}{2}}\ln 2}{\Gamma^2}$
Peak amplitude of negative lobe	$B = -Y_{max}\left(\frac{2}{\Gamma^2}\right)$	$B = -Y_{max}\frac{2\ln 2}{\Gamma^2}$

Table 2.1 : Equations for Lorentzian and Gaussian lineshapes (Wertz and Bolton 1986, p. 33)

Figure 2.4 shows the shape of the Lorentzian and Gaussian lines along with their first and second derivatives. Table 2.1 gives the parameters and equations describing these lines.

EPR spectra in this work are recorded as the first derivative of their absorption spectra. Table 2.1 gives the equations for the 1st derivative Gaussian and Lorentzian lineshapes. Using a computer these equations are used to fit the experimental EPR spectra and thus the broadening mechanisms may be interpreted. The next section describes the equations required to describe the Voigt lineshape.

2.1.3 Voigt convolution profile.

In the general case of inhomogeneous broadening of the EPR signal the lineshape is a convolution of a Gaussian and Lorentzian line. Figure 2.3 shows the make up of this signal which can be thought of as a summation of Lorentzian lines in a Gaussian envelope. Between two extremes of Gaussian and Lorentzian this lineshape is called a Voigt profile or lineshape. This section outlines the equations required to simulate an EPR spectrum which exhibits a Voigt profile instead of the more common Lorentzian or Gaussian lineshape.

Poole (1983, p. 490) states that the Voigt lineshape has the following form.

$$Y(B-B_0)=\frac{\sqrt{(\ln 2)}}{\pi}\left(\frac{{}^{L}\Delta H_{1/2}}{{}^{G}\Delta H_{1/2}}\right)\int_{-\infty}^{\infty}\frac{e^{-x^2}\,dx}{\left({}^{L}\Delta H_{1/2}/{}^{G}\Delta H_{1/2}\right)^2\ln 2+\left(2\sqrt{\ln 2}\left[(B-B_0)/{}^{G}\Delta H_{1/2}\right]-x\right)^2}$$

(2.13)

where
${}^{L}\Delta H_{1/2}$ = The full width at half maximum for the Lorentzian component.
${}^{G}\Delta H_{1/2}$ = The full width at half maximum for the Gaussian component.
B_0 = The magnetic field at which the resonance occurs.

In order to simulate an EPR 1st derivative spectrum differentiation of equation 2.13 is necessary. The spectrum which we wish to simulate has two experimentally measurable parameters, namely the total peak-to-peak width of the Voigt lineshape (${}^{V}\Delta B_{pp}$) and B_0. The only other parameter required to simulate the Voigt EPR

lineshape is the ratio (V_R) of the peak-to-peak linewidth of the Lorentzian component ($^L\Delta B_{pp}$) to Gaussian component ($^G\Delta B_{pp}$). From these three parameters all the necessary variables in equation 2.13 can be found.

Stoneham (1972) gives a relationship between the total Voigt linewidth ($^V\Delta B_{pp}$) and $^L\Delta B_{pp}$ and $^G\Delta B_{pp}$. By rearrangement of the Stoneham (1972) formula we can calculate from $^V\Delta B_{pp}$ and V_R ($V_R=^L\Delta B_{pp}/^G\Delta B_{pp}$) values for $^L\Delta B_{pp}$ and $^G\Delta B_{pp}$. The relationships are given below.

$$^G\Delta B_{pp} = \frac{^V\Delta B_{pp} + 0.4621\,^V\Delta B_{pp} \times V_R}{1 + 0.9085V_R + 0.4621V_R^2} \quad (2.14)$$

$$^L\Delta B_{pp} = {}^G\Delta B_{pp} \times V_R \quad (2.15)$$

And from the equations in table 2.1 $^L\Delta B_{pp}$ and $^G\Delta B_{pp}$ are related to $^L\Delta H_{1/2}$ and $^G\Delta H_{1/2}$ as follows.

$$^L\Delta H_{1/2} = \sqrt{3}\,{}^L\Delta B_{pp} \quad (2.16)$$

$$^G\Delta H_{1/2} = \sqrt{2\ln 2}\,{}^G\Delta B_{pp} \quad (2.17)$$

With all the variables in equation 2.13 now known it is possible to simulate a Voigt EPR signal. Since the integral in equation 2.13 has no analytical solution it can only be evaluated numerically. A computer program was written in order to do this and generate the simulated line. This program calculates values of Y (absorption curve) over a range of H (magnetic field, whose range is defined by the operator). For each simulated point Y the integral of x is calculated for a suitable range using Simpson's rule. A suitable range was found by trail and error to be x= -4 to +4 in steps of x that were proportional to the values of $^L\Delta H_{1/2}$ and $^G\Delta H_{1/2}$ used. The final simulated absorption Voigt line is then differentiated using the following equation

$$\frac{dy}{dx}(n) = \frac{1}{h}\left[y(n-2) - 8y(n-1) + 8y(n+1) - y(n+3)\right] \quad (2.18)$$

where

n is the n^{th} data point in 'm' equally spaced (along the x-axis) data points, 'm' is an even number

and h is equal to x(n)-x(n+1).

The final 1^{st} derivative Voigt line may then be used to fit measured EPR spectra by varying B_0, ${}^{V}\Delta B_{pp}$ and V_R.

2.1.4 Powder pattern lineshape.

When the spin-orbit coupling referred to in section 2.1.1 is strong (little quenching) the g-value may vary greatly from the free electron g_e value. Generally in these cases the Zeeman energy separation is dependant upon the angle the magnetic field makes with the axes of symmetry determined by the local environment surrounding the electron. The amount of anisotropy is dependant upon the strength of the spin-orbit coupling. This gives rise to an anisotropic g-value. The measured g-value now has an angular dependence. In general the g-value may be represented by a 3×3 matrix. This leads to equation 2.9 becoming:

$$\vec{H} = \mu_B \vec{B} \cdot \vec{g} \cdot \vec{J} \qquad (2.19)$$

When suitable principal axes are chosen this matrix becomes diagonal and this matrix is shown beneath:

$$\vec{g} = \begin{bmatrix} g_{xx} & 0 & 0 \\ 0 & g_{yy} & 0 \\ 0 & 0 & g_{zz} \end{bmatrix} \qquad (2.20)$$

For an arbitrary orientation of the crystal the g-value may be obtained from the equation below (Poole 1983, p. 7; Atherton 1993, p. 45):

$$g = (g_{xx}^2 \cos^2\theta_x + g_{yy}^2 \cos^2\theta_y + g_{zz}^2 \cos^2\theta_z)^{1/2} \qquad (2.21)$$

Where θ_x is the angle between the x-axis and the magnetic field, θ_y and θ_z are similarly defined.

If the g tensor has axial symmetry i.e. $g_{\|} = g_{zz}$ and $g_{\perp} = g_{xx} = g_{yy}$ equation 2.21 reduces to the following:

$$g = (g_{\perp}^2 \cos^2\theta + g_{\|}^2 \cos^2\theta)^{1/2} \qquad (2.22)$$

Where θ is the angle between the symmetry axis (along $g_{\|}$)and the magnetic field.

In certain solids such as amorphous, polycrystalline or powdered crystal all possible orientations relative to the magnetic field exist. If these solids have an anisotropic g-matrix as in equation 2.20 then the g-value will now spread over a range calculated by equation 2.21 for all possible angles or by equation 2.22 if the solid has axial symmetry. This spread in g-values is equivalent to a spread in the magnetic field at which resonance occurs (B_0) in equation 2.9. This resultant lineshape EPR is called a powder pattern. The shape of this powder pattern may be calculated by integrating equation 2.21 or 2.22 over all allowable angles for a suitable range of magnetic field. Assuming that the resonance at each possible angle is a delta function Poole (1983, p. 510) solved equation 2.20 analytically. Equations 2.21 and 2.22 must be solved numerically for a non-zero linewidth (Gaussian or Lorentzian). This is achieved by ourselves for equation 2.22 by writing the necessary computer program. Also we used commercially available software (from Bruker) to solve these equations and simulate EPR powder patterns.

2.1.5 Relaxation times.

In this section we deal with the equations needed to determine the spin-lattice (T_1) and spin-spin (T_2) relaxation times and how they are measured experimentally in this work. The section below deals only with the solutions for a S=½ homogeneously broadened system.

Prior to irradiation by microwaves the ratio of the population of the upper spin energy levels (N_2) to that of the lower spin energy levels (N_1) at thermal equilibrium is given by the Boltzmann distribution as follows:

$$\frac{N_2}{N_1} = \exp(\frac{-\Delta E}{kT}) = \exp(\frac{-h\nu}{kT}) = \exp(\frac{-g_e \mu_B B_0}{kT}) \qquad (2.23)$$

When the paramagnetic system is irradiated by microwaves transitions between the spin states occur. In the absence of relaxation eventually the population of the two levels would equalise (strictly speaking only after an infinite time) and the spin system is said to be saturated (Poole 1983, p. 577).

If no other process was involved the spin system would now have this infinite temperature after the irradiation was stopped and it would retain it forever. Of course the spins system loses its energy via vibration to the surrounding atomic lattice (in solids) at a rate of $1/T_1$. Where T_1 is called the spin-lattice relaxation time. These mechanisms ensure that the populations of the spins states return to their thermal equilibrium values after irradiation is stopped. Saturation only sets in when the microwave power is sufficient to significantly alter the thermal equilibrium populations. This is not the only mechanism by which the spins transfer energy. Because of inhomogeneities in the magnetic field experienced by each spin only certain spins will be at resonance with the microwaves. The spins can also transfer this energy amongst themselves a rate $1/T_2$ via dipolar and exchange interactions. T_2 is referred to as the spin-spin relaxation time. If the microwave power is sufficiently low the spins will remain in thermal equilibrium with each other. As saturation sets in at higher microwave powers the rate of energy absorption will slow down and eventually cease. Usually in solids $T_1 >> T_2$ (Poole 1983, p. 579).

The peak-to-peak height and linewidth of the EPR signal is related to T_1 and T_2 as follows (Poole 1983, p. 590-591):

$$h_{pp} \propto B_1 \left(\frac{1}{1 + B_1^2 \gamma^2 T_1 T_2} \right)^{3/2} \qquad (2.24)$$

$$\Delta B_{pp} = \frac{2}{\sqrt{3}\gamma T_2} \sqrt{1 + B_1^2 \gamma^2 T_1 T_2} \qquad (2.25)$$

$$\Delta B_{pp}^{0} = \lim_{B_1 \to 0} \Delta B_{pp} = \frac{2}{\sqrt{3}\gamma T_2} \qquad (2.26)$$

$$\gamma = \frac{g\mu_B}{\hbar} \cong 1.7609 \times 10^{11} \mathrm{T}^{-1}\mathrm{s}^{-1} \text{ (for g}\approx 2.00) \qquad (2.27)$$

Where
B_1 = The magnetic field of the rotating component of the incident microwaves (Proportional to the square root of the microwave power).
γ = The gyromagnetic ratio.
ΔB_{pp} = EPR 1st derivative linewidth.
h_{pp} = Peak-to-peak height of the of the EPR signal.

Using equation 2.24 it is possible to determine $T_1 \times T_2$ by plotting h_{pp} against B_1. When the resulting curve is fitted by computer using the least squares method the value of $T_1 \times T_2$ is obtained. Figure 2.5 shows the such a determination of $T_1 \times T_2$ for a sample of amorphous hydrogenated carbon. Because the defects studied in this work have g-values close to that of a free electron ($g_e \approx 2.00$) γ squared is taken to be $3.10 \times 10^{22} \mathrm{T}^{-1}\mathrm{s}^{-1}$.

Where the curve of h_{pp} against B_1 remains linear ($\sqrt{1 + B_1^2 \gamma^2 T_1 T_2} \approx 1$) the linewidth ΔB^0_{pp} is measured as the experimental linewidth. Using this linewidth and equation 2.26, T_2 can be calculated. T_1 can now be calculated by division of $T_1 \times T_2$ by T_2.

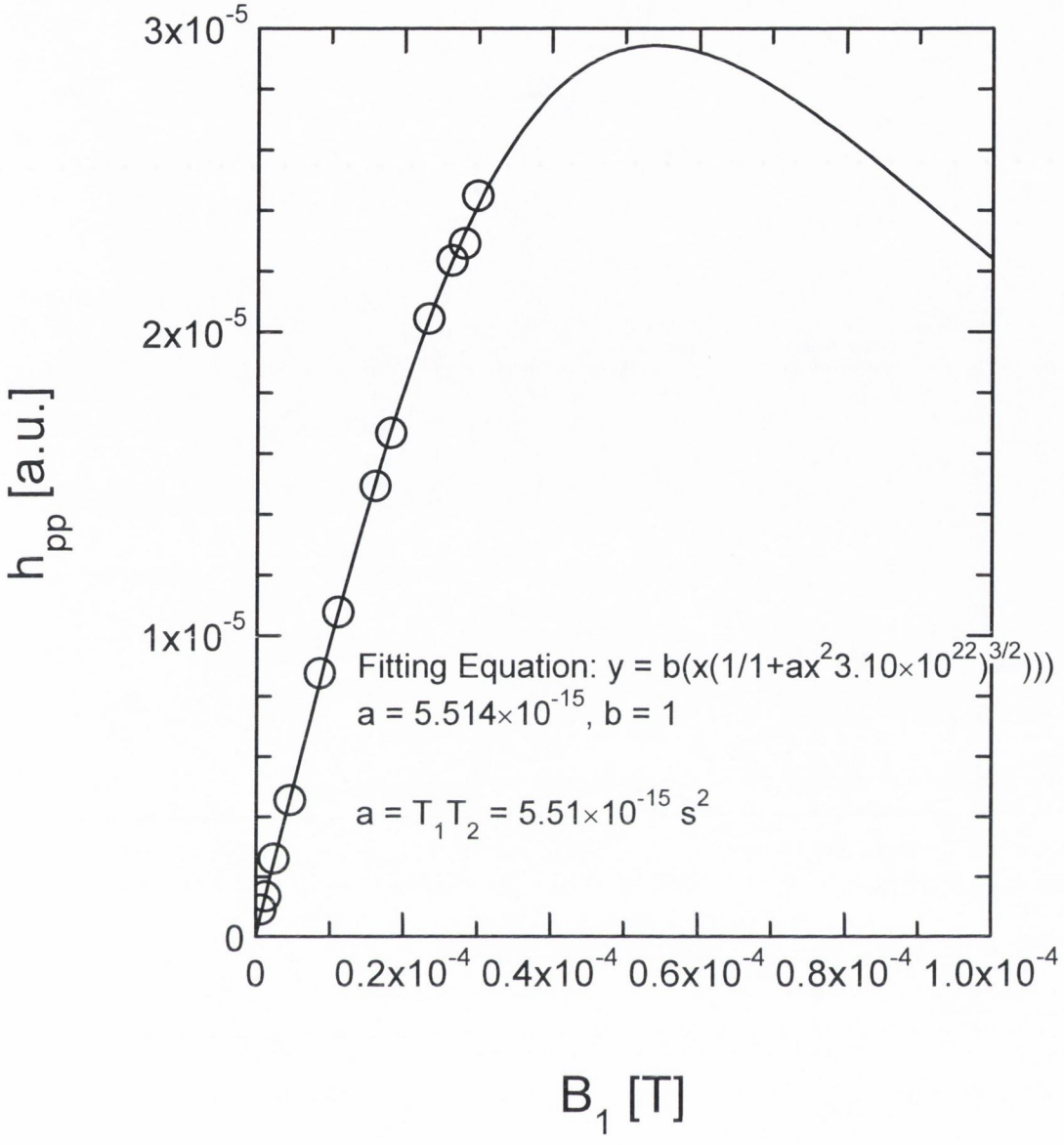

Figure 2.5 : h_{pp} against B_1 for the a-C:H film named DC160.

Experimentally only a ratio of the incident microwave power ($\sqrt{P/P_0}$) to the maximum incident power (P_0) can be determined. In order to calculate B_1 from this ratio a standard with known relaxation times (T_1 and T_2) is used. The standard used in this work is α-α-diphenyl-β-picryl-hydrazyl (DPPH). Bloembergen and Wang (1954) and Lloyd and Pake (1953) give values for T_1 and T_2 for DPPH. The values are T_1=6.4×10^{-8}s, T_2=6.0×10^{-8}s (Bloembergen and Wang 1954) T_1=6.3×10^{-8}s and T_2=6.3×10^{-8}s (Lloyd and Pake 1953). Bloembergen and Wang (1954) and Lloyd and Pake (1953) state that T_1=T_2 for DPPH. We take the average all these values and use T_1=T_2=6.25×10^{-8}s for DPPH.

In practice because of reduction of microwave power due to dielectric losses in the samples the calibration of B_1 is carried out with the DPPH and the sample together. The EPR signal from DPPH is much larger than the signal from sample being examined. Therefore only the DPPH signal is observed. This calibration is carried out for each sample studied because of different dielectric losses in each sample.

Since g = 2.0036 for DPPH (Poole 1983 , p. 443; Wertz and Bolton 1986, p. 465) therefore $\gamma = 1.7609\times10^{11}T^{-1}s^{-1}$ and $\gamma^2T_1T_2 = 1.21124\times10^{8}T^{-2}$. For DPPH equation 2.24 becomes:

$$h_{pp} \propto B_1\left(\frac{1}{1+B_1^2 1.21124\times10^{8}}\right)^{3/2} \qquad (2.28)$$

In order to calibrate $\sqrt{P/P_0}$ in terms of B_1 this equation is rewritten as follows:

$$h_{pp} = b\left(a\sqrt{P/P_0}\right)\left(\frac{1}{1+\left(a\sqrt{P/P_0}\right)^2 1.21124\times10^{8}}\right)^{3/2} \qquad (2.29)$$

This equation is fitted by computer using the least squares method and the values 'a' and 'b' are determined. Figure 2.6 shows the fitting of this equation on the experimental data for DPPH and an amorphous hydrogenated carbon sample (DC160). $B_1 = a\sqrt{P/P_0}$ so now it possible to plot h_{pp} against B_1 (as in figure 2.5) for a sample with unknown values of T_1 and T_2. This allows us as, mentioned earlier, to determine the values of T_1 and T_2 for the sample.

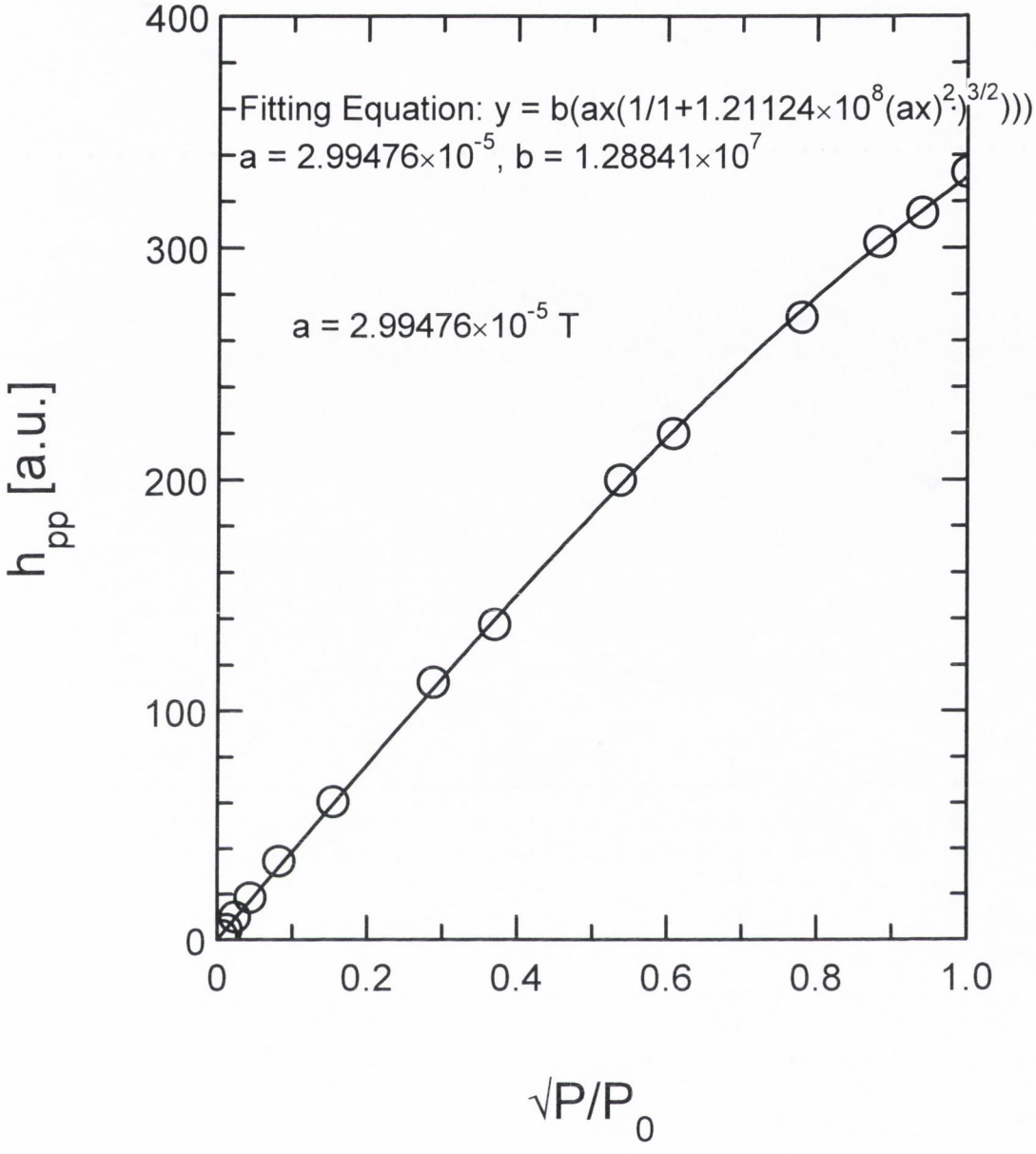

Figure 2.6 : h_{pp} against $\sqrt{P/P_0}$ for DPPH and a-C:H (DC160).

2.1.6 Temperature dependence.

This section of the chapter deals with the temperature dependence of common EPR signals. For a system with S = ½ the population of the spins in the upper (N_2) and the lower (N_1) energy levels is given by equation 2.23. Poole (1983 , p. 410) states that the height of the EPR signal is proportional to the difference in this population (N_1-N_2) and can determined by the following equation.

$$h_{pp} = h_{pp}^{0}\left(\frac{N_1 - N_2}{N_1 + N_2}\right) = h_{pp}^{0}\left[\frac{1-\exp\left(-\frac{h\nu}{kT}\right)}{1+\exp\left(-\frac{h\nu}{kT}\right)}\right] \qquad (2.30)$$

Where
h_{pp} = EPR signal height [a.u.]
h^{0}_{pp} = EPR signal height at $T = 0$ K

When $h\nu << kT \exp(-h\nu/kT) \cong 1 - -h\nu/kT$ and equation 2.30 becomes

$$h_{pp} = h_{pp}^{0}\left(\frac{h\nu}{2kT}\right) = h_{pp}^{0}\left(\frac{g\mu B_0}{2kT}\right) \qquad (2.31)$$

From this equation it can be seen that the EPR signal is proportional to $1/T$ (when $h\nu << kT$). It should be noted that the signal heights referred to are the height measured before saturation sets in i.e. where h_{pp} against B_1 remains linear (see section 2.1.5).

2.2 Experimental technique of EPR.

This section of the chapter deals with the actual EPR experimental set-up and how the spectrum is numerically analysed.

2.2.1 Experimental apparatus.

From the previous discussion in section 2.1.1 it is clear that in order to observe electron paramagnetic resonance the following are necessary;

1. An external static magnetic field in order to separate the otherwise degenerate spin states (The Zeeman effect). This static field must be slowly scanned though the resonance in order to detect the EPR transitions.
2. Microwaves with a sinusoidal magnetic component, B_1, perpendicular to the static magnetic field. This is required in order to stimulate EPR transitions (see section 2.1.1). In order to facilitate this a cavity within which microwaves resonate i.e. which sets up a standing wave is used,

samples are placed at the point at which B_1 is a maximum and at which B_1 is linearly polarised perpendicular to B_0.

3. A detection and recording system. Detection is by a diode and the recording system can be a chart recorder or a computer.

The EPR spectrometer used in this work contained a X-band microwave reflex klystron with a Hewlett-Packard power supply. The microwaves travel though waveguides to a critically coupled TM_{110} mode microwave cavity (work involving low temperature is carried out in a TE_{102} mode cavity). The frequency of the microwaves produced by the klystron was controlled by a Bruker automatic frequency control (AFC) unit. This frequency was measured using a digital frequency counter. This frequency is set to match the mode frequency of the resonant microwave cavity.

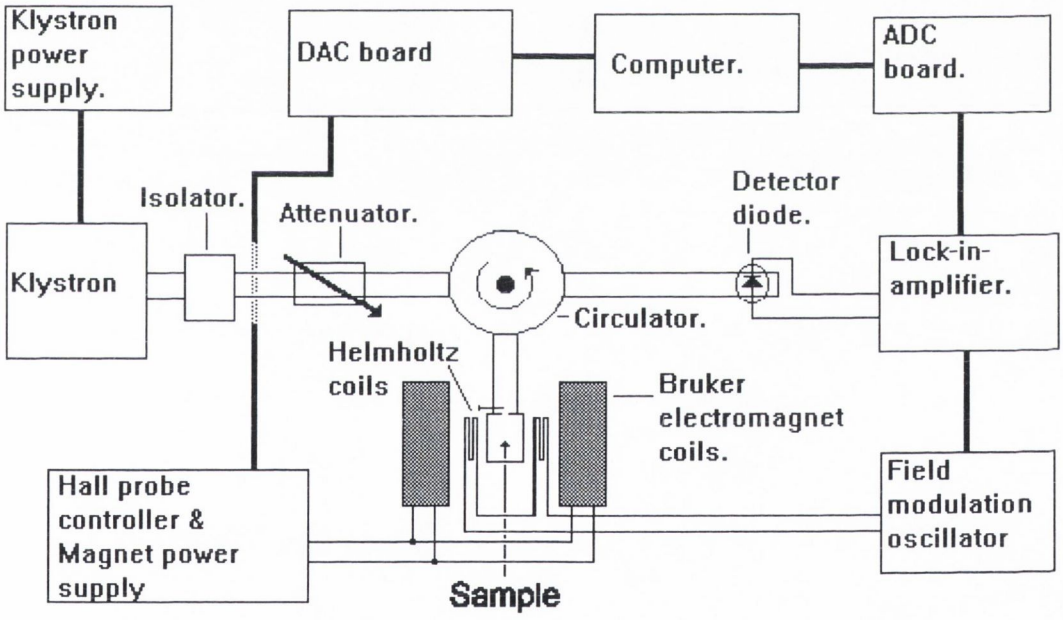

Figure 2.7: The main components of the EPR spectrometer.

The static magnetic field is supplied by a Newport electromagnet. This static magnetic field is regulated by a Hall probe and controller. This static magnetic field is perpendicular to the magnetic field component of the microwaves at the position of the sample. To reduce noise, phase sensitive detection is used, so a lock-in-amplifier is required. In order to use the lock-in-amplifier the static magnetic field is modulated. This modulation is obtained by Helmholtz modulation coils placed on

each side of the TM_{110} (TE_{102}) cavity. The static magnetic field is scanned via a computer connected to the Hall probe controller unit.

When the static magnetic field is scanned though the resonance (B_0) the sample inside the cavity absorbs microwave power; this causes the cavity to go out of critical coupling and causes some of the microwave power to be reflected from the cavity to the detector diode. The amount of power reflected is proportional to the power absorbed by the sample. This reflected signal which was modulated at 100kHz by the Helmholtz coils and is sent to the lock-in-amplifier (LIA) whose reference is connected to the oscillator driving the Helmholtz coils at 100kHz. The output of the LIA is sent to a computer via an analogue-to-digital converter (ADC) board for recording (or alternatively directly to a chart recorder). Because the EPR signal is obtained by the use of magnetic field modulation the recorded signal is the first derivative of the microwave power absorption curve (Wertz and Bolton 1986, p. 32).. In order not to distort the EPR signal, the magnitude of modulation is kept below one third of the linewidth of the smallest EPR feature of interest (Wertz and Bolton 1986, p.453).

2.2.2 Computerised analysis.

The determination of the number of paramagnetic centres in the various samples is carried out as follows.

First, correction factors for the dielectric losses caused by eddy currents produced by the microwave in each sample are determined. This correction factor will henceforth be referred to as the Q-correction factor. In order to calculate this Q-correction factor it is assumed that a sample of MgO containing F^+-centres (which is also used as a g-marker) has negligible dielectric losses. This means the Q-correction factor for the 'MgO g-marker' is 1 while a sample with dielectric losses has a value of less than 1. The EPR signal of this 'MgO g-marker' is first recorded with no other sample present in the TM_{110} cavity and then again under the same conditions of incident microwave power, gain and LIA phase settings with the sample also present. As the samples in this investigation have much smaller EPR signals than the 'MgO g-marker' the reduction in the recorded 'MgO signal' when a sample is present is assumed to be caused by dielectric losses in the sample only. The Q-correction factor

of the sample is worked out by dividing the peak-to-peak height of spectrum of sample plus MgO by the peak-to-peak height of the MgO on its own ($Q= h_{pp(Sample+MgO)}/h_{pp(MgO)}$).

Because the modulating magnetic field is not uniform a correction for a non point like samples must be used. The correction factor called 'the sample scale length factor' takes this into account (Sealy and Barklie 1992). The value of the correction factor may be looked upon as a calibration curve of 'sample scale length factor' against sample length. The length of the sample is measured along the axis joining the two access holes of the cavity.

Once the two correction factors for the sample are known the EPR signals of the sample are recorded. The various parameters of incident microwave power, gain, B-Field modulation amplitude, B-Field centre point, B-Field scan range, scan time and area of sample are also recorded. To calculate the spin population of each sample, the area under the absorption curve (i.e. the 2^{nd} integral of the EPR spectrum) of the sample is compared with the area under the absorption curve of a standard with a known number of spins. Pitch in KCl is used as the standard. The standard is placed in the cavity and its EPR signal recorded as well as its various collection parameters listed above. Since the area under the absorption curve is proportional to the B-Field modulation ($\Delta B_{pp(mod)}$), LIA gain, square root of the incident microwave power ($\sqrt{P}$) and inversely proportional to the B-Field scan range (ΔB) it must be normalised. The absorption area of the sample and standard are then normalised by dividing the absorption area by the LIA gain, $\sqrt{P}$, $\Delta B_{pp(mod)}$ and multiplying it ΔB. Then this normalised area was multiplied by the Q-correction factor (Q) and the sample scale length factor (k). The spin population is then calculated from the ratio of the corrected normalised sample area divided by the corrected normalised standard area multiplied by the total number of spins in the standard. Finally the total spin population in each sample is divided by its surface area in order to find the spin population per unit area, in order to compare one sample with another of different dimensions. This spin population per unit area is referred to as the areal spin population (N_A).

The total equation is listed below.

$$N_A = \frac{N_{std}}{Sample\ Area}\left(\sqrt{P^{std}/P^{s}}\,\frac{Q^{std}\,Area^{s}\,Gain^{std}\,\Delta B^{std}_{pp(\mathrm{mod})}\,k^{s}\,\Delta B^{s}}{Q^{s}\,Area^{std}\,Gain^{s}\,\Delta B^{s}_{pp(\mathrm{mod})}\,k^{std}\,\Delta B^{std}}\right)$$

Where
N_A = Areal spin population. [cm^{-2}]
N_{std} = Total number of spins in standard.
Sample Area = Surface area of sample. [cm^2]
$Area^s$, $Area^{std}$ = Area under the absorption curves of the sample and standard. [a.u.]
$Gain^s$, $Gain^{std}$ = Gain setting of the ADC times the setting of the LIA for the sample and standard respectively.
P^s , P^{std} = Incident microwave power on the sample and standard respectively. [a.u.]
Q^s , Q^{std} = Q-correction factors for the sample and standard.
k^s , k^{std} = The 'sample length scale factor' of the sample and standard.
$\Delta B^s_{pp(\mathrm{mod})}$, $\Delta B^{std}_{pp(\mathrm{mod})}$ = Peak to peak amplitude of the B-field modulation, for the sample and standard. [T]
ΔB^s, ΔB^{std} = B-Field scan ranges of sample and standard [T]

There are two methods of calculating the area under the absorption curve. The area in each case may be worked out by a double numerical integration of the EPR spectrum or the EPR signal peak-to-peak height may be used. The peak-to-peak height of the EPR signal is related to the area under the absorption curve by the following equation.

$$Area \propto k h_{pp} \Delta B_{pp}^2$$

Where
Area = Area under the absorption curve.[a.u.]
h_{pp} = EPR signal height.
k = Lineshape constant.
ΔB_{pp} = Peak to peak line width of signal.

The lineshape constant depends upon the type of lineshape in the EPR spectrum (Lorentzian = 1.82, Gaussian =0.511 and pitch in KCl =2.63). Since only the ratio of the areas under the absorption curves are used, the absolute values and units are unimportant. Both methods are used in this work, but the peak-to-peak signal height method can only be used if k is known.

The g-values of each sample are calculated using a sample of MgO containing F^+ centres as the g-marker. The EPR spectra of the sample and g-marker are collected for the same magnetic centre-field and scan range. The difference in magnetic field at resonance of the sample and g-marker is recorded. The magnetic field lags behind the voltage used to determine the magnet current. This lag will shift the EPR spectrum

and to allow for this the scan time (i.e. the lag) is kept constant for both the sample and g-marker. The g-values of each sample are calculated using the following equations. These equations are used for isotropic EPR signals only.

$$g = \frac{h\nu}{\mu_B B} \quad , \qquad B = \frac{h\nu_{std}}{g_{std}\mu_B} + K\Delta C$$

where
μ_B = Bohr magneton [$J.T^{-1}$]
h = Plank's constant [J.s]
ν = Microwave frequency for sample collected. [GHz]
ν_{std} = Microwave frequency for standard collected. [GHz]
ΔC = Difference in ADC channels between sample and the standard.
K = Calibration constant (depends on the range of magnetic field scanned).
[T $channel^{-1}$]
g_{std} = Known g-value for the standard.
g = g-value for the sample.

For our experimentally recorded EPR spectra, we quote g_0-values. This is found from the field at which the EPR spectrum crosses the zero baseline. In general it may be different from the actual g-values because it is possible the that there is more than one EPR spectral line present which normally produces an asymmetrical lineshape.

2.3 PECVD reactors

This section of the chapter will deal with the workings of PECVD (plasma enhanced chemical vapour deposition) reactors. Most of the work in this thesis is concerned with paramagnetic defects in a-C:H grown by PECVD. Therefore we will examine how the deposition conditions effect the structure of a-C:H films deposited by PECVD.

Figure 2.8 displays a typical PECVD reactor.

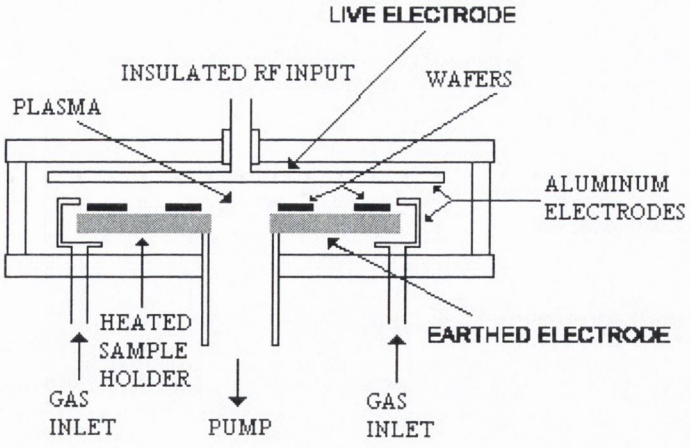

Figure 2.8 : A cross section of a typical PECVD reactor (Sze 1985, p. 355).

The typical reactor chamber consists of a cylindrical glass or aluminium chamber sealed with aluminium endplates. Inside a PECVD reactor there are two electrodes, usually aluminium, one earthed and the other live. A radio-frequency power supply is connected to the live electrode. Substrate wafers upon which the films are to be deposited may be placed on either the live or earthed electrode. Air is pumped out of the reactor chamber and reactant gases, which depend upon the type of film being deposited, are pumped into the chamber. Both the pressure inside the reactor and the reactants flow rates can be varied. The RF voltage produces a plasma between the electrodes. This energy supplied to the reactant gases by the RF voltage allows deposition of films within the chamber to occur at lower temperatures than necessary in conventional CVD deposition. This is one of the major advantages of PECVD. When depositing films in PECVD reactors the earthed electrode is usually used to support the substrate wafers. Commonly this electrode may be heated from ≈50 to ≈400°C by resistance heaters (Sze 1985, p. 356).

For depositing a-C:H films common reactant gases are methane (CH_4), butane (C_4H_{10}) and ethyne (acetylene) (C_2H_2). The reactant gas is usually combined with an inert noble gas such as He or Ar. The presence of the noble gas aids the formation of the plasma.

A negative self-bias (V_b) is induced between the live electrode and the plasma and this is dependant on the power supplied to the plasma by the radio-frequency power supply (Silva et al. 1996). This negative self-bias develops because of the greater mobility of the electrons compared to the ions in the plasma. A sheath forms above each electrode which maintains the plasma at a positive potential to the

electrodes. The smaller size of the live electrode causes this electrode to develop a net negative bias with respect to the grounded electrode. For films deposited upon substrates on the live electrode the kinetic energy of the ions accelerated towards the live electrode depends on both the pressure (P) and V_b (K.E. $\propto V_b P^{(-½)}$) (Bubenzer et al. 1983). Therefore the energy supplied to atoms in the plasma, impinging onto the live electrode, is controlled by the power of the radio-frequencies used. Films produced with ions having a low kinetic energy produce polymeric a-C:H films (Robertson 1993, 1994; Schwan et al. 1996). Such films may be produced on the earthed electrode as V_b between it and the plasma is very low (i.e. low kinetic energy) A greater acceleration of the ions, i.e. a larger V_b, would produce diamond like a-C:H films (DLC) (Weiler et al. 1996; Robertson 1993, 1994). While a further increase in the energy per atom (i.e. negative self-bias) would produce graphite like a-C:H (GLHC) (Weiler et al. 1996). Thus this negative self-bias can be used to control the sp^2/sp^3 ratio.

There also exists PECVD reactors with magnetically confined plasmas. A hollow cylindrical permanent magnet is placed around the plasma; the magnet is coated with a low sputter yield material to prevent sputtering of the magnet material during deposition. Magnetic confinement increases the ionisation of the plasma. This higher ionisation lowers the sheath resistance without effecting the electrode capacitance. This reduces V_b by roughly three fold compared to unconfined conditions. Thus magnetic confinement causes a higher ionisation and a lower self-bias voltage (V_b) at a given RF power (Silva et a. 1995).

2.4 References

Atherton, N. M. (1993). Principles of Electron Spin Resonance.

Ellis Horword and Prentice Hall, New York.Bloembergen, N. and Wang, S. (1954).

Physical Review, **93**, 72-83.

Bubenzer, A. Dischler, B. Brant, G. and Koidl, P. (1983). Journal of Applied

Physics,**54**, 4590.

Lloyd, J. P. and Pake, G. E. (1953). Physical Review, **92**, 1576.

Poole, C. P. (1983). Electron Spin Resonance, A Comprehensive Treatise On

Experimental Techniques, (2^{nd} edn). John Wiley and Sons, New York.

Robertson, J. (1993). Diamond and Related Materials, **2,** 984.

Robertson, J. (1994). Diamond and Related Materials, **3,** 361.

Schwan, J., Ulrich, S., Roth, H., Ehrhardt, H., Silva, S. R. P., Robertson, J., Samlenski,

R. and Brenn, R. (1996). Journal of Applied Physics, **79,** 1416.

Sealy, L. and Barklie, R. (1992). Journal of Magnetic Resonance, **97,** 611.

Silva, S. R. P., Clay, K. J., Speakman, S. P. and Amaratunga, G. A. J. (1995).

Diamond and Related Materials, **4**, 977.

Silva, S. R. P., Robertson, J., Rusli, Amaratunga, G. A. J. and Schwan, J. (1996).

Philosophical Magazine B, **74**, 369.

Stoneham, A. M. (1972). Journal of Physics D: Applied Physics, **5**, 670-672.

Sze, S. M. (1985). Semiconductor Devices: Physics and Technology. Wiley, New

York.

Weiler, M., Sattel, Giessen, T. S., Jung, K., Ehrhardt, H., Veerasamy, V. S. and

Robertson, J. (1996). Physical Review B, **53,** 1594.

Wertz, E. J. and Bolton, J. R. (1986). Electron Spin Resonance, Elementary Theory

and Practical Applications. Chapman and Hall, New York.

Chapter 3:

An EPR study of polymeric a-C:H and a-C:H,N

3.1 Introduction

Polymeric amorphous carbon has a high photoluminescence (PL) efficiency (Cernogora 1997) and a wide band gap and because of this it is a promising material for the active material in electroluminescent (EL) devices (Kim and Wager 1988; Yoshimi et al. 1992). Polymeric a-C:H and nitrogenated polymeric a-C:H,N may also be a suitable substance for use in field-emission displays (Shah 1997). Polymeric or polymer-like a-C:H (PLC) contains a high percentage of hydrogen (≈50at.%) and high percentage of sp^3 hybridised bonds. Because of the reported correlation between the spin concentration of paramagnetic defects in polymeric a-C:H and the photoluminescence efficiency (González-Hernández et al. 1988) and because is believed that paramagnetic defects act as non-radiative recombination centres (Robertson 1996b), it is of interest to examine the paramagnetic defects present in polymeric a-C:H. It is the aim of the work carried out in this chapter to study with EPR the paramagnetic defects in polymeric a-C:H grown by PECVD and to examine the effect of changing the film thickness, nitrogen content, annealing temperature, substrate deposition temperature and ion implantation dose of boron, carbon, and nitrogen.

3.2 Defects in polymeric a-C:H and the effect of changing the film thickness.

It is of interest to investigate the nature of the defects present in polymeric a-C:H films because of the conflicting cross-over g_0-values reported by several authors. These range from $g_0 \approx 2.0027$ (Giorgis et al. 1998; Miller and McKenzie 1983; Schutte et al. 1993; Rusli et al. 1995) to 2.0040-2.0045 (Ristein et al. 1995; Sadki et al. 1996). For diamond-like carbon (DLC) deposited upon Si substrates there is evidence that a SiC interface layer forms between the DLC layer and the Si substrate (Zhang et al. 1998). In fact the existence of a SiC interface layer between hydrogenated carbon layers and Si substrates has been reported by several groups (Sch·fer et al. 1997; Sandner et al. 1987; Ugolini et al. 1989; Kawasaki et al. 1990).

One aim of the measurements reported in this section of the chapter is to identify the defects present in polymeric a-C:H films. A further aim is to measure the depth profile of defects. To achieve these aims we shall examine the paramagnetic defects present in polymeric a-C:H as a function of the thickness of the film.

3.2.1 Sample preparation.

The samples used in this study were produced in a Plasma Technology DP800 radio frequency (13.56MHz) driven plasma enhanced chemical vapour deposition (PECVD) reactor. The details of this type of reactor have been dealt with in chapter 2. The deposited films were grown on the earthed electrode of the PECVD reactor. In this case the dc self-bias between the sample and the plasma is only a few volts. Due to the low accelerating bias the films produced in this manner are polymeric a-C:H (Robertson 1993, 1994; Schwan et al. 1996). A greater acceleration of the ions would be needed to produce diamond-like a-C:H films (Weiler et al. 1996; Robertson 1993, 1994). These samples were produced at the Electronic and Electrical Engineering Department of the University of Surrey by J. V. Anguita under the supervision of Dr. S. R. P. Silva.

Tables 3.1-3.3 show the thickness and the PECVD reactor conditions that were used in preparing these films. The substrates were (100) crystalline silicon. The

films were deposited using CH_4 with or without He and an RF power of 100W or 200W. Table 3.1-3.3 lists the PECVD deposition conditions.

The unit 'sccm' used in the following tables is a flow rate of a standard cubic cm per minute. A standard cubic cm is the equivalent volume a gas would have at standard temperature and pressure (S.T.P.) in cm^3. It is equivalent to $1/(2.24\times10^4)$ moles.

The substrates upon which the samples were deposited were given a five minute three-stage clean in methanol, propanone (acetone) and 2-propanol (isopropyl alcohol) and finally washed with distilled water. This was then followed by a 3 minute pre-clean in a He plasma (75sccm He, RF power:200W and pressure:200mtorr). The tables below list the subsequent film deposition conditions that were used.

Name	Thickness [nm]
Jar-2-33	5.1
Jar-2-32	6.8
Jar-2-30	8.4
RS004	21
Jar-2-31	22.6
RS003	55
RS002	80
RS001	168
RS005	330

Table 3.1 : Thickness of a-C:H films deposited with Plasma gas: 10sccm CH_4 only, RF power: 200W, Pressure: 200mtorr, Substrate at room temperature.

Name	Thickness [nm]
Jar-2-10	27.2
Jar-2-11	61.7
Jar-2-12	137.9
Jar-2-13	221.8
Jar-2-14	481.2

Table 3.2 : Thickness of a-C:H films deposited with Plasma gases: 30sccm CH_4 + 75sccm He, RF power: 100W, Pressure: 200mtorr, Substrate at room temperature.

Name	Thickness [nm]
Jar-2-35	11.4
Jar-2-36	30.5

Table 3.3 : Thickness of a-C:H films deposited with Plasma gases: 30sccm CH_4 + 75sccm He, RF power: 200W, Pressure: 200mtorr, Substrate at room temperature.

3.2.2 EPR results for polymeric a-C:H.

In this section we shall give the EPR results and analysis for polymeric a-C:H as a function of thickness. In figure 3.1 and figure 3.2 we display selected spectra as a function of thickness. Figure 3.1 shows spectra from the set of samples described in table 3.1 (Plasma = 10sccm CH_4 only, 200W, 200mtorr & RT) while figure 3.2 shows spectra from the samples described in table 3.2 (Plasma = 30sccm CH_4 + 75sccm He, 100W, 200mtorr & RT). The ordinate scale in these figures is arbitrary. The spectra for samples Jar-2-35 and Jar-2-36 (table 3.3) are not displayed because they were collected with over-modulation and so their shapes are distorted. Even so the two EPR spectra obtained for these samples are symmetric and very similar in shape to the spectrum in figure 3.2 of the sample with a thickness of 27.2nm.

It can be seen in both figures 3.1 and 3.2 that the shape of the EPR spectra for these samples varies with thickness. The asymmetry of the lineshape increases with increasing thickness. The total linewidth of the spectra can also be seen to increase with increasing thickness. The EPR spectra as a function of thickness for both sets of samples behave in a very similar manner. This similar behaviour indicates that changing the RF power from 100W to 200W has little effect on the defects present in polymeric a-C:H films.

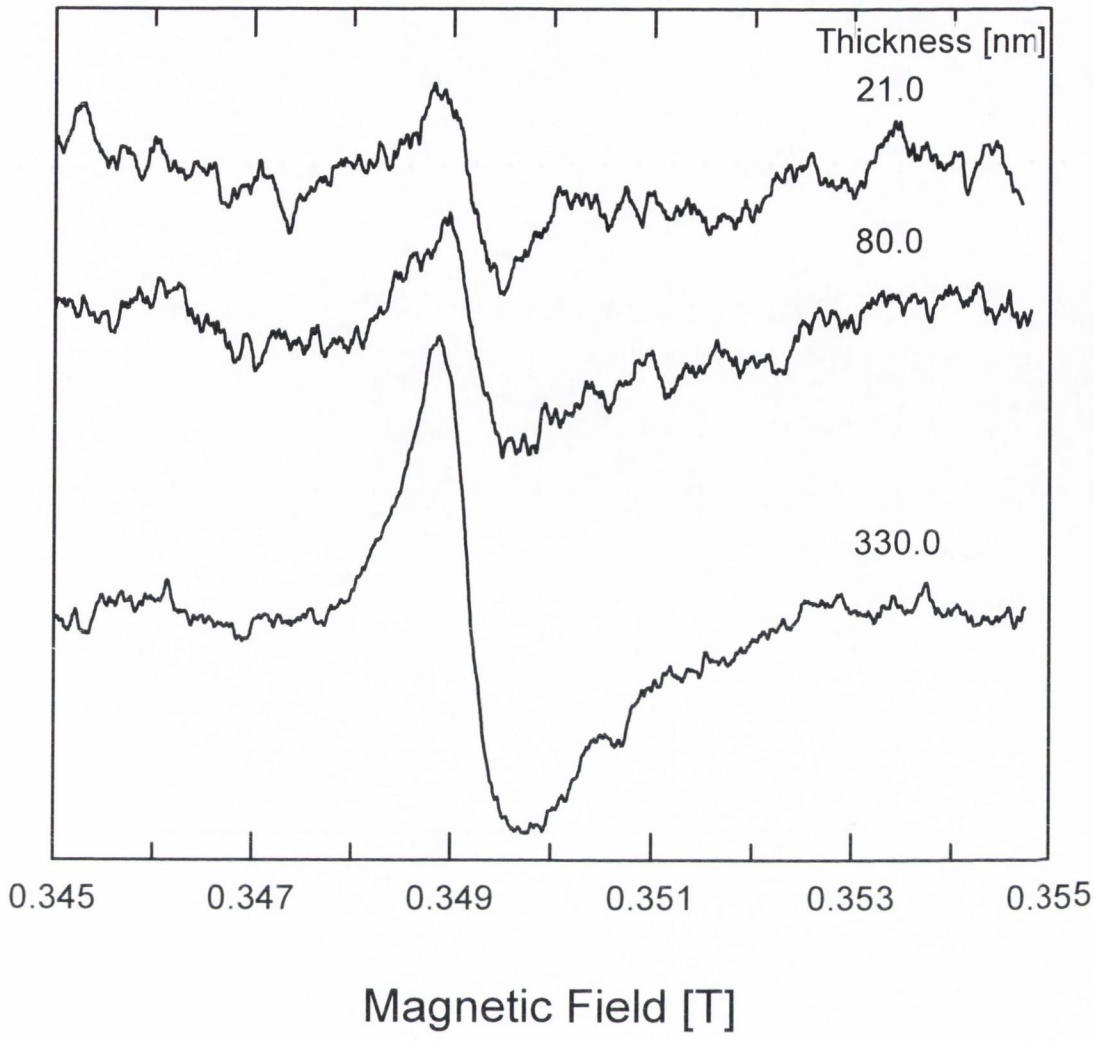

Figure 3.1 (ν = 9.8GHz): EPR spectra as a function of thickness. The deposition conditions used were Plasma = 10sccm CH_4 only, 200W, 200mtorr & RT (table 3.1).

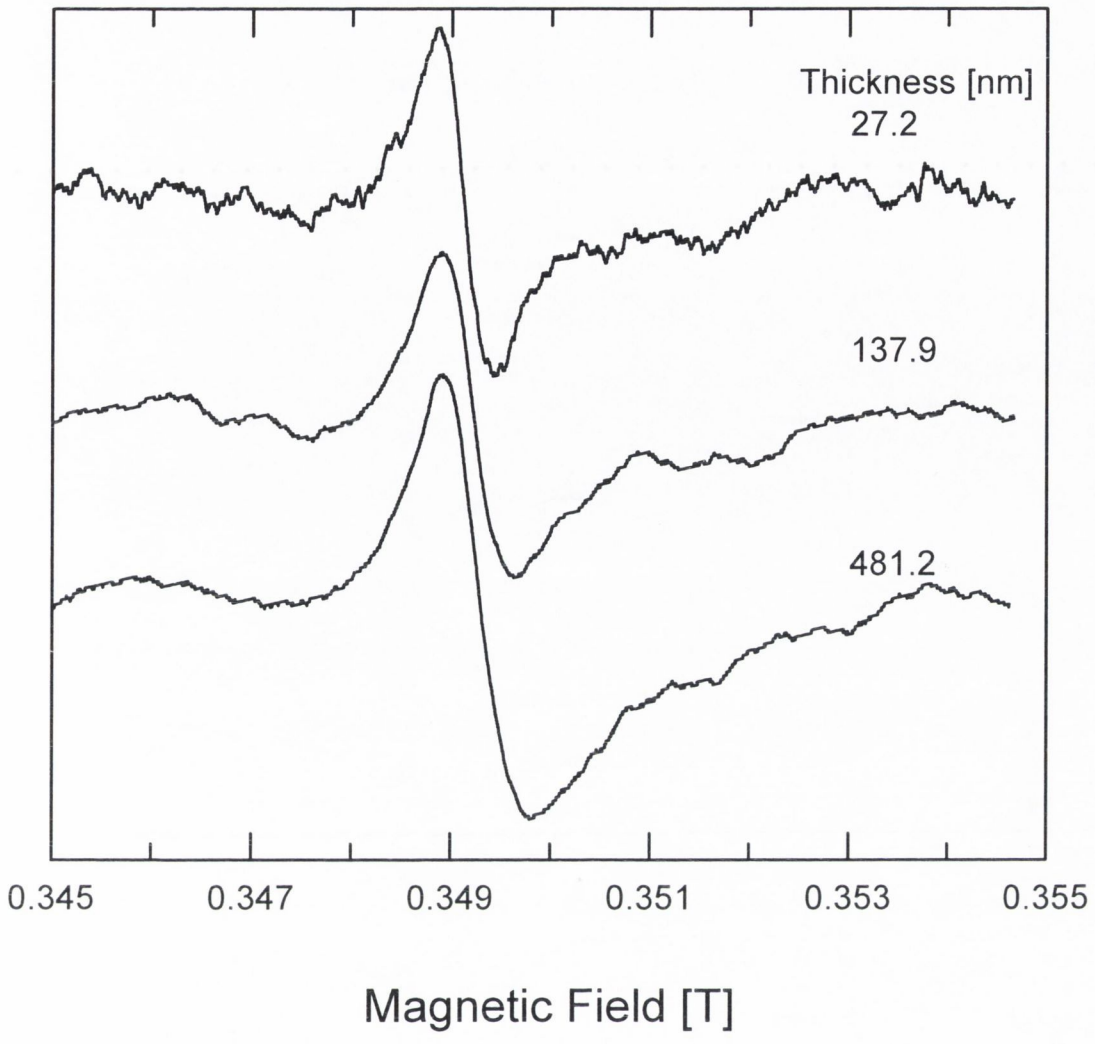

Figure 3.2 (ν = 9.8GHz): EPR spectra as a function of thickness. The deposition conditions used were Plasma = 30sccm CH_4 + 75sccm He, 100W, 200mtorr & RT (table 3.2).

Figure 3.3 displays the EPR data for all the samples listed in table 3.1-3.3. We can see in figure 3.3 that the addition of He or changing the RF power from 100W to 200W has no significant effect on the EPR data obtained. The g_0-value (cross-over), ΔB_{pp} (peak-to-peak linewidth) and N_A (areal spin population) do however depend on the thickness of the film. The g_0-value displayed is the experimental cross-over g-value, i.e. where the EPR spectrum crosses the zero base line.

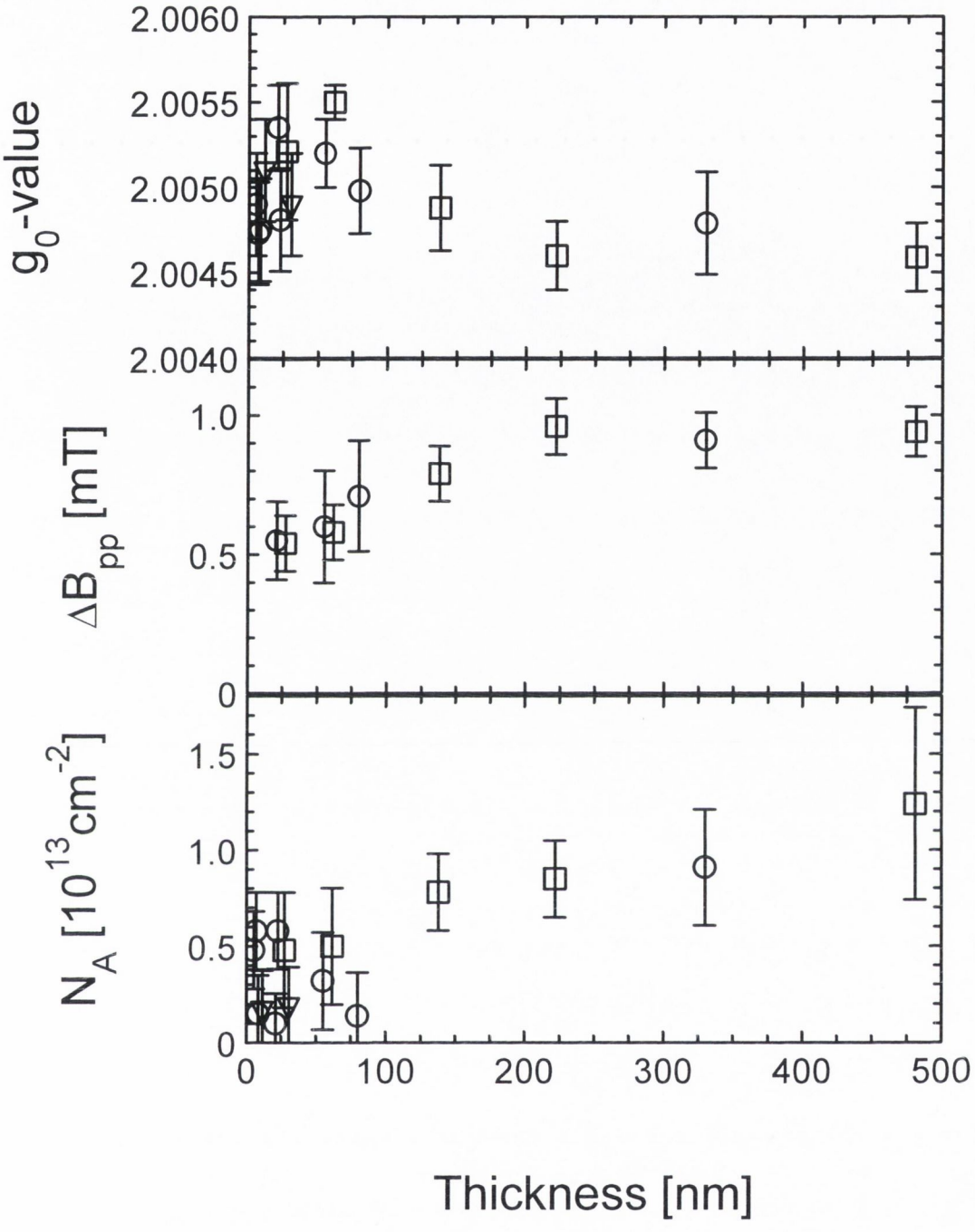

Figure 3.3 : EPR data for polymeric a-C:H as a function of thickness.

O : *a-C:H (Table 3.1): Plasma = 10sccm CH_4 only, 200W, 200mtorr & RT.*

□ : *a-C:H (Table 3.2): Plasma = 30sccm CH_4 + 75sccm He, 100W, 200mtorr & RT*

∇ : *a-C:H (Table 3.3): Plasma = 30sccm CH4 + 75sccm He, 200W, 200mtorr & RT.*

Figure 3.3 shows that the areal spin population does not increase in proportion to the film thickness and does not extrapolate to zero at zero thickness. ΔB_{pp} increases from ≈0.6mT to ≈0.95mT with increasing thickness. The cross-over g_0-value falls from

≈2.0055 to ≈2.0045 as the films get thicker. From examining figures 3.1 and 3.2 it can be seen that as the thickness increased the shape of the spectra changes from roughly symmetric to asymmetric.

One possible explanation for all these changes is that two distinct paramagnetic defects contribute to the EPR signal. If there exists two EPR signals, one with a lower g-value that the other, and the former dominates for the thicker films then this could account for the drop in the cross-over g_0-value. The presence of two unresolved lines may explain the increase in ΔB_{pp} with increasing thickness as initially one line may be dominant the overall but as the thickness increases a second line begins to appear thus increasing ΔB_{pp}. Furthermore, the failure of N_A to extrapolate to zero at zero thickness strongly suggests that one of these signals originates from defects either at a film interface or in the substrate.

In order to examine this a Si substrate without any a-C:H deposited upon it was studied. The EPR signal from this Si substrate can be seen in figure 3.4. As there is indeed a Si substrate 'background' signal it must be taken into account when analysing the polymeric a-C:H films as a function of thickness.

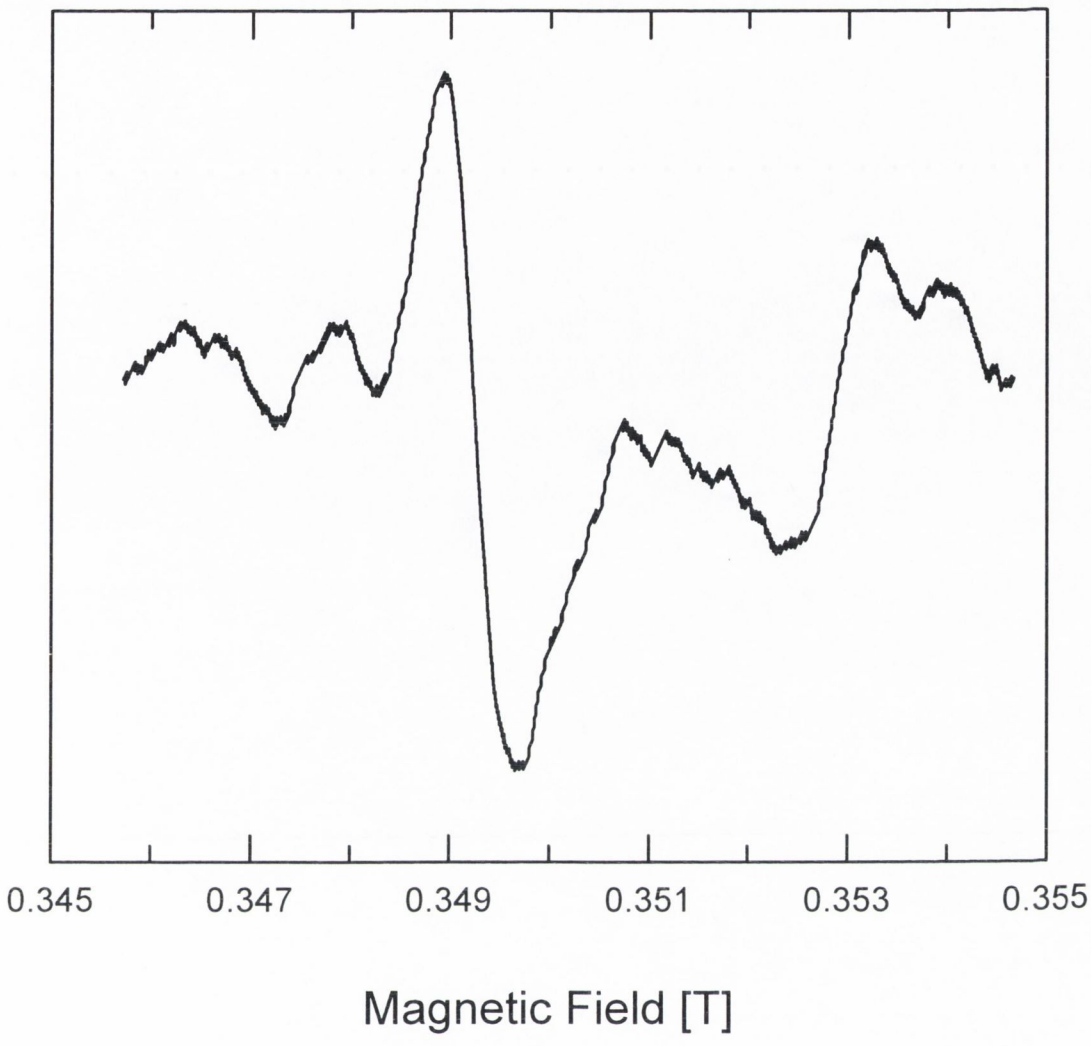

Figure 3.4 (ν = 9.8GHz): EPR signal from the Si substrate alone.

Table 3.4 lists the EPR data of the Si substrate signal.

Name	g_0-value	ΔBpp [mT]	$N_A[10^{13}cm^{-2}]$
Si substrate	2.0053 ± 0.0004	0.79 ± 0.09	0.20 ± 0.10

Table 3.4 : EPR data for the Si substrate alone.

In order to correct for this 'background' signal, the 'background' areal spin population (N_A) of $(0.2\pm0.1)\times10^{13}cm^{-2}$ may be subtracted from the N_A values obtained for the polymeric a-C:H films deposited on Si.

As there probably are also other defects in the polymeric a-C:H films it would be useful to examine these films without and Si substrate.

Our first attempt to do this involved the deposition of a polymeric a-C:H film upon spin-free quartz; unfortunately defects were subsequently created in the quartz substrate presumably by the UV radiation produced by the PECVD plasma. This can been seen in figure 3.5 which shows a characteristic E' centre spectrum (Nishikawa et al. 1990; Nishikawa et al. 1993).

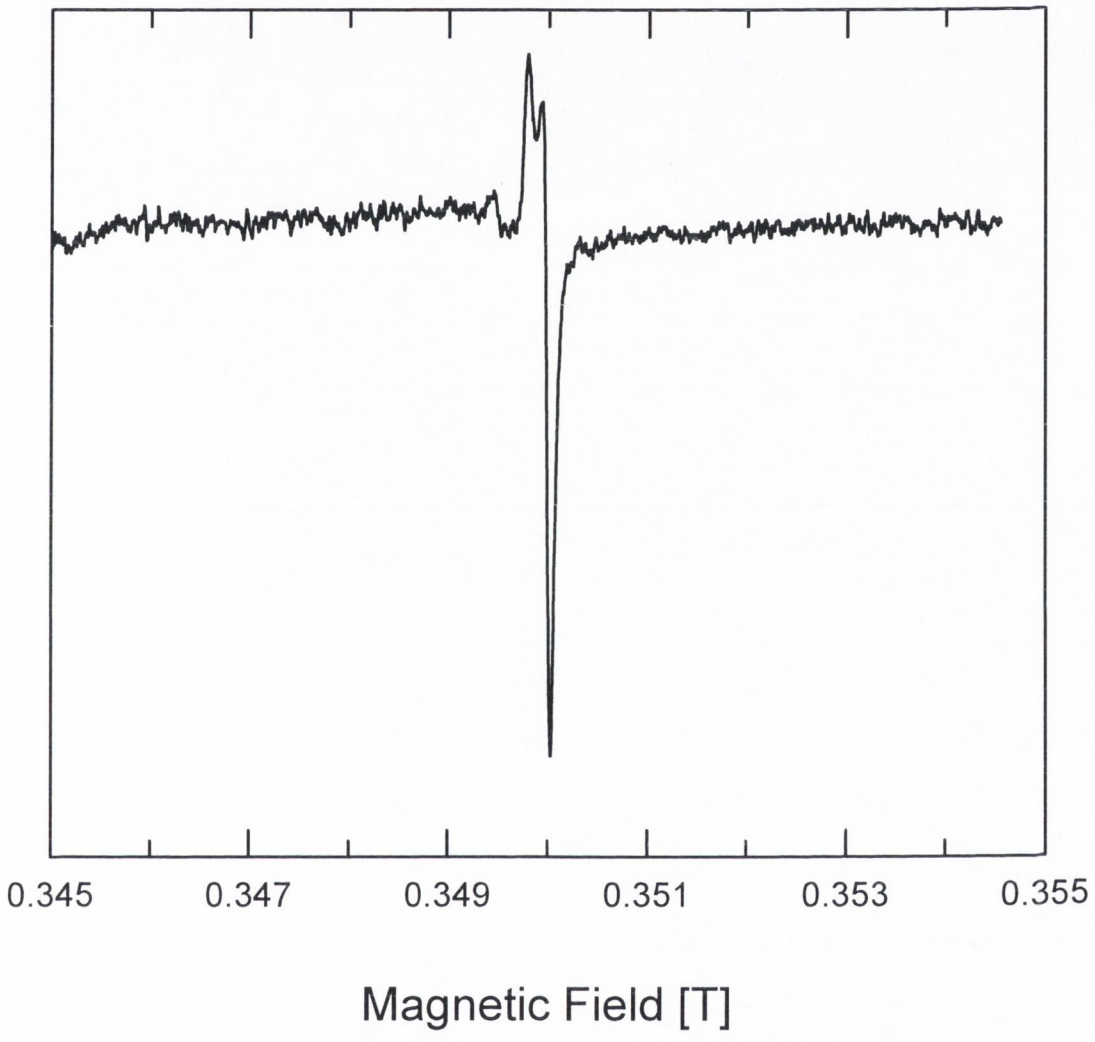

Figure 3.5 (ν = 9.8GHz): EPR signal for a sample of polymeric a-C:H deposited upon quartz.

In a second attempt to obtain the EPR signal of a-C:H we collected polymeric a-C:H powder. This powder was removed using a glass scraper, from a-C:H films grown on approximately 12 Si substrates. Before insertion in the microwave cavity the powder was placed upon a spin-free quartz slide and covered with adhesive tape.

Table 3.5 shows the preparation conditions for this 'bulk' sample.

Name	Mass [g]
Bulk a-C:H sample	< 0.0001

Table 3.5 : The bulk a-C:H sample deposited with Plasma gas: 30sccm CH_4 + 75sccm He, RF power: 200W, Pressure: 200mtorr, Substrate at room temperature. 60 minute deposition onto ≈12 substrates and removed with a glass microscope slide.

Two spectra were recorded for this sample. Figure 3.6 shows that the spectra obtained for this bulk sample are roughly symmetric. This is a possible indication that only one type of defect is present in this bulk polymeric a-C:H powder. The other EPR signal due to the Si substrate 'background' and possibly the SiC interlayer is not observed as the Si substrates have been removed.

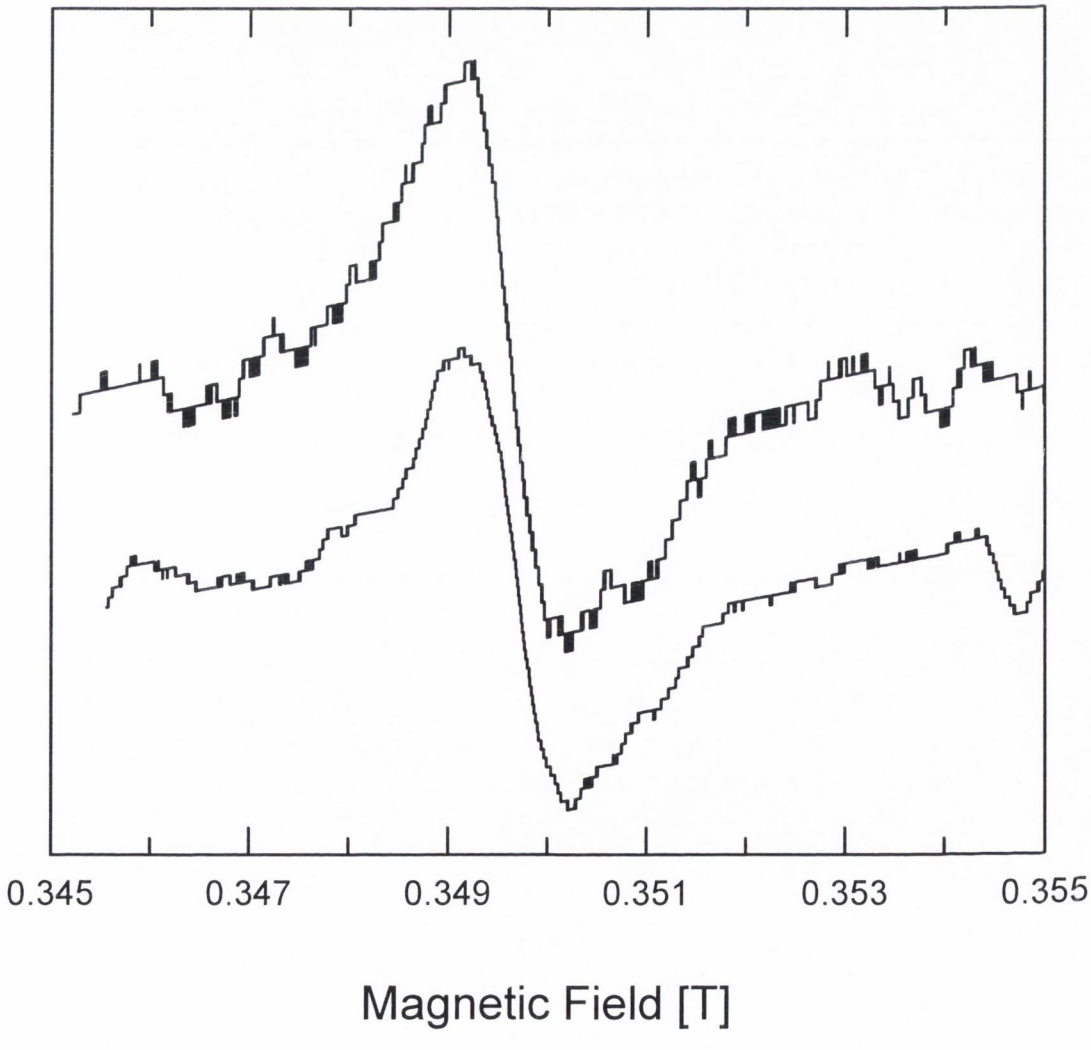

Figure 3.6 (ν = 9.8GHz): EPR spectra for the bulk polymeric a-C:H sample.

To determine the lineshape, we calculated the ratio of $\Delta B_l/\Delta B_{pp}$ for the two spectra shown in figure 3.6. ΔB_l is the full width at half maximum of the integral of the recorded spectrum while ΔB_{pp} is the peak-to-peak linewidth of the recorded spectrum. For a Lorentzian this ratio has a value of 1.73 while for a Gaussian it is 1.18 (McClintock and Orr 1968; Poole 1983, p. 476). Table 3.6 displays the ratios calculated for the two spectra recorded.

Name	ΔB_{pp} [mT]	ΔB_l [mT]	$\Delta B_l / \Delta B_{pp}$
Bulk a-C:H	1.11±0.06	1.78±0.2	1.60±0.26
Bulk a-C:H	1.13±0.09	1.61±0.06	1.42±0.16
Mean	1.12±0.08	1.70±0.13	1.51±0.21

Table 3.6 : Ratios of $\Delta B_l / \Delta B_{pp}$ for the bulk a-C:H sample.

The value of 1.5(2) for ΔB_l / ΔB_{pp} indicates that the EPR signal in the bulk possibly has a lineshape between the two extremes of either a Lorentzian or Gaussian. Due to the weakness of the signal we did not attempt to fit it with a Voigt lineshape.

The EPR results for the bulk polymeric a-C:H sample are summarised below in table 3.7. The g_0-value displayed is the experimental cross over g-value. N_S is the total number of unpaired spins in the sample (the mass is too small for us to measure).

Name	T [nm]	g_0-value	ΔB_{pp} [mT]	N_S [10^{13}]
Bulk a-C:H	N/A	2.0026±0.0002	1.11±0.06	4.2
Bulk a-C:H	N/A	2.0024±0.0003	1.13±0.09	2.5
Mean	N/A	2.0025±0.0002	1.12±0.08	3.4±1

Table 3.7 : EPR data for the bulk a-C:H sample.

We now have two types of defect which give rise to the EPR signals in our polymeric a-C:H films on silicon. One has a cross-over g_0-value ≈2.0055 and is either in the Si substrate and/or also possibly in an interface region between Si and the a-C:H layer. The second defect has a cross-over g_0-value of ≈2.0027 and is found in the bulk of the a-C:H.

The possibility that defects with g_0 ≈2.0055 are present in the air/a-C:H interface can be ruled out as no such defects are detected for the bulk powder a-C:H sample which has a very high air/a-C:H interface area. The fall in g_0 as a function of

thickness (figure 3.3) can be explained by the fact that as the thickness increases the bulk a-C:H defects with a lower g-value will begin to dominate the EPR signal and so the overall cross-over g_0-value will fall. This also account for the increase in ΔB_{pp} and the asymmetry of the spectra as the thickness increases because the presence of two unresolved EPR lines produces a larger ΔB_{pp} than of each line individually.

In order to check this view we visually fitted the spectra with two superimposed EPR spectral lines. These two lines have g-values close to 2.0055 and 2.0026 and represent the Si dangling bond defects (and possibly defects at the Si/a-C:H interface) and the bulk a-C:H defects respectively. After the 'background' Si signal is subtracted from the areal spin population (N_A), the value of N_A still does not intercept the origin of the plot in figure 3.4. This possibly indicates that the component with g $\approx$2.0055 does not arise from the Si substrate signal alone and may also be due to defects at or near the Si/a-C:H interface.

These two-line fits are generated by superimposing two Lorentzian lines upon each other. Figure 3.7 shows selected spectra with their two-line fit superimposed. It can be seen that a two-line fit, based on a line with g $\approx$2.0055(4), ΔB_{pp} = 0.56(2)mT and another with g=2.0027(2), ΔB_{pp} = 0.83(4)mT, gives a very reasonable fit to the experimental spectra.

A Lorentzian lineshape was used for both lines as it was felt that this lineshape was closer to the experimental data than that of a Gaussian, even though we already stated that the a-C:H bulk sample gave a shape somewhere between the two extremes. Trying to used a line with a shape between these lineshapes (e.g. a Voigt) would be overly complex considering the noise in the data.

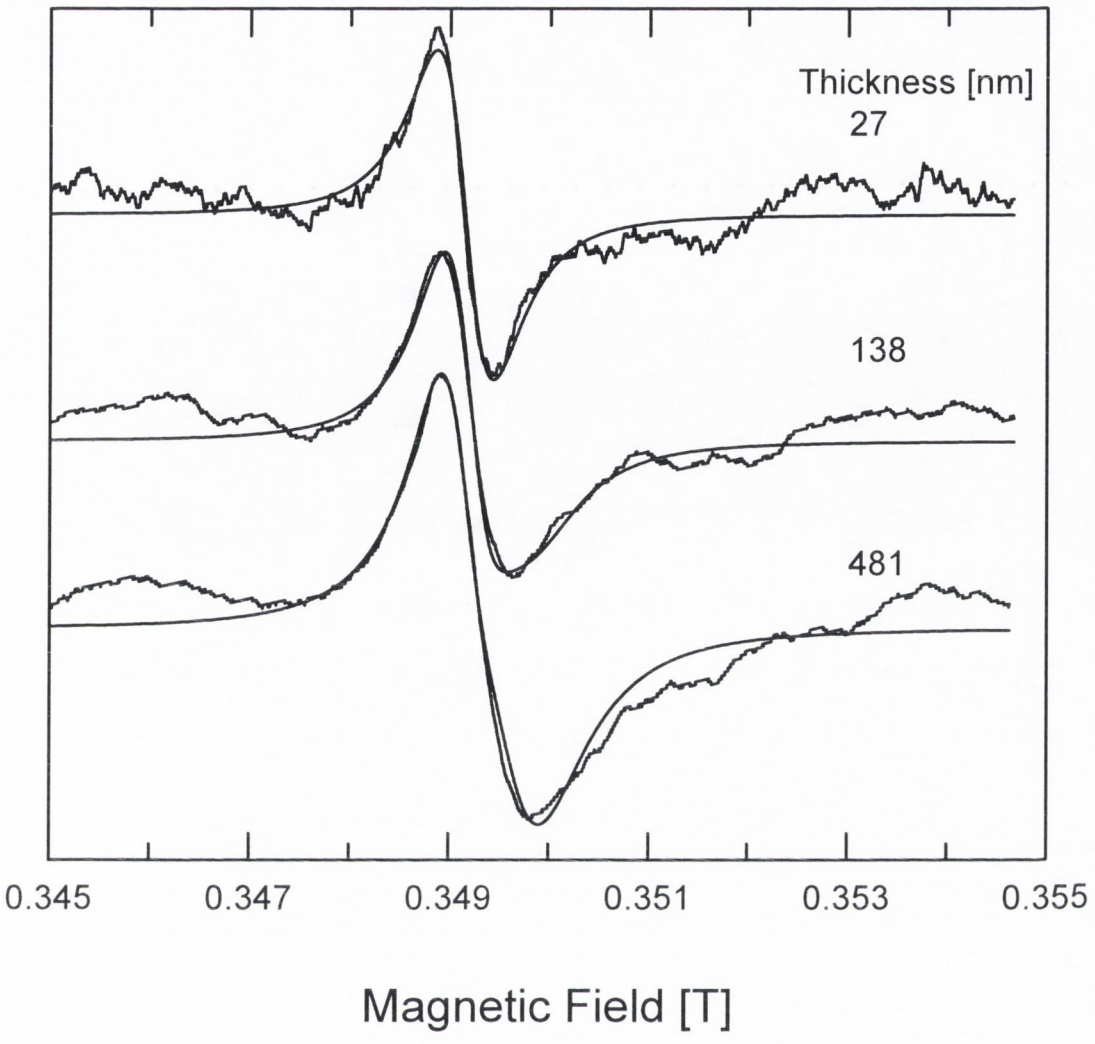

Figure 3.7 (ν = 9.8GHz): EPR spectra as a function of thickness with their fits superimposed.

Table 3.8 shows the parameters for the two component lines as determined by fitting the spectra. In this table sample RS005 is included with samples Jar-2-10 to Jar-2-14 because as mentioned earlier the deposition conditions have little effect on the films. The spectra that are fitted with two lines were chosen because of their better signal to noise ratios. The 1st line in table 3.8 refers to the defect line from the Si substrate and possibly the Si/a-C:H interface. The 2nd line refers to the defects in the bulk of the a-C:H films. The values called 'corrected 1st N_A' were calculated by subtracting the value of $0.2\times10^{13}cm^{-2}$ from the measured values of the '1st N_A'; this is done in order to remove the contribution to this line of the Si substrate background. As this 'corrected 1st' N_A value does not equal approximately zero, this indicates that

there possibly is a residual areal spin concentration due to defects at the Si/a-C:H interface.

1st lineshape = Lorentzian						2nd lineshape = Lorentzian		
Name	Thickness [nm]	1st g-value	1st ΔB_{pp} [mT]	1st N_A [$10^{13}cm^{-2}$]	Corrected 1st N_A[$10^{13}cm^{-2}$]	2nd g-value	2nd ΔB_{pp} [mT]	2nd N_A [$10^{13}cm^{-2}$]
Jar-2-10	27.2	2.0054	0.576	0.680	0.48±0.3			0.2±0.2
Jar-2-11	61.7	2.0053	0.588	0.697	0.50±0.3			0.2±0.2
Jar-2-12	137.9	2.0051	0.551	0.592	0.39±0.16	2.0027	0.801	0.39±0.04
Jar-2-13	221.8	2.0051	0.551	0.406	0.21±0.14	2.0028	0.801	0.64±0.06
Rs005	330	2.0055	0.551	0.401	0.20±0.17	2.0032	0.876	0.71±0.13
Jar-2-14	481.2	2.0055	0.551	0.374	0.17±0.2	2.0031	0.851	1.07±0.30
Mean			0.56±0.02	0.53±0.15	0.33±0.2		0.83±0.04	

Table 3.8 : Parameters used in generating the two-line fits for a-C:H as a function of thickness.

A homogeneous defect distribution should have N_A values which increase linearly with increasing thickness. A defect associated with the Si/a-C:H interface should have an N_A value which is independent of the thickness above a minimum thickness, equal to the thickness of the interface region itself. In order to examine the depth profile of the two types of defects, i.e. with g ≈2.0027 and g ≈2.0055, we plot in figure 3.8 the areal spin population (N_A) for two component lines whose parameters are given in table 3.8.

It can be seen from figure 3.8 that N_A remains constant with thickness for the line with g=2.0055(4), ΔB_{pp} = 0.56(2)mT. This is a very strong indication that this line is indeed due to defects in the Si substrate and possibly defects at the Si/a-C:H interface. The value for N_A for the line with g ≈2.0055 is $(0.53\pm0.15)\times10^{13}cm^{-2}$ compared to $(0.2\pm0.1)\times10^{13}cm^{-2}$ from the Si substrate on its own. Unfortunately it is very difficult to be sure whether defects from the Si/a-C:H are present because the values of N_A for this line are very close to those for the Si background. The mean value of N_A for this line after subtraction of the background signal is $(0.33\pm0.2)\times10^{13}cm^{-2}$.

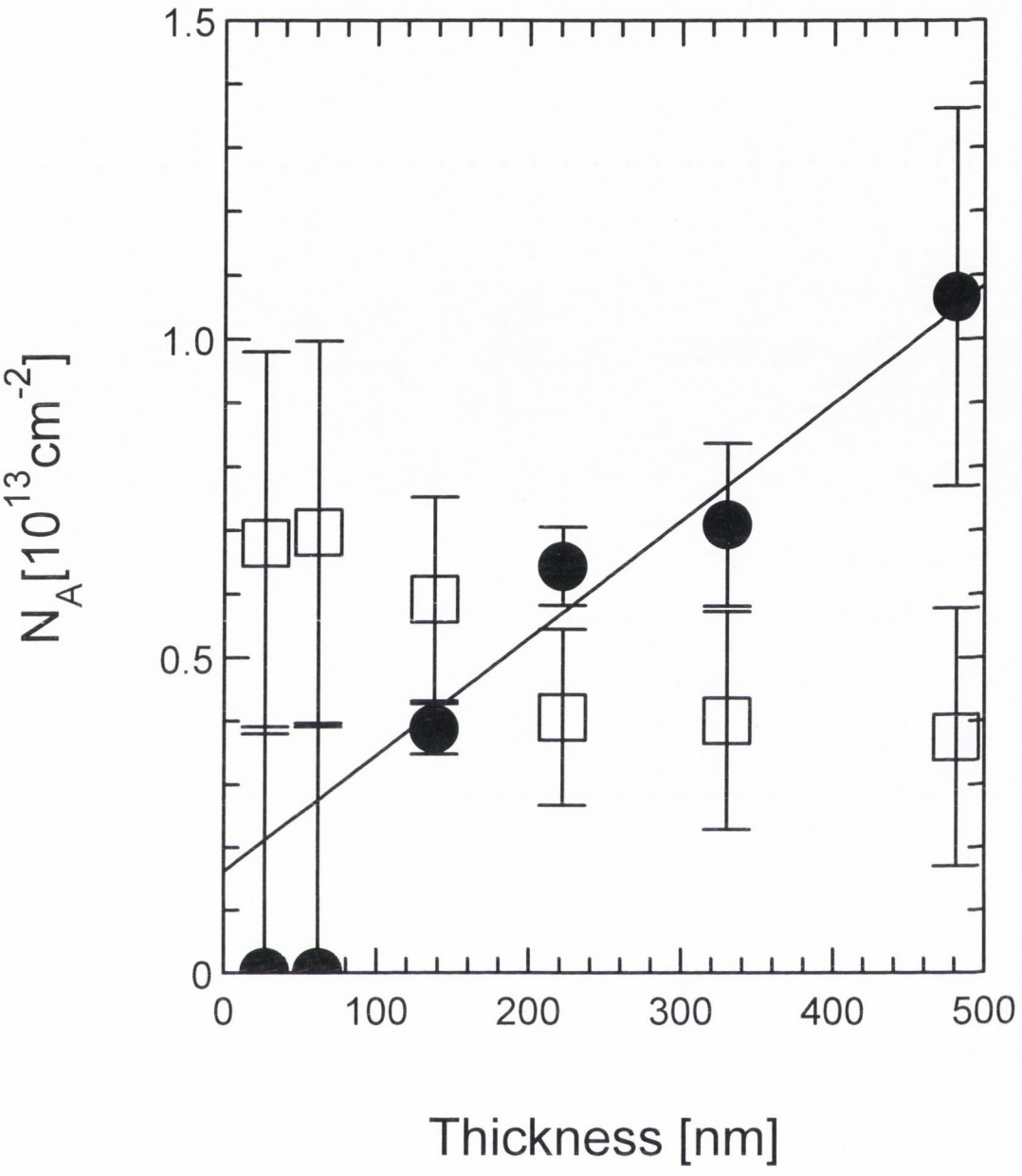

Figure 3.8 : Areal spin population of polymeric a-C:H as a function of thickness, for each component line of the two-line fit.

□ *: Line with g ≈2.0055, ΔB_{pp} = 0.56(2)mT.*

● *: Line with g ≈2.0027, ΔB_{pp} = 0.83(4)mT.*

The line with g ≈2.0027, ΔB_{pp} = 0.83(4)mT shows a linear increase in N_A with thickness. This is consistent with this defect being homogeneously distributed though the film. A linear fit of N_A versus thickness for this component line gives a slope of $(1.8\pm0.3)\times10^{17}cm^{-3}$. This is the spin concentration per unit volume (N_V). Also this

linear fit passes within error through the origin. This shows that these defects are not present in either the Si/a-C:H interface or the Si substrate. The first two points with N_A values of zero are not used in the linear fit as they are felt to be far less reliable than the other four points.

3.2.3 Discussion of the EPR results for polymeric a-C:H

Now we discuss the EPR results which we have obtained for polymeric a-C:H films of varying thickness.

As already mentioned in section 3.1.2 the deposition conditions which were varied during deposition of the films, i.e. gas composition (CH_4 or CH_4 and He), their flow rates and the RF power, had a negligible effect on the EPR signal of the polymeric a-C:H. This indicates that changing these conditions has no major effect on the defects present in the films.

The independence of these films on their preparation conditions may be explained as follows. The RF power of the plasma only controls the dc self-bias voltage between the plasma and the live electrode in the PECVD reactor and not the bias between the plasma and the earthed electrode. The self-bias voltage controls the energy at which ions from the plasma impinge onto the substrate and this determines the structure of the films produced (Schwan et al. 1996). So changing the RF power level should have little effect on the films produced on the earthed electrode. The addition of He into the reactor, while aiding the formation of a plasma, does not change the chemical composition of the a-C:H films. Finally, changing the CH_4 flow rate changes only the deposition time and this should not have much effect on the structure of the films or the paramagnetic defects present.

We consider now what may be the defects responsible for the two lines with g=2.0055(4), ΔB_{pp}=0.56(2) and g=2.0027(2), ΔB_{pp}= 0.83(4)mT.

Sealy et al. (1995) recorded a signal in a Si substrate implanted with Si which gave a g-value of 2.0058(2). They associate this EPR signal with dangling bonds in amorphous Si. Our g_0-value of 2.0053(4) for the Si substrate 'background' signal is in close agreement with this and thus it is reasonable to assume that this 'background' signal is due to Si dangling bonds, these may be on the surface and edges of the Si

substrate. We also find that an EPR line with g =2.0055(4) ΔB_{pp} = 0.56(2)mT possibly exists at the C/Si interface. Unfortunately we cannot say for sure that there are any interface.

The g_0-value of 2.0025(2) for the bulk polymeric a-C:H sample is much lower than the g_0-values obtained for any of the polymeric a-C:H films. The g_0-value 2.0025(2) and ΔB_{pp} (linewidth) of 1.12(8)mT measured for this sample are close to those measured by Giorgis et al. (1998) for polymeric and graphite-like a-C:H. Miller and McKenzie (1983) found a g-value of 2.0027 for a-C:H films deposited by glow discharge of a d.c. magnetron. This g-value is also very close to our value.

Tanaka et al. (1994) stated that the g-value of 2.0023-2.0026 found in doped poly(3-methylthiophene) indicates that the defect present in this polymer is due to π-electrons being delocalised over the carbon skeleton of the polymer. Tanaka et al. (1994) also found that the lineshapes of their oligothiophenes are between that of a Lorentzian and Gaussian; they stated that this is due to spatial confinement of the π-radicals within their thiophene oligomers. We find a similar lineshape for the bulk polymeric a-C:H sample. Robertson (1986, p. 339) states that because it is energetically favourable for unpaired electrons to exist in a π-orbital rather than a σ-orbital, the majority of unpaired electrons present in polymeric a-C:H would be in π-orbitals, even though there is a high sp^3 content (a high proportion of σ bonding). The fact that our g_0-value for the bulk a-C:H sample agrees closely with that obtained by Tanaka et al. (1994) indicates that the defects present in bulk polymeric a-C:H are unpaired electrons in π-orbitals on carbon atoms.

As polymeric a-C:H contains a high proportion of sp^3 bonds (i.e. its sp^3/sp^2 ratio was high) it is unlikely that the paramagnetic electrons are widely delocalised, and so exchange interaction between spins is unlikely. This is consistent with the result that the lineshape is not Lorentzian. Dipolar interaction between like spins also gives rise to a Lorentzian lineshape but the low spin concentration indicates that this effect is not significant enough to explain the linewidth (ΔB_{pp}). Due to the high hydrogen content in polymeric a-C:H, hydrogen hyper-fine splitting (hfs) of the EPR line is a possibility; when unresolved this would give rise to a Gaussian lineshape (Seidel and Wolf 1968; Poole 1983, p. 583). The lineshape could also have been a Voigt convolution of a Gaussian and Lorentzian. This possibility may be explained by the presence of both hfs and to some extent dipolar interaction.

Abragam (1996) predicts that in magnetically dilute substances the dipolar broadening of a line for films with less that one unpaired electron per 100 carbon atoms is given by the following equation (this equation uses cgs units). The resultant lineshape is Lorentzian with

$$\frac{1}{2}\Delta H_{1/2} = \frac{2\pi^2}{3\sqrt{3}} g\mu_B N_V \qquad (3.1)$$

Taking this equation together with eq. 2.15 and g = 2.0025 we get

$$\Delta B_{pp} = 8.12 \times 10^{-20} N_V \qquad (3.2)$$

where the units of spin concentration (N_V) are cm^{-3} and the units of peak-to-peak linewidth (ΔB_{pp}) are Gauss.

The linewidth calculated from the average N_V value, using equation 3.2, is to small to explain the measured linewidth. For dipolar broadening to account for the linewidth the local defect spin concentration must be higher than the average value of the spin concentration (N_V). This would indicate that the defects are clustered together. Another possibility is that the signal is due to a superposition of a Lorentzian and Gaussian lineshapes. This may be possible if one considers that the spins exist in two different environments. One environment with a strong dipolar interaction (with possibly some exchange interaction) gives rise to a Lorentzian lineshape. This can occur if the defects are clustered together. The other environment experiences hfs due to the hydrogen present and experiences very little dipolar or exchange interaction. This environment gives rise to a Gaussian lineshape. Unfortunately, due to the weak signal detected from the bulk polymeric a-C:H sample, it is impossible to determine the exact lineshape. This means that any information obtained from the lineshape of this sample is rather speculative.

The main information obtained from the bulk sample is that the paramagnetic defects present in the bulk sample have an unpaired electrons in π-orbitals on carbon atoms. Robertson (1986, p. 361) states that these unpaired π-electrons in a-C:H can come from either aromatic clusters which contain an odd number of benzene ring units

(a minimum of 3) or linear chains of conjugated double bonds (containing an odd number of carbon atoms). The reason for the odd number of benzene ring units or carbon atoms is that this stabilises the system. He also states that a cluster with an odd number of π-orbitals would produce an energy level near E=0 which is half filled (i.e. it has an unpaired electron). The two simplest sites are analogous to the perinaphtene radical and allyl radical. The larger the cluster or polymer chain the more the unpaired electrons can move from one carbon atom to another i.e. the more they would be delocalised. Robertson (1996a) modifies this idea, stating that the clusters contain mainly olefinic chains (conjugated chains of double bonds) and very few fused six-fold aromatic rings.

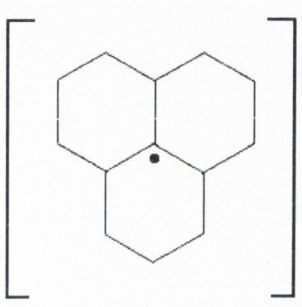

Perinaphtene radical

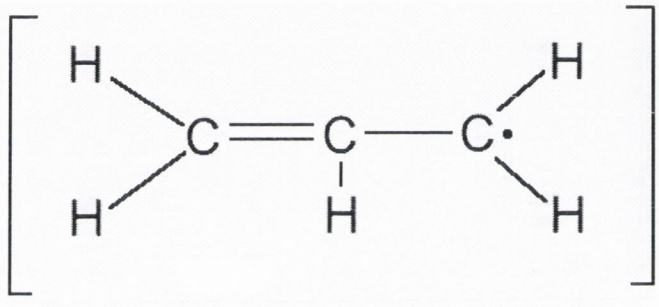

Allyl radical

Since polymeric a-C:H contains both a high concentration of hydrogen (≈50%) and a high sp^3/sp^2 ratio it is reasonable to assume that linear polymer chains of conjugated double bonds are more abundant than fused aromatic clusters. This is because the smallest chain (analogous to the allyl radical) contains 6 sp^2 carbon bonds per unpaired π-electron while the smallest aromatic ring cluster (analogous to the perinaphtene radical) contains 39 sp^2 bonds per unpaired π-electron. This may possibly explain why the lineshape is Voigt, because it allows both dipolar interaction (the spins were clustered along the chain) along with any possible exchange narrowing, and hyper-fine splitting (hfs) caused by the proximity of hydrogen to the chains.

For our polymeric a-C:H films we find that at least two types of defects exist. We can say that the 2-line fitting of the EPR spectra for these polymeric a-C:H films, as a function of thickness, leads us to believe that there is a homogeneous distribution of bulk defects with a spin concentration (N_V) of $(1.8\pm0.3)\times10^{17}cm^{-3}$, a g-value of ≈2.0027(2) and ΔB_{pp} of 0.83(4)mT. This g-value is very close to that found for the

bulk polymeric a-C:H sample. So it is very likely that these defects are the same as those present in the bulk a-C:H sample and are thus associated with unpaired electrons on carbon atoms. These unpaired electrons are probably in π-orbitals (Robertson 1986 p. 361; Tanaka et al. 1994); however the presence of some unpaired electrons in σ-orbitals cannot be completely ruled out.

In conclusion then, we find that in our polymeric a-C:H films the presence of at least two types of paramagnetic defects. One defect has g ≈2.0055 which we attribute to the Si dangling bond present in the Si substrate and possibly at or near the Si/a-C:H interface. This indicates that there may be a SiC interlayer between the Si substrate and the polymeric a-C:H film. The other defect has a g-value of ≈2.0027 and we attribute this defect to unpaired π-electrons probably from chains of conjugated double bonds and also possibly from aromatic clusters made up of an odd number fused benzene-like aromatic rings. The latter type of defect we find to be homogeneously distributed though out the polymeric a-C:H film.

The g_0-values of 2.0040-2.0045 reported by Ristein et al. (1995) and Sadki et al. (1996) may arise due to a combination of these two types of defects.

3.3 Defects present in nitrogenated polymeric a-C:H

Due to the practical importance in semiconductor technology of electronic doping of intrinsic semiconductor materials, efforts have been made to dope a-C:H by adding nitrogen (Schwan et al. 1998; Silva et al. 1997). Also nitrogenated a-C:H is a promising material for use as a cathode material in field-emission displays (Amaratunga and Silva 1996) due to its high emission currents. It is the aim of the measurements reported in this section to examine the effects on the paramagnetic defects of adding nitrogen.

3.3.1 Sample preparation.

In order to examine the effect that adding nitrogen has on polymeric a-C:H we examine a set of nitrogenated polymeric a-C:H films containing various amounts of nitrogen.

The samples used in this study, as in section 3.2.1, were produced in a Plasma Technology DP800 radio frequency (13.56MHz) driven plasma enhanced chemical vapour deposition reactor. The details of the reactor were dealt with in chapter 2. The only difference is the presence in the plasma gases of nitrogen. Table 3.9 lists the deposition conditions.

Name	N_2 [sccm]	Thickness [nm]
Jar-2-19	0	221.8
Jar-2-20	2.5	212.6
Jar-2-21	5	300.6
Jar-2-22	7.5	271.0
Jar-2-23	10	286.6
Jar-2-24	15	288.1

Table 3.9 : Thickness and nitrogen flow rate of a-C:H,N films deposited with Plasma gases = 75sccm He + 30sccm CH_4, RF power: 200W, Pressure: 200mtorr, Substrate at room temperature.

3.3.2 EPR results for polymeric a-C:H,N

This section gives the EPR results for the a-C:H,N films as a function of the nitrogen flow rate used during deposition, i.e. nitrogen content. Figure 3.9 displays selected EPR spectra as a function of the nitrogen flow rate used.

We can see in figure 3.9 that is little change in the EPR spectrum when nitrogen was incorporated into the polymeric a-C:H films

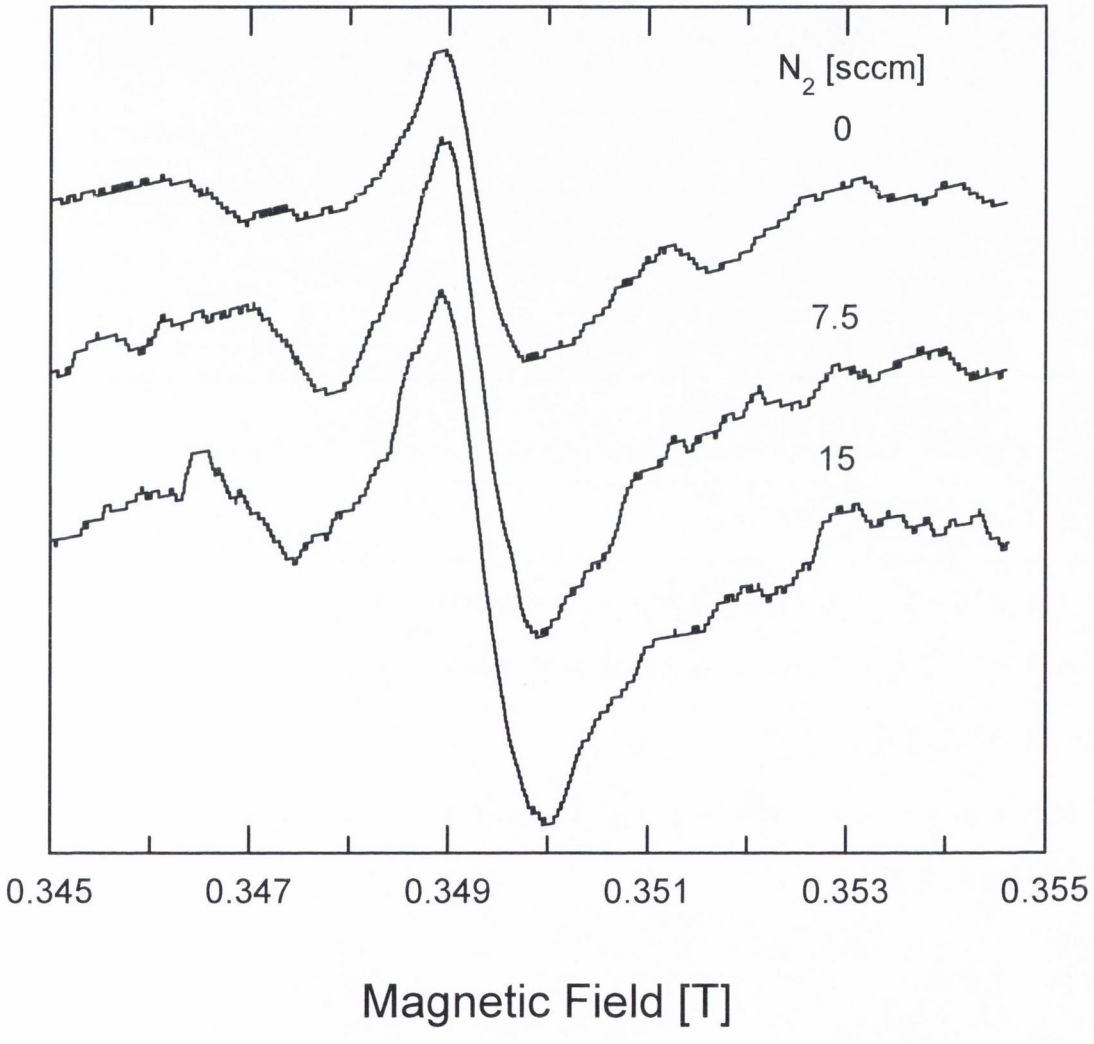

Figure 3.9 (ν = 9.8GHz) EPR spectra as a function of nitrogen flow rate used during deposition (table 3.9).

Figure 3.10 shows the EPR data for the a-C:H,N films as a function of nitrogen flow rate used during deposition. Figure 3.10 shows that, within error, the g_0-value, linewidth (ΔB_{pp}) and the spin concentration of the polymeric a-C:H,N films remain

unchanged as the nitrogen flow rate is altered. So the presence of nitrogen in polymeric a-C:H films has no significant effect on the paramagnetic defects in the films.

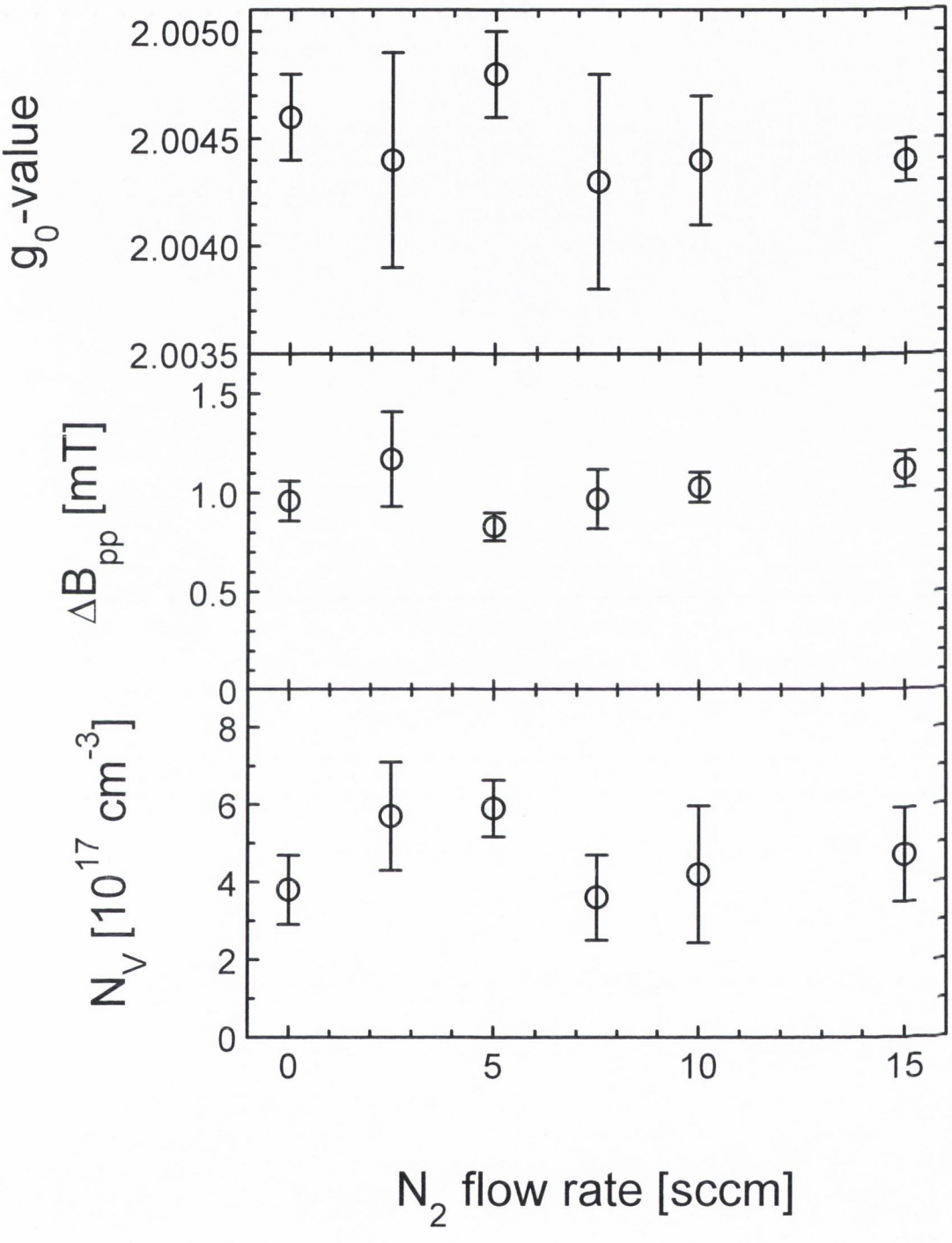

Figure 3.10 : EPR data for polymeric a-C:H,N films as a function of nitrogen flow rate.

3.3.3 Discussion of the EPR results for polymeric a-C:H,N.

As far as we can tell the N_2 flow rate during deposition has very little effect on the paramagnetic defects present. The film which contained no nitrogen (Jar-2-19) was already fitted with a two-line fit (table 3.8). As the lineshape did not change as nitrogen is introduced we believe that nitrogen has no effect on either type of paramagnetic defect. The defects present in polymeric a-C:H,N are the same as those found in the polymeric a-C:H films.

Nitrogen normally has a valency of three or five i.e. it has three or five bonds (Lee 1991). Nitrogen is most likely incorporated into polymeric a-C:H through substitution of carbon atoms (Silva et al. 1997). For electrical doping to occur the nitrogen needs to be incorporated into the polymeric a-C:H with 4-fold co-ordination which would allow its remaining unpaired electron to enter the conduction band and contribute to electrical conduction. This will only happen if the excess electrons from the nitrogen atoms are not localised. If they were free to move and enter the conduction band some of these free electrons supplied by the nitrogen could have combined with the unpaired electrons at the defect sites. If this happened the number of paramagnetic defects in the film would have dropped. That there is no drop in the number of paramagnetic spins combined with the fact that we do not see an EPR signal due to unpaired electrons on nitrogen (Hoinkis et al. 1991) indicate that the nitrogen is not incorporated into a-C:H with 4-fold co-ordination to any great extent.

Robertson (1986, p. 368) stated that when group V (e.g. N) atoms are incorporated into a-C:H, 4-fold co-ordination sites are formed but they are rare because they are energetically less favourable. If this is true for polymeric a-C:H then this would support the case that the nitrogen is not incorporated into the a-C:H with 4-fold co-ordination to any great extent.

In conclusion then, we find that the defects present in polymeric a-C:H,N films are the same as those we find in polymeric a-C:H films. The addition of nitrogen has no effect on the paramagnetic defects present. We find no evidence to support the idea that nitrogen forms 4-fold co-ordination bonding in polymeric a-C:H,N films. This indicates that electronic doping by nitrogen may be very inefficient.

3.4 Effect of annealing polymeric a-C:H and a-C:H,N

Annealing is an important tool in semiconductor processing, usually used to remove damage and defects and to activate ions which may have been implanted (Sze 1985, p. 417). Also high temperature processes may be used after deposition in the fabrication of devices. Therefore it is the of aim the work in this section of the chapter to examine the effect annealing has upon the defects present in polymeric a-C:H and a-C:H,N films.

In order to examine the effect that the annealing at different temperatures has on the defects in polymeric a-C:H we chose to anneal sample RS005, which was the thickest film (table 3.1). To study the effect the annealing temperature upon the defects in polymeric a-C:H,N we chose to anneal the sample Jar-2-23, which was produced with 10sccm of N_2 gas in the plasma (table 3.9). Each sample was successively annealed at 100, 200, 300, 350, 400, 450, 500, 550, 600 and 700°C. The samples were annealed at each temperature for 10 minutes in an Argon over-pressure inside an electric furnace before being allowed to cool to room temperature at which the EPR spectra were recorded. From now on we shall refer to this process as step annealing.

3.4.1 EPR results for annealed polymeric a-C:H and a-C:H,N

In this section we shall give the EPR results and analysis of polymeric a-C:H and a-C:H,N annealed at various temperatures. Figure 3.11 shows selected EPR spectra as a function of annealing temperature for our polymeric a-C:H film (RS005). The shape of the EPR spectra changes with increasing annealing temperature (T_a). It can be seen from this figure that the asymmetry of the lineshape decreases with increasing T_a. We can see that ΔB_{pp} falls with increasing T_a. The lineshape goes from asymmetric at room temperature to Lorentzian at 550°C.

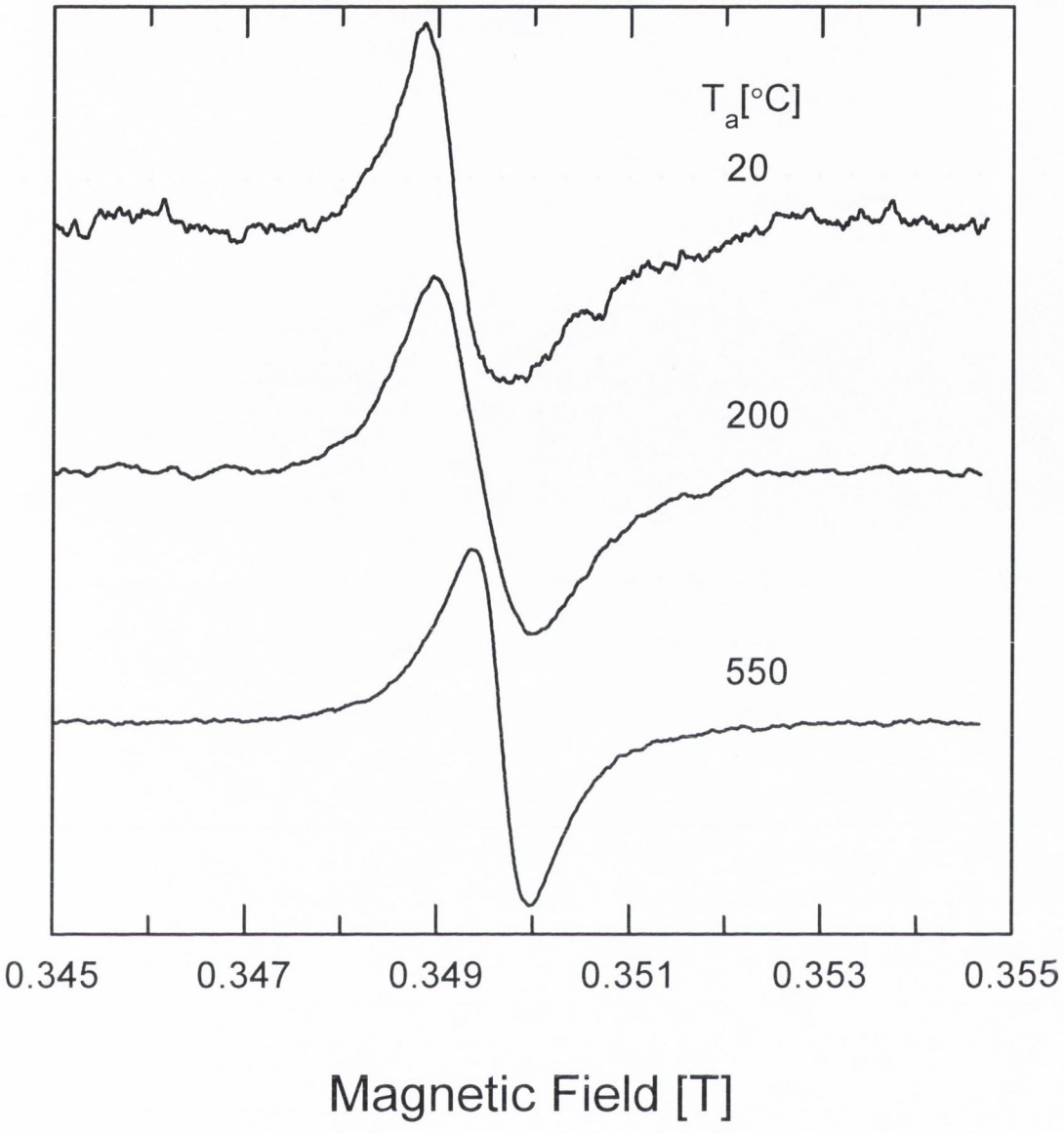

Figure 3.11 (ν = 9.8GHz) : EPR spectra as a function of annealing temperature for our polymeric a-C:H sample RS005 (table 3.1).

We can see in figure 3.12 selected spectra for our a-C:H,N film (Jar-2-23) as a function of annealing temperature (T_a). Again it can be seen that the shape of the line changes from asymmetric to symmetric with increasing T_a. We can also see that ΔB_{pp} falls with increasing T_a. This is very similar to the change we find in polymeric a-C:H (figure 3.11). The lineshape at 550°C is Lorentzian.

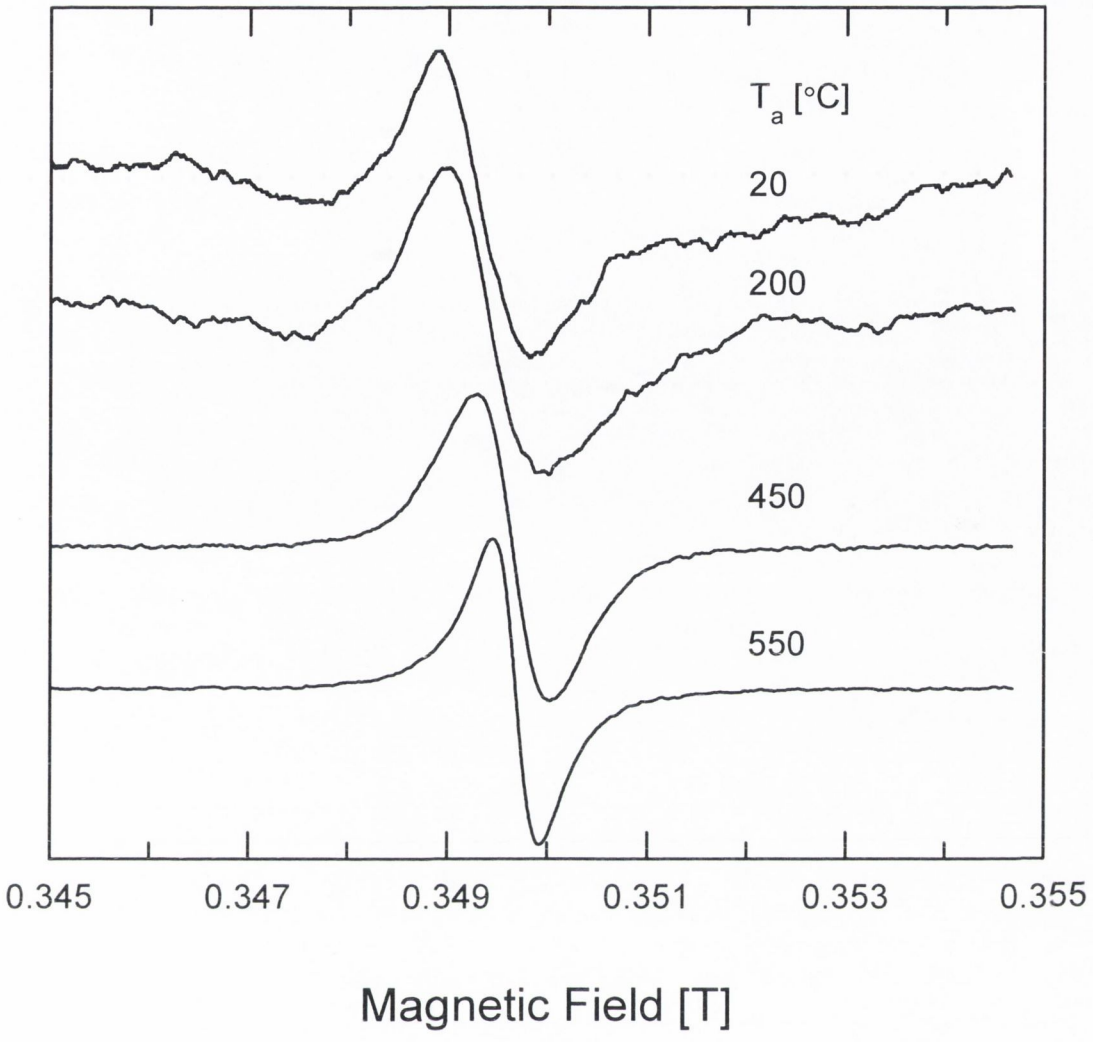

Figure 3.12 (ν = 9.8GHz) : EPR spectra as a function of annealing temperature for our polymeric a-C:H,N sample Jar-2-23 (table 3.9).

Figure 3.13 displays the EPR data for both the polymeric a-C:H and a-C:H,N samples which we annealed (RS005 and Jar-2-23 respectively). We can see that the EPR data for both samples is very similar. This figure shows that the cross-over g_0-value, for both samples, falls when T_a increases. The linewidths (ΔB_{pp}) remain at ≈1mT until 350°C after which they narrow. The total spin concentration (N_V) rises until a temperature of 550°C after which it falls very rapidly for both samples. The very similar behaviour of the EPR data as a function of annealing temperature is further proof that the defects present in polymeric a-C:H are unaffected by the incorporation of nitrogen.

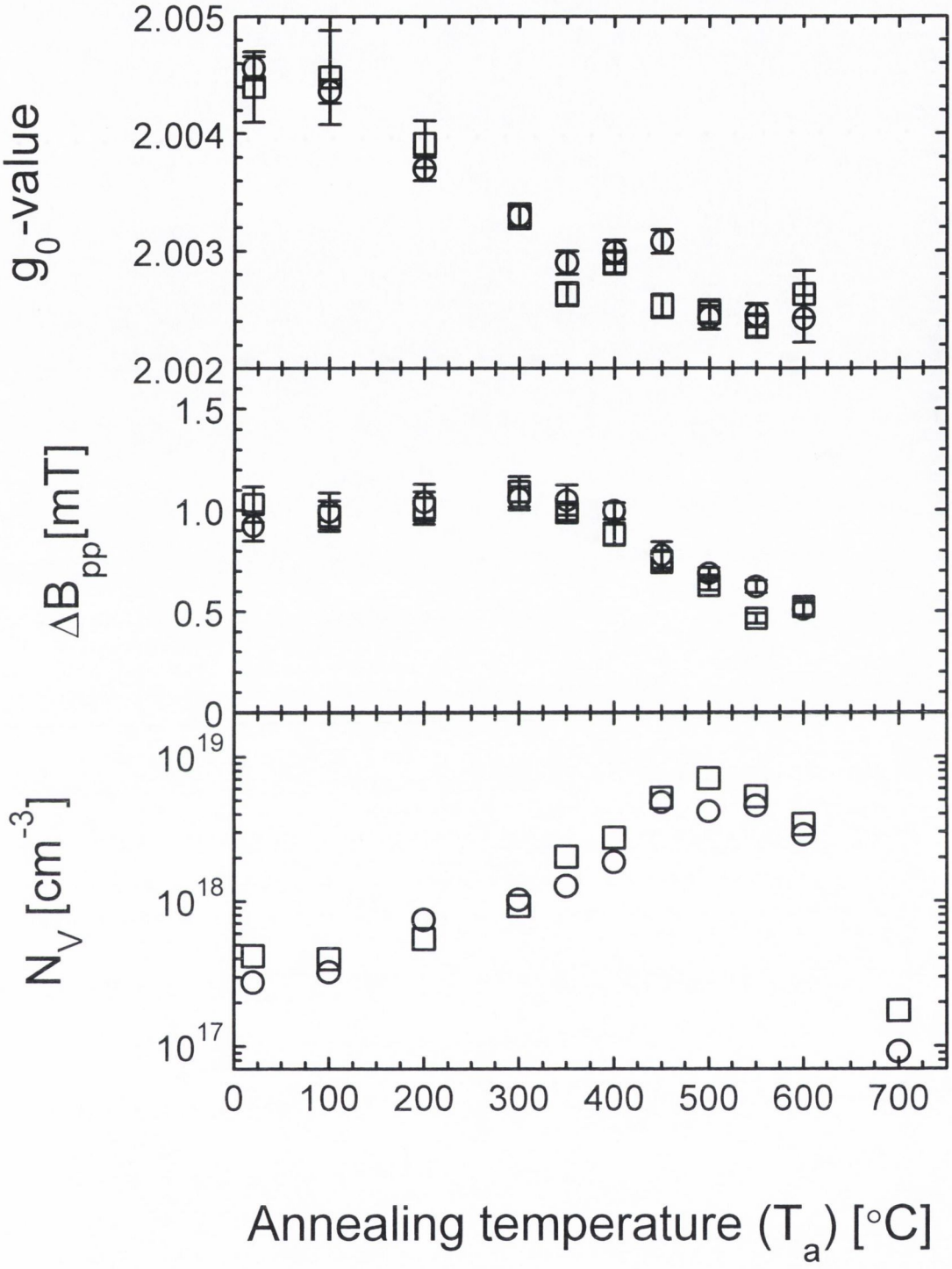

Figure 3.13 : EPR data for polymeric a-C:H and a-C:H,N as a function of annealing temperature (T_a).

O : *Polymeric a-C:H (RS005: Table 3.1)*

□ : *Polymeric a-C:H,N (Jar-2-23: Table 3.9)*

We have already found that two types of defects are present in polymeric a-C:H and a-C:H,N. We previously found that these two defects had Lorentzian lines with g=2.0055(4), ΔB_{pp}=0.56(2) and g=2.0027(2), ΔB_{pp}= 0.83(4)mT. Fits consisting of a superimposition of two such Lorentzian lines has already been carried out for the a-C:H and a-C:H,N spectra at room temperature. Therefore it may be possible to fit the spectra in figures 3.11 and 3.12, for T_a> room temperature, to two-line fits with roughly constant g-values (g=2.0055(4) and g=2.0027(2)) and linewidths (ΔB_{pp}=0.56(2) and ΔB_{pp}= 0.83(4)mT) by only altering the heights of the two lines.

Therefore we generated such two-line fits by superimposing two Lorentzian lines for both of these films as a function of annealing temperature. For the a-C:H film, at temperatures above 400°C the line with g=2.0055(4), ΔB_{pp}=0.56(2) is insignificant in size compared to the line with g=2.0027(2), ΔB_{pp}= 0.83(4)mT and so only a single Lorentzian is observed (g=2.0027(2) and ΔB_{pp}= 0.83(4)mT). Similarly only the line with g=2.0027(3) and ΔB_{pp}= 0.83(4)mT is observed above 350°C for the a-C:H,N film. In this case the lineshape was not a Lorentzian, we will discuss this later. The parameters of the two-line fits are given in tables 3.10 (a-C:H $T_a \leq 400$°C) and 3.11 (a-C:H,N $T_a \leq 350$°C). Figures 3.14 and 3.15 show selected spectra with their two-line fits superimposed for the polymeric a-C:H ($T_a \leq 400$°C) and a-C:H,N ($T_a \leq 350$°C) films respectively. In these figures we see that a two Lorentzian line fit is in good agreement with the experimental data (for a-C:H $T_a \leq 400$°C and a-C:H,N $T_a \leq 350$°C).

1st lineshape = Lorentzian					2nd lineshape = Lorentzian			
T_a [°C]	1st g-value	1st ΔB_{pp} [mT]	1st N_A [10^{13}cm^{-2}]	Corrected 1st N_A [10^{13}cm^{-2}]	2nd g-value	2nd ΔB_{pp} [mT]	2nd N_A [10^{13}cm^{-2}]	2nd N_V [10^{17}cm^{-3}]
20	2.0055	0.551	0.401±0.07	0.20±0.17	2.0032	0.876	0.71±0.13	2.15±0.39
100	2.0053	0.551	0.422±0.07	0.22±0.17	2.0029	0.801	0.85±0.13	2.58±0.41
200	2.0052	0.551	0.520±0.04	0.32±0.16	2.0027	0.839	2.13±0.16	6.46±0.49
300	2.0051	0.551	0.524±0.03	0.32±0.15	2.0027	0.851	3.04±0.17	9.22±0.52
350	2.0050	0.551	0.521±0.02	0.32±0.14	2.0026	0.851	3.86±0.18	11.7±0.53
400	2.0052	0.551	0.549±0.02	0.35±0.13	2.0027	0.801	5.80±0.18	17.6±0.55
Mean				0.29±0.15				

Table 3.10 : Parameters used in generating the two-line Lorentzian fits for polymeric a-C:H (RS005) as a function of annealing temperature.

1^{st} lineshape = Lorentzian					2^{nd} lineshape = Lorentzian			
T_a [°C]	1^{st} g-value	1^{st} ΔB_{pp} [mT]	1^{st} N_A [$10^{13}cm^{-2}$]	Corrected 1^{st} N_A [$10^{13}cm^{-2}$]	2^{nd} g-value	2^{nd} ΔB_{pp} [mT]	2^{nd} N_A [$10^{13}cm^{-2}$]	2^{nd} N_V [$10^{17}cm^{-3}$]
20	2.0056	0.526	0.339±0.08	0.139±0.18	2.0031	0.776	1.06±0.12	3.70±0.42
100	2.0055	0.526	0.284±0.09	0.084±0.19	2.0031	0.801	1.06±0.14	3.68±0.49
200	2.0053	0.513	0.300±0.07	0.100±0.17	2.0029	0.826	1.47±0.17	5.13±0.59
300	2.0054	0.513	0.303±0.04	0.103±0.14	2.0028	0.864	2.55±0.16	8.89±0.56
350	2.0055	0.513	0.189±0.05	0±0.15	2.0025	0.864	5.80±0.18	20.2±0.6
Mean				0.09±0.05				

Table 3.11 : Parameters used in generating the two-line Lorentzian fits for polymeric a-C:H,N (Jar-2-23) as a function of annealing temperature.

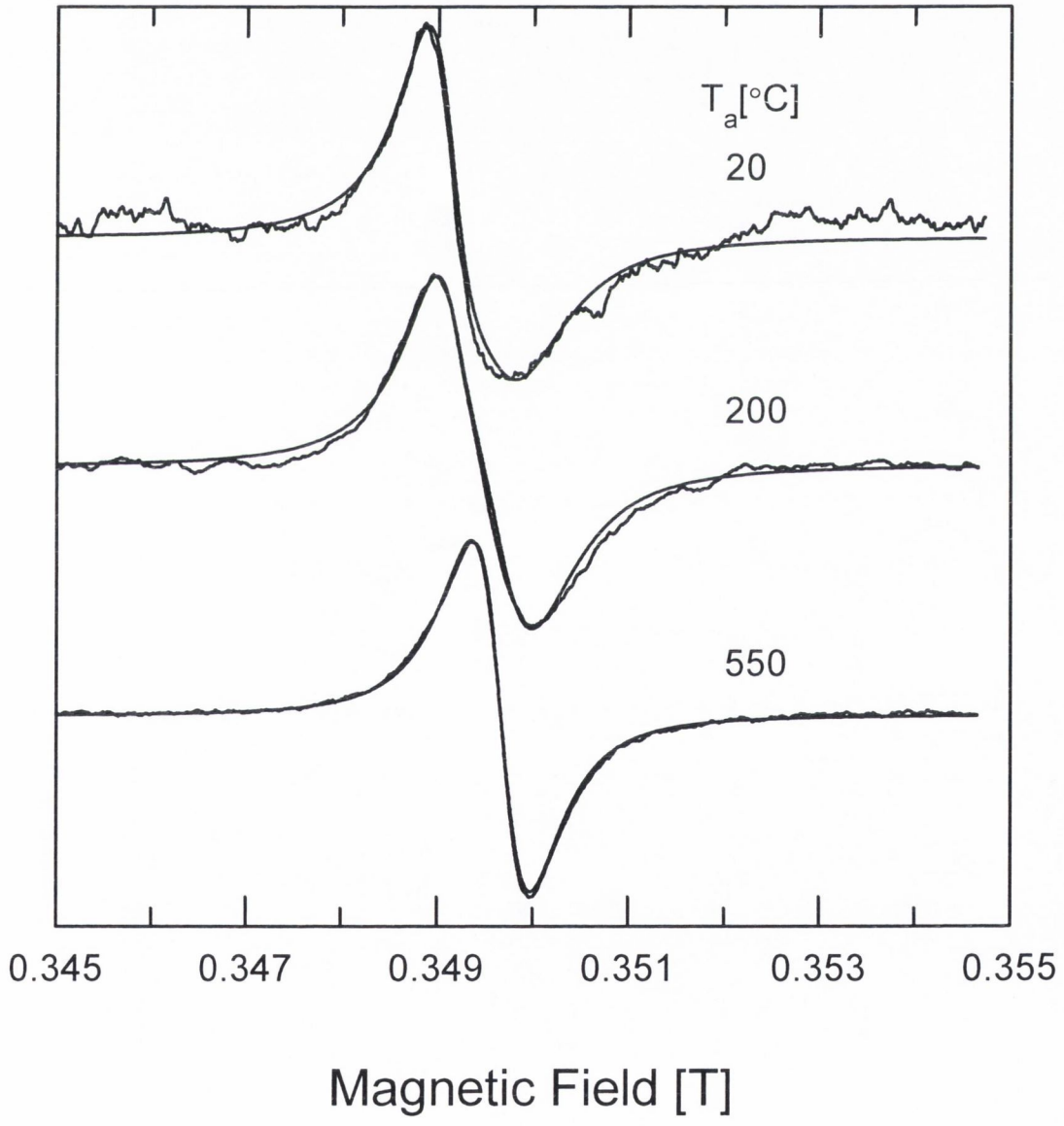

Figure 3.14 (ν = 9.8GHz) : EPR spectra as a function of annealing temperature for our polymeric a-C:H sample RS005 with their fits superimposed.

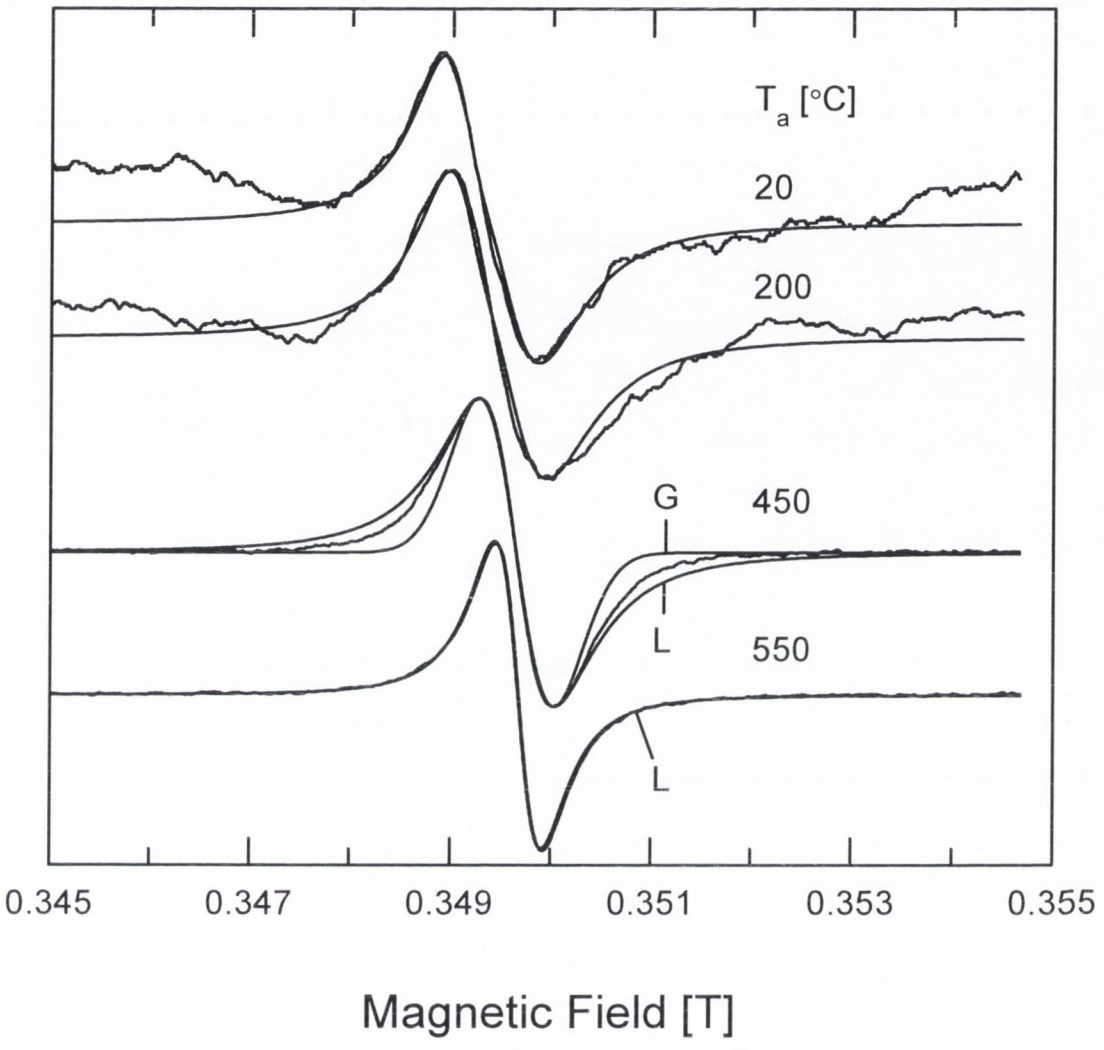

Figure 3.15 (ν = 9.8GHz) : EPR spectra as a function of annealing temperature for our polymeric a-C:H,N sample Jar-2-23 with their fits superimposed.

As mentioned only the line with g=2.0027(2) and ΔB_{pp}= 0.83(4)mT is observed above 400°C for the a-C:H film and above 350°C in a-C:H,N film. For the a-C:H film this line has a Lorentzian shape above 400°C. In figure 3.15 we can see that the spectrum for the a-C:H,N film at T_a=450°C is neither a Lorentzian (denoted by a L) or a Gaussian (denoted by a G). At 550°C we see that the shape of the spectrum is a Lorentzian. For the a-C:H,N film, between the annealing temperatures (T_a) of 400°C and 500°C the spectra are symmetric, these spectra are neither Gaussian of Lorentzian but somewhere in between these two lineshapes. Since these lineshapes lie between a Gaussian and a Lorentzian we may fit the spectra to a Voigt shape. Another possibility is that the lineshape could be due to the superposition of the

signals of two distinct defects, one with a Lorentzian lineshape and the other with a Gaussian. We will first attempt to fit these spectra to a Voigt profile.

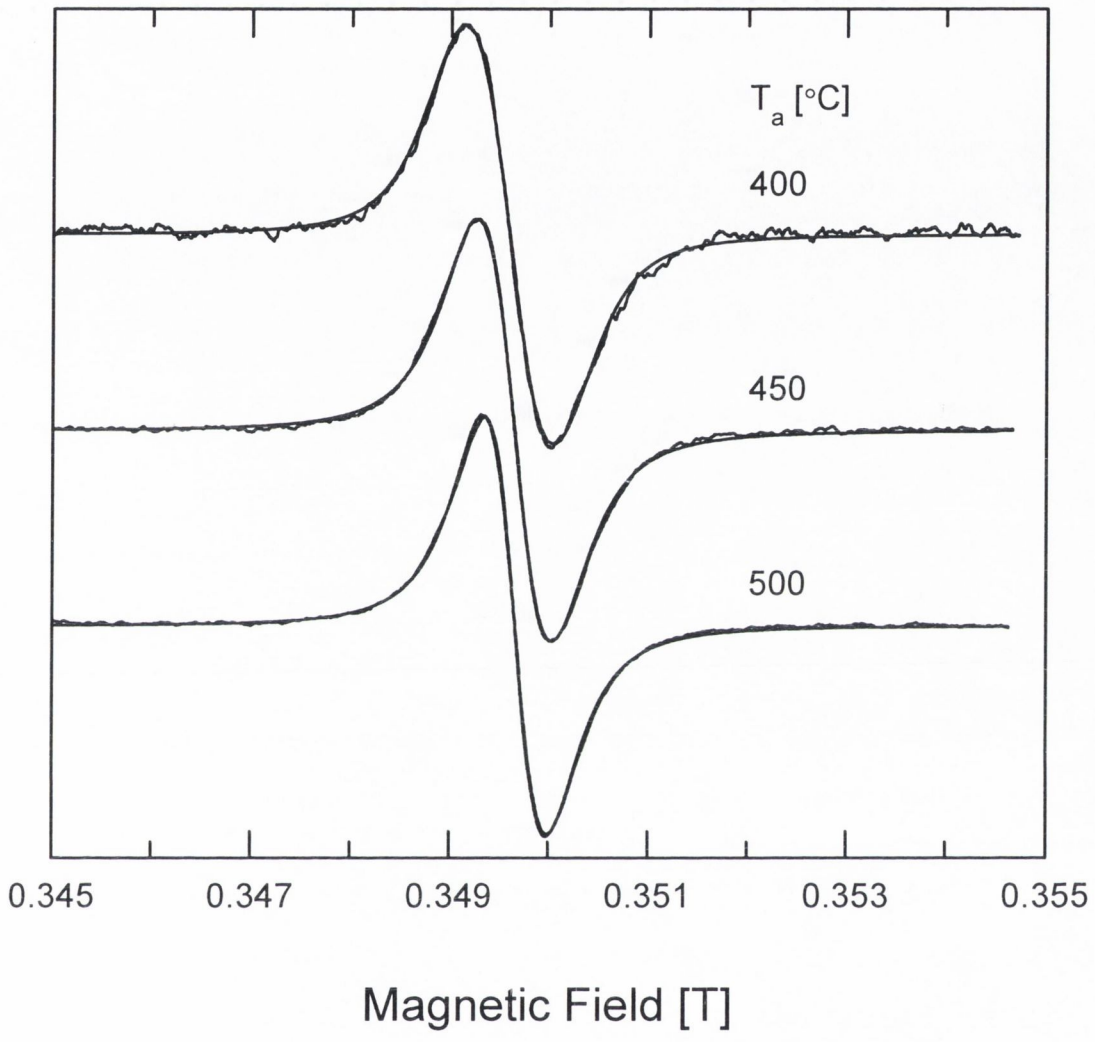

Figure 3.16 (ν = 9.8GHz) : EPR spectra for polymeric a-C:H,N as a function of annealing temperature (T_a) with their Voigt fits superimposed.

Figure 3.16 shows these spectra with their Voigt line fits. From this figure it can be seen that the Voigt lineshape fits the experimental data very well.

The parameters obtained by fitting these 3 spectra (i.e. T_a = 400, 450 and 500°C) with a Voigt lineshape are given in table 3.12. $\Delta B_{pp}{}^{V}$ is the linewidth of the total Voigt convolution, $\Delta B_{pp}{}^{L}$ is the linewidth of the Lorentzian of the individual spin packets and $\Delta B_{pp}{}^{G}$ is the linewidth of the Gaussian envelope (See chapter 2 for more information about Voigt lineshapes).

Annealing Temperature (T_a) [°C]	g-value	ΔB_{pp} [mT]	ΔB_{pp}^{V} [mT]	ΔB_{pp}^{L} [mT]	ΔB_{pp}^{G} [mT]
400	2.0029	0.88	0.889	0.398	0.663
450	2.0025	0.75	0.764	0.495	0.45
500	2.0025	0.63	0.689	0.500	0.357

Table 3.12 : Parameters used in generating the Voigt fits for a-C:H,N.

In table 3.12 it can be seen that the Lorentzian component of the Voigt lineshape begins to dominate the signal with increasing annealing temperature (T_a) i.e. that ΔB_{pp}^{L} becomes wider than ΔB_{pp}^{G}.

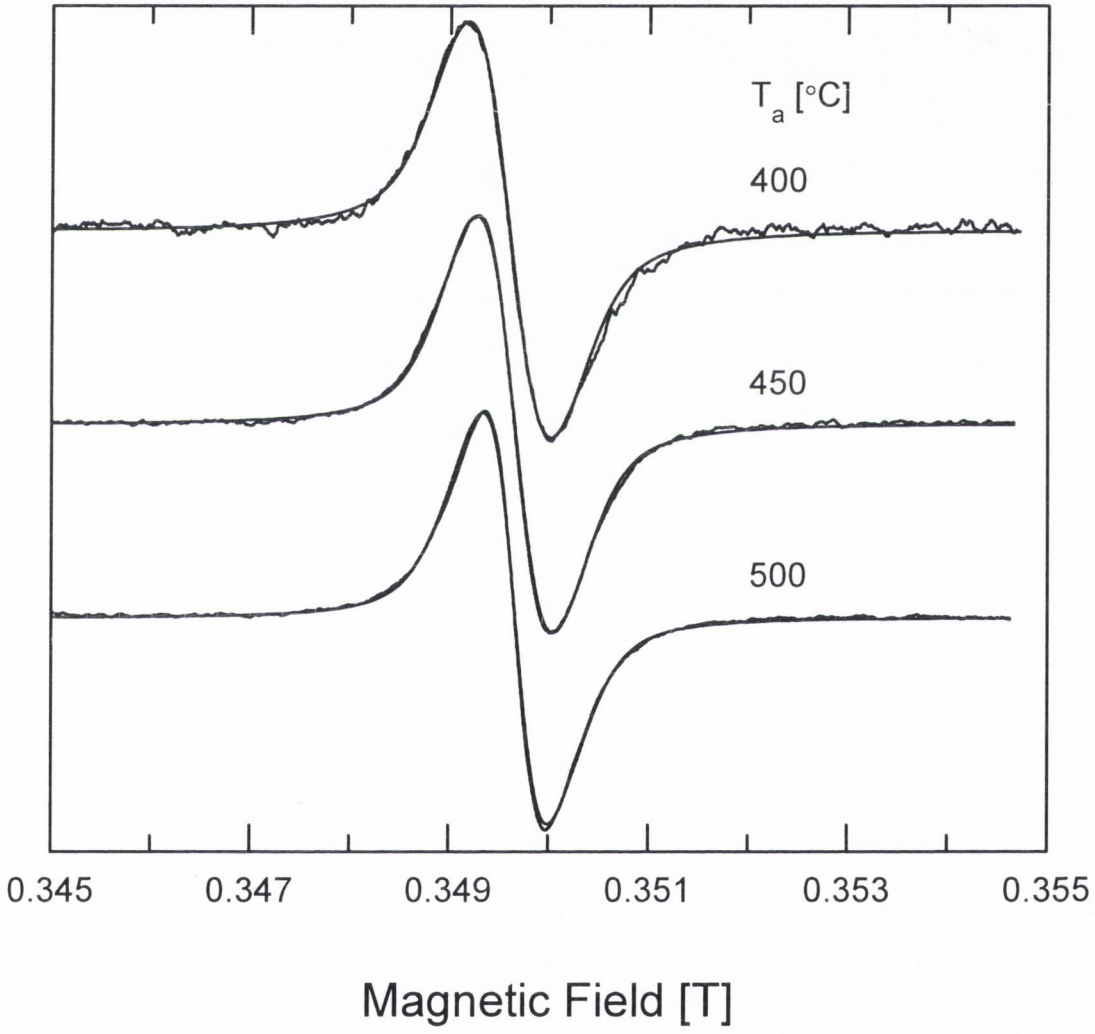

Figure 3.17 (ν = 9.8GHz) : EPR spectra for polymeric a-C:H,N as a function of annealing temperature (T_a) with their two-line fits superimposed (Gaussian + Lorentzian lines).

Next we fit these spectra with a two-line fit produced by superimposing a Gaussian and a Lorentzian line. Figure 3.17 shows these spectra with their two-line fits superimposed. Again we can see that the fits are very close to the experimental spectra.

Table 3.13 lists the parameters determined by fitting the spectra with these two lines.

	1st lineshape = Lorentzian				2nd lineshape = Gaussian			
T_a [°C]	1st g-value	1st ΔB_{pp} [mT]	1st N_A [10^{13}cm^{-2}]	1st N_V [10^{17}cm^{-3}]	2nd g-value	2nd ΔB_{pp} [mT]	2nd N_A [10^{13}cm^{-2}]	2nd N_V [10^{17}cm^{-3}]
400	2.0029	0.839	6.11	21.3	2.0029	0.864	1.74	6.08
450	2.0025	0.739	11.2	39.4	2.0025	0.839	3.56	12.4
500	2.0025	0.601	16.2	56.4	2.0025	0.839	4.12	14.4

Table 3.13 : Parameters used in generating the two-line fits for a-C:H,N

As we can see from figures 3.16 and 3.17 the lineshape for a-C:H,N over this temperature range (400 to 500°C) can be determined equally well by fitting with a Voigt or a superposition of a Gaussian and Lorentzian.

Two types of defects with g=2.0055(4), ΔB_{pp}=0.56(2) and g=2.0027(2), ΔB_{pp}= 0.83(4)mT exist in both the polymeric a-C:H (for $T_a \leq 400$°C and a-C:H,N ($T_a \leq 350$°C) films. In order to see how the areal spin population for these two types of defects (N_A) varies as function of annealing temperature for both a-C:H and a-C:H,N we plot this data in figure 3.18. N_A instead of N_V values are plotted as we believe that the defects with g≈2.0055 are present in the Si substrates and possibly in the Si/a-C:H,(N) interfaces.

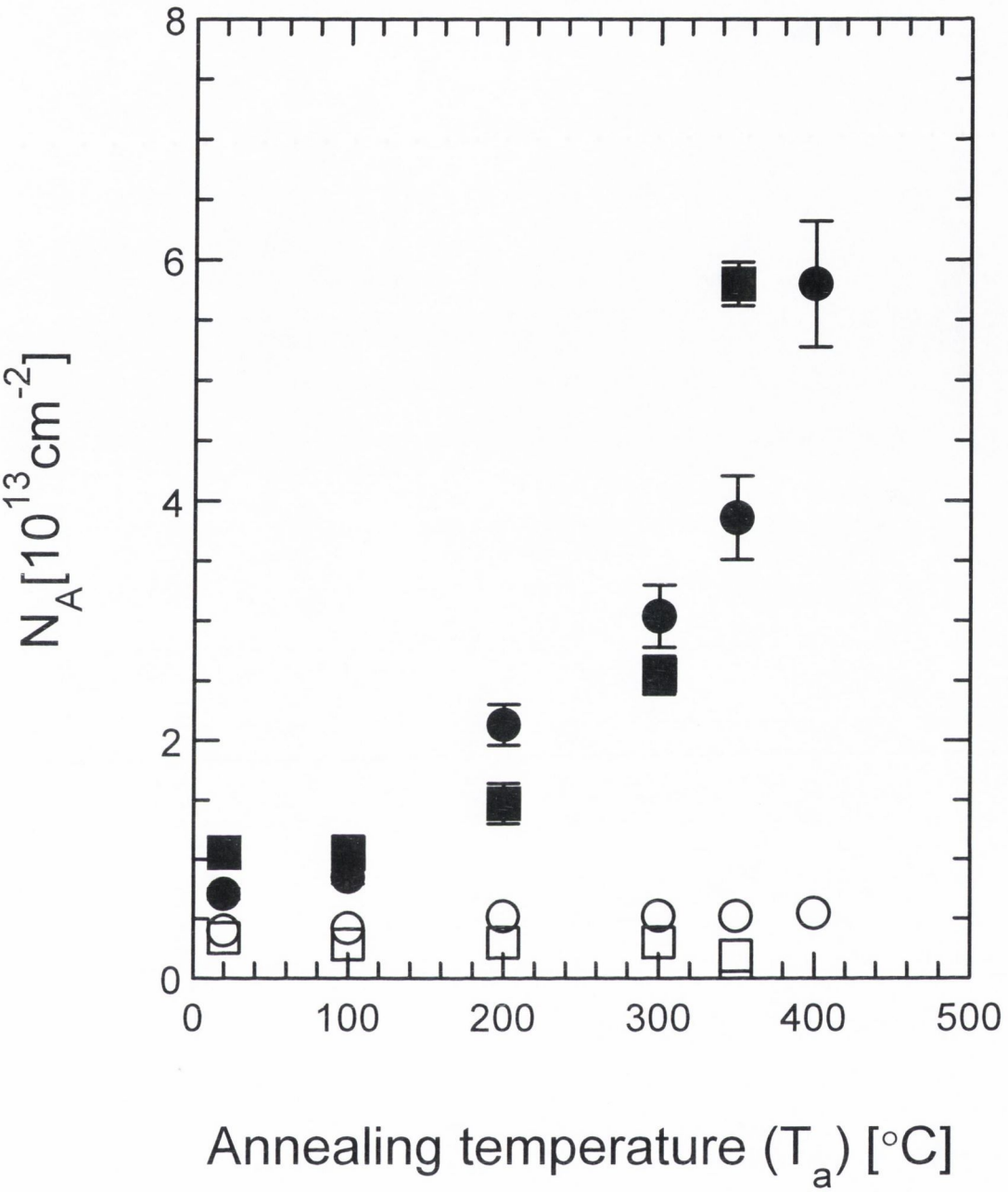

Figure 3.18 : N_A as a function of annealing temperature (T_a).

O *: Polymeric a-C:H line with g ≈ 2.0055 (Table 3.10),*

□ *: Polymeric a-C:H,N line with g ≈ 2.0055 (Table 3.11),*

" *: Polymeric a-C:H line with g ≈ 2.0027 (Table 3.10),*

∝ *: Polymeric a-C:H,N line with g ≈ 2.0027 (Table 3.11).*

In figure 3.18 the areal spin population (N_A) of the defects which have g≈2.0055 for both a-C:H and a-C:H,N remains constant up to T_a = 400°C (i.e. the O

and □ lines respectively); the g≈2.0055 signal is undetectable above 400°C in both samples because it becomes obscured by the g≈2.0027 line (i.e. the ″ and ∝ lines respectively). So annealing up to 400°C has no noticeable effect on the g≈2.0055 defects associated with the Si substrate and the possible Si/a-C:H interface. The growth in the areal spin populations (N_A) for the defects which have g≈2.0027 compared to those which have g≈2.0055 explains the fall in the cross-over g_0-values we plotted in figure 3.13.

In order to look only at the effect on the bulk a-C:H and a-C:H,N paramagnetic defects we plot in figure 3.19 the linewidths (ΔB_{pp}) and spin concentrations (N_V) for these defects only, i.e. the line with g≈2.0027.

We can see in figure 3.19 that the spin concentrations and linewidths (ΔB_{pp}) for these defects in both films, which have g≈2.0027, behave in a very similar manner as a function of annealing temperature. The spin concentrations increases with annealing temperature up to T_a ≈550°C, after which they drop sharply. The linewidths remain at ≈0.85mT until a temperature of 350°C is reached after which they fall to ≈0.5mT at 600°C. It should be noted that the spin concentrations are calculated assuming that the thickness of the polymeric a-C:H and a-C:H,N films remain constant; in fact the thickness of similar films falls with increasing annealing temperature (T_a) (R. W•chter and A. Cordery, personal communication).

So in figure 3.18 and 3.19 we can see that the two types of defects present in polymeric a-C:H and a-C:H,N behave in a very similar manner, as a function of annealing temperature (T_a) up to at least about 400°C. We noticed no effect on defects with g≈2.0055 up to ≈400°C. One exception to this similar behaviour is that in the temperature range 400 to 500°C the lineshape for the a-C:H,N film is not a Lorentzian, a Gaussian or a superposition of two Lorentzians while we find the lineshape is a single Lorentzian for the a-C:H film above 400°C.

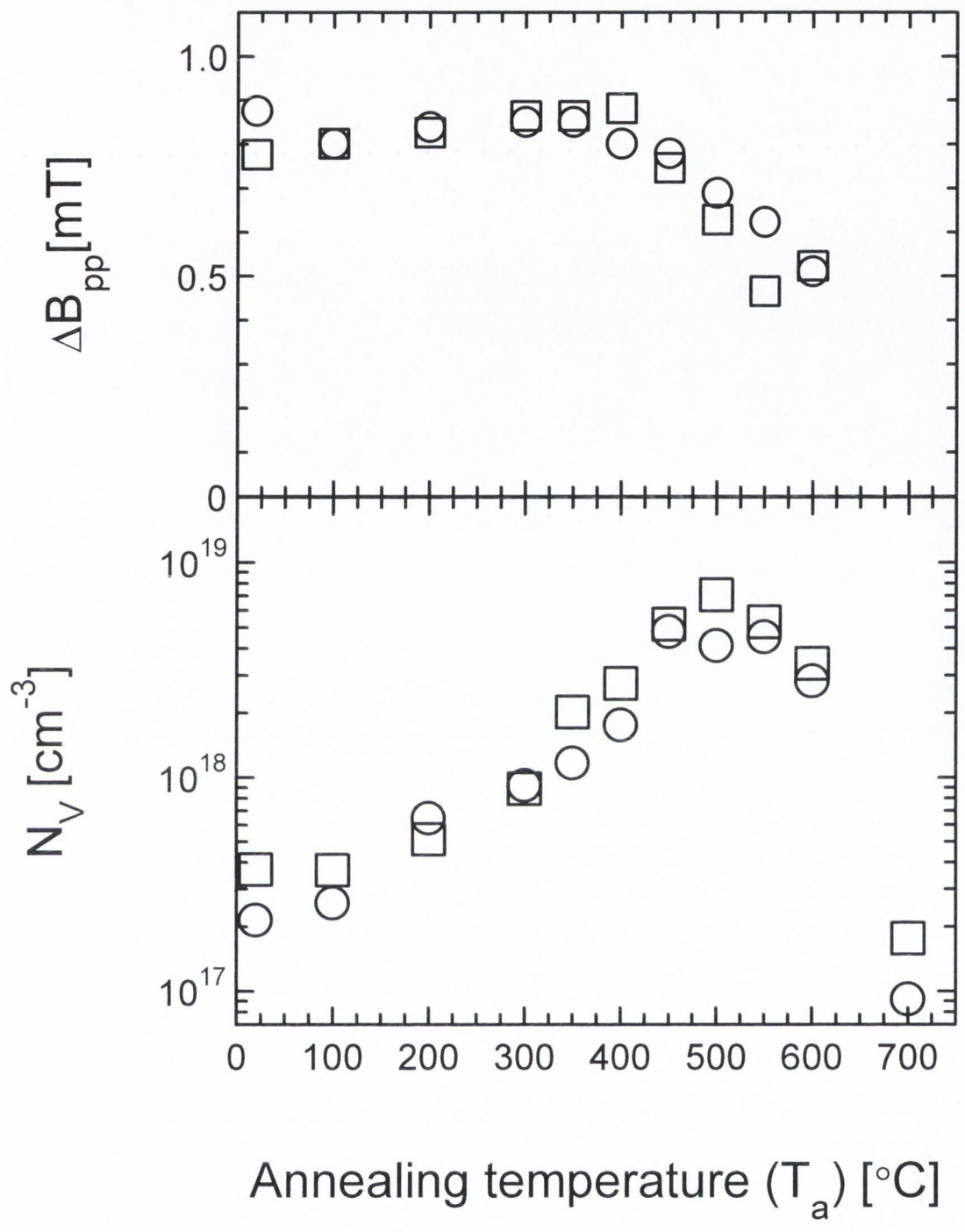

Figure 3.19 : N_V as a function of annealing temperature (T_a).

O : Polymeric a-C:H line with g ≈ 2.0027 (RS005: Table 3.10),

□ : Polymeric a-C:H,N line with g ≈ 2.0027 (Jar-2-23: Table 3.11).

3.4.2 Discussion of the effect of annealing on polymeric a-C:H and a-C:H,N

In this section we discuss the EPR results we have obtained for annealing polymeric a-C:H and a-C:H,N.

The annealing behaviour of defects present in the polymeric a-C:H and a-C:H,N films is very similar. In each case the defects present in the Si substrates and possibly present in the Si/a-C:H,(N) interfaces show no signs of annealing at up to $T_a \approx 400°C$. The fall in the cross-over g_0-values with increasing annealing temperature can be explained by the growth in the areal spin populations (N_A) of the defects with $g \approx 2.0027$ relative to the defects with $g \approx 2.0055$. Table 3.14 compares our experimental cross-over g_0-values with those reported by Sadki et al. (1996) for polymeric a-C:H grown by electron beam evaporation of graphite in a butane plasma.

Annealing temperature (T_a) [°C]	g_0-value (a-C:H)	g_0-value (a-C:H,N)	g_0-value (From Sadki et al. (1996))
20	2.0048	2.0044	2.0045
200	2.0037	2.0039	N/A
250	N/A	N/A	2.0037
300	2.0033	2.0033	N/A
350	2.0029	2.0026	2.0028

Table 3.14 : Comparison of g_0-values as a function of annealing temperature (T_a).

Table 3.14 shows that the results obtained by Sadki et al. (1996) closely match ours at 20 and 350°C while our values at 200°C closely match theirs at 250°C. Therefore we believe that the fall in cross-over g_0-value reported by Sadki et al. (1996) is also due to the growth in the areal spin population (N_A) of the defects with $g \approx 2.0027$ relative to the defects with $g \approx 2.0055$. Their results (Sadki et al. (1996)) can also be explained by the presence of two defects, one in the bulk of polymeric a-C:H film, the second present in the Si substrate and possibly in the Si/a-C:H interface.

We next examine the reasons why the defect spin concentrations (N_V) plotted in figure 3.19, for the line with $g \approx 2.0027$, increase with annealing temperature until ≈550°C is reached, after which they fall sharply.

Hydrogen has been reported to evolve from polymeric a-C:H (R. W•chter and A. Cordery, personal communication) grown by PECVD and from polymeric a-C:H

grown by graphite evaporation in a d.c. butane plasma (Sadki et al. 1996) at low annealing temperatures (<500°C). Austen et al. (1958) found that hydrogen was also released during the carbonisation of liquid hydrocarbons at low annealing temperatures (<500°C). Sadki et al. (1996), Austen et al. (1958) and Miller and McKenzie (1983) (deposited by glow discharge of a d.c. magnetron) found that the spin concentration (N_V) in polymeric a-C:H increased with annealing temperature until ≈500°C was reached. Jansen et al. (1984) reported that increased hydrogenation reduced the spin concentration (N_V) in their films produced by ion beam sputter deposition (IBSD) while Austen et al. (1958) also found this to be true for their samples.

It therefore seems reasonable from these results that the initial rise in spin concentrations (N_V) detected by us are due to the loss of hydrogen and possibly also nitrogen in the case of a-C:H,N. C-H bonds must be broken leaving behind unpaired electrons on the carbon atoms. Austen et al. (1958) believe that these unpaired electrons are initially in σ-orbitals but become stabilised by interaction with other carbon atoms, finally transforming into a π-bonded system. They believed that the broken bond has both partial π and σ-orbital characteristics. The π characteristics of this unpaired electron are also analogous to the unpaired π-electron found in the methyl radical $CH_3\bullet$ (• represents an unpaired electron) (Morrison and Boyd 1987).

It has been found (R. W·chter and A. Cordery, personal communication) that the fraction of sp^2 bonding increases with increasing annealing temperature (T_a) while Weiler et al. (1996) reported an almost linear decrease in the spin concentration (N_V) when the fraction of sp^2 bonding increased in their a-C:H films grown by an ethyne (acetylene) plasma beam source. It seems likely that the drop in the spin concentrations (N_V) for annealing temperatures above 550°C is due to an increase in the fraction of sp^2 bonding in our films. Basically the films are turning slowly to graphite above this temperature and this rearrangement is removing the unbound electrons. Sadki et al. (1996), Austen et al. (1958) and Miller and McKenzie (1983) give the same explanation for the effect annealing has on their samples. An increase in the sp^2 bonding may cause the polymer conjugated double bond chains (or aromatic clusters), in which the unpaired π-electrons reside, to grow; this allows greater delocalisation of these electrons. The π-electron can be delocalised over anything

from three carbon atoms (analogous to the allyl radical) in short chains to ≈20 carbon atoms in long chains of polyethyne (polyacetylene) (Su et al. 1979).

In summary the spin concentrations (N_V) in these films increases due to the loss of hydrogen up to T_a≈550°C, and possibly nitrogen in the case of the a-C:H,N film. Above T_a≈550°C the spin concentrations (N_V) fall due to an increase in the fraction of sp^2 bonding (the films became more graphite like).

In figure 3.19 it can be seen that the linewidths (ΔB_{pp}), for the bulk defects (g≈2.0027), fall from ≈0.8mT to ≈0.5mT when the films are annealed up to 600°C. A similar decrease in linewidth (ΔB_{pp}), when the annealing temperature is increased up to ≈550°C, has been reported before (Austen et al. (1958); Miller and McKenzie (1983); Sadki et al. (1996)). Weiler et al. (1996) reportes that the linewidth (ΔB_{pp}) falls when the fraction of sp^2 bonding increases. So it is possible that this decrease in the linewidths (ΔB_{pp}) up to T_a=600°C is due to narrowing caused by exchange interaction between the unpaired electrons. An increase in the fraction of sp^2 bonding would allow the polymer conjugated double bond chains (or aromatic clusters) in which the unpaired π-electrons reside to grow and this would allow a greater delocalisation of these electrons. This would enhance the exchange narrowing. For the polymeric a-C:H film this idea is supported by the fact that the lineshape is Lorentzian which is characteristic of narrowing caused by exchange interaction.

The a-C:H,N film in the range of temperatures 400 to 500°C has a lineshape which may be either a Voigt lineshape or superposition of a Gaussian and a Lorentzian line.

A Voigt lineshape is a convolution of a Gaussian and a Lorentzian line; such a lineshape would arise if the unpaired spins experience simultaneously at least two types of line broadening which individually give rise to a Lorentzian and a Gaussian. The Voigt lineshape we observe may be due to the presence of both unresolved hyper fine splitting (hfs) caused by the hydrogen and possibly the nitrogen present, which gives rise to a Gaussian line (Seidel and Wolf 1968; Poole 1983, p. 583), and dipolar interaction between like electron spins, which gives rise to a Lorentzian. The linewidths due to dipolar broadening based upon the N_V values and equation 3.2 are 0.022, 0.042 and 0.057mT for T_a = 400, 450 and 500°C respectively. We can see that these values are not in agreement with our ΔB_{pp}^{L} values (table 3.12) of 0.398, 0.495 and 0.50mT for T_a = 400, 450 and 500°C respectively. Therefore for dipolar

broadening to account for these linewidths the local spin concentration, which actually determines the amount of broadening, must be much higher than the average spin concentration (N_V) though the presence of exchange narrowing cannot be excluded. The strength of the dipolar broadening is dependant upon the distance between spins and thus the local spin concentration (Poole 1983, p. 552). This is strong evidence that the spins are clustered together which gives rise to a higher local spin concentration. The increase in annealing temperature (T_a) drives off hydrogen and possibly nitrogen from the film. This would explain why the Lorentzian component (i.e. $\Delta B_{pp}{}^{L}$) of the Voigt began to dominate the Gaussian (i.e. $\Delta B_{pp}{}^{G}$). The loss of hydrogen and possibly nitrogen would reduced the strength of the hyper fine splitting (hfs) the spins experience and thus reduce $\Delta B_{pp}{}^{G}$, this is seen in table 3.12. This would allow the dipolar interaction to dominate the signal and the lineshape would become Lorentzian, which it finally does when an annealing temperature (T_a) of 550°C is reached. The fact that the lineshape may be a Voigt for the a-C:H,N film, for T_a = 400 to 500°C, compared to a Lorentzian for the a-C:H film may be due to the presence of nitrogen. The presence of nitrogen may increase the amount of broadening due to hyperfine splitting (hfs) in a-C:H,N thus making the lineshape a Voigt instead of a Lorentzian.

The other possible case is that the lineshape for a-C:H,N, in the temperature range 400 to 500°C, is due to the superposition of a Lorentzian and a Gaussian. This may be possible if we consider that the spins exist in two different environments.

In one environment the defects might have a strong dipolar interaction (with possibly some exchange interaction) and hence give rise to a Lorentzian lineshape. The linewidths (ΔB_{pp}) due to dipolar broadening we calculate from the N_V values (table 3.12) and equation 3.2 to be 0.017, 0.032 and 0.046 for T_a = 400, 450 and 500°C respectively. The linewidths (ΔB_{pp}) we determine from fitting this Lorentzian line (table 3.12) are 0.839, 0.739 and 0.601 for T_a = 400, 450 and 500°C respectively. These are much smaller than those predicted by dipolar broadening and this indicates that defects are either clustered together or the line is exchange narrowed.

The defects in the second environment may be experiencing unresolved hfs (hyper-fine splitting) due to the presence of hydrogen and possibly nitrogen, and also experienced very little dipolar or exchange interaction and this would give rise to a Gaussian lineshape. In this environment the unpaired electrons could not be closely

clustered together as dipolar interaction between like-spins is not observed, i.e. the lineshape is not a Lorentzian. Also, in this environment the electrons do not experience exchange narrowing (i.e. not Lorentzian), which indicates that the unpaired electrons are not delocalised. While it is energetically favourable for these electrons to be π-electrons they may be in sp^3 (i.e. σ-bonded) sites on carbon atoms. This would explain the lack of delocalisation.

It is extremely difficult to be sure whether the line is a Voigt or a two-line superposition of a Gaussian and a Lorentzian. So we cannot say whether there exists one or two distinct types of defects in the bulk of the a-C:H,N film. Nonetheless, in both scenarios, for dipolar broadening to account for the linewidth of either the Lorentzian component of the Voigt ($\Delta B_{pp}{}^{L}$) or the Lorentzian line in the two-line fit (Gaussian + Lorentzian) the spins must be clustered together. In the case of the Voigt all the spins may be clustered while in the case of the two-line fit only the spins in the environment producing a Lorentzian are clustered. The previous explanation for the rise and fall of N_V and the fall in ΔB_{pp} are unaffected by either possibility. The fall in ΔB_{pp} with increasing T_a may still be due to an increase in the sp^2 content of the polymeric a-C:H,N film as this would reduce $\Delta B_{pp}{}^{L}$ in the Voigt, or ΔB_{pp} of the Lorentzian in the two-line fit.

In conclusion then, we find that the defects due to the Si substrates and possibly defects present in the Si/a-C:H,(N) interfaces are unaffected by thermal annealing up to ≈450°C. The spin concentrations (N_V) of the bulk defects, which have g≈2.0027, increases with annealing temperature up to 550°C because of the loss of hydrogen and possibly nitrogen in the case of the a-C:H,N film. The fall in N_V for both films for T_a values above 600°C is most likely due to the onset of graphitization. The drop in linewidths (ΔB_{pp}) for these defects, when T_a is increases from ≈300 to ≈600°C, may be because of an increase in exchange narrowing, due to an increase the amount of sp^2 bonding within the films.

We find that the a-C:H,N film displays a lineshape for these defects which is neither a Gaussian or a Lorentzian for T_a values in the range 400 to 500°C . We determined this lineshape to be either a Voigt or a two-line superposition produced by the combination of a Lorentzian and a Gaussian. It was not possible to determine

which lineshape was correct but in both cases we find evidence that all or some of the unpaired spins are clustered together.

3.5 Effect of changes in deposition temperature on polymeric a-C:H

The substrate temperature during the deposition can affect the structure, the optical and the electrical properties of a-C:H films (Chhowalla et al. 1997). It is the aim of this section of the chapter to examine the effect upon the defects of changing the substrate temperature during deposition.

3.5.1 Sample preparation

A set of samples deposited with different substrate temperatures (T_S) was produced. They were produced in the same manner as described in section 3.2.1. Table 3.15 displays the conditions used in preparing these films.

Name	Substrate temperature (T_S) [°C]	Thickness [nm]
Jar-2-15	50	149.6
Jar-2-1	98	101
Jar-2-2	150	85.7
Jar-2-16	200	84.9

Table 3.15 : Thickness and substrate temperature (T_S) for a-C:H films deposited with Plasma gas: 30sccm CH_4 only, RF power: 200W, Pressure: 200mtorr.

3.5.2 EPR results for a-C:H as a function of substrate temperature

In this section we examine the EPR results for polymeric a-C:H as a function of substrate temperature (T_S) and analyse these results. Figure 3.20 displays selected EPR spectra as a function of substrate temperature (T_S). It is clear from this figure that the signal intensity and hence the number of defects increases as T_S is increased above 98°C.

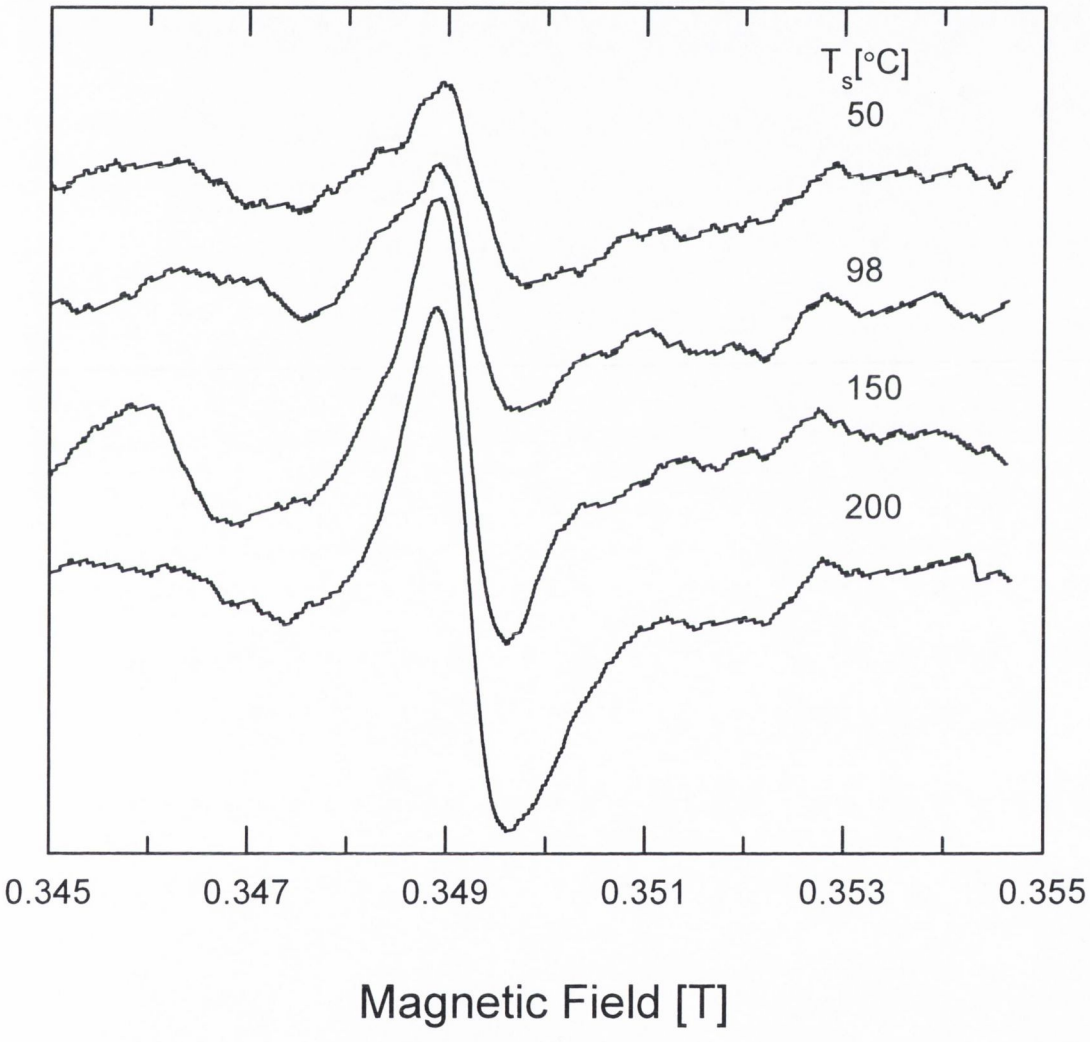

Figure 3.20 (ν = 9.8GHz) : EPR spectra for a-C:H as a function of substrate temperature (T_S).

Figure 3.21 is a graph of the EPR data of the samples listed in table 3.15. This figure shows that the cross-over g_0-value remains roughly constant as T_S increases.

The linewidth (ΔB_{pp}) remains at ≈0.8mT. The spin concentration (N_V) increases as the substrate temperature (T_S) is raised.

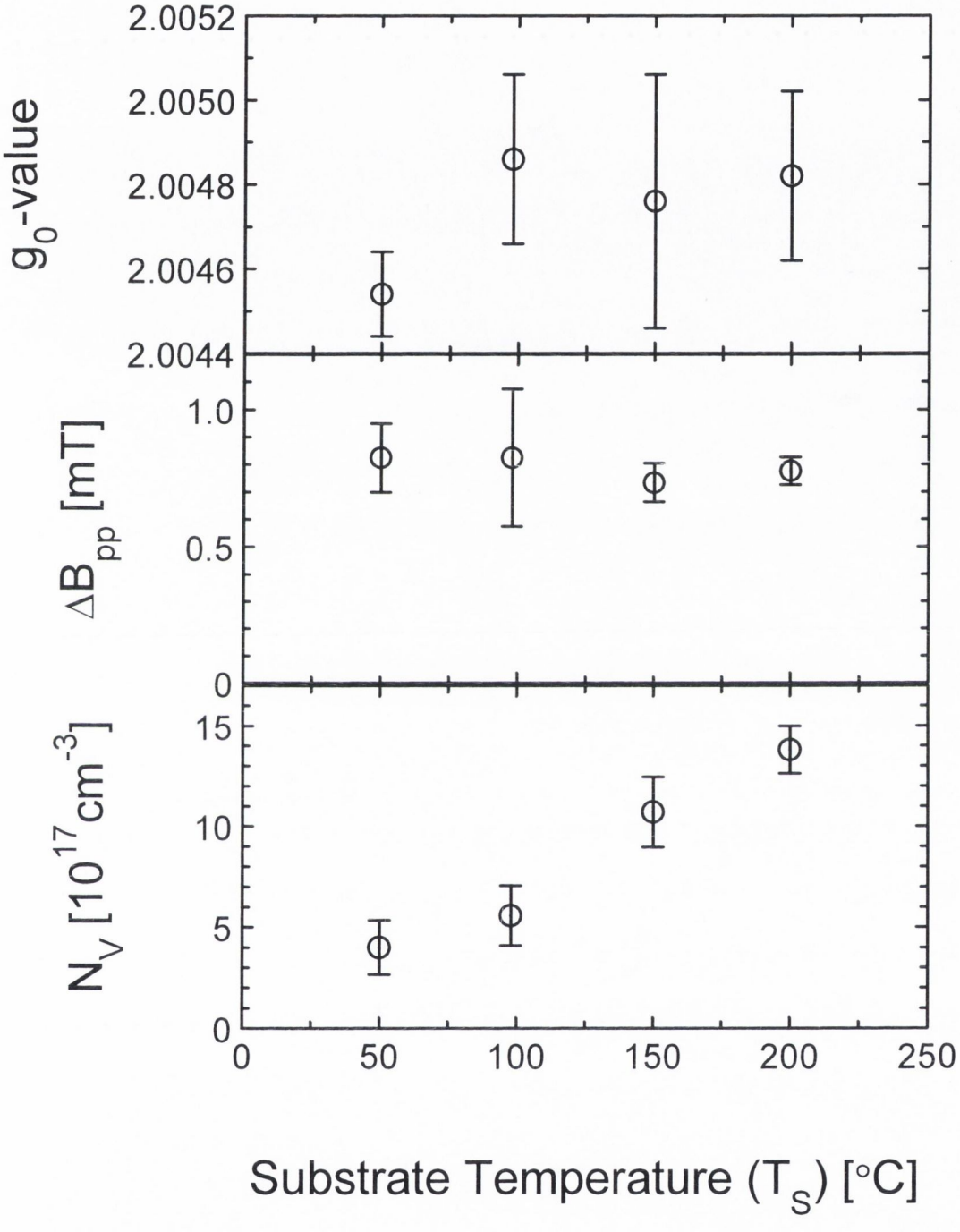

Figure 3.21 : EPR data for polymeric a-C:H as a function of substrate temperature (T_S).

It is again reasonable to assume from the shapes of the spectra in figure 3.20, that the same two types of defects are present in our samples. To determine the effect on each type of defect of changing the deposition temperature (T_S) a two-line fit was

carried out on each EPR spectra. We fitted the spectra with two EPR spectral lines, with g-values close to 2.0055 and 2.0027 which represented the Si dangling bond background (and possibly Si/a-C:H interface defects) and the bulk a-C:H defects respectively. Again the two lines used in fitting the spectra were Lorentzian.

Figure 3.22 shows the spectra with their two-line fits. It can be seen that the fits are reasonably good.

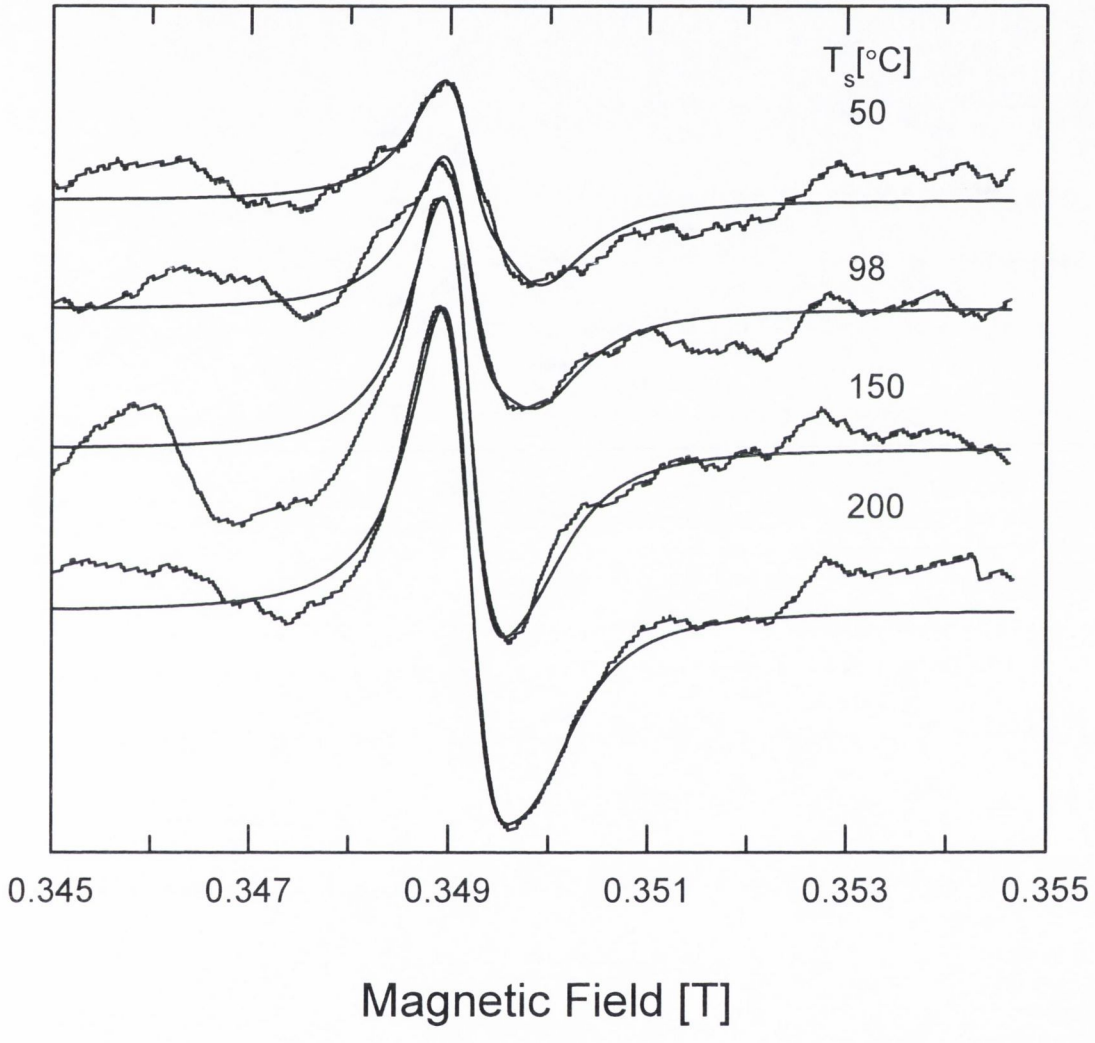

Figure 3.22 (ν = 9.8GHz) : EPR spectra for polymeric a-C:H as a function of substrate temperature (T_S) with their two-line fits superimposed.

Table 3.16 lists the parameters used in fitting the spectra at each substrate temperature (T_S). The values called 'corrected 1^{st} N_A' were calculated by subtracting the value of $0.2\times10^{13}cm^{-2}$ from the measured values of the '1^{st} N_A'; this was done in order to remove the contribution to this line from the Si substrate signal.

1st lineshape = Lorentzian					2nd lineshape = Lorentzian			
T_S [°C]	1st g-value	1st ΔB_{pp} [mT]	1st N_A [$10^{13}cm^{-2}$]	Corrected 1st N_A [$10^{13}cm^{-2}$]	2nd g-value	2nd ΔB_{pp} [mT]	2nd N_A [$10^{13}cm^{-2}$]	2nd N_V [$10^{17}cm^{-3}$]
50	2.0053	0.551	0.23±0.08	0.03±0.18	2.0027	0.804	0.37±0.12	2.5±0.8
98	2.0053	0.551	0.27±0.07	0.07±0.17	2.0027	0.804	0.29±0.08	2.9±0.8
150	2.0052	0.576	0.62±0.10	0.42±0.20	2.0028	0.801	0.30±0.05	3.5±0.6
200	2.0051	0.576	0.73±0.06	0.53±0.16	2.0027	0.804	0.44±0.04	5.2±0.4
Mean				0.26±0.18				

Table 3.16 : Parameters used in generating the two-line fits for a-C:H as a function of substrate temperature (T_S).

We cannot plot a graph of N_A values as a function of T_S because the thickness of each film was different. If we assume that the changes in the thickness have no major effect, then we can see that the areal spin population (N_A) for the line with g≈2.0053 remained roughly constant, within experimental error, as a function of substrate temperature (T_S) (table 3.16). This indicates that this defect is unaffected by the changes made in the substrate temperature during deposition (T_S) up to T_S=200°C. The spin concentration (N_V) versus substrate temperature (T_S) of defects with g≈2.0027 is plotted in figure 3.23.

Figure 3.23 compares the effect on the concentration, N_V, of the g≈2.0027 defects of raising T_S with that of raising the annealing temperature (T_a). The annealing data was previously obtained for the sample named RS005. Clearly from this figure we can see that the effect of raising T_S is very similar to that of raising T_a.

In conclusion the effect on the defects in polymeric a-C:H films of raising the substrate temperature to 200°C is very similar to that of raising the anneal temperature to the same value.

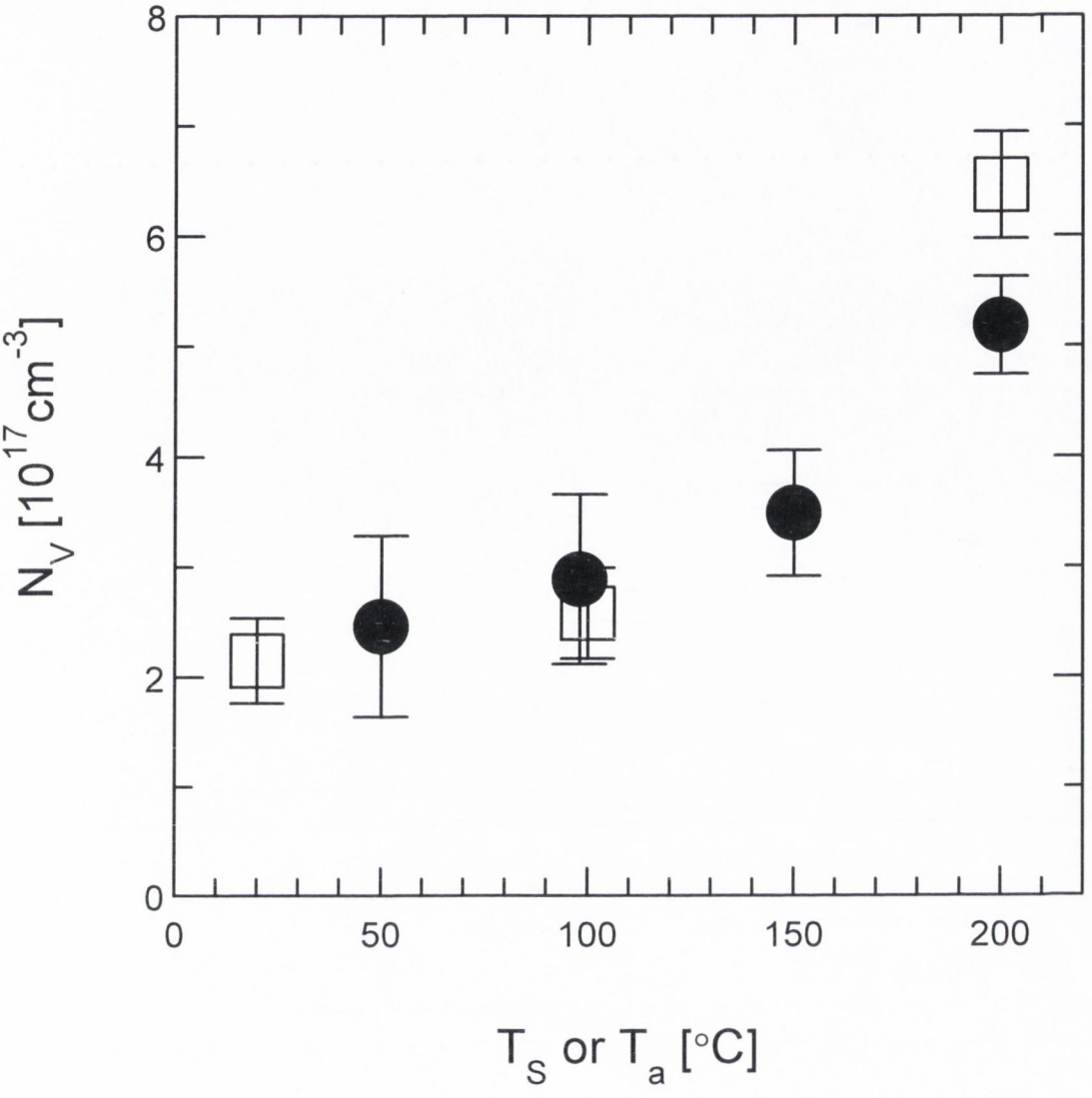

Figure 3.23: The dependence on T_S (●) and T_a (□) of the volume concentration, N_V, of the g≈2.0027 defects.

3.6 Ion implantation of polymeric a-C:H

Ion implantation is mainly used in the semiconductor industry to introduce dopant into semiconductors (Sze 1985, p. 405). Its main advantages over diffusion are that it is more precise and more reproducible. It is of practical interest to examine the effects of ion implantation on polymeric a-C:H. The ions used in this study are nitrogen, boron and carbon. In Si nitrogen is an n-type dopant while boron is a common p-type dopant. Meyerson and Smith (1980) report that phosphorous and boron can dope a-C:H n-type and p-type respectively. Therefore it is of interest to examine the defects produced by ion implantation of nitrogen (a possible n-type dopant) and boron (a possible p-type) into polymeric a-C:H. We study the effect of carbon implantation only to examine the defects produced by ion implantation without any possible doping effect. Therefore it is the aim of this section of the chapter to study the paramagnetic defects produced by implantation of boron, nitrogen and carbon ions into polymeric a-C:H.

3.6.1 Sample preparation.

The polymeric a-C:H films used in this study were produced in the manner described in section 3.2.1. The implantation was a double implantation at two energies; half of the total ion dose was implanted with an ion energy of 20keV and the other half with an energy of 32.5keV. Table 3.17 lists the film deposition conditions and the implantation dose for each sample.

Name	Thickness [nm]	Implantation ion	Total dose [cm^{-2}]	Tauc optical band gap E_T [eV]
Ce13	91.3	Carbon	2×10^{13}	2.5
Ce14	97.6	Carbon	2×10^{14}	2.5
Ce15	73.8	Carbon	2×10^{15}	0.75-1.25
Be14	97.1	Boron	2×10^{14}	2.5
Be15	70.9	Boron	2×10^{15}	0.75-1.25
Be16	45.2	Boron	2×10^{16}	0.25
Ne12	93.6	Nitrogen	2×10^{12}	2.55
Ne13	99.9	Nitrogen	2×10^{13}	2.5
Ne14	96.0	Nitrogen	2×10^{14}	2.5
Ne15	66.3	Nitrogen	2×10^{15}	0.75-1.25

Table 3.17 : Implantation doses and ion used for a-C:H films deposited with Plasma gases = 75sccm He + 30sccm CH_4, RF power: 200W, Pressure: 200mTorr,Substrate at room temperature.

The Tauc optical gap before implantation is ≈2.6eV.

3.6.2 EPR results for ion implantation into polymeric a-C:H

In this section of the chapter we shall give the EPR results and analysis for our polymeric a-C:H films which were implanted with nitrogen, boron and carbon ions. Figure 3.24 shows selected spectra from these implanted samples. This figure and table 3.18 show that the way in which the spectra change with ion dose is similar for each type of ion. At a dose of $2\times10^{14}cm^{-2}$ or less the lineshape is nearly symmetric, $g_0\approx2.0060$ and $\Delta B_{pp}\approx0.7mT$. This signal probably arises from Si defects in the Si substrate. The ion range and damage profiles calculated by 'TRIM96' indicate that many of the ions enter the Si substrate. However as a dose of $2\times10^{15}cm^{-2}$ the lineshape has clearly changed for the B and N implants and the g_0-value has decreased for B, N and C. For the implant of 2×10^{15} N cm^{-2} an excellent fit to the spectrum is obtained (figure 3.25) by superimposing two Lorentzian lines with g=2.0057 and g=2.0026; the other parameters are given in table 3.19. The latter signal undoubtedly

comes from carbon unpaired spins in bulk of the a-C:H film which may not in this case be uniformly distributed and N_V represents the average within the film. The creation of such defects is also apparent for the 2×10^{15} B cm^{-2} implant though less clear at a dose of 2×10^{15} C cm^{-2}. The only implant at a dose of $2\times10^{16}cm^{-2}$ is for Boron and the spectrum is dominated by the sharp line, $\Delta B_{pp}=0.14\pm0.02$, at g=2.0027 due to the defects in the film; the signal from defects in the Si substrate is completely obscured. It is noteworthy that between 2×10^{15} and 2×10^{16} B cm^{-2} N_A increases by a factor of about 30. The reason for this is unclear but probably is associated with hydrogen loss. In addition table 3.17 shows that the Tauc gap drops for doses $\geq2\times10^{15}cm^{-2}$ and this must reflect an increasing graphitization of the film. This will lead to an increased delocalisation of the C unpaired electrons and hence the increased possibility of exchange interaction which probably accounts for the line narrowing.

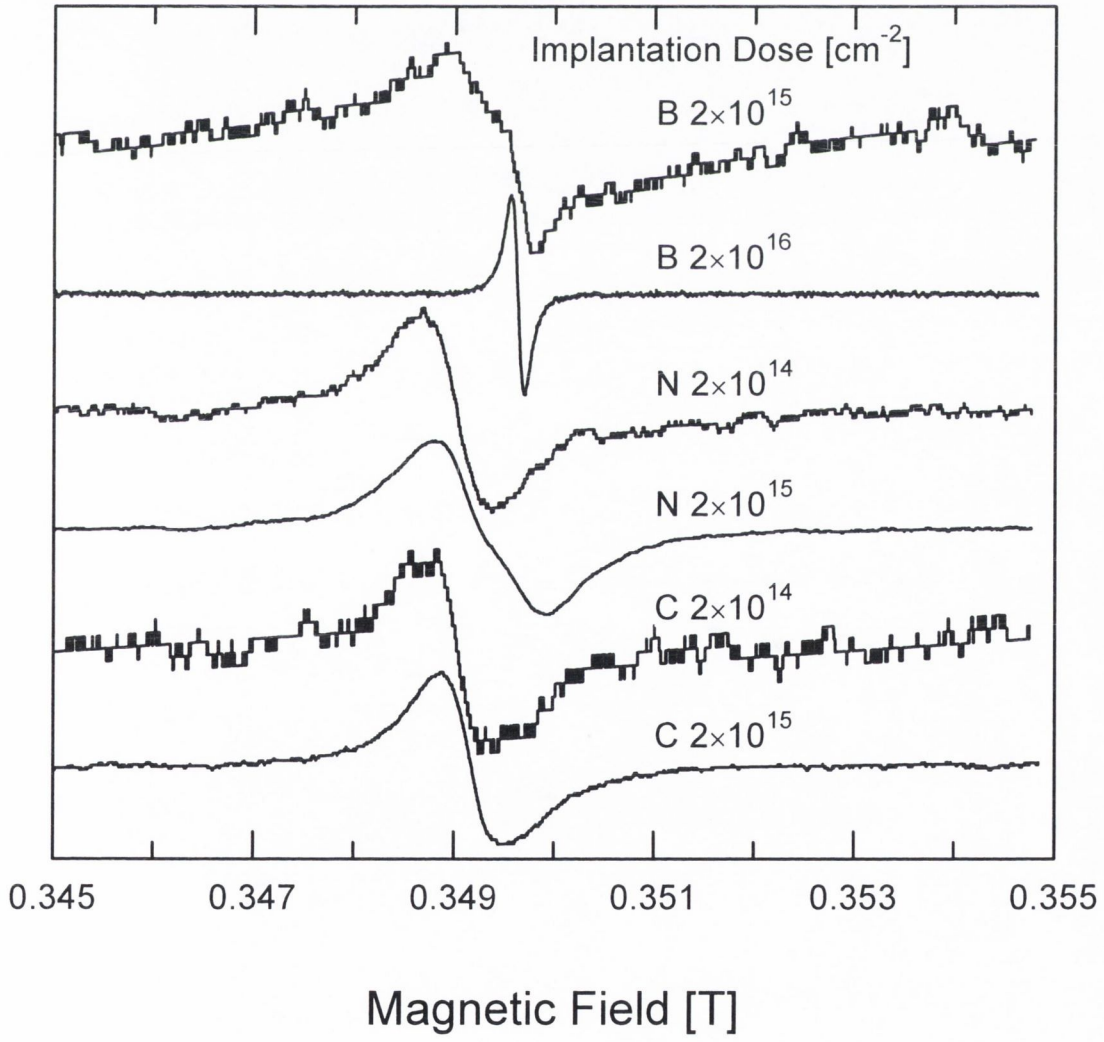

Figure 3.24 (ν = 9.8GHz) : EPR spectra for the ion implanted polymeric a-C:H films (table 3.17).

Double implantation: Energies = 20keV & 32.5keV				
Implantation ion: Boron				
Dose [cm^{-2}]	Thickness [nm]	g_0	ΔBpp[mT]	$N_A[10^{13}cm^{-2}]$
2×10^{14}	97.1	2.0061±0.0002	0.60±0.11	2.61
2×10^{15}	70.9	2.0031±0.0010	0.89±0.22	3.23
2×10^{16}	45.2	2.0027±0.0001	0.14±0.02	94.2
Implantation ion: Carbon				
Dose [cm^{-2}]	Thickness [nm]	g_0	ΔBpp[mT]	$N_A[10^{13}cm^{-2}]$
2×10^{13}	9.13	N/A	1.06±0.9	0.54
2×10^{14}	97.6	2.0061±0.0002	0.71±0.25	2.56
2×10^{15}	73.8	2.0053±0.0001	0.65±0.1	10.6
Implantation ion: Nitrogen				
Dose [cm^{-2}]	Thickness [nm]	g_0	ΔBpp[mT]	$N_A[10^{13}cm^{-2}]$
2×10^{12}	93.6	N/A	N/A	N/A
2×10^{13}	99.9	2.0059±0.0002	0.64±0.35	1.22
2×10^{14}	96.0	2.0061±0.0002	0.72±0.17	3.78
2×10^{15}	66.3	2.0048±0.0001	1.12±0.08	17.5

Table 3.18 : EPR data for polymeric a-C:H films implanted with boron, carbon and nitrogen ions.

1^{st} lineshape = Lorentzian					2^{nd} lineshape = Lorentzian			
Name	Thickness [nm]	1^{st} g-value	1^{st} ΔB_{pp} [mT]	1^{st} N_A $[10^{13}cm^{-2}]$	2^{nd} g-value	2^{nd} ΔB_{pp} [mT]	2^{nd} N_A $[10^{13}cm^{-2}]$	2^{nd} N_V $[10^{19}cm^{-3}]$
Ne15	66.3	2.0057	0.724	10.21	2.0026	0.701	7.24	2.63

Table 3.19 : Parameters used in the two-line fit for the polymeric a-C:H film implanted with $2\times10^{15}cm^{-2}$ nitrogen ions.

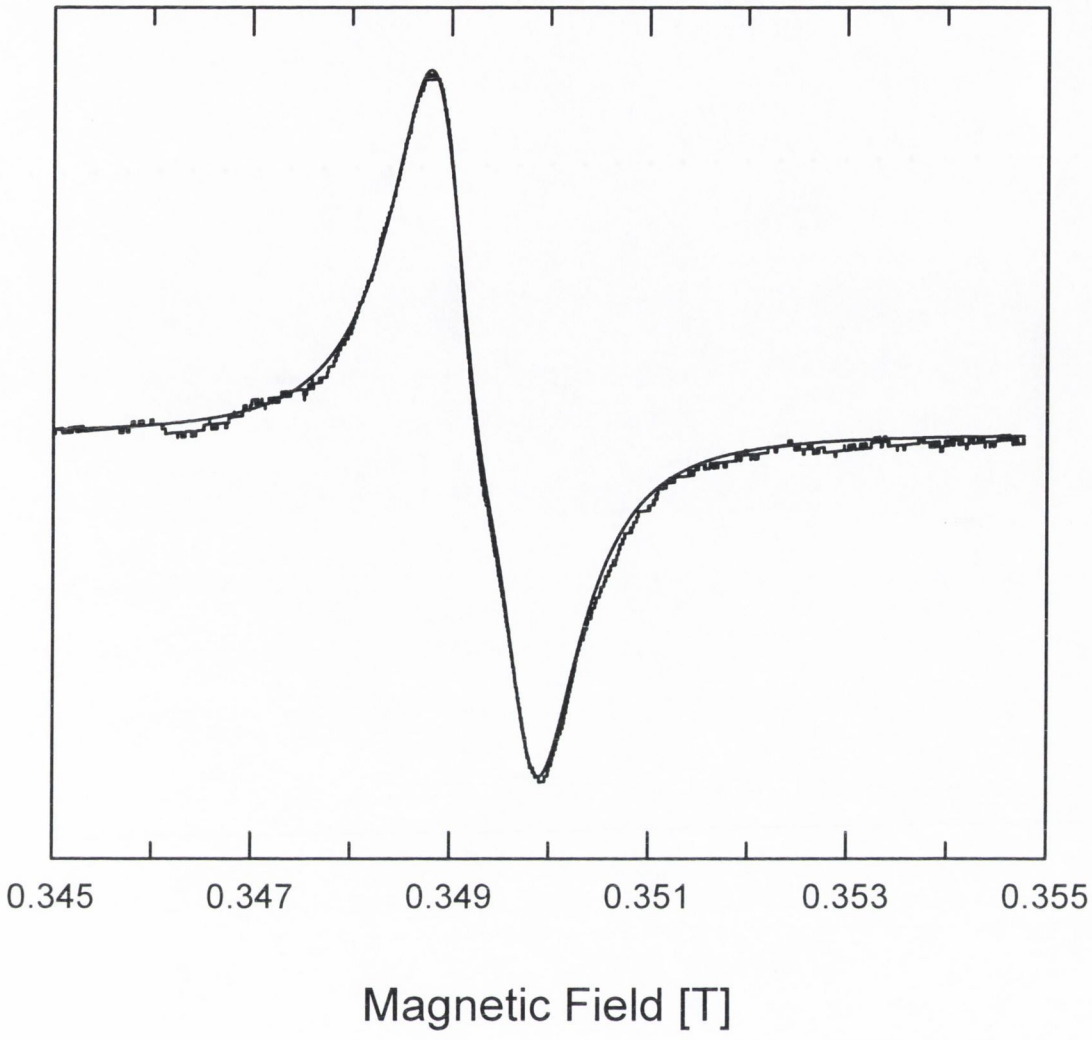

Figure 3.25 (ν = 9.8GHz) : EPR spectrum and two-line fit for the polymeric a-C:H film implanted with $2\times10^{15}cm^{-2}$ nitrogen ions.

So to conclude, implantation of boron, nitrogen and carbon into polymeric a-C:H gives rise to two types of defects: one in the a-C:H films which we believe are due to unpaired π-electrons on conjugated olefinic chains or on aromatic clusters with an odd number of fused rings, the other due to dangling bonds produced in the Si substrate. The rate at which defects are produced, as a function of implantation dose, is roughly the same for carbon and nitrogen ions. Implantation of $2\times10^{16}cm^{-2}$ boron ions causes a rapid increase in the number of bulk a-C:H defects present (N_A). We believe that this rapid increase may be due to the loss of hydrogen.

3.7 Conclusions

In the bulk polymeric a-C:H powder grown by PECVD, we find a paramagnetic defect which is situated on carbons atoms. These unpaired electrons are most likely π-electrons and they probably reside in chains of conjugated double bonds similar to polyethyne (polyacetylene). Less probable is that the π-electrons are situated in clusters made up of an odd number of aromatic rings (i.e. benzene rings). However both cases may exist to a lesser or greater extent.

In the polymeric a-C:H films deposited on Si substrates we find two types of paramagnetic defects; one is the same as mentioned above, the other is most likely due to dangling bonds in the Si substrate, but we cannot rule out the presence of an unknown defect in the region close to the Si/a-C:H interface. Annealing the a-C:H films produces an increase in the defect density probably due to the loss of hydrogen. This evolution of hydrogen occurs mainly over the temperature range of ≈100°C to ≈500°C. ΔB_{pp} fall with increasing T_a, we believe that this is due to ratio of sp^2 hybridised bonds to sp^3 bonds on the carbon atoms increasing with annealing temperature, which may allow greater delocalisation and increase the exchange narrowing of the line. The dependence of the defect density on the substrate temperature during deposition is found to have a very similar to its dependence on post-deposition annealing temperature.

The addition of nitrogen into polymeric a-C:H films seems to have very little effect on the paramagnetic defects present. Again the two paramagnetic defects mentioned above are found. We found no evidence to support the idea that nitrogen forms 4-fold co-ordination bonding in polymeric a-C:H,N films. This basically means the nitrogen has a poor doping efficiency in polymeric a-C:H.

Annealing affects the a-C:H,N defects in the same way as it does those in a-C:H. Over the annealing temperature range of 400°C to 500°C the lineshape of the EPR is found to be neither Gaussian or Lorentzian. This leads us to believe that the linewidth of the signal from the bulk paramagnetic defect (most likely π-electrons residing in chains of conjugated double bonds) arises from dipolar interaction, unresolved hyper-fine splitting and possibly exchange narrowing in this temperature range. Each defect may experience all these effects giving rise to a Voigt lineshape. Or there may be two types of defects, one experiencing dipolar broadening and

possibly exchange narrowing in an environment where the spins are clustered, the π-electrons possibly delocalised and hydrogen atoms far removed, the second experiencing hyper-fine splitting caused by the proximity of hydrogen and very little dipolar or exchange interactions. This would give rise to a superposition of a Lorentzian and a Gaussian line.

Implantation into polymeric a-C:H gives rise to two types of defects; one in the a-C:H films which we believe are unpaired π-electrons on conjugated olefinic chains or on aromatic clusters with an odd number of fused rings, the other due to dangling bonds produced in the Si substrate. The type of ion used in the implantation has very little effect on the paramagnetic defects that are produced. Loss of hydrogen is probably a significant factor in producing defects in the a-C:H film when the implantation dose is $2\times10^{16}cm^{-2}$. It would have been better to have studied much thicker samples using the same ion energies. This is because Si dangling bonds would not have been produced by implantation as the ions would not have reached the substrate.

3.8 References

Abragam, A. (1996). Principals of Nuclear Magnetism, p. 126. Clarendon press, Oxford.

Amaratunga, G. A. J. and Silva, S. R. P. (1996). Applied Physics Letters, **68**, 2529.

Austen, D. E. G., Ingram, D. J. E. and Tapley J. G. (1958). Transactions of the Faraday Society, **54**, 400.

Cernogora, J. (1997). Physica Status Solidi, **201**, 303.

Chhowalla, M., Robertson, J., Chen, C. W., Silva, S. R. P., Davis, C. A. and Amaratunga, G. A. J. (1997). Journal of Applied Physics, **81**, 139.

Giorgis, F., Tagliaferro, A. and Fanciulli, M. (1998). In Amorphous Carbon: State Of The Art, (ed. S. R. P. Silva, J. Robertson, W. I. Milne and G. A. J. Amaratunga), p. 143. World Scientific, Singapore.

González-Hernández, J., Asomoza, R. and Reyes-Mena, A. (1988). Solid State Communications, **67**, 1085.

Hoinkis, M., Weber, E. R., Landstrass, M. I., Plano, M. A., Han, S. and Kania, D. R. (1991). Applied Physics Letters, **59**, 1870.

Kawasaki, M., Vandentop, G. J., Salmeron, M. and Somorjai, G. A. (1990). Surface Science, **227**, 261.

Kim, S. M. and Wager, J. F. (1998). Applied Physics Letters, **53**, 1880.

Lee, J. D. (1991). Concise Inorganic Chemistry, (4^{th} edn), p. 468. Chapman & Hall, London.

McClintock, I. S. and Orr, J. C. (1968). Physica Status Solidi, **29**, K157.

Meyerson, B. and Smith, F. W. (1980). Solid State Communications, **34**, 531.

Miller, D. J. and McKenzie, D. R. (1983). Thin Solid Films, **108**, 257.

Morrison, R. T. and Boyd, R. N. (1987). Organic Chemistry, (5th edn), p. 65. Allyn and Bacon.

Nishikawa, H., Nakamura, R., Tohmon, R., Ohki, Y., Sakurai, Y., Nagaswa, K. and Hama Y. (1990). Physical Review B, **41**, 7828.

Nishikawa, H., Nakamura, R., Ohki, Y. and Hama Y. (1993). Physical Review B, **48**, 15584.

Poole, C. P. (1983). Electron Spin Resonance, A Comprehensive Treatise On Experimental Techniques, (2nd edn). Wiley, New York.

Ristein, J., Sch·fer, J. and Ley, L. (1995). Diamond and Related Materials, **4**, 508.

Robertson, J and O'Reilly, E. P. (1987). Physical Review B, **35**, 2946.

Robertson, J. (1986).Advances in Physics, **35**, 317.

Robertson, J. (1993). Diamond and Related Materials, **2,** 984.

Robertson, J. (1994). Diamond and Related Materials, **3,** 361.

Robertson, J. (1996a). Journal of Non-Crystalline Solids, **198-200**, 615.

Robertson, J. (1996b). Physical Review B, **53**, 16302.

Rusli, Amaratunga, G. A. J. and Silva, S. R. P. (1995). Thin Solid Films, **270**, 160.

Sadki, A., Bounouh, Y., Theye, M. L., von Bardeleben, J., Cernogora, J. and Fave, J. L. (1996).Diamond and Related Materials, **5**, 439.

Sandner, P., Kaiser, U., Altebockwinkel, M., Wiedmann, L., Benninghoven, A., Sah, R. E. and Koidl P. (1987). Journal of Vacuum Science Technology A, **5**, 1470.

Sch·fer, J., Ristein, J. and Ley, L. (1997). Diamond and Related Materials, **6**, 730.

Sch✧tte, S., Will, S., Mell, H. and Fuhs, W. (1993). Diamond and Related Materials, **2**, 1360.

Schwan, J., Ulrich, S., Roth, H., Ehrhardt, H., Silva, S. R. P., Robertson, J., Samlenski, R. and Brenn R. (1996). Journal of Applied Physics, **79,** 1416.

Schwan, J., Batori, V., Ulrich, S., Ehrhardt, H. and Silva, S. R. P. (1998). Journal of Applied Physics, **84**, 2071.

(1996). Journal of Applied Physics, **79,** 1416.

Sealy, L., Barklie, R. C., Lulli, G., Nipoti, R., Balboni, R., Milita, S. and Servidori, M. (1995). Nuclear Instruments and Methods in Physics Research B, **96**, 215.

Seidel, H. and Wolf, H. C. (1968). Physics of Color Centers, (ed. W. Fowler), p. 557. Academic Press, New York.

Shah, I. (1997). In Physics World, (ed. P. Rogers), p.45. Institute of Physics Publishing, Bristol.

Silva, S. R. P., Robertson, J., Amaratunga, G. A. J., Rafferty, B., Brown, L. M., Schwan, J., Franceschini, D. F. and Mariotto, G. (1997). Journal of Applied Physics, **81**, 2626.

Su, W. P., Schrieffer, J. R., and Heeger, A. J. (1979). Physics Review Letters, **42**, 1698.

Sze, S. M. (1985). Semiconductor Devices: Physics and Technology. Wiley, New York.

Tanaka, K., Matsuura, Y., Oshima, Y., Yamabe, T. and Hotta, S. (1994).Synthetic Metals, **66**, 295.

Ugolini, D., Eitle, J., Oelhafen, P. and Wittmer, M. (1989). Applied Physics A: Solids Surfaces, **48**, 549.

Weiler, M., Sattel, Giessen, T. S., Jung, K., Ehrhardt, H., Veerasamy, V. S. and Robertson, J. (1996).Physical Review B, **53,** 1594.

Yoshimi, M., Shimizu, H., Hattori, K., Okamoto, H. and Hamakawa, Y. (1992). Optoelectronic Device Technology, **7**, 69.

Zhang, Q., Yoon, Rusli, S. F., Ahn, J., Yang, H. and Bahr D. (1998). Journal of Applied Physics, **84**, 5538.

Chapter 4:

An EPR study of non-polymeric a-C:H

4.1 Introduction

Many forms of a-C:H can be produced by various methods and deposition conditions. For films produced in a PECVD reactor on the live electrode a very important parameter which controls the type of a-C:H produced is the negative self-bias voltage (V_b). Depending upon the V_b value a-C:H films ranging polymeric (with a low sp^2/sp^3 ratio and high hydrogen content) to diamond-like a-C:H (DLC) (with a low sp^2/sp^3 ratio and low hydrogen content) and finally on to graphite-like a-C:H (GLHC) (with a high sp^2/sp^3 ratio and low hydrogen content) can be prepared (Giorgis et al. 1998; Silva et al. 1996). Diamond-like a-C:H has practical application as a hard coating (Tsai and Bogy 1987). We already examined the defects present in polymeric a-C:H in the previous chapter. It is the aim of the work presented in this chapter to examine, using EPR, the paramagnetic defects present in a range of a-C:H films ranging from diamond-like (DLC) to graphite-like (GLHC) produced under a range of negative self-bias voltages (V_b). To further our understanding of the defects present in a-C:H films we will also measure the spin-lattice (T_1) and spin-spin (T_2) relaxation times as a function of V_b. We will also the examine, using EPR, the effect annealing has on the defects present in several a-C:H films produced with different negative self-bias voltages (V_b).

4.2 Defects present in a-C:H as a function of V_b

In this section of the chapter we examine what effect changing the negative self-bias voltage has on the defects present in amorphous hydrogenated carbon (a-C:H) films. We shall use the technique of electron paramagnetic resonance (EPR) to examine the paramagnetic defects present in a range of a-C:H films produced with different V_b values.

4.2.1 Sample preparation.

The films used in this study were on the live electrode in a PECVD reactor. The preparation conditions were similar to those outlined in section 3.2.1. The negative self-bias induced between the live electrode and the plasma is dependant on the power supplied to the plasma by the radio-frequency power supply (Silva et al. 1996). The a-C:H films were deposited over a range of negative self-bias (V_b)values. The only exception is the polymeric a-C:H sample which was produced on the earthed electrode. This polymeric sample was studied in the previous chapter and the details of its deposition conditions can be found in table 3.5. The negative self-bias voltage (V_b) for this sample is roughly -10V and it was produced in the university of Surrey by Dr. J. D. Carey. The negative sign shall be omitted from here on for convenience.

The remaining samples were produced at the Engineering Department of the University of Cambridge by Dr. S. R. P. Silva. The thickness, hydrogen content and the sp^2 content of these films was also measured at the Engineering Department of the University of Cambridge. Table 4.1 below list the preparation conditions that were used.

Name	Atomic percentage of H [%]	Percentage of sp^2 bonding [%]	Negative self-bias voltage (V_b) [-V]	Thickness [nm]
Bulk a-C:H	≈50	N/A	10	N/A
P5	25	63	50	220
P2	13	54	100	200
DC271	N/A	≈78	190	62
DC270	N/A	72	265	83
DC274	N/A	80	320	88
DC160	N/A	76-90	400	35
DC275	N/A	90-100	500	72
DC182	N/A	≈100	540	58

Table 4.1 : Thickness, V_b, hydrogen and sp^2 bonded content of a-C:H films deposited with Plasma gases: 10% CH_4 and 90% Ar, Pressure: 300mTorr, Substrate at room temperature. The hydrogen content of the films for V_b>100V probably only decreases slightly from the value of 13at.%.

4.2.2 EPR results for non-polymeric a-C:H as a function of V_b

In this section of the chapter we give the results for non-polymeric a-C:H as a function of V_b used during deposition. We will also analyse these EPR results. Figure 4.1 shows the EPR spectra with increasing negative self-bias (V_b). The heights of the spectra have been normalised. The main change we can see in this figure is the linewidth narrowing as V_b increases. The spectrum for V_b = 50V is neither Lorentzian (denoted by L) or a Gaussian (denoted by G) while the lineshapes are very close to Lorentzians for the a-C:H films deposited with V_b>50V.

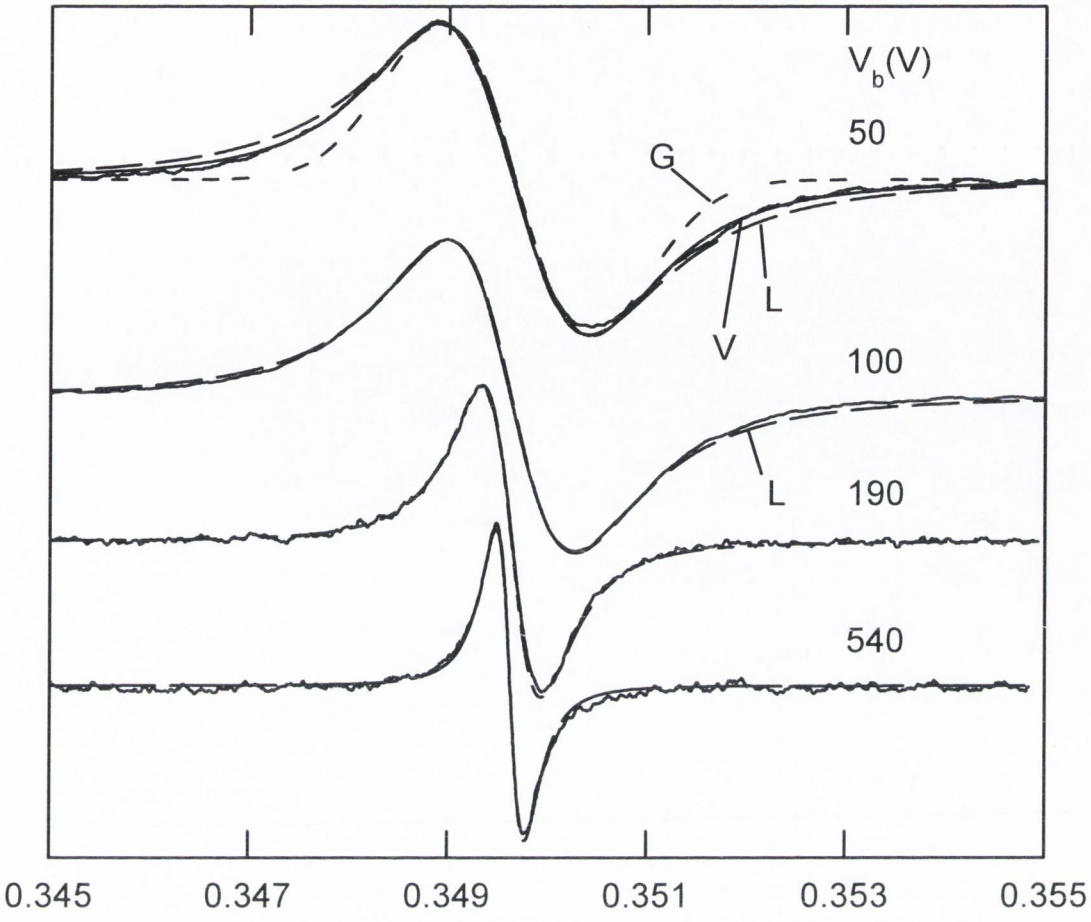

Figure 4.1 : EPR spectra as a function of V_b. (table 4.1)

Figure 4.2 is a graph of the EPR data for these samples (table 4.1). We can see in this figure that the cross-over g_0-value remains constant with increasing negative bias voltage (V_b). The linewidth (ΔB_{pp}) starts at 1.12mT for V_b=10V then increases until a bias-voltage of 50V is reached and then falls until it equals ≈0.3mT for V_b=540V. A similar decrease in ΔB_{pp} (for V_b > 50V) was found by Kleber et al. (1991), they report a ΔB_{pp} value of ≈1.8mT for an ion energy of 30eV, this is equivalent to V_b = 75V (Robertson 1998), which then falls with increasing ion energy (i.e. V_b). Schutte et al. (1993) find for their cathode-type films a maximum ΔB_{pp} value of 2.03mT which then falls with increasing ion energy, they also find a trend similar to ours, i.e. containing a turning point in the ΔB_{pp} values, for their anode-grown films.

The spin concentration (N_V), shown in figure 4.2, initially increases very rapidly after which it rises more slowly with increasing V_b, for $V_b < 400V$. For $V_b \geq 400V$ the values of N_V are scattered. Two low values of N_V are noted for bias-voltages of 400V and 540V. These two had lower N_V values than their neighbouring data points.

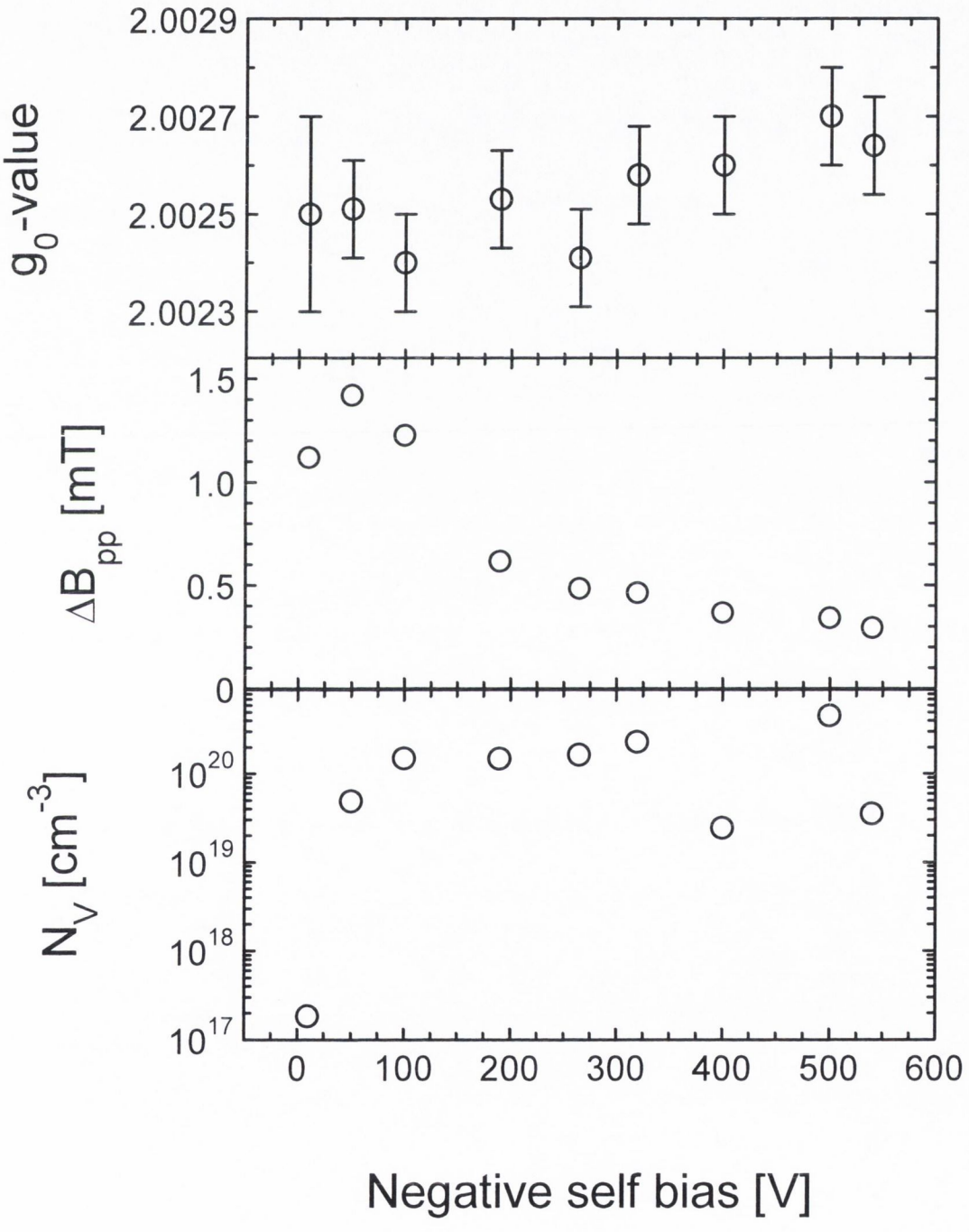

Figure 4.2 : EPR data for a-C:H films as a function of negative self-bias (V_b).

The nature of the defects present in the a-C:H films, based upon the static g_0-values, are unaffected by changing V_b during deposition. Therefore we believe that the defects present in the non-polymeric a-C:H films ($V_b \geq 10V$) are the same as those found in polymeric a-C:H ($V_b = 10V$). Thus the defects present in the all the a-C:H films are due to unpaired π-electrons on carbon atoms. These unpaired electrons reside in chains of conjugated double bonds or in clusters of fused aromatic six-fold rings.

The linewidth is not caused by a spread of lines with different g-values (i.e. it was a single line) because the lineshape is Lorentzian, for $V_b \geq 100V$, and the linewidth (ΔB_{pp}) has been reported to be independent of the microwave frequency (i.e. the magnetic field) at which the spectrum was recorded (Hoinkis et al. 1992).

The lineshape of the spectrum for the bulk defects in polymeric a-C:H was found in chapter 3 be neither a Gaussian or a Lorentzian but possibly a Voigt. In figure 4.1 we can see that the lineshape for a-C:H produced with V_b=50V,and less obviously for V_b=100V, are neither Gaussian or Lorentzian. In order to quantify how close these lineshapes are to a Lorentzian or a Gaussian we calculated values of the ratio $\Delta B_{½} / \Delta B_{pp}$; these are given in table 4.2. $\Delta B_{½}$ is the full width at half maximum of the integral of the recorded spectrum while ΔB_{pp} is the standard peak-to-peak linewidth of the spectrum. A value of 1.73 for $\Delta B_{½} / \Delta B_{pp}$ is characteristic of a Lorentzian lineshape while a value of 1.18 is characteristic of a Gaussian (McClintock and Orr 1968; Poole 1983, p. 476).

Name	V_b [V]	ΔB_{pp} [mT]	ΔB_1 [mT]	$\Delta B_1 / \Delta B_{pp}$
Bulk a-C:H	10	1.12±0.08	1.70±0.13	1.51±0.21
P5	50	1.55±0.08	2.29±0.02	1.48±0.09
P2	100	1.30±0.09	2.04±0.02	1.58±0.12
DC271	190	0.62±0.03	1.01±0.02	1.63±0.11
DC270	265	0.48±0.02	0.82±0.02	1.69±0.11
DC275	500	0.34±0.02	0.59±0.02	1.72±0.16
DC182	540	0.29±0.02	0.53±0.02	1.80±0.19

Table 4.2 : Ratios of $\Delta B_1 / \Delta B_{pp}$ for a-C:H as a function of V_b.

As we can see in table 4.2 the ratio of $\Delta B_{½} / \Delta B_{pp}$ increases with increasing V_b. This shows that the lineshape begins as neither a Gaussian or a Lorentzian but somewhere between the two and becomes more Lorentzian in shape when V_b

increases. The lineshape for V_b = 50V, in figure 4.1 is clearly not a Lorentzian (denoted by L) or a Gaussian (denoted by G) but between these two extremes. We can see in figure 4.1 that a Voigt lineshape(denoted by V) gives a very reasonable fit to this spectrum. While a Voigt lineshape gives a good fit so does a superposition of a Gaussian and a Lorentzian together. Voigt fits were carried out for V_b = 50V and 100V but not for V_b = 10V as this signal contains too much noise. Similarly two-line fits consisting of a Gaussian and a Lorentzian were carried out for V_b = 50V and 100V. Unfortunately it is impossible to distinguish which type of fit is better as they both are very close to the experimental spectra.

Table 4.3 lists the parameters as determined by fitting the spectra (V_b = 50V and 100V) with Voigt convolution lineshapes (See section 2.13 in chapter 2 for more information about the Voigt convolution). ${}^{V}\Delta B_{pp}$ is the total peak-to-peak linewidths of the Voigt convolution while ${}^{L}\Delta B_{pp}$ is the peak-to-peak linewidth of the Lorentzian component and ${}^{G}\Delta B_{pp}$ is the peak-to-peak linewidth of Gaussian component.

Name	V_b [V]	ΔB_{pp} [mT]	${}^{V}\Delta B_{pp}$ [mT]	${}^{L}\Delta B_{pp}$ [mT]	${}^{G}\Delta B_{pp}$ [mT]
P5	50	1.55±0.08	1.55±0.08	1.11±0.05	0.82±0.05
P2	100	1.30±0.09	1.30±0.09	1.17±0.05	0.51±0.05

Table 4.3 : Voigt parameters for a-C:H films as a function of V_b.

Table 4.4 lists the parameters as determined by fitting these spectra with a superposition of a Lorentzian and a Gaussian line. ${}^{L}\Delta B_{pp}$ is the peak-to-peak linewidth of the Lorentzian line and ${}^{G}\Delta B_{pp}$ is the peak-to-peak linewidth of Gaussian line. ${}^{L}h_{pp}/{}^{G}h_{pp}$ is the ratio of the height peak-to-peak of the Lorentzian line to that of the Gaussian line.

Name	V_b [V]	${}^{L}\Delta B_{pp}$ [mT]	${}^{L}h_{pp}/{}^{G}h_{pp}$	${}^{G}\Delta B_{pp}$ [mT]
P5	50	1.53	1.3	1.63
P2	100	1.32	2.9	1.58

Table 4.4 : Parameters determined from the two-line fits (Gaussian + Lorentzian) of a-C:H as a function of V_b.

While fitting worked in both cases, i.e. Voigt and Lorentzian + Gaussian fits, the one major item to note is that the lineshape becomes closer to a Gaussian as V_b reduces.

The lineshapes for V_b>50V are extremely close to, or exactly, Lorentzian. Table 4.1 shows that the sp^2 content increases with increasing V_b, a similar effect was seen by Weiler et al. (1996). This drop in linewidth with increasing sp^2 content ($V_b \geq 100V$) is reportedly (Miller and McKenzie 1983; Schütte et al. 1993; Weiler et al. 1996; Chhowalla et al. 1997) caused by an increase in the exchange interaction between the spins. This is consistent with the lineshape being Lorentzian. Thus the decrease in linewidth (figure 4.2) as the self-bias (V_b) increases may be explained by an increase in exchange narrowing.

While exchange narrowing is indeed the most likely cause of this narrowing it would be reasonable to carry out further experiments to test this idea.

Measurements of the spin-spin (T_2) and spin-lattice (T_1) relaxation times may support the argument that exchange interaction causes the narrowing we observe. In order to examine whether exchange narrowing increases with increasing V_b we carried out measurements of T_1 and T_2.

4.2.3 T_1 and T_2 for a-C:H as a function of V_b

In this section of the chapter we examine the results we obtained by measuring the spin-lattice (T_1) and spin-spin (T_2) relaxation time for a-C:H films as a function of V_b. We compare our measurements with the effect, upon T_1 and T_2, that increasing exchange interaction has in α-α-diphenyl-β-picryl-hydrazyl (DPPH) in polystyrene (Goldsborough et al. 1960).

Before we examine the results of T_1 and T_2 we will first review some of the theoretical models for the behaviour of T_1 and T_2. The methods we use to experimentally determine T_1 and T_2 have already been described in chapter 2. These methods require that the lineshape is a Lorentzian. To recap these methods involve the calculation of T_2 from the inverse of the linewidth (ΔB_{pp}) and $T_1 \times T_2$ from the saturation behaviour of the peak-to-peak height (h_{pp}) as a function of B_1 (the rotating magnetic field component of the microwaves). Poole (1983, p. 590-591) lists the

equations which relate these measurable parameters to T_2 and $T_1 \times T_2$. These two equations are given in equations 4.1 and 4.2.

$$\Delta B_{pp}^{0} = \lim_{B_1 \to 0} \Delta B_{pp} = \frac{2}{\sqrt{3}\gamma T_2} \qquad (4.1)$$

$$h_{pp} \propto B_1 \left(\frac{1}{1 + B_1^2 \gamma^2 T_1 T_2} \right)^{3/2} \qquad (4.2)$$

Where

B_1 = The magnetic field of the rotating component of the microwaves (Proportional to the square root of the microwave power).

γ = The gyromagnetic ratio.

ΔB_{pp} = EPR 1st derivative peak-to-peak linewidth.

h_{pp} = Peak-to-peak height of the of the EPR signal.

To further our examination of the relaxation times we shall use the density matrix method of Redfield described by Slichter (1992) and Poole (1983, p. 529). This is appropriate to the case of the relaxation times being affected by the motion of spins. The unpaired spins are supposed to be perturbed by a time dependant random magnetic (B_{random}) field in addition to the static field (B_0). This fluctuating magnetic (B_{random}) field has components B_x, B_y and B_z while the static field B_0 is parallel to the z-axis. Such a fluctuating magnetic field may arise from variations in the dipolar or hyperfine fields produced by motion or effective motion of other nearby spins. This motion of the unpaired spins arises from possibly hopping or the effective motion produced by spin-spin exchange. If we assume that B_{random} decays exponentially as $\exp(-t/\tau_c)$ then Poole (1983, p. 530) states that the following equations apply to the relaxation times.

$$\frac{1}{T_1} = \gamma^2 \left(\overline{B_x^2} + \overline{B_y^2} \right) \frac{\tau_c}{1 + \omega_0^2 \tau_c^2} \qquad (4.3)$$

$$\frac{1}{T_2} = \gamma^2 \overline{B_z^2} \tau_c + \frac{1}{2} \left(\overline{B_x^2} + \overline{B_y^2} \right) \frac{\gamma^2 \tau_c}{1 + \omega_0^2 \tau_c^2} \qquad (4.4)$$

Where

ω_0 = Larmor frequency

τ_c = The correlation time

and the bar above the variables indicates that they are average values.

The correlation time (τ_c) is analogous to the correlation time found for the Brownian motion of a liquid and is a measure to the speed of the motion. If we assume that the fluctuating magnetic fields are isotropic i.e. $\overline{B_z^2} = \overline{B_x^2} = \overline{B_y^2} = \overline{B^2}$ then equations 4.3 and 4.4 become

$$\frac{1}{T_1} = \frac{2\gamma^2 \overline{B^2} \tau_c}{1+\omega_0^2 \tau_c^2} \qquad (4.5)$$

$$\frac{1}{T_2} = \gamma^2 \overline{B^2} \tau_c + \frac{\gamma^2 \overline{B^2} \tau_c}{1+\omega_0^2 \tau_c^2} \qquad (4.6)$$

Defining $\omega_p^2 = \gamma^2 \overline{B^2}$ and $\omega_c = 1/\tau_c$ we now get

$$\frac{1}{T_1} = \frac{2\omega_p^2 \tau_c}{1+\omega_0^2 \tau_c^2} \qquad (4.7)$$

$$\frac{1}{T_2} = \omega_p^2 \tau_c + \frac{\omega_p^2 \tau_c}{1+\omega_0^2 \tau_c^2} \qquad (4.8)$$

Figure 4.3 shows how T_1 and T_2 change with increasing τ_c. These values were arbitrarily calculated for a range of τ_c values from equations 4.7 and 4.8 assuming that $\omega_p = \omega_o = 1$. We can see from equation 4.7 and figure 4.3 that decreasing τ_c causes T_1 to decrease reach a minimum and then increase again. In this final region ($\tau_c << \omega_p$ and ω_o) the values of T_1 equal those of T_2. Also from equation 4.8 and figure 4.3 we

can see that decreasing τ_c causes T_2 to increase. The minimum value of T_1 can be found by setting the derivative of equation 4.7 equal to 0 i.e.

$$\frac{\omega_0^2}{\omega_p^2} - \frac{1}{2}\frac{1+\omega_0^2\tau_c^2}{\omega_p^2\tau_c} = 0$$

$$\Rightarrow 2\tau_c^2 = \frac{1}{\omega_0^2} + \tau_c^2 \text{ and finally}$$

$$\frac{1}{\tau_c} = \omega_c = \omega_0 \text{ for minimum } T_1 \text{ value.} \qquad (4.9)$$

When $\omega_p < \omega_c < \omega_o$ equations 4.7 and 4.8 can be simplified to

$$\frac{1}{T_1} \approx \frac{2\omega_c\omega_p^2}{\omega_0^2} \qquad (4.10)$$

$$\text{and } \frac{1}{T_2} \approx \frac{\omega_p^2}{\omega_c} \qquad (4.11)$$

Using equations 2.16 and 2.26 from chapter 2 with equation 4.11 we find that

$$\frac{1}{2}\Delta H_{1/2} = \frac{\omega_p^2}{\gamma\omega_c} \qquad (4.12)$$

Where $\Delta H_{1/2}$ = The full width at half maximum for a Lorentzian line (this line is the integral of the standard 1st derivative EPR line).

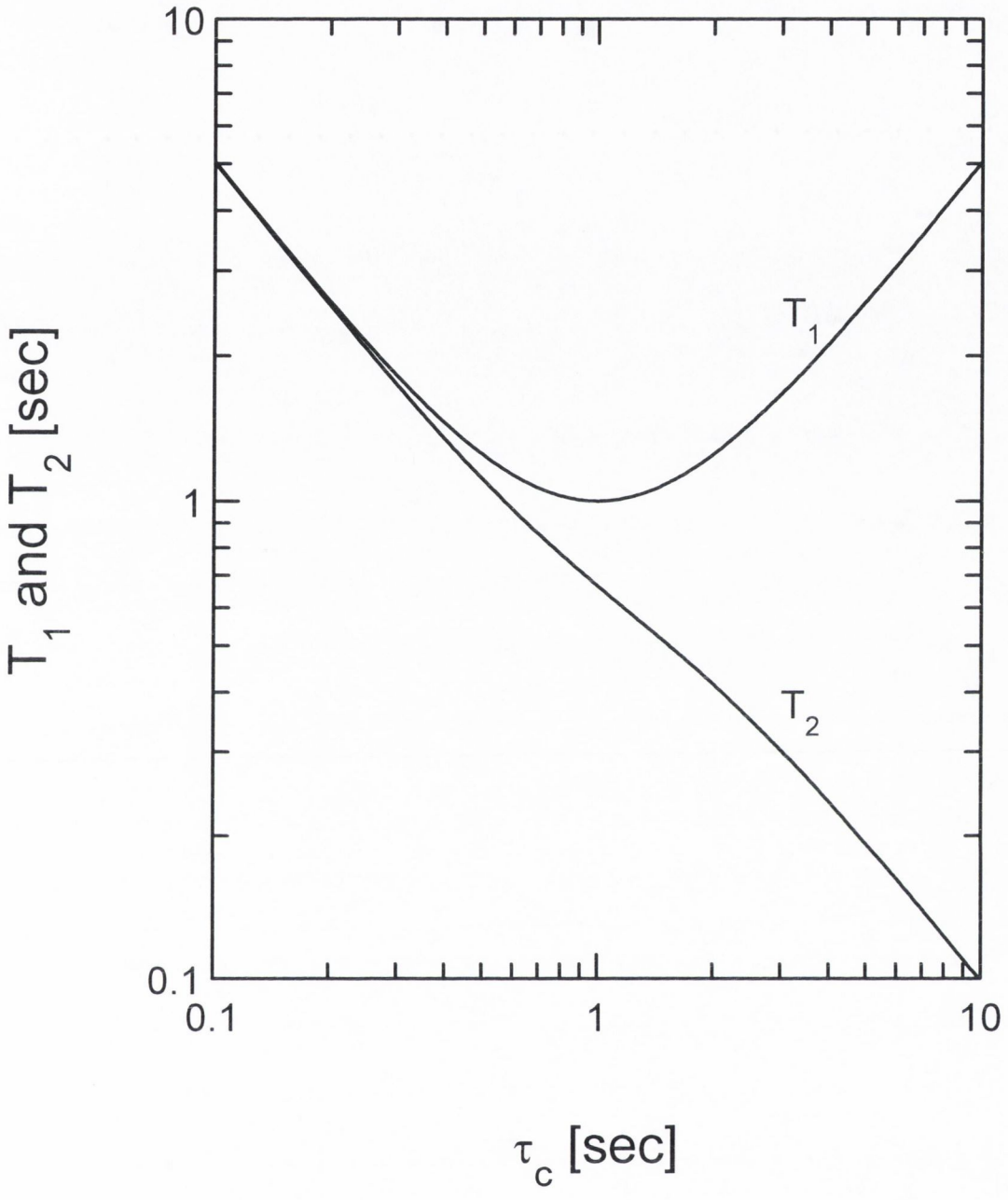

Figure 4.3 : Behavior of T_1 and T_2 as a function of τ_c (Arbitary values).

In the slow motion limit, $\tau_c >> T_2$, this model breaks down. The linewidth in this case is due to a distribution of the static magnetic field at each unpaired site as well as a possible spread in g-values. This would give rise to a Gaussian lineshape. For our films ($V_b \geq 100V$) the lineshape does not arise by a spread lines of different g-values (i.e. it was a single line), because as mentioned earlier the lineshape is Lorentzian, for $V_b \geq 100V$, and the linewidth (ΔB_{pp}) is independent of the microwave frequency at which the spectrum was recorded (Hoinkis et al. 1992). Therefore this

model may be used to explain the behaviour of T_1 and T_2 in our a-C:H films, with $V_b \geq$ 100V, i.e. they are not in the slow motion limit ($\tau_c >> T_2$).

In this section of the chapter we examine the results we obtain by measuring T_1 and T_2 for our a-C:H films. We will compare our results with the behaviour of T_1 and T_2 as exchange interaction increases in order to see if a similar behaviour is found. We will also see if the model outlined above can be used to explain the behaviour of our T_1 and T_2 values.

In order to examine whether the drop in ΔB_{pp} can be explained by exchange narrowing we measured the spin-lattice T_1 and spin-spin T_2 relaxation times as a function of self-bias voltage (V_b). Figure 4.4 displays the saturation behaviour of selected a-C:H films as a function of V_b. In this figure is displayed the experimental data with fits superimposed generated according to equation 4.2. The higher the value of T_1T_2 the lower the B_1 value required for h_{pp} to reach a maximum. We can see in figure 4.4 that the film produced with V_b=50V (O) reaches a maximum at the lowest B_1, followed by the film produced with V_b=540V (●) finally followed by the film produced with V_b=190V (□). This indicates that T_1T_2 value for film with V_b=50V (O) is greater than for the film with V_b=540V (●) which in turn is greater than for the film with V_b=190V (□). We can see this trend by looking at the values of T_1T_2 calculated from these fits in table 4.5.

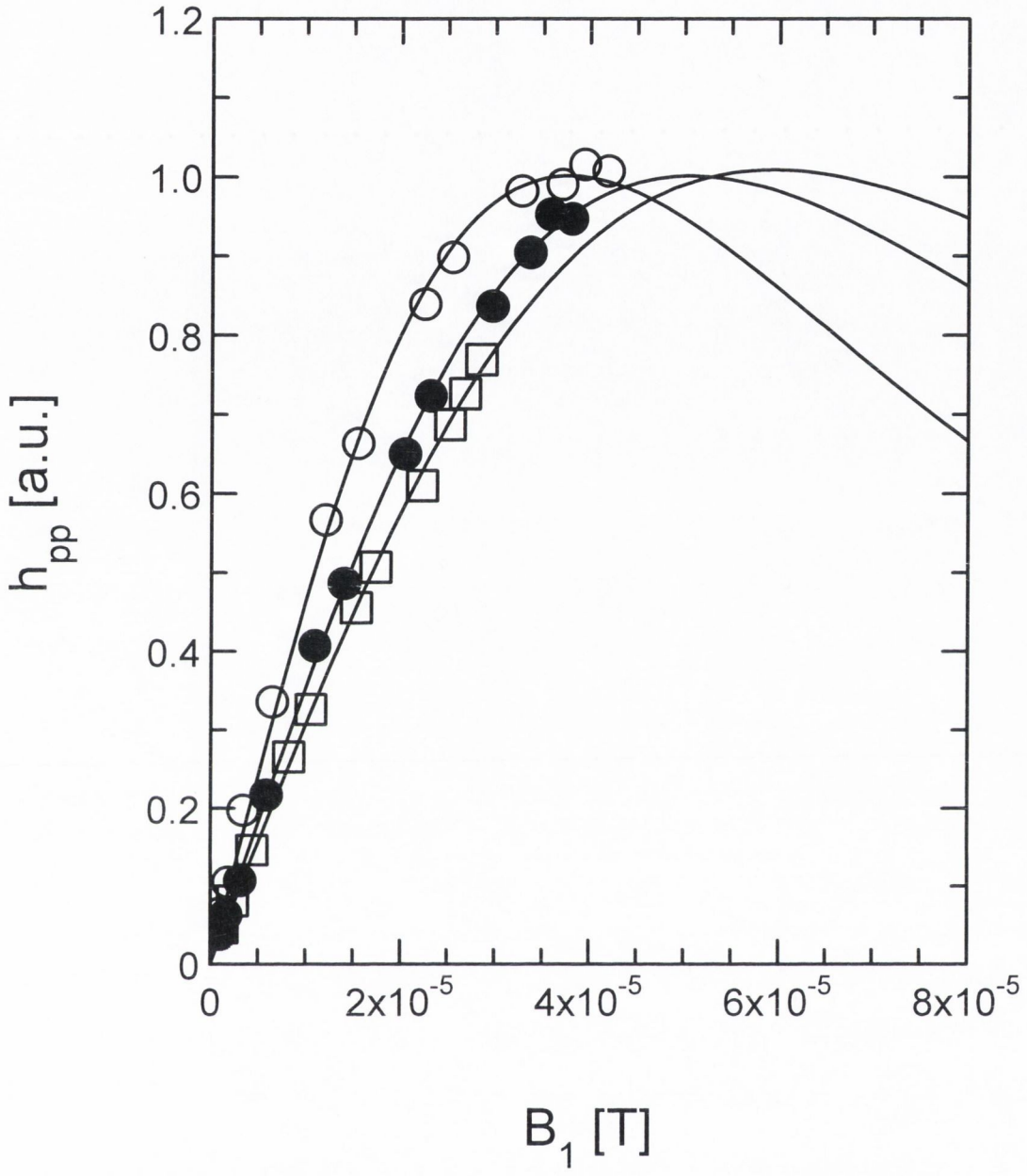

Figure 4.4 : Saturation behaviour of a-C:H films as a function of V_b.

O : *a-C:H film grown with V_b=50V (T_1T_2=11.3×10^{-15}s^2)*

● : *a-C:H film grown with V_b=540V (T_1T_2=6.30×10^{-15}s^2)*

□ : *a-C:H film grown with V_b=190V (T_1T_2=4.58×10^{-15}s^2)*

Table 4.5 lists the values we obtained for T_2, T_1T_2 and T_1. Because the spectra for V_b = 10V and 50V (figure 4.1) are not Lorentzian, the equations 4.1-4.2 do not apply. For completeness we still estimate approximate values of T_1 and T_2 by ignoring this fact and using the method for measuring T_1 and T_2 described in chapter 2. The spectrum for V_b = 100V (figure 4.1) is very close to a Lorentzian and thus the

values of T_1 and T_2 for this sample must be very close to the actual values. Although the spectrum of the polymeric a-C:H (V_b =10V) sample is not a Lorentzian, and the values for T_1 and T_2 are approximate it is nevertheless clear that T_1 is much longer than the values for the other samples. The values in table 4.5 were measured at 300K.

Name	Negative self bias voltage (V_b) [V]	ΔBpp [mT]	T_2 [$\times 10^{-8}$ s]	$T_1 \times T_2$ [$\times 10^{-15}$ s^2]	T_1 [$\times 10^{-6}$ s]
Bulk a-C:H	10	1.12	0.585	182	31.2
P5	50	1.42	0.462	11.3	2.45
P2	100	1.23	0.533	8.0	1.50
DC271	190	0.616	1.06	4.58	0.430
DC274	320	0.463	1.42	4.71	0.333
DC160	400	0.366	1.79	5.51	0.308
DC182	540	0.293	2.24	6.30	0.281

Table 4.5 : T_1 and T_2 for a-C:H as a function of V_b.

Our values of T_1 and T_2 agree roughly with values found by Giorgis et al. (1998) for a-C:H. Table 4.6 compares our T_1 and T_2 values with those found by Giorgis et al. (1998) at 300K. The values of T_2 from Giorgis et al. (1998) are calculated from their reported values of ΔB_{pp} at 300K and equation 4.1. We can see that their values are close to the values we measure.

Lable used by Giorgis et al. (1998)	V_b [V]	T_1 [s] (Our values)	T_1 [s] (Giorgis et al. 1998)	T_2 [10^{-8}s] (Our values)	T_2 [10^{-8}s] (Giorgis et al. 1998)
Polymeric	10	0.312×10^{-4}	2×10^{-4}	0.585	0.4
Diamond like	540	2.81×10^{-7}	2×10^{-7}	2.24	2.5
ta-C	400	3.08×10^{-7}	$< 10^{-7}$	1.79	1.8

Table 4.6 : T_1 and T_2 values for a-C:H reported by Giorgis et al. 1998.

Now we shall compare our values of T_1 and T_2 to those measured in a material where the exchange interaction exists.

Figure 4.5 shows that T_1 decreases and T_2 increases as the bias voltage V_b increases. In α-α-diphenyl-β-picryl-hydrazyl (DPPH) in polystyrene a similar trend is reported (Goldsborough et al. 1960) as the spin concentration (N_V) increases. This increase in spin concentration increases the exchange interaction in DPPH in

polystyrene, thus reducing the values of T_1 and increasing the values of T_2 (i.e. narrowing ΔB_{pp}). In order to compare the effect increasing N_V (i.e. increasing exchange interaction) has on DPPH with the effect that increasing V_b has on our samples, selected pairs of values of T_1 and T_2 from the DPPH data are plotted in figure 4.5 (Goldsborough et al. 1960). The position these points take along the x-axis are arbitrary but they are plotted so that the values of T_2 for DPPH closely match our T_2 values for a-C:H. Table 4.7 lists the T_1 and T_2 data pairs we use in this comparison, it also gives the N_V values for the DPPH in polystyrene samples (Goldsborough et al. 1960). The values of V_b in table 4.7 are arbitrary and are chosen only so that the values of T_2 for DPPH in polystyrene closely match the T_2 values we recorded.

N_V for DPPH [$10^{20}cm^{-3}$]	V_b (arbitrary values) [V]	T_2 [$\times 10^{-8}$ s]	T_1 [$\times 10^{-6}$ s]
0.01	10	0.5	13
1	70	0.5	1.5
3	220	1	0.33
5	650	3	0.11

Table 4.7 : T_1 and T_2 for DPPH.

For DPPH in polystyrene both T_1 and T_2 become roughly independent of the spin concentration when $N_V < 10^{18}cm^{-3}$ and their values are very similar to those of T_1 and T_2 for our polymeric a-C:H sample (V_b = 10V). In figure 4.5 it can be seen that our values of T_1 for a-C:H match very well the values for DPPH in polystyrene (Goldsborough et al. 1960), remembering that our T_2 values were set to match the T_2 values for DPPH.

In DPPH T_1 decreased and T_2 increases as the exchange interaction increases. In figure 4.5 an almost matching decrease in T_1 and increase in T_2 is found as V_b increases in our a-C:H samples.

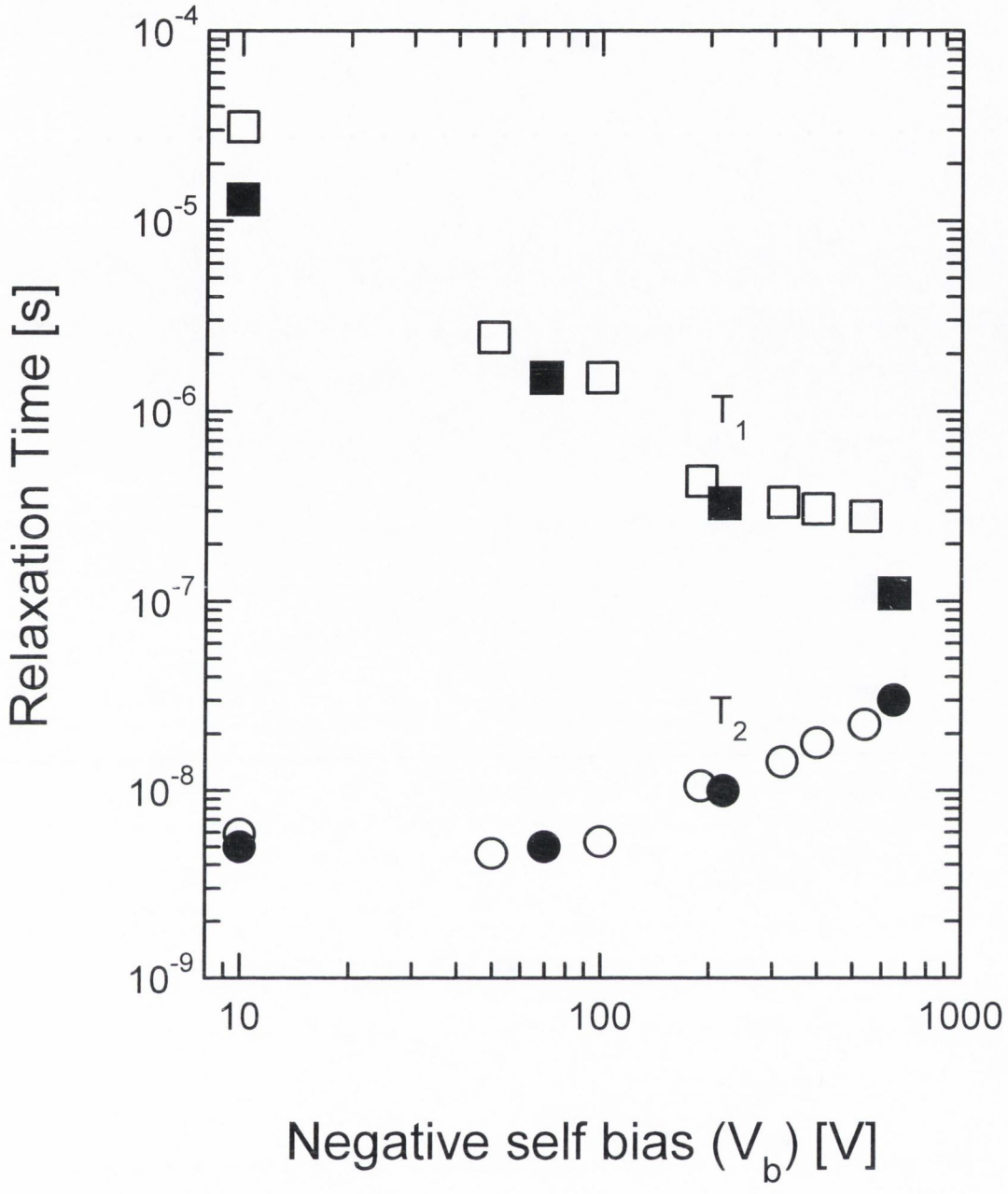

Figure 4.5 : T_1 and T_2 as a function of V_b.

□ *: a-C:H (Table 4.5): T_1 values.*

O *: a-C:H (Table 4.5): T_2 values.*

■*: DPPH in polystyrene (Table 4.7): T_1 values.*

● *: DPPH in polystyrene (Table 4.7): T_2 values.*

The behaviour of T_1 and T_2 as a function of V_b may be due to either an increase in exchange interaction, as in DPPH, between like spins or motion due to variable range hopping. Conduction by variable range hopping has been observed in ion-beam

sputtered a-C (Dawson and Adkins 1995; Sullivan et al. 1998; Ilie et al. 1998) and is also likely to be present in ta-C:H (Ilie et al. 1998). Therefore how can we be sure that our observed changes in T_1 and T_2 are due to increasing exchange interaction? For variable range hopping, the conductivity typically falls by 3 orders of magnitude when the temperature drops from 300K to 40K (Dawson and Adkins 1995; Sullivan et al. 1998; Ilie et al. 1998). This is due to the change in the probability of an upward energy hop. It is fair to assume that if the linewidth is determined by motional effects due to variable range hopping then the linewidth would be expected to have a significant dependence on the temperature. The linewidth for diamond-like carbon, graphite like carbon and polymeric a-:C:H has been found to change by $\leq 20\%$ over the temperature range of 300K to 40K (Giorgis et al. 1998). This lack of a significant change in the linewidth with temperature means that we can rule out variable range hopping as the cause of the change we observe in T_1 and T_2. This leaves exchange interaction as the most likely factor which controls T_1, T_2 and ΔB_{pp}, in our samples with $V_b > 100V$.

In the case of DPPH the increase in exchange interaction is caused by an increase in N_V but no such increase in N_V is seen in figure 4.2 for our a-C:H films ($V_b \geq 100V$). Therefore an increase in exchange interaction may be caused in our films by an increase in the overlap of the wavefunctions of the unpaired electrons due to increasing delocalisation of these unpaired electrons which in turn is caused by an increase in the sp^2 content (table 4.1) of these films. Also T_1 for carbon radicals in dextrose is found to decrease when the pyrolytic temperature is raised from 250 to 450°C (Pastor and Hoskins 1960). We propose that this decrease in T_1 in dextrose is due to the same reason as the decrease in a-C:H, basically that there is increased delocalisation and thus an increase in exchange interaction.

This is very strong evidence that increasing the self-bias (V_b) (i.e. increasing the sp^2 content) increases the exchange interaction between spins in a-C:H.

Finally, to sum up, we can say that from our relaxation time results we believe that the lineshape narrows (for $V_b \geq 100V$) due to exchange narrowing caused by the increasing sp^2 content of the films. This increase in sp^2 content increases the size of the clusters which allows the unpaired π-electrons to delocalise over a greater area.

This delocalisation increases the overlap of the wavefunctions of unpaired electrons which increases the strength of the exchange interaction.

Next we examine if our values of T_1 and T_2 behave in the manner described by the model earlier, i.e. if they obey equations 4.7-4.11. An equation relating τ_c to the relaxation times (T_1 and T_2) and ω_0 is found by dividing equations 4.11 by 410, rearranging and using the fact that $\tau_c=1/\omega_c$. Thus the values of τ_c are calculated from

$$\tau_c = \frac{1}{\omega_0}\sqrt{\frac{2T_1}{T_2}}$$

The values of ω_0 can be evaluated from equation 2.11. Figure 4.6 shows these two sets of relaxation times (for DPPH and a-C:H) plotted against τ_c. We can see in figure 4.6 that the values of T_1 and T_2 for a-C:H do follow closely those of DPPH, again supporting the idea that exchange interaction increased with increasing sp^2 content. As $\omega_p < \omega_c < \omega_o$ equations 4.10 and 4.11 can be applied to our values of T_1 and T_2 respectively. In figure 4.6 the solid lines are the fits for T_1 and T_2 using these equations. These fits were calculated using the least squares method. These two lines give estimates of ω_p equal to 7.2×10^8rad s^{-1} and 7.6×10^8rad s^{-1} using equations 4.10 and 4.11 respectively. Therefore ω_p is $\approx7.4\times10^8$rad s^{-1} for our a-C:H films ($V_b\geq100$V). Using this value of ω_p and equations 4.12 and 2.16 we estimate that the linewidth calculated from this model, for V_b=100V, to be 1.39mT. This compares favourably with the actual ΔB_{pp} of 1.23mT. This indicates that little exchange narrowing occurs in this film V_b=100V as these two values of ΔB_{pp} are alike, i.e. if exchange is present we expect the actual ΔB_{pp} to be less than that calculated from ω_p and equations 4.12 and 2.16.

Finally therefore for $V_b>100$V we suggest that the linewidth narrows as V_b increases because of increasing exchange interaction. This is also consistent with the lineshape being a Lorentzian.

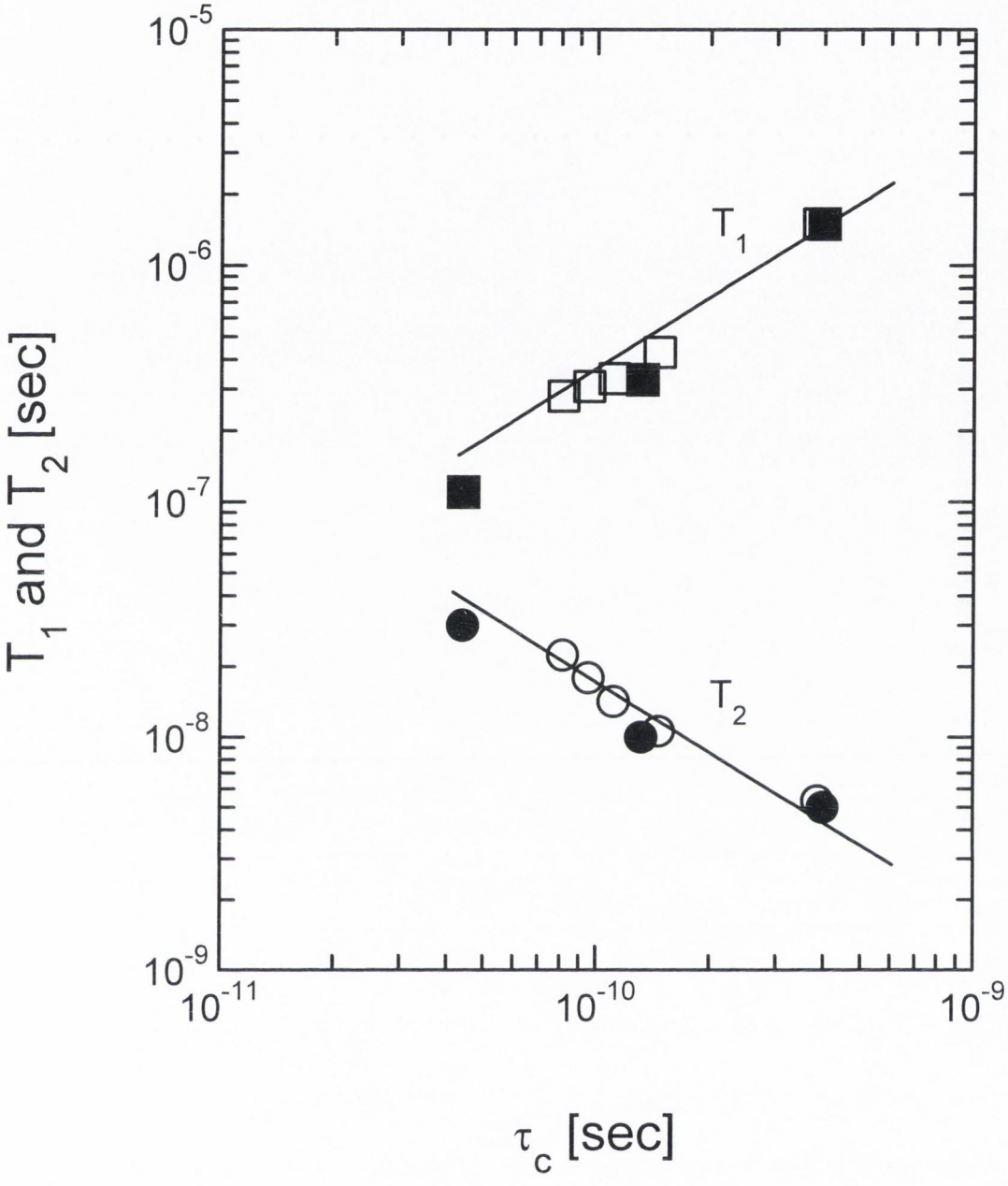

Figure 4.6 : T_1 and T_2 as a function of τ_c.

□ : *a-C:H : T_1.* O : *a-C:H : T_2.*

∝ : *DPPH in polystyrene : T_1.* ● : *DPPH in polystyrene : T_2.*

4.2.4 Discussion of the EPR results for a-C:H ($V_b \geq 100V$).

In this section we shall consider the lineshape and linewidth for the samples prepared with $V_b \geq 100V$. The lineshape remains Lorentzian while the linewidth decreases with increasing self-bias (V_b). The sp^2 content, given in table 4.1, increases with increasing V_b, as also has been reported by Weiler et al. (1996). The drop in linewidth with increasing sp^2 content ($V_b \geq 100V$) has been reported (Miller and McKenzie 1983; Schütte et al. 1993; Weiler et al. 1996; Chhowalla et al. 1997) as being caused by increasing exchange interaction between the spins. Based upon the behaviour of T_1 and T_2 reported in the previous section we believe that exchange interaction is the cause of the fall in ΔB_{pp} as V_b increases.

Now we examine the contribution of dipolar broadening to the linewidth. Abragam (1996) described the effect of dipolar interaction in magnetically dilute substances. For dipolar broadening of the line, for films with less that one unpaired electron per 100 carbon atoms, Abragam (1996) predicts that the linewidth of the resultant Lorentzian is given by the following equation (this equation uses cgs units).

$$\frac{1}{2}\Delta H_{1/2} = \frac{2\pi^2}{3\sqrt{3}} g\mu_B N_V \qquad (4.13)$$

Taking this equation together with $\Delta H_{1/2} = \sqrt{3}\Delta B_{pp}$ and g = 2.0025 we get

$$\Delta B_{pp} = 8.12 \times 10^{-20} N_V \qquad (4.14)$$

Where the units of spin concentration (N_V) are cm^{-3} and the units of peak-to-peak linewidth (ΔB_{pp}) are Gauss.

Using equation 4.14 the linewidth due to dipolar broadening only is calculated from the spin concentration (N_V), these values are displayed in table 4.8. We can see that for $V_b < 100V$ dipolar broadening of the line is insufficient to account for the measured linewidths also the lineshapes are not Lorentzian which is incompatible with

dipolar broadening between like spins. We shall deal with these two samples later ($V_b < 100V$).

For $V_b = 100V$ we can see in table 4.8 that the measured values of ΔB_{pp} and ΔB_{pp} from the dipolar interaction (from eq. 4.14) are in very good agreement. Therefore dipolar interaction without any other broadening of narrowing mechanism (e.g. exchange or hyperfine splitting) would give rise to the lineshape and linewidth (i.e. Lorentzian and $\Delta B_{pp} = 1.23mT$) for the sample with $V_b = 100V$. This is consistent with value of ΔB_{pp} (1.39mT) we calculated from ω_p and equation 4.12 and 2.16.

This is analogous to the case for DPPH in polystyrene (Goldsborough et al. 1960) where ΔB_{pp} (or T_2) is unaffected by exchange narrowing when $N_V < 10^{20} cm^{-3}$.

V_b [V]	N_V [10^{20} cm^{-3}]	ΔB_{pp} [mT]	ΔB_{pp} [mT] Dipolar broadening (eq. 4.14)	J/k [K]
10	0.0018	1.12	0.0015	N/A
50	0.491	1.42	0.40	N/A
100	1.50	1.23	1.22	0.02
190	1.49	0.62	1.21	0.05
320	2.30	0.46	1.87	0.07
400	0.244	0.37	0.20	0.08
540	0.353	0.293	0.29	0.09

Table 4.8 : Dipolar boradening and the exchange integral (J) for a-C:H films as a function of V_b.

Next we consider dipolar broadening for $V_b > 100V$. There is a scatter in our N_V values for $V_b > 265V$ so we shall exclude the possibly anomalous values of ΔB_{pp} calculated from eq. 4.14 for $V_b = 400$ and 540V from our discussion. So for $V_b > 100V$ we can see in table 4.8 that the measured values of ΔB_{pp} were smaller that those predicted due to dipolar broadening. Based upon our relaxation time measurements in the previous section, our explanation of this difference is that exchange narrowing is taking place due to an increase in the delocalisation of unpaired electrons. This increased delocalisation is due to an increase in the sp^2 content of these films (table 4.1). Therefore the decrease in the linewidth (ΔB_{pp}) with increasing V_b (for $V_b \geq 100V$) is not due to a decrease in dipolar broadening because there was no corresponding decrease in N_V values in figure 4.2 (the values were scattered). The fall in ΔB_{pp} with increasing V_b ($V_b \geq 100V$) is due to an increase in exchange narrowing only.

Finally if we assume that $\omega_e = \omega_c$ for a-C:H (i.e. exchange narrowing was present) then the exchange constant (or integral) J can be calculated from $\omega_e \approx J/\hbar$. Value of J/k are shown in table 4.8. We can see in table 4.8 that J increase with V_b for $V_b \geq 190V$ which agrees with the idea that the exchange interaction increases.

Next we examine whether unresolved hyperfine splitting is involved in broadening the EPR line for films produced with $V_b \geq 100V$.

If the line ($V_b \geq 100V$) is broadened by unresolved hyperfine splitting caused by the presence of hydrogen then the lineshape (for $V_b \geq 100V$) would be a Gaussian (Seidel and Wolf 1968; Poole 1983, p. 583); we found it to be Lorentzian. Kleber et al. (1991) found that increasing the ion energy from 30eV to 170eV,which approximately corresponds to increasing V_b from 75V to 425V (Robertson 1998), causes a decrease in ΔB_{pp} from 18G to 3G while the hydrogen content only drops from 45% to 32%. Weiler et al. (1996) found that ΔB_{pp} falls from 3.8G to 1.8G in their samples when the hydrogen content drops from 27% to 22%. The linewidth for a-C (amorphous carbon) which contains no hydrogen was also found to vary in a similar manner to a-C:H (Chhowalla et al. 1997). So changing the hydrogen content in this type of a-C:H (i.e. for $V_b \geq 100V$) appears to have little effect on ΔB_{pp}. This indicates that unresolved hyperfine splitting caused by the presence of hydrogen is not a major contributor to the linewidth (ΔB_{pp}) for our a-C:H films grown with $V_b \geq 100V$.

Therefore declining hyperfine splitting and falling dipolar broadening can be ruled out as the causes of the reduction in ΔB_{pp} with increasing V_b (for $V_b \geq 100V$). This leaves the most likely explanation; that the linewidth narrows because of increasing exchange interaction. This increase in exchange is due to increasing delocalisation of unpaired electrons caused by the increase in sp^2.

In this section we examine the possible changes in the structure of these films which allows the greater delocalisation of unpaired electrons in a-C:H films as V_b increases.

Increasing the bias voltage (V_b) as mentioned earlier increased the sp^2 content of the films (for $V_b \geq 100V$). An increase in sp^2 content in the films causes a corresponding decrease in the optical gap of the films (Sch✣tte et al. 1993; Risten et

al. 1995; Silva et al. 1996; Kleber et al. 1991; Weiler et al. 1996; Chhowalla et al. 1997). Sattel et at. (1997) found a relationship between the gap and the linewidth (ΔB_{pp}). As already mentioned it is believed (Robertson 1986, p. 361; Robertson and O'Reilly 1987) that these unpaired π-electrons in a-C:H reside in aromatic clusters which contain an odd number of fused benzene ring units (a minimum of three). In general Robertson and O'Reilly (1987) show that the sp^2 bonds within the film are stabilised by forming clusters of fused six-fold (analogous to benzene) aromatic rings, as the size of these clusters increases the gap decreases. Robertson (1996) later modified this theory stating that clustering is limited to very few aromatic six-fold sp^2 rings (analogous to benzene) and short polymer chains of conjugated double bonds (olefinic). Figure 4.7 shows a schematic diagram of this type of a-C-H network (from Robertson 1996).

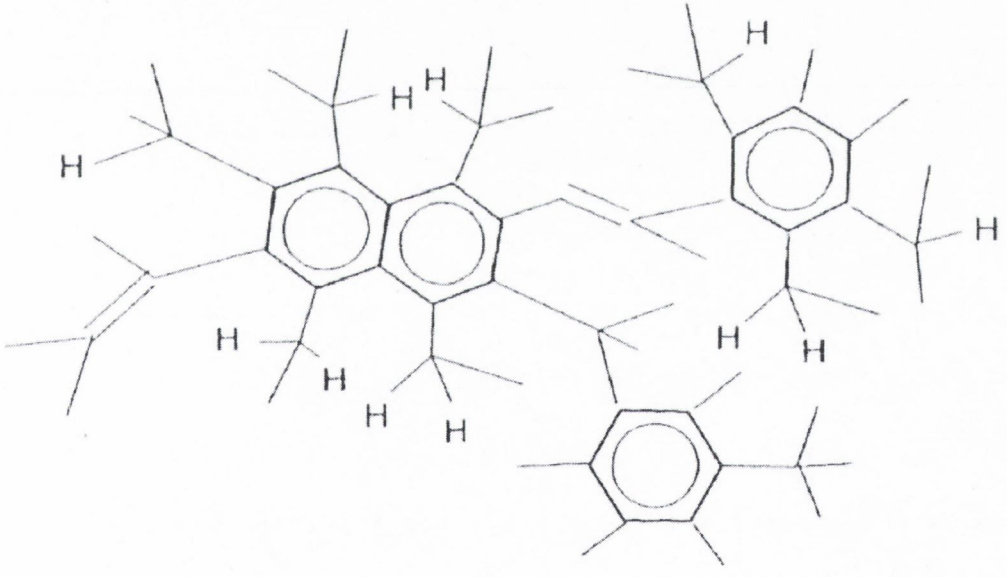

Figure 4.7 : Schematic diagram of an a-C:H network.

So increasing the sp^2 in our films (for $V_b \geq 100V$) may increase the size of these clusters.

This increase in the size of the clusters, with increasing sp^2 content, would allow the unpaired π-electrons to delocalise over a greater area. This delocalisation would increase the overlap of the wavefunctions of unpaired electrons which would increase the strength of the exchange interaction.

4.2.5 Discussion of the EPR results for a-C:H (V_b < 100V).

The linewidth (ΔB_{pp}) in figure 4.2 starts at 1.12mT at V_b = 10V then increases until a bias-voltage of 50V was reached and then narrows until it is ≈0.3mT at V_b=540V. We have already explained the fall in ΔB_{pp} for $V_b \geq 100V$ and we shall now attempt to explain the fall in going from V_b =50 to 10V. Previously we explained the linewidth for V_b = 100V as being due to dipolar broadening alone, now as V_b is reduced to less than 100V the values of N_V fall. In table 4.8 we see that the linewidth (ΔB_{pp}) that dipolar broadening alone predicts is much narrower than the actual measured ΔB_{pp}. We suggest therefore that for our a-C:H films produced with V_b < 100V that unresolved hyperfine slitting (hfs) due to the presence of hydrogen make an increasingly large contribution to the linewidth as V_b decreases. For our samples reducing the bias voltage (V_b) from 100V to 10V increases the hydrogen content in the films from ≈13At.% to ≈50At.% (table 4.1) a similar increase in hydrogen content with decreasing V_b has also been reported by others (Kleber et al. 1991; Tamor et al. 1991). Unresolved hyperfine splitting gives rise to a Gaussian lineshape. The full width at half height is given by the following equation (Seidel and Wolf 1968).

$$\sqrt{\Delta B_{1/2}} = \left(8\ln(2) / g^2 \mu_B^2\right) \sum_{i,I} N_I \xi_i A_{i,I}^2 \frac{\left[I_{i,I}\left(I_{i,I}+1\right)\right]}{3} \qquad (4.15)$$

Where

N_I = The number of nulcei in the I^{th} shell,

ξ_I = The relative abundance of the i^{th} isotope,

$A_{i,I}$ = The hyperfine interaction with the nuclei i in the I^{th} shell.

In the case of hydrogen (H^1), and using the fact that $\Delta B_{½} = (2\ln 2)^{½} \Delta B_{pp}$ for a Gaussian line, equation 4.15 becomes

$$\left(\Delta B_{pp}\right)^2 = \sum_I N_I A_I^2 \qquad (4.16)$$

Where A_I is here expressed in units of magnetic field.

Therefore we suggest that for V_b < 100V the linewidths and lineshapes were determined by a combination of dipolar broadening and unresolved hyperfine splitting caused by the presence of hydrogen. Because these effects are independent of each other the lineshape would therefore be a convolution of a Lorentzian (caused by the dipolar broadening) and a Gaussian (caused by the unresolved hyperfine splitting), such a convolution is called a Voigt profile.

Thus as V_b decreases below 100V the dipolar broadening falls because of the reduction in N_V and the effect of hyperfine splitting (hfs) increases because of the rapid increase in the hydrogen content of the a-C:H films. So the lineshape should change from a Lorentzian (dipolar broadening) to a Voigt profile (both dipolar and hfs effects) to finally a Gaussian (unresolved hfs only).

The lineshape is extremely close to Lorentzian for V_b = 100V it becomes a Voigt at 50V and was between a Lorentzian and a Gaussian for 10V (this spectrum is very noisy). We have already fitted the V_b = 50V spectrum with a Voigt profile and this fit and the parameters used can be found in figure 4.1 and table 4.3. As already mentioned the spectrum could also be fitted by the superposition of a Gaussian and Lorentzian lineshape (table 4.4). It is impossible to say from the goodness of the fit alone whether the lineshape is a Voigt or a combination of a Lorentzian and a Gaussian for V_b =50V. Sadki et al. (1996) found a lineshape which was between a Gaussian and Lorentzian for their polymeric a-C:H sample, though their g_0-value was 2.0045 and as mentioned in chapter 3 this may be due to the presence of defects both in the Si substrate and the a-C:H film. Ristein et al. (1995) found that for $V_b \geq 50V$ that the shape of their spectra were Lorentzian but they did not however determine what the lineshape was for V_b < 50V. Silva et al. (1996) and Schütte et al. (1993) claim that the lineshapes for their sample at all bias voltages (V_b) were Lorentzian. So while our lineshapes for $V_b \geq 100V$ agree with the lineshapes reported above, our lineshapes did not agree with those reported above (Ristein et al. 1995; Silva et al. 1996; Schütte et al. 1993) for V_b < 100V.

We believe that for V_b < 100V the lineshape is due to the presence of dipolar broadening and unresolved hyperfine splitting. We shall now examine the contributions that each had on the lineshape and width. For V_b = 50V we suppose that the Lorentzian component of the Voigt profile is due to dipolar broadening and the linewidth ($^L\Delta B_{pp}$) can be predicted by equation 4.14 based upon the spin

concentration (N_V). The Gaussian component was due to hyperfine splitting and this linewidth ($^G\Delta B_{pp}$) is related to equation 4.16.

In this section we examine quantitatively if the assumption that both these effects, i.e. unresolved hfs and dipolar broadening, account for the linewidth and shape for a-C:H films grown by us and other with V_b<100V.

We shall first examine our polymeric a-C:H sample (V_b = 10V) and polymeric a-C:H samples grown by others. All these films are produced at very low bias voltage, just like our sample produced with V_b = 10V. In table 4.9 we list the Voigt parameters (table 4.3) for our polymeric sample (V_b=10V) together with estimated Voigt parameters for the for polymeric a-C:H reported by others. In order to estimate the values of $^L\Delta B_{pp}$ and $^G\Delta B_{pp}$ from the EPR data reported by others we first assumed that $^L\Delta B_{pp}$ can be calculated from equation 4.14 as this linewidth is supposed to arise from dipolar broadening. Then taking the total width of the Voigt profile ($^V\Delta B_{pp}$) as equal to the measured values of ΔB_{pp} we evaluate $^G\Delta B_{pp}$ from the following equation given by Stoneham (1972)

$$^V\Delta B_{pp} = \frac{^G\Delta B_{pp}^2 + 0.9085\,^G\Delta B_{pp}\,^L\Delta B_{pp} + 0.4621\,^L\Delta B_{pp}^2}{^G\Delta B_{pp} + 0.4621\,^L\Delta B_{pp}} \qquad (4.17)$$

$^V\Delta B_{pp}$ [mT]	$^L\Delta B_{pp}$ [mT]	$^G\Delta B_{pp}$ [mT]	N_V [10^{18} cm^{-3}]	V_b [V]	Atomic percentage of H [%]	At.% H based on eq. 4.18	Optical gap [eV]	Reference
0.87*	0.030	0.85	4.00	N/A	N/A	50±15	2.22 (E_{03})	Schütte et al. (1993)
0.82	0.006	0.82	0.73	0	N/A	48±14	4.00 (E_{04})	Ristein et al. (1995)
0.32	0.050	0.30	6.00	12	24		3.55 (E_{04})	Silva et al. (1996)
0.80	0.001	0.80	0.15	N/A	45-50		3.3 (E_{03})	Sadki et al. (1996)
1.13	0.002	1.13	0.30	10	50		3.4 (E_{04})	Our sample

*Table 4.9 : Voigt parameters for a-C:H samples grown with V_b≈10V. * This sample was grown on the anode.*

Now we can see in table 4.9 that for polymeric a-C:H (i.e. grown with a low bias) the $^G\Delta B_{pp}$ values are in the range 0.8 to 1.1mT with the exception of that found

by Silva et al. (1996). This low value of ${}^{G}\Delta B_{pp}$ = 0.3mT found by Silva et al. (1996) may be due to the very low hydrogen content (24at.%) in this film compared to our film (50at.% H) and since ${}^{G}\Delta B_{pp}$ is expected to be related to the hydrogen content through equation 4.14 it is reasonable that the value found by Silva et al. (1996) is so low.

Now let us consider if the values of ${}^{G}\Delta B_{pp}$ = 0.8 to 1.1mT are reasonable for films containing 50at.% of hydrogen. Polyethyne (polyacetylene) with a high proportion of the cis bonded configuration has an almost Gaussian shaped EPR spectrum with a g-value very near 2 and ΔB_{pp} = 0.85mT at 295K and 1.1mT at 82K (Weinberger et al. 1980). This compares to polyethyne (polyacetylene) with a high proportion of the trans bonded configuration which has a motionally narrowed Lorentzian lineshape. Cis rich polyethyne (polyacetylene) has been fitted with an immobile, delocalised soliton which has been computed to have a Gaussian lineshape with ΔB_{pp} = 1.2mT, due to unresolved hyperfine splitting caused by the proximity of hydrogen (Weinberger et al. 1980). Therefore the cis configuration of polyethyne (polyacetylene) gives an EPR signal analogous to the Gaussian component (${}^{G}\Delta B_{pp}$) for our polymeric a-C:H film grown with V_b = 10V. We can also compare the unresolved hfs in our film to the isotropic hyperfine splitting for benzene, naphthalene and anthracene anions. Using hyperfine interaction constants from Carrington and McLachlan (1967) values of ΔB_{pp} are calculated (R. C. Barklie, personal communication). All these spectra have Gaussian lineshape envelopes.

For $C_6H_6^-$ $|A_1|$ = 0.375mT and N_1 = 6 (Carrington and McLachlan 1967, p. 83), all six carbon sites are equivalent in benzene so using equation 4.16 we get

$({}^{G}\Delta B_{pp})^2 = 6\times(0.375\text{mT})^2 \Rightarrow {}^{G}\Delta B_{pp} = 0.92\text{mT}$ for the benzene anion.

Similarly for the naphthalene anion with $|A_1|$ = 0.490mT, N_1 = 4, $|A_2|$ = 0.183mT and N_2 = 4 (Carrington and McLachlan 1967, p. 77), i.e. with two sets of 4 equivalent sites we get

$({}^{G}\Delta B_{pp})^2 = 4\times(0.490\text{mT})^2 + 4\times(0.183\text{mT})^2 \Rightarrow {}^{G}\Delta B_{pp} = 1.05\text{mT}$ for the naphthalene anion.

And finally for the anthracene anion with $|A_1|$ = 0.274mT, N_1 = 4, $|A_2|$ = 0.157mT, N_2 = 4, $|A_9|$ = 0.556mT and N_9 = 2 (Carrington and McLachlan 1967, p. 90), we get

$({}^{G}\Delta B_{pp})^2 = 4\times(0.274\text{mT})^2 + 4\times(0.157\text{mT})^2 + 2\times(0.556\text{mT})^2 \Rightarrow {}^{G}\Delta B_{pp} = 1.01\text{mT}$ for the anthracene anion.

The above values of ${}^{G}\Delta B_{pp}$ are reasonable as they were all roughly half of the 'extent' of the spectrum i.e. the spacing between the outermost lines in the spectrum. The 'extent' for the benzene, naphthalene and anthracene anions are 2.25, 2.73 and 2.27mT respectively (Wertz and Bolton 1972, p. 117). All the above calculated values of ${}^{G}\Delta B_{pp}$ = 0.92, 1.05 and 1.01mT for the benzene, naphthalene and anthracene anions respectively compare well with our range of ${}^{G}\Delta B_{pp}$ values of 0.8 to 1.1mT.

A similar calculation for the alkyl radical $-CH_2-\dot{C}H-$ containing only σ orbitals (including the one the unpaired electron resides in) yields a ${}^{G}\Delta B_{pp}$ value of 7.0mT while for the ally radical $-CH_2-\dot{C}H-CH=CH-CH_2-$ which contains both π and σ orbitals yields a value of 5.0mT.

Therefore for our polymeric a-C:H film (V_b = 10V) and those reported by others the range of values of ${}^{G}\Delta B_{pp}$ = 0.8 to 1.1mT is in agreement with those predicted by unresolved hyperfine splitting due to hydrogen for unpaired π-electrons on polymer chain of conjugated double bonds or aromatic rings. This range of ${}^{G}\Delta B_{pp}$ values (0.8-1.1mT) is inconsistent with the unpaired electrons being σ-electrons or mixed π/σ electrons.

For these polymeric a-C:H films it might be possible to relate the ${}^{G}\Delta B_{pp}$ value to the hydrogen content of the film. From equation 4.16 we propose that the ${}^{G}\Delta B_{pp}$ values might be proportional to (at.% of hydrogen)^{½}, but changing the hydrogen content also is likely to change the hyperfine splitting constants A_l. As we can see from our calculations for the anions above that there would be a range of N_l and A_l values associated with the films. Therefore only an empirical relationship can be measured for these polymeric a-C:H films. Therefore from the values of ${}^{G}\Delta B_{pp}$ in table 4.9 for the films where the hydrogen content is known, i.e. the last three films listed in table 4.9, we get the following relationship

$$^{G}\Delta B_{pp}\,[mT] = (0.017\pm0.005)\times(at.\%\ H) \qquad (4.18)$$

We can use this equation to estimate the hydrogen content of polymeric a-C:H films when the value of $^{G}\Delta B_{pp}$ is known. In table 4.9 we list the estimates of at% H based upon this equation for the films where the hydrogen content is unknown. We can see in table 4.9 that the values of at.% H produced are very reasonable for these polymeric a-C:H films i.e. ≈50at% H.

Now we examine the contributions of unresolved hfs and dipolar broadening to the linewidths and lineshapes for our a-C:H film produced with V_b=50V and a-C:H samples grown under similar conditions by others.

In table 4.10 we list the Voigt parameters for our V_b = 50V sample (table 4.3), which is closer to DLC, together with our estimates of the Voigt parameters from the EPR data for a-C:H films reported by others which had the highest ΔB_{pp} values. Estimates of the values of $^{L}\Delta B_{pp}$ and $^{G}\Delta B_{pp}$ are made in same way as in table 4.9. All these films are diamond like a-C:H (DLC) or in the transition region between DLC and polymeric a-C:H.

$^{V}\Delta B_{pp}$ [mT]	$^{L}\Delta B_{pp}$ [mT]	$^{G}\Delta B_{pp}$ [mT]	N_V [10^{20} cm^{-3}]	V_b [V]	Atomic percentage of H [%]	Optical gap [eV]	Reference
2.03[a]	1.62	0.91	2.00	N/A	N/A	2	Schütte et al. (1993)
1.72	0.57	1.40	0.70	N/A	N/A	1.88	Schütte et al. (1993)
1.46	1.05	0.77	1.30	90	N/A	2.45	Ristein et al. (1995)
1.20	1.62	0	2.00	34	24	3.05	Silva et al. (1996)
1.80	1.30	0.92	1.60	75[b]	45	1.9	Kleber et al. (1991)
1.54	0.4	1.32	0.49	50	50	N/A	Our sample

Table 4.10 : Voigt parameters for a-C:H samples grown with V_b equvalent to 50V.
[a] This sample was grown on the cathode.
[b] This value of bias voltage is estimated by assuming it is equal to 2.5 times the ion energy (Robertson 1998).

In table 4.10 the values of $^{G}\Delta B_{pp}$ are very high considering that the hydrogen content has fallen, assuming that $^{G}\Delta B_{pp}$ is indeed dependant upon the hydrogen content. Indeed in some cases is even larger than that obtained for polymeric a-C:H.

One possible explanation for these very high values of ${}^{G}\Delta B_{pp}$ is that the values of ${}^{L}\Delta B_{pp}$ are underestimated because as ${}^{L}\Delta B_{pp}$ decreases ${}^{G}\Delta B_{pp}$ increases (see equations 4.17, 2.14 and 2.15). As the values of ${}^{L}\Delta B_{pp}$ are based upon the values of N_V an underestimation of N_V causes an underestimation of ${}^{L}\Delta B_{pp}$. There are two possibilities which explain such an underestimation of N_V values the first being experimental error. For $N_V > 10^{20}cm^{-3}$ only a small increase of ≈20%, which is reasonable for N_V values, will reduce ${}^{G}\Delta B_{pp}$ to ≤ 0.5mT while for $N_V \approx 10^{19}cm^{-3}$ an increase of ≈100% would be required. The second possibility is that the local N_V concentration value is higher than the average N_V value over the entire film. If this is the case ${}^{L}\Delta B_{pp}$ would be underestimated (i.e. ${}^{G}\Delta B_{pp}$ is overestimated) because the dipolar broadening (i.e. ${}^{L}\Delta B_{pp}$) depends upon the local N_V value and not the average value. This is possible, if during the transition from DLC (V_b = 50V) to polymeric (V_b=10V), the increase in the hydrogen content is not uniform i.e. when the hydrogen is added, the decrease in the spin concentration is not uniform. This is credible because as the bias voltage is reduced from 100V to ≈0V, i.e. during the transition from DLC to polymeric, the amount of four-fold coordinated carbon bonded to hydrogen increases more rapidly than three-fold coordinated carbon bonded to hydrogen (Tamor et al. 1991). Since our unpaired spins are associated with π-electrons, i.e. three-fold coordinated carbon, the reduction in spin concentration would be inhomogeneous over the film. Finally for polymeric a-C:H with $N_V \leq 10^{18}cm^{-3}$ such a variation in the average or local values of N_V would have little effect on ${}^{G}\Delta B_{pp}$ because the values of ${}^{L}\Delta B_{pp}$ due to dipolar broadening are already very small.

In summary, for a-C:H films grown with V_b<100V the lineshape and width are determined by dipolar broadening and unresolved hfs. As V_b decreases the degree of dipolar broadening falls because N_V falls and the contribution of the unresolved hfs increases because the hydrogen content increases.

4.2.6 Interpretation of the lineshape of a-C:H observed by others

In this section we see if our interpretation of the lineshape of a-C:H films can be used to explain the results obtained by Hoinkis et al. (1992). Hoinkis et al. (1992)

found that ΔB_{pp} (measured in a vacuum) reached a minimum value of 0.28mT for a hydrogen content of ≈24at.%. As the hydrogen content increases above this ΔB_{pp} increases while N_V decreases. ΔB_{pp}=0.8mT and $N_V=1.5\times10^{20}cm^{-3}$ for 36at.% H and ΔB_{pp}=1.0mT and $N_V=0.5\times10^{20}cm^{-3}$ for 39at.% H. Hoinkis et al. (1992) interpreted this rise in ΔB_{pp} with increasing hydrogen content, for > 24at.% H, as due to an increase in the unresolved hyperfine splitting caused by the increase in the hydrogen present. We interpret this effect differently. From equations 4.14 and 4.18 the dipolar and hyperfine contributions to the linewidths can be calculated while the total linewidth can be calculated from equation 4.17. These yield for the Hoinkis et al. (1992) sample with 24at.% H the following results, ${}^{L}\Delta B_{pp}$=3.7mT (dipolar contribution), ${}^{G}\Delta B_{pp}$=0.45±0.12mT (hyperfine contribution) and ΔT=3.72mT (total width i.e. ΔB_{pp}). The measured value of ΔB_{pp} = 0.28mT is much less than our calculated total linewidth (3.72mT). Therefore we suggest that exchange narrowing is taking place because the sp^2 content is very high which allows the delocalisation of unpaired π-electrons, allowing an overlap of their wavefunctions. For 36at.% H the same calculation yields ${}^{L}\Delta B_{pp}$=1.22mT, ${}^{G}\Delta B_{pp}$=0.65mT and ΔT=1.5mT. The value of ΔT is closer to the measured value of ΔB_{pp} = 0.8mT but still too large. In this case we suggest that exchange narrowing is still present but reduced compared to the 24at.% H film because the increase in hydrogen content reduces the sp^2 content of the film. For 39at.% H the same calculation yields ${}^{L}\Delta B_{pp}$ = 0.4mT, ${}^{G}\Delta B_{pp}$ = 0.7mT and ΔT = 0.9mT. This value of ΔT agrees with the measured value of ΔB_{pp} = 1.0mT. So in the region 24-36at.% H the dominant contributions to the linewidth are dipolar broadening combined with exchange narrowing which gives rise to the Lorentzian lineshapes which are observed (Hoinkis et al. 1992). These contributions fall with increasing hydrogen content because dipolar broadening is dependant on N_V (which falls) and exchange narrowing is dependant upon the sp^2 content of the film (which also falls). Only at 39at.% H does the unresolved hyperfine interaction make a significant contribution to the linewidth and this combined with dipolar broadening without exchange narrowing explains the linewidth observed for this sample (39at.% H). We predict that the lineshape for this EPR spectrum is a Voigt profile. The effect of decreasing the hydrogen content from 39 to 24at.% is similar to the effect of increasing the bias voltage (V_b) in our samples from 50 to 540V.

Hoinkis et al. (1992) explain the increase in ΔB_{pp} with decreasing hydrogen content < 24at.% H as being due to a reduction in the spin-lattice relaxation times (T_1) due to the interaction of unpaired π-electrons with conduction electrons. This is in agreement with the increase in conductivity with decreasing hydrogen content, below 24at.% H, which they observed. While such an effect is not observed in our samples it has been reported that this effect is responsible for the increase in ΔB_{pp} observed after annealing at high enough temperatures (Miller and McKenzie 1983; González-Hernández et al. 1988).

4.3 Conclusions of varying V_b

We have found that varying the bias voltage (V_b) has a major effect on the EPR signal and the defects present in the a-C:H films. All the unpaired electrons in all our samples are attributed to π unpaired electrons and not σ unpaired electrons. We can break the transitions of the films as V_b was varied into three regions.

The first region was for very low bias voltages (V_b=10V) where the film is polymeric i.e. it has a low sp^2 content and a high hydrogen content (table 4.1). The EPR lineshape and linewidth are likely to be due to the presence of both dipolar broadening and broadening caused by unresolved hyperfine splitting caused by hydrogen. Unfortunately the noisy nature of the signal did not allow us to fit this spectrum but we still found that the lineshape was between that of a Gaussian and Lorentzian which agreed with the idea that these two contributions to the linewidth and shape are present.

The second region is when the films are in transition from polymeric to DLC (containing a low sp^2 and hydrogen content), these have bias voltages in the range 10V to 100V. Again for V_b=50V the EPR lineshape and linewidth are likely to be due to the presence of both dipolar broadening and broadening caused by unresolved hyperfine splitting caused by hydrogen. However, in this case there might have been clustering of the π unpaired electrons due to the high values of $^{G}\Delta B_{pp}$ observed (table 4.10).

The final region is where the films transform from DLC to graphite-like a-C:H (containing a high sp^2 and a low hydrogen content) with $V_b \geq 100V$. Here the effect of unresolved hyperfine splitting due to hydrogen is negligible. The linewidth and

lineshape could be accounted for by the presence of both dipolar broadening and exchange narrowing which increased as V_b increased. This increase in exchange narrowing is due to the increase in the sp^2 content of the film which allows the unpaired π-electrons to delocalise over a greater area allowing for a greater overlap of their wavefunctions. We found evidence supporting this increase in exchange narrowing in the decrease in T_1 (spin-lattice relaxation time) and the increase in T_2 (spin-spin relaxation time) with increasing V_b. This is very similar to the way the relaxation times varied for DPPH as its concentration increases, which is due to increased exchange interaction.

4.4 Annealing of a-C:H deposited with various values of V_b

As mentioned in chapter 3 annealing is an important process in the semiconductor industry. It is used to activate implanted ions and to removed damage and defects. High temperature processes are commonly used in post-deposition fabrication of electronic devices. We have already studied the effect of annealing on polymeric a-C:H in chapter 3. Therefore it is our aim, in this section, to extend our understanding of the effect that annealing has on the defects present in a wide variety of a-C:H films. To achieve this aim we shall examine the effect annealing has on the paramagnetic defects present in a-C:H films grown with a range of V_b values. This will help us understand how annealing effects a-C:H films as the structure changes from diamond like a-C:H (DLC) ($V_b \approx 50V$) to graphite like a-C:H (GLHC) ($V_b \approx 540V$).

The samples chosen P5, P2, DC160 and DC182 were grown with V_b values of 50, 100, 400 and 540V respectively (table 4.1). Over this range of V_b values the films went through a transition from diamond like a-C:H (DLC), i.e. with a low sp^2 and hydrogen content, to graphite like a-C:H (GLHC), i.e. with a high sp^2 and low hydrogen content. The preparation conditions used in growing these samples can be found in table 4.1.

4.4.1 EPR results of annealing on a-C:H as a function of V_b

In this section we present the EPR results obtained by annealing a-C:H films as a function of V_b. We will also analyse these results. The annealing procedure for all the a-C:H films was to anneal each sample for 10 minutes at successively higher temperatures in an Ar atmosphere. This process we referred as step annealing, see chapter 3 for more details. After each anneal the sample was cooled to room temperature and the spectrum recorded.

Figures 4.8 to 4.11 show selected spectra from the four a-C:H films we annealed, i.e with V_b = 50, 100, 400, and 540V. The spectra in these figures have been normalised. We can see that the signal intensity falls because N_V falls with increasing T_a. There is no change in the position of the spectra in figures 4.8 to 4.11 and hence g_0 remains constant within error. In figures 4.8 and 4.9 (V_b=50 and 100V) we see that ΔB_{pp} falls with increasing T_a. In contrast ΔB_{pp} increases with increasing T_a in figures 4.10 and 4.11 (V_b=400 and 540V).

Figure 4.12 to 4.15 are plots of the EPR data as a function of annealing temperature (T_a) obtained for the a-C:H films grown with V_b=50, 100, 400 and 540V respectively. In all these figures we can see that annealing has no effect the g_0-values, it remains constant at ≈2.0027. This indicates that annealing has no effect on the nature of the defects present in these a-C:H films, i.e. the defect remain unpaired π-electrons in clusters of conjugated olefinic chains or aromatic rings.

In figures 4.12 and 4.13 (V_b=50 and 100V) we see a fall in ΔB_{pp} as T_a increases from 200 to 450°C reaching a minimum of ≈0.8mT at 450°C. After this in figure 4.13 we see a slight increase in ΔB_{pp}. In comparison ΔB_{pp} in figures 4.14 and 4.15 (V_b=400 and 540V) remains constant up to 400°C after which it increases with increasing T_a. In figures 4.13 to 4.15 N_V falls as T_a increases though the temperature where N_V begins to fall increases going from figure 4.13 to 4.15. Thus the temperature where this fall begins is highest for V_b=540V which higher than for V_b=400V which is higher than for V_b=100V. In figure 4.12, N_V falls with increasing T_a, up to T_a=450°C above which it rises until 600°C after which it falls very rapidly.

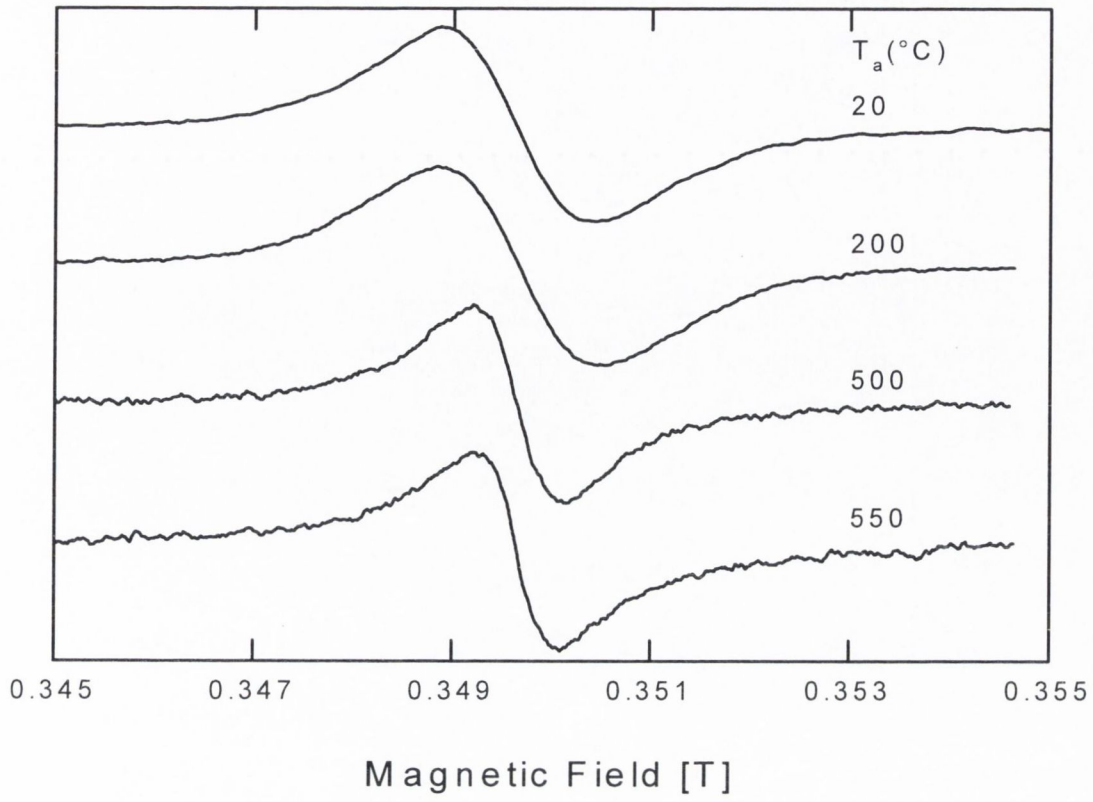

Figure 4.8 (ν = 9.8GHz) : EPR spectra for a-C:H deposited with V_b=50V as a function of annealing temperature (Ta).

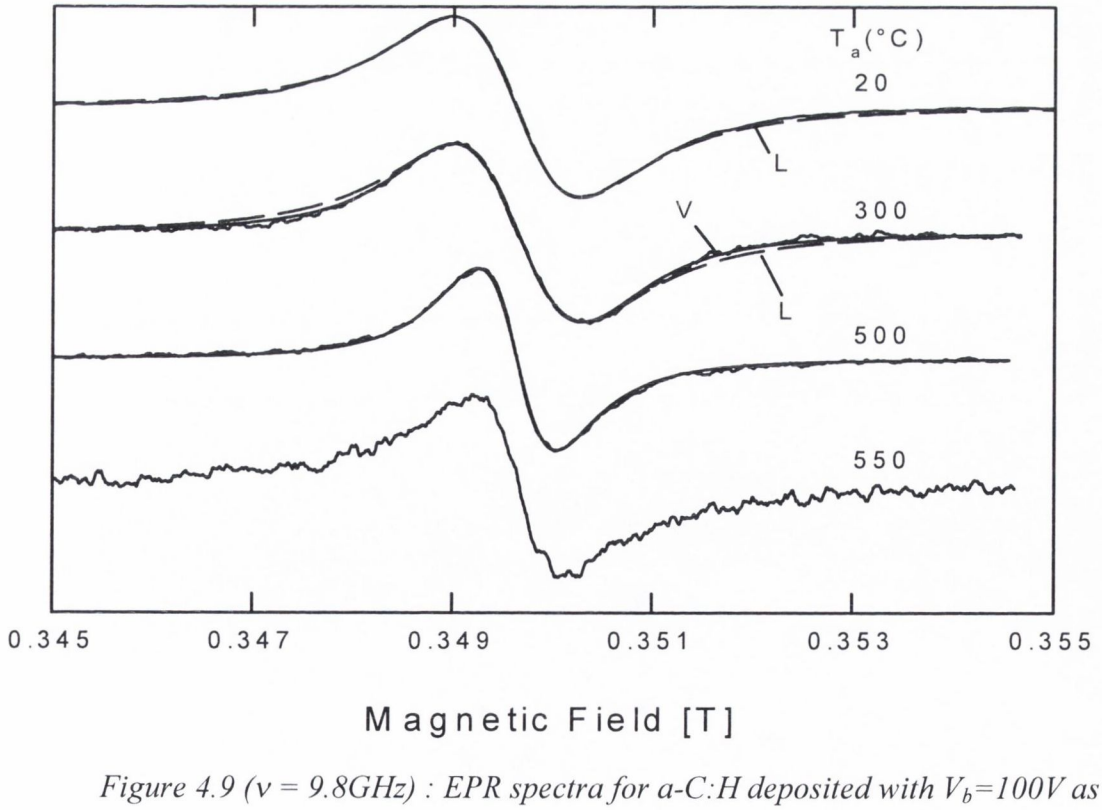

Figure 4.9 (ν = 9.8GHz) : EPR spectra for a-C:H deposited with V_b=100V as a function of annealing temperature (Ta).

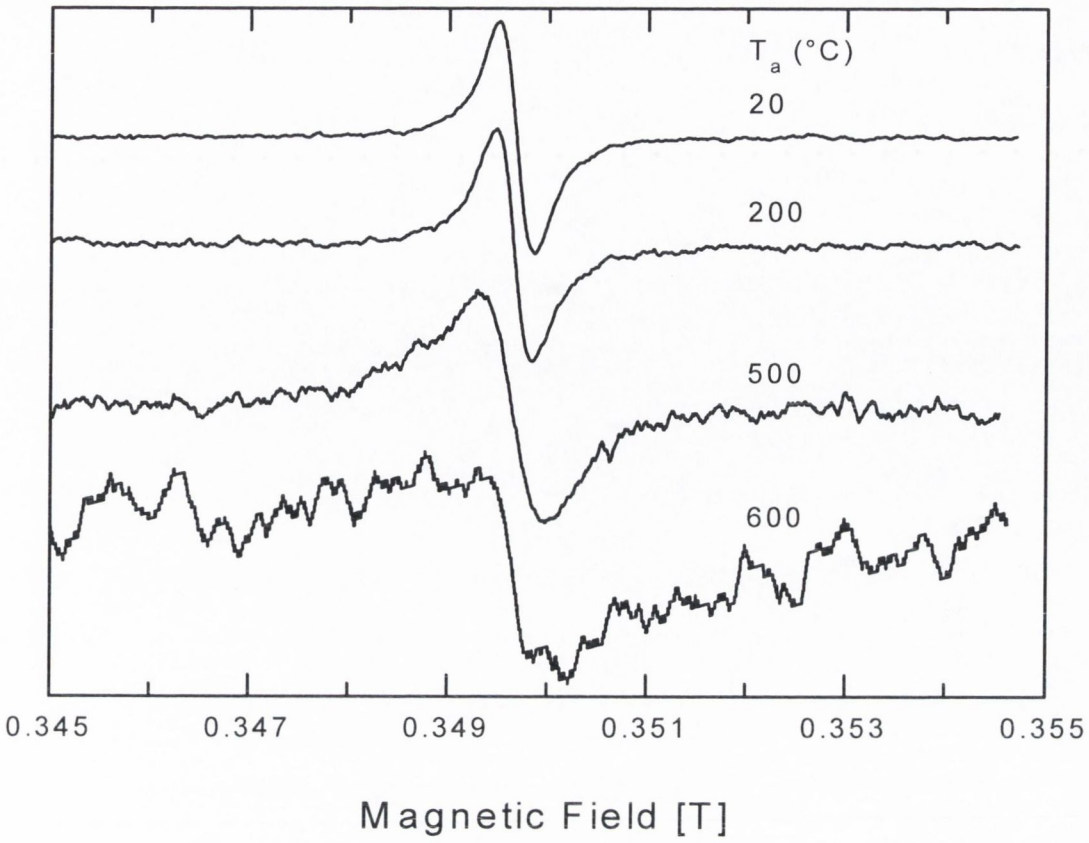

Figure 4.10 (ν = 9.8GHz) : EPR spectra for a-C:H deposited with V_b=400V as a function of annealing temperature (Ta).

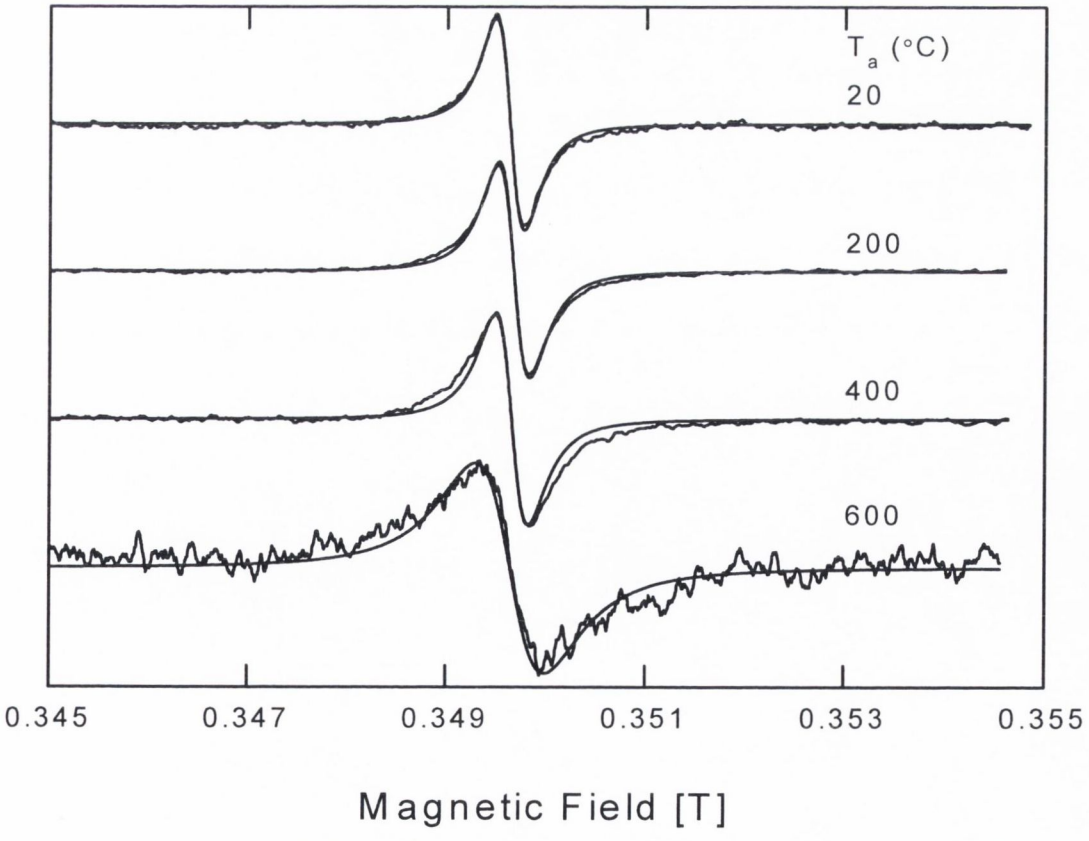

Figure 4.11 (ν = 9.8GHz) : EPR spectra for a-C:H deposited with V_b=540V as a function of annealing temperature (Ta).

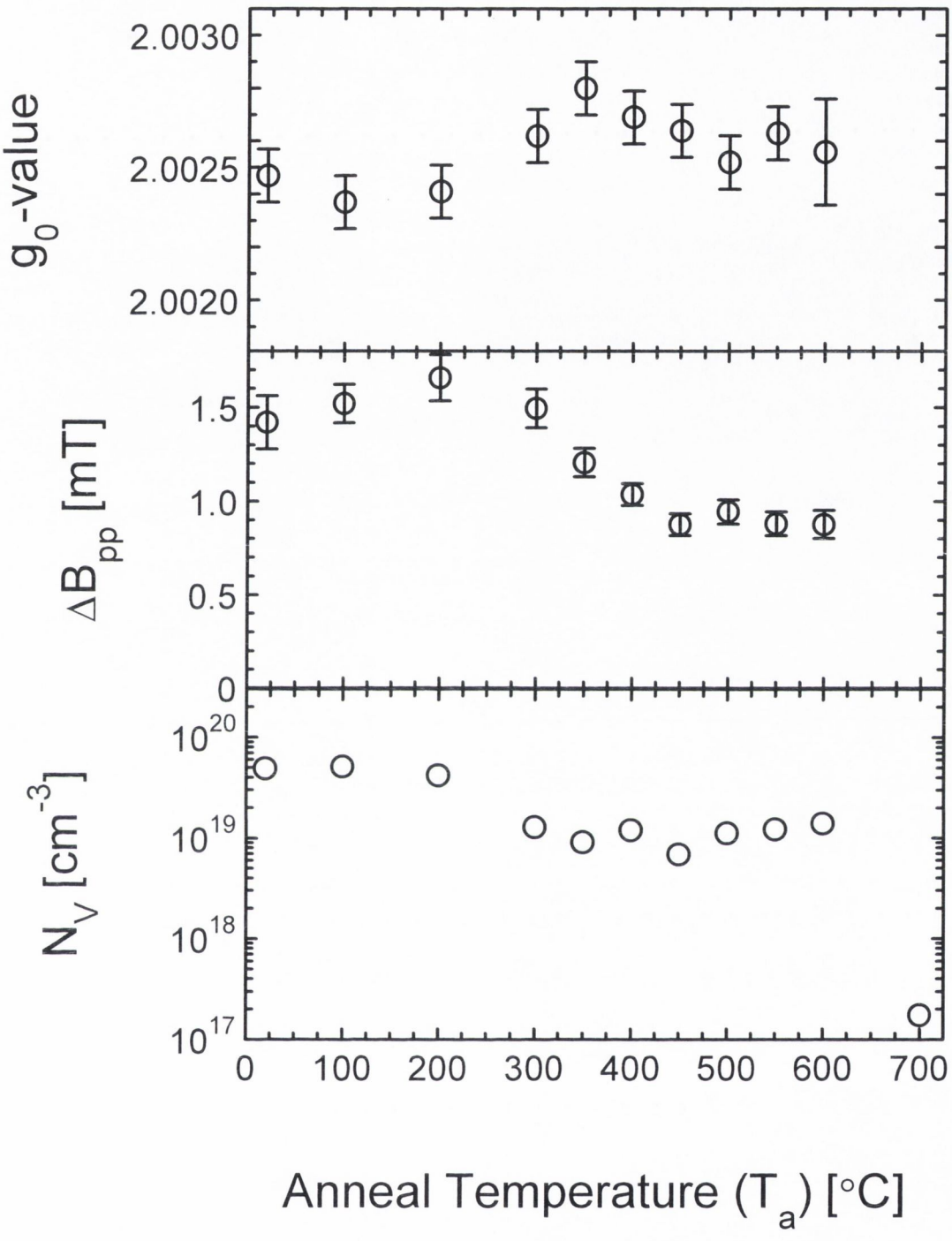

Figure 4.12 : EPR data for a-C:H grown with V_b=50V as a function of T_a.

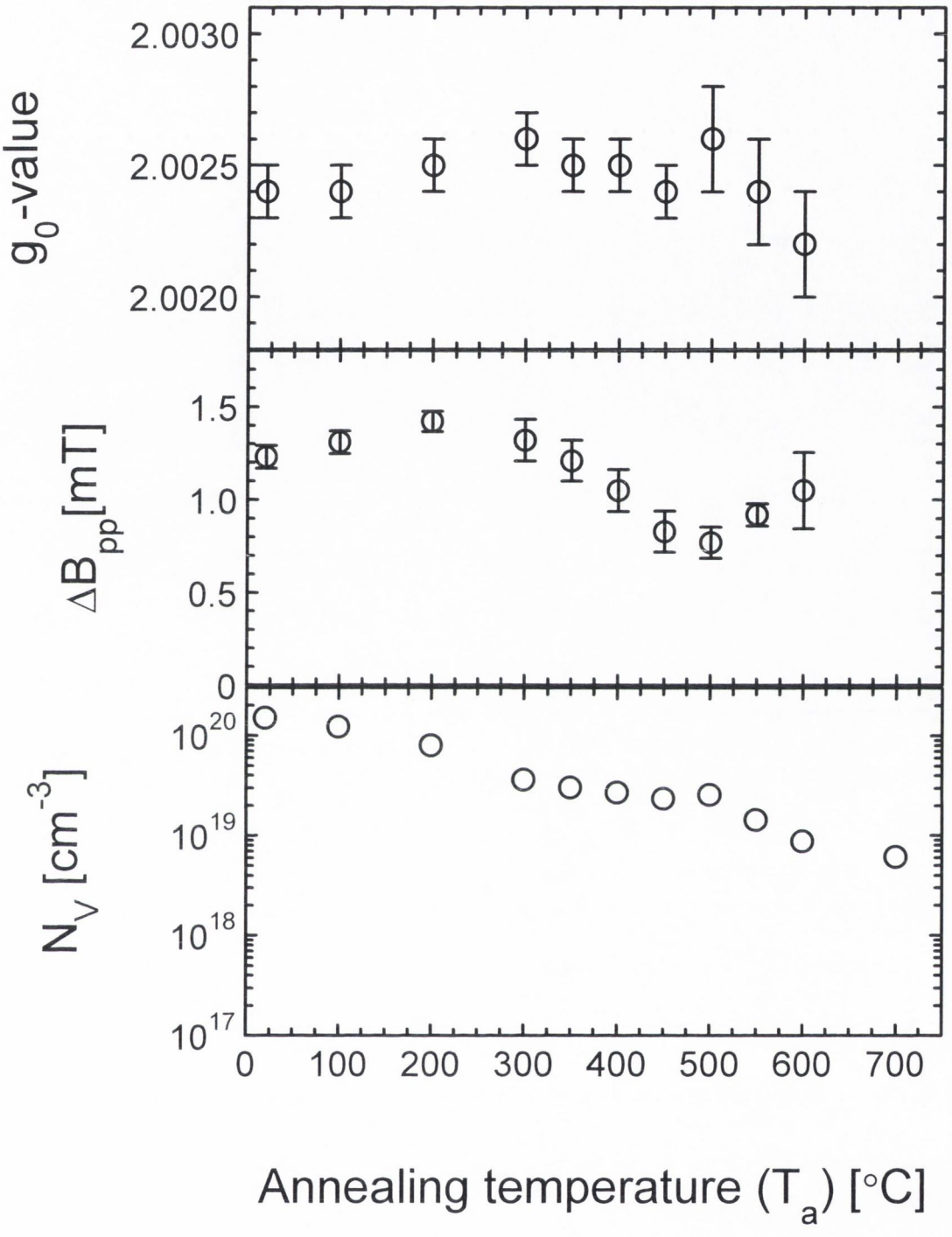

Figure 4.13 : EPR data for a-C:H grown with V_b=100V as a function of T_a.

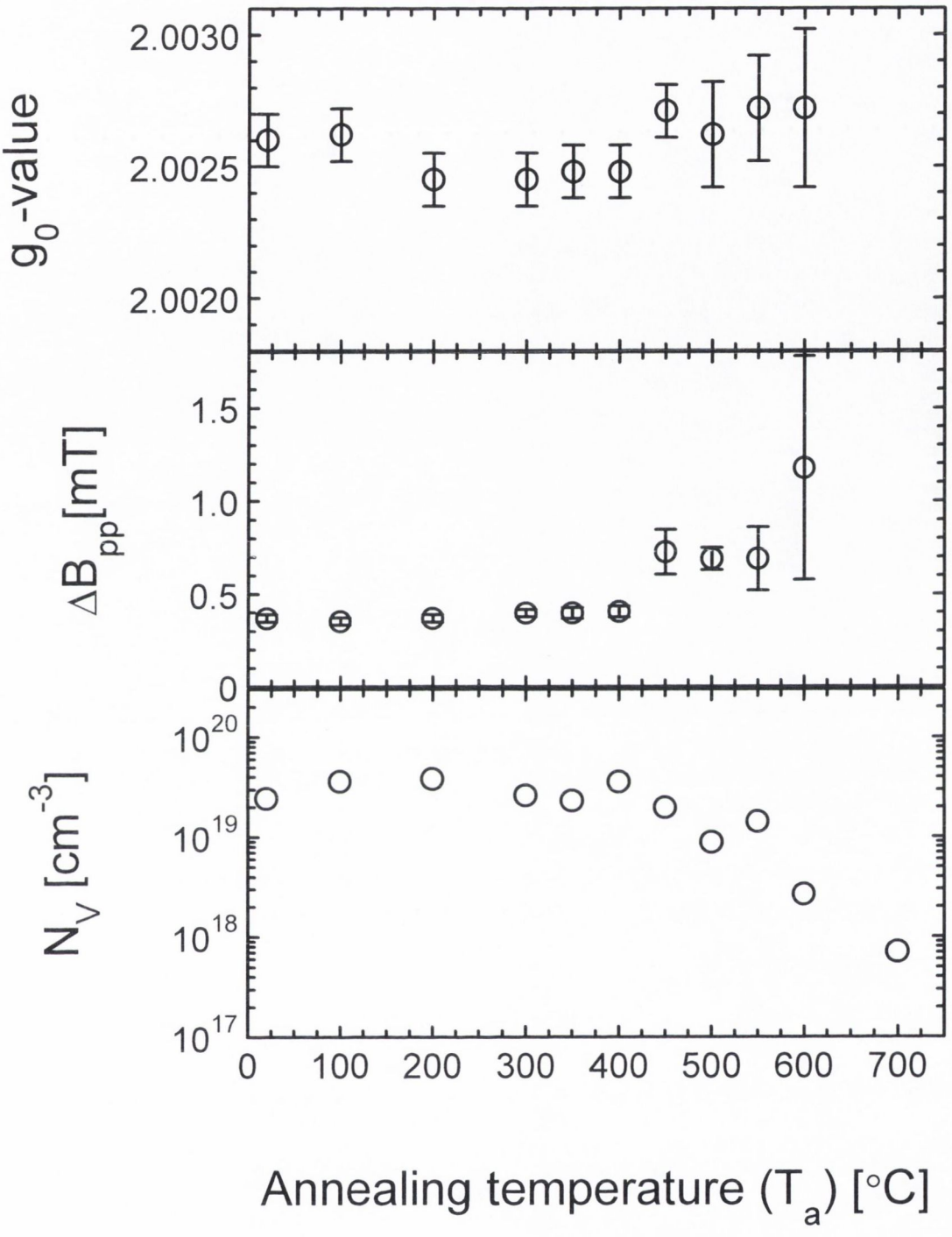

Figure 4.14 : EPR data for a-C:H grown with V_b=400V as a function of T_a.

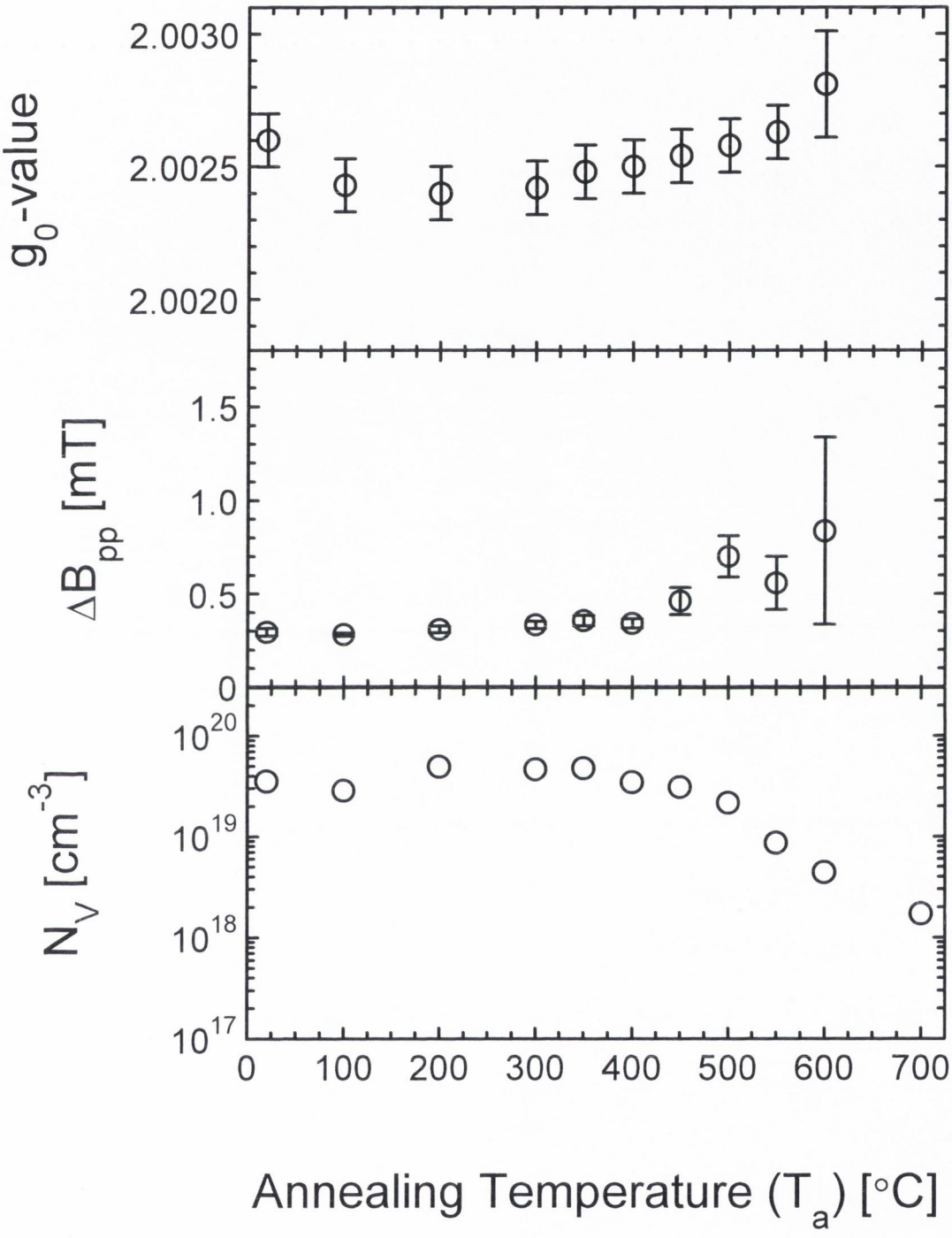

Figure 4.15 : EPR data for a-C:H grown with V_b=540V as a function of T_a

We will now examine the lineshapes of these a-C:H films as T_a increases. In figures 4.10 and 4.11 (V_b=400 and 540V) the lineshapes are Lorentzian until $T_a \approx 500°C$ and $T_a \approx 400°C$. In figure 4.11 (V_b=540V) superimposed upon the spectra are single Lorentzian line fits. We can see in this figure that for $T_a \geq 400°C$ the lineshape fall off more slowly in the wings than a Lorentzian.

The lineshape in figure 4.8 (V_b=50V) becomes roughly Lorentzian at 500°C, above this temperature the spectra fall of more slowly in the wings that a Lorentzian The lineshape of the spectrum at room temperature in figure 4.9 is close to a Lorentzian (denoted by 'L'). We can see that the for T_a=300°C that the Voigt profile fits this spectrum (denoted by 'V'), we can see this clearly in figure 4.16. In fact the lineshape can be fitted with a Voigt profile for the range of temperatures 20 to 450°C. As the temperature is increased above 450°C we see that the lineshape begins to becomes a Lorentzian(designated with 'L') at 500°C.

We now fit the spectra for the a-C:H film with V_b=100V with a Voigt profile for the range of temperatures 20 to 450°C. Figure 4.17 shows the Voigt parameters we determined by fitting the spectra (for V_b = 100V) as a function of T_a. The spectra for T_a = 500 and 550°C are Lorentzian above 550°C the signal became too noisy to determine the lineshape.

Table 4.11 lists the Voigt profile parameters we determined by fitting the spectra (for V_b = 100V) for the range of temperatures 20 to 450°C. A Voigt fit is used for 20°C because it gives a slightly better fit than a Lorentzian. Also in table 4.11 are the values of ΔB_{pp} calculated from equation 4.14 as the contributions to the linewidth from dipolar broadening.

Annealing temperature (T_a) [°C]	ΔT [mT]	${}^{L}\Delta B_{pp}$ [mT]	${}^{G}\Delta B_{pp}$ [mT]	ΔB_{pp} calculated from eq. 4.14
20	1.32	1.05	0.58	1.22
100	1.36	1.01	0.67	1.00
200	1.44	1.07	0.72	0.65
300	1.30	0.80	0.80	0.29
350	1.20	0.74	0.74	0.25
400	1.06	0.65	0.65	0.22
450	0.83	0.54	0.49	0.19

Table 4.11 : Voigt parameters for a-C:H grown with V_b=100V as a function of T_a.

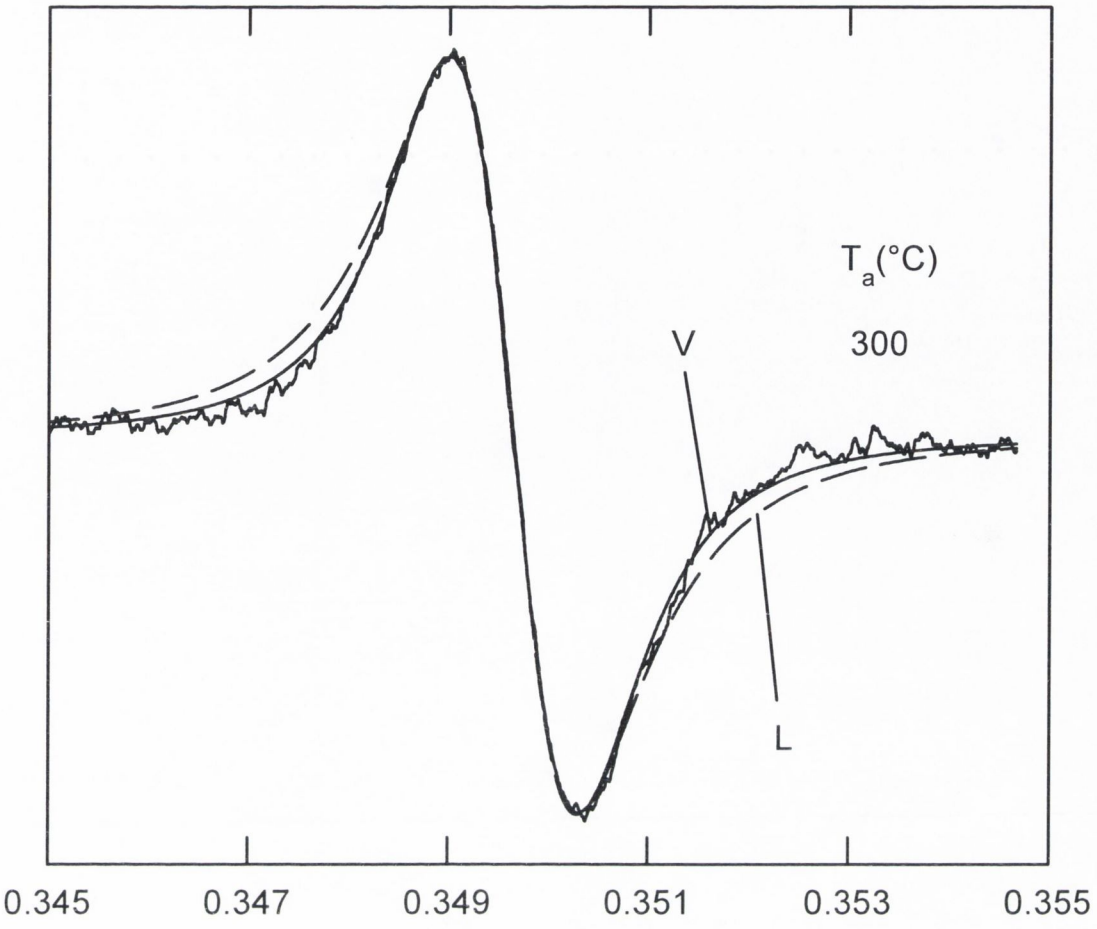

Figure 4.16 : EPR spectrum for a-C:H deposited with V_b=100V and annealed at 300°C. A Voigt (V) and a Lorentzian (L) fit are superimposed.

In figure 4.17 we can see that the linewidth of the Lorentzian component ($^{L}\Delta B_{pp}$) of the Voigt profile remains constant with increasing T_a up to 200°C, after which it falls, though it increases again at 500°C. The linewidth of the Gaussian component ($^{G}\Delta B_{pp}$) increases slightly with increasing T_a up to $T_a \approx 300$°C after which it narrows. This behaviour may be explained if, as before, the linewidth of the Gaussian component ($^{G}\Delta B_{pp}$) is due to unresolved hyperfine splitting caused by the presence of hydrogen while dipolar broadening and exchange narrowing determine the linewidth of Lorentzian component ($^{L}\Delta B_{pp}$). $^{G}\Delta B_{pp}$ may remain roughly constant with increasing T_a for $T_a \leq 300$°C. This indicates that the hydrogen content remains approximately constant because $^{G}\Delta B_{pp}$ is dependant upon the hydrogen content. This agrees with the fact that the majority of the hydrogen and small hydrocarbons (e.g.

methane etc.) are emitted from a-C:H occurs at temperatures greater than 400°C (Kon'kov et al. 1997). Finally ${}^{G}\Delta B_{pp}$ drops with increasing T_a for T_a > 300°C possibly because of the loss of the majority of the hydrogen content in the film above ≈400°C.

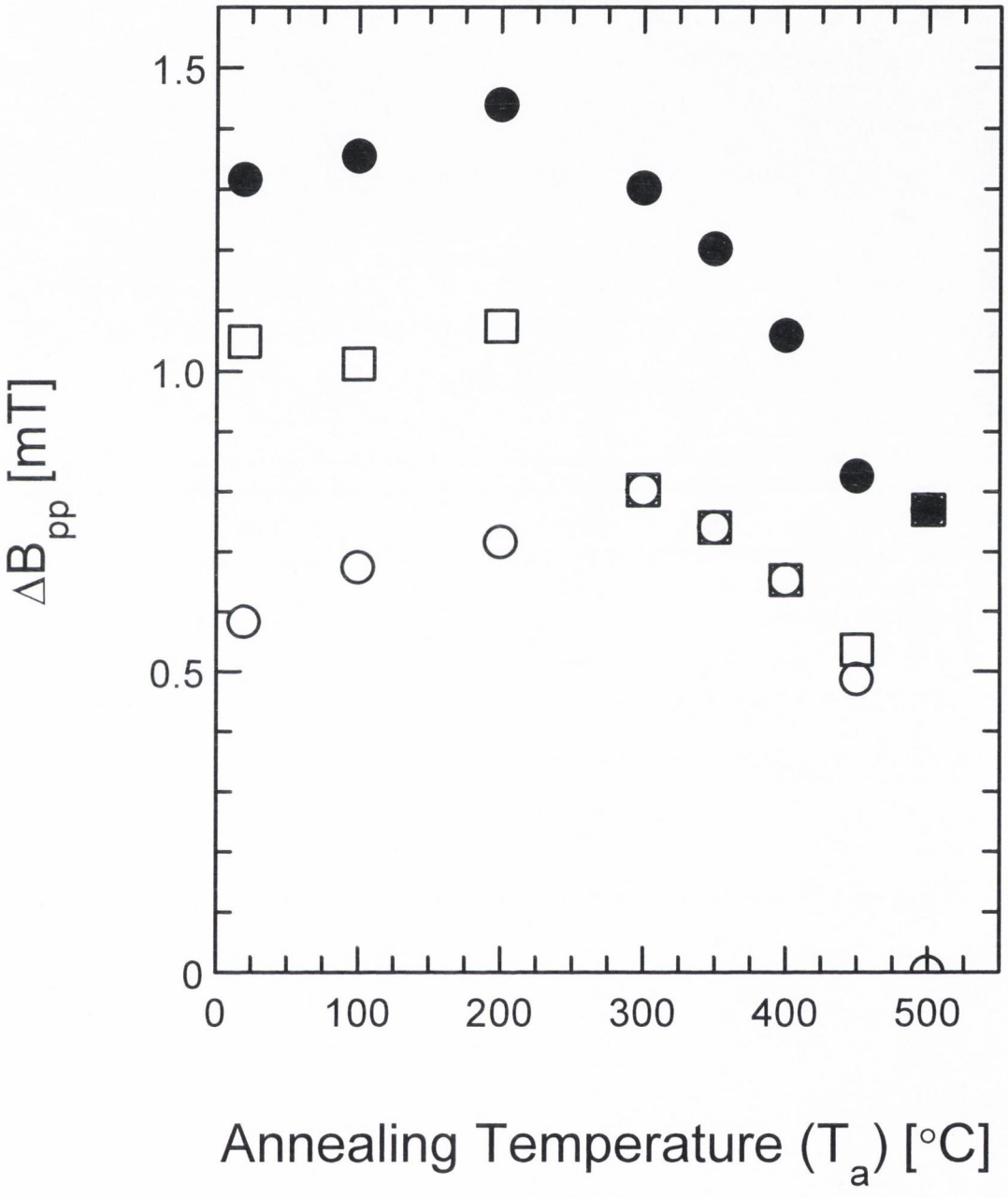

Figure 4.17 : Voigt parameters for a-C:H deposited with V_b=100V as a function of T_a.

□ : ${}^{L}\Delta B_{pp}$ *(Lorentzian conponent linewidth).*

O : ${}^{G}\Delta B_{pp}$ *(Gaussian conponent linewidth).*

● : ${}^{V}\Delta B_{pp}$ *(Total linewidth).*

Next we look at the behaviour of ${}^{L}\Delta B_{pp}$ as a function of T_a. The contribution due from dipolar broadening (in table 4.11, calculated from equation 4.14) falls with increasing T_a while ${}^{L}\Delta B_{pp}$ remained constant up to 200°C. Even still the values of ΔB_{pp} calculated from equation 4.14 do roughly match ${}^{L}\Delta B_{pp}$. It is reasonable to assume that both dipolar broadening and exchange interaction changed little in the film up to an annealing temperature of 200°C. ${}^{L}\Delta B_{pp}$ falls with increasing T_a, for $T_a >$ 200°C. This fall may be due to the decreasing contribution to the linewidth from the dipolar interaction, which falls with increasing T_a (table 4.11). It may also be due to increasing exchange interaction (caused by increasing delocalisation) because of an increase in sp^2 content of the film. The increase in ${}^{L}\Delta B_{pp}$ at 500°C may be caused by the interaction of the π-electrons with conduction electrons. The above interpretations of the changes found in the Voigt parameters as a function of T_a are rather speculative.

4.4.2 Discussion of the effect of annealing on a-C:H as a function of V_b.

In figures 4.12, 4.13, 4.14 and 4.15 we can see that the g_0-value remains constant with increasing annealing temperature (T_a). This indicates that the source of the paramagnetic defects present in the all these a-C:H films remained unchanged by annealing. As the g_0-values remained ≈2.0027 we believe that the defects arise from unpaired π-electrons on carbon atoms. As mentioned previously it is believed (Robertson 1986, p. 361; Robertson and O'Reilly 1987) that these unpaired π-electrons in the a-C:H films reside in aromatic clusters which contain an odd number of fused benzene ring units (a minimum of three) or on linear polymer chains of conjugated double bonds (containing an odd number of carbon atoms). Robertson (1996) modified this theory, stating that clustering is limited to very few aromatic six-fold sp^2 rings (analogous to benzene) and short polymer chains of conjugated double bonds (olefinic) (See figure 4.7).

We shall now look at the change in the spin concentration (N_V) and linewidth (ΔB_{pp}) as a function of increasing annealing temperature (T_a). The variation of N_V for polymeric a-C:H has already been dealt with in chapter 3. In figures 4.12 and 4.13 the values of N_V for the two samples P5 and P2 (V_b=50 and 100V) show a very similar trend, in that N_V falls at about 200°C with increasing T_a but increases slightly with

increasing T_a around 500 to 600°C before falling again. For sample P2 with V_b=100V ΔB_{pp} increases above 500°C.

González-Hernández et al. (1988) reported a similar behaviour in N_V when annealing a-C:H grown by RF glow-discharge as did Orzeszko et al. (1984) for annealing a-C:H grown by arc deposition in a low pressure hydrogen atmosphere. Austen et al. (1957) also found a reasonably similar behaviour when carbonising organic materials. Miller and McKenzie (1983) found a similar trend in ΔB_{pp}, for a-C:H grown by D.C. glow-discharge, to that we found for our sample grown with V_b=100V (P2) as does González-Hernández et al. (1988) for their a-C:H sample.

The initial fall in N_V in our samples (V_b = 50 and 100V) with increasing T_a up to T_a ≈450°C may be due to the reconstruction of less stable defect sites (González-Hernández et al. 1988), a decrease in the disorder of the films (Conway et al. 1998), which is basically the same process, or the thermal activation of weakly bound hydrogen which diffuses and bonds with unpaired electrons at defect sites (González-Hernández et al. 1988; Conway et al. 1998). Such passivation of the unpaired electrons via thermal activation of hydrogen may occur the in the following manner (taken from Conway et al. 1998).

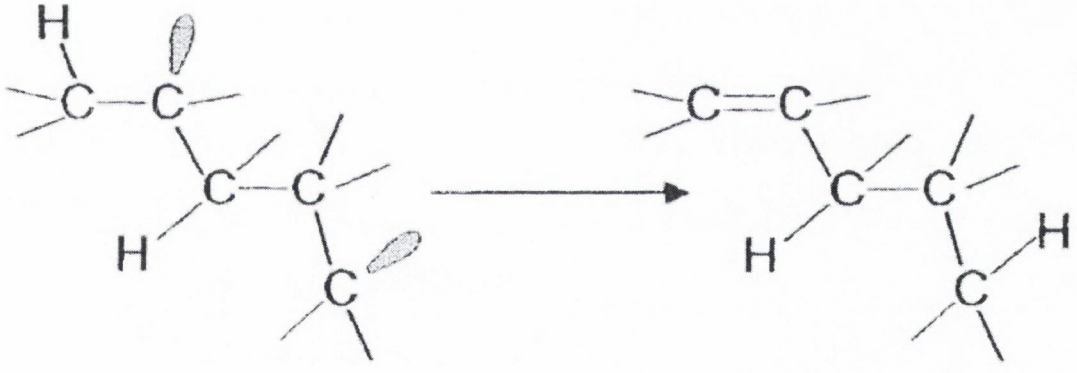

The passivation of the unpaired electrons by thermal activation of hydrogen is certainly reasonable due to the initial high hydrogen content of these films compared to those produced with V_b >100V. The decrease in ΔB_{pp} with increasing T_a in the temperature range 200°C to 500°C for these two samples is most likely due to an increase in sp^2 content which allows increased exchange narrowing of the line (Weiler et al. 1996) together possibly with the reduction of dipolar broadening due to the reduction of the number of spins present. The increase in N_V with increasing

annealing temperature for T_a in the range of 450 to 600°C is likely to have been due to the loss of hydrogen, which breaks C-H bonds, leaving behind unpaired π-electrons. This agrees with the measurements of the effusion of hydrogen and small hydrocarbons (e.g. methane etc.) reported to evolve from DLC (Malhotra and Kumar 1997) and from a-C:H (Kon'kov et al. 1997) mostly for temperatures >400°C. Above 600 and 500°C the spin concentration (N_V) falls rapidly for our samples with V_b = 50 and 100V respectively (figures 4.12 and 4.13). This final fall in N_V is most likely due to the onset of graphitization due to the increasing sp^2 content of the films at these high annealing temperatures (Bounouh et al. 1995). Basically the film turns slowly into graphite above this temperature and this rearrangement removes the unpaired electrons. Sadki et al. (1996), Austen et al. (1958) and Miller and McKenzie (1983) believed the same when explaining this fall in N_V values at high annealing temperatures (T_a) for their samples. For sample P2 (V_b = 100V) ΔB_{pp} increases with T_a for temperatures above 500°C. If the linewidth in this region is dependent upon dipolar broadening or exchange narrowing then the linewidth should continue to fall with increasing T_a as N_V falls (reducing the dipolar broadening) and the sp^2 content increases, i.e. increasing the delocalisation of the unpaired electrons (Fink et al. 1984) thus increasing exchange narrowing. We do not observe this. One explanation for this increase in ΔB_{pp} is that the increasing conductivity with increasing sp^2 content (i.e. increasing T_a) allows interaction between conduction electrons and the unpaired π-electrons. Miller and McKenzie (1983) and Austen et al. (1958) believed this to be the case in the samples they annealed. Austen et al. (1958) believed that this interaction would allow the unpaired electrons to lose their spin energy more efficiently to the lattice, i.e. the this shortens the spin-lattice relaxation time (T_1) and shortens the spin-spin relaxation time (T_2) which would broaden the linewidth (ΔB_{pp}).

Next we shall look at the effect annealing had on the more graphite-like a-C:H films.

In figures 4.14 and 4.15 we can see that the dependence of both N_V and ΔB_{pp} on annealing temperature for the more graphite-like a-C:H (GLHC) samples DC160 and DC182 (V_b = 400 and 540V) is different to that of the previous two samples (V_b = 50 and 100V). N_V and ΔB_{pp} for these samples remains roughly constant until ≈400°C. In comparison these parameters fall for the more diamond like a-C:H (DLC) samples

grown with V_b=50 and 100V. Due to the high sp^2 content of these two films (V_b=400 and 540V), which is ≈90% (table 4.1), there may be less unstable defect sites. So a fall in N_V due to the reconstruction of less stable defect sites is less likely. Also because these films contain less hydrogen (table 4.1) a fall in N_V due to the thermal activation of hydrogen is less probable. Disorder in the films may also be lower, so a fall in N_V due a decrease in the disorder of the films is also less likely, than for the DLC samples (V_b=50 and 100V). The final possibility that N_V (T_a <400°C) falls due to weakly bound hydrogen being thermally activated and bonding with unpaired electrons is also less probable. This is because of the reduced hydrogen content (<13at.%) of these films and because more of the hydrogen is bonded at sp^2 sites which is more stable than hydrogen bonded at sp^3 sites (R. W·chter and A. Cordery, personal communication). As ΔB_{pp} and the sp^2 content can depend upon each other (Weiler et al. 1996), the sp^2 content is unlikely to change with increasing annealing temperature for T_a ≤400°C because ΔB_{pp} does not change. We observe no increase in N_V, due to hydrogen loss, in the temperature range of 450 to 600°C. However it in this range the N_V values are already greater or equal to the corresponding values for the DLC samples (V_b = 50 and 100V). Another possibility is that this increase is much smaller than previously because of the much lower hydrogen content in these films (<13at.%). Above ≈400°C, N_V falls with increasing annealing temperature while ΔB_{pp} increases for these samples (V_b=400 and 540V). This fall in N_V can be explained in the same manner as that seen in the DLC films (V_b = 50 and 100V). That is to say the fall in N_V is most likely due to the onset of graphitization due to the increasing sp^2 content of the films at these high annealing temperatures. This produces more ordered films with less defects. The increase in ΔB_{pp} with increasing T_a (for T_a >400°C) can be explained in the same way as before, i.e. that there may be an interaction between conduction electrons and the unpaired π-electrons that shortens the spin-spin relaxation time (T_2), i.e. broadens ΔB_{pp}, and shortens the spin-lattice relaxation time (T_1)

In order to examine if this indeed is the case in for a-C:H films, we measured T_1 and T_2 as a function of T_a for the film DC160 (V_b=400V).

4.4.3 Measurement of T_1 and T_2 as a function of T_a.

In this section we examine how the relaxation times (T_1 and T_2) change with annealing temperature for the a-C:H film DC160 (V_b = 400V). Figure 4.18 dispalys the saturation behaviour of this film at room temperature and 450°C. We can see in this figure that for T_a=450°C (□) h_{pp} reaches a maximum at the lower B_1 than than when the film is annealed at T_a=20°C (O). This indicates that T_1T_2 value for film at T_a=450°C (O) is greater than for the film at T_a=20°C (□).

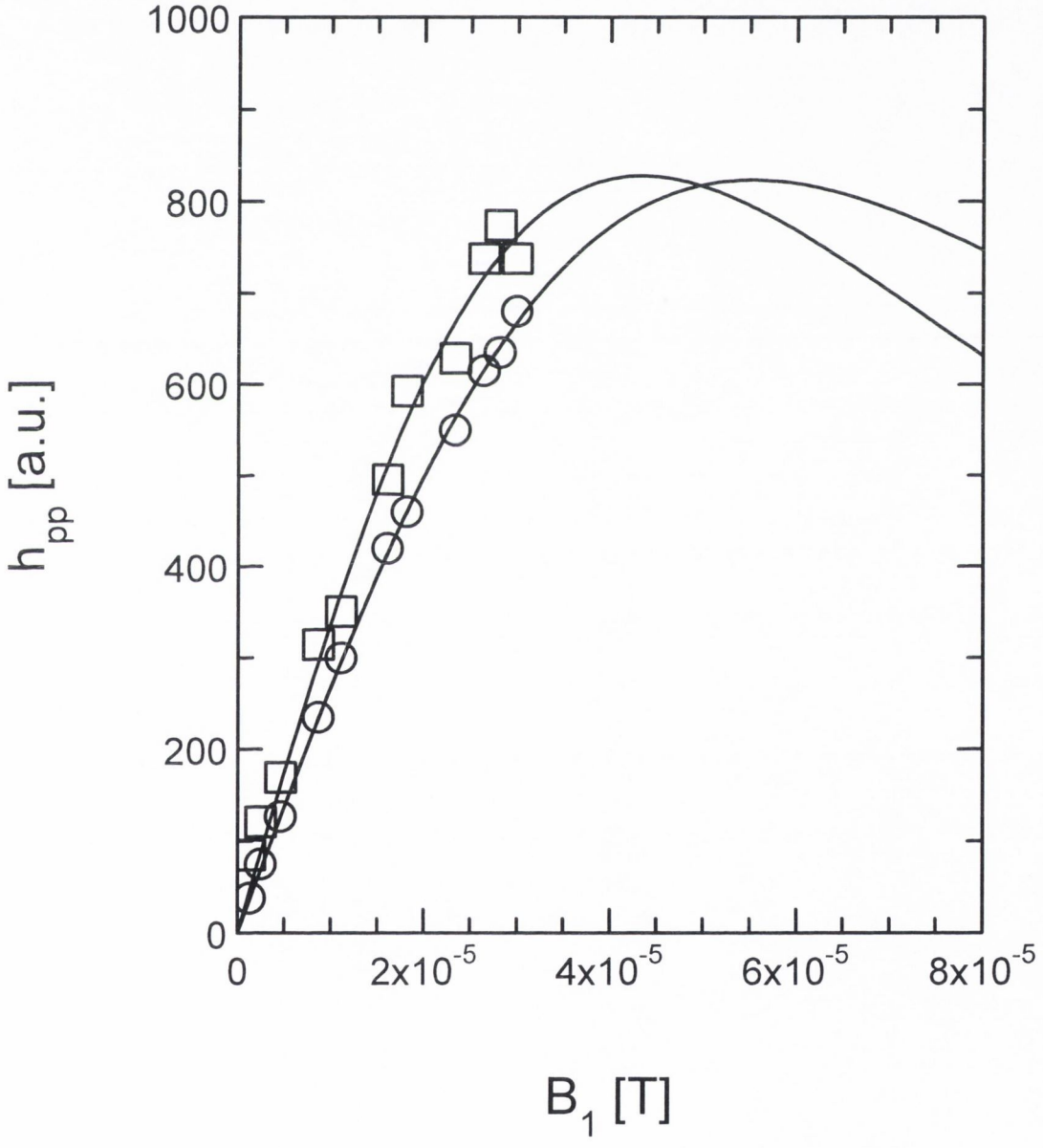

Figure 4.18 : Saturation behaviour of a-C:H with V_b=400V.

O : *a-C:H film annealed at T_a=20°C (T_1T_2=5.4×10^{-15}s^2)*

□ : *a-C:H film annealed at T_a=450°C (T_1T_2=9.0×10^{-15}s^2)*

Table 4.12 lists the spin-spin relaxation time (T_2) and the spin-lattice relaxation time (T_1) for DC160 as a function of annealing temperature (T_a). The equations and method which we use in determining both T_1 and T_2 were dealt with in chapter 2.

Annealing Temperature (T_a)[°C]	T_2 [10^{-8}s]	$T_1 \times T_2$ [$10^{-15}s^2$]	T_1 [10^{-6}s]	τ_c[10^{-10}s]
20	1.82	5.4	0.30	0.93
100	1.86	5.9	0.32	0.95
200	1.78	5.7	0.32	0.98
300	1.65	6.0	0.36	1.08
350	1.65	6.8	0.41	1.15
400	1.62	5.7	0.35	1.08
450	0.90	9.0	1.00	2.42
500	0.95	10.6	1.12	2.50
550	0.95	18.5	1.94	3.29
600	N/A	N/A	N/A	N/A
700	N/A	N/A	N/A	N/A

Table 4.12 : T_1, T_2 and τ_c as a function of T_a for a-C:H film DC160 (V_b=400V).

Figure 4.19 shows how T_1 and T_2 change with increasing annealing temperature. We can see in this figure that T_1 and T_2 remains unchanged up T_a=400°C, above which T_1 increases and T_2 decreases. The lack of change in both T_1 and T_2 below 400°C indicates that the sp^2 content of the film (V_b=400V) does not change greatly for $T_a \leq 400$°C because we see no increase in exchange interaction. Above 400°C T_1 increases while T_2 decreases with increasing T_a.

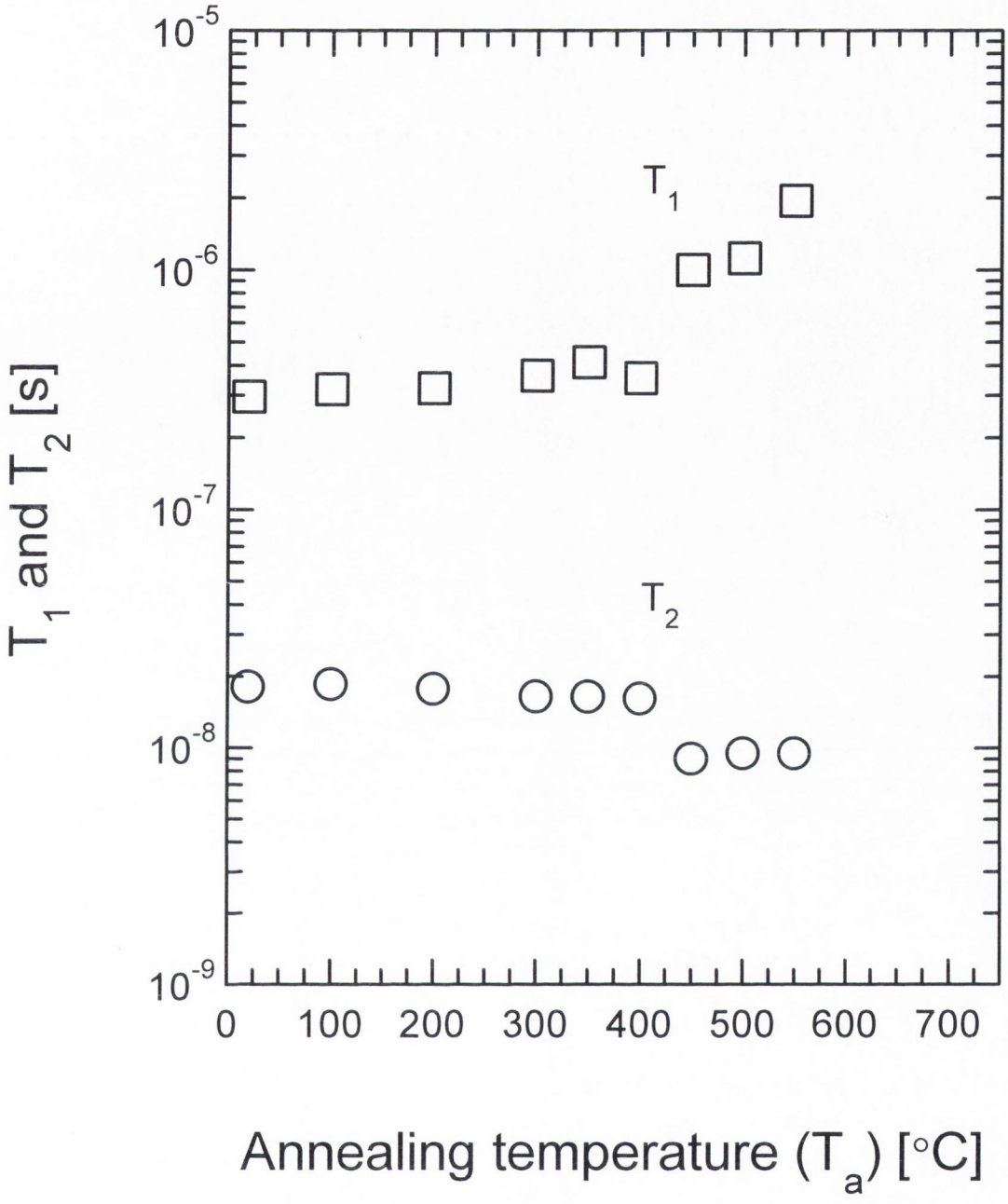

Figure 4.19 : T_1 and T_2 for DC160 (V_b=400V) as a function of T_a.

□ *: T_1 as a function of T_a (table 4.12).*

O *: T_2 as a function of T_a (table 4.12).*

In order to examine if our T_1 and T_2 measurements behave it the manner predicted by equations 4.10 and 4.11 respectively, as $\omega_p<\omega_c<\omega_o$, we plot T_1 and T_2 against the correlation time (τ_c) in figure 4.20.

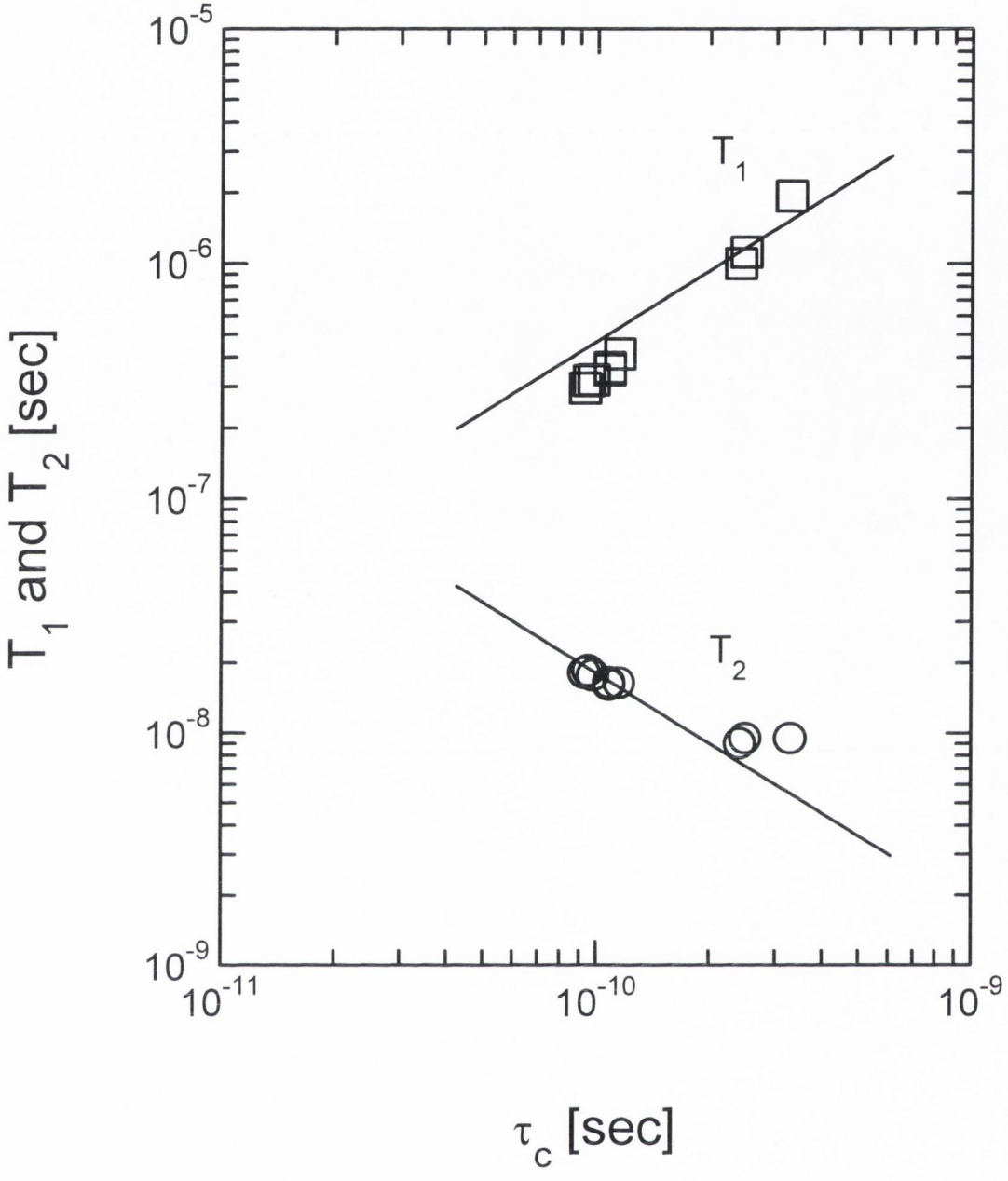

Figure 4.20 : T_1 and T_2 for DC160 (V_b=400V) as a function of τ_c.

In this figure (4.20) the solid lines are the fits for T_1 and T_2 using equations 4.10 and 4.11. We see that these equations can be applied to our T_1 and T_2 values for this film (V_b = 400V). These two lines give estimates of ω_p equal to 6.3×10^8rad s^{-1} and 7.4×10^8rad s^{-1} using equations 4.10 and 4.11 respectively. Therefore ω_p is $\approx6.9\times10^8$rad s^{-1} for our a-C:H film with V_b=400V, based upon the T_1 and T_2 values as a function of T_a. Since we don't believe that exchange interaction is decreasing with increasing T_a, for T_a>400°C it is unclear why T_1 and T_2 behave in this manner.

The increase in ΔB_{pp} (in figure 4.14) with increasing T_a (for T_a >400°C) we previously explained as due to interaction between conduction electrons and the unpaired π-electrons which broadens ΔB_{pp} (Miller and McKenzie 1983; Austen et al. 1958). But Austen et al. (1958) states that the interaction between conduction electrons and unpaired π-electrons allows the energy of the spins to be lost more efficiently to the lattice, i.e. that the spin-lattice relaxation time (T_1) would shorten. As can be seen in figure 4.19 our result are contrary to this, in that T_1 increases with increasing T_a for temperatures above 400°C when it is believed that the unpaired electrons are interacting with conduction electrons in the film. Therefore it is unclear from our results if indeed this interaction between the unpaired electrons and the conduction electrons is taking place.

4.5 Conclusions of annealing a-C:H films as a function of V_b.

We annealed a range of a-C:H film whose structures ranged from diamond like carbon (DLC) to graphite like hydrogenated carbon (GLHC) by selecting a-C:H films grown with different negative self-bias voltages (V_b). We found that annealing a-C:H had different effects which depended upon the initial structure if the film. The DLC film and the film in the transition region from DLC to GLHC (V_b=50 and 100V) show initially a reduction in the number of unpaired spins (N_V), which may be due to the passivation of unpaired spins by hydrogen. Another possibly is that the film became more ordered which removes the π-unpaired electrons. For the films with a more GLHC character (V_b=400 and 540V), i.e. higher sp^2 and low hydrogen content this initial drop in N_V is not observed probably because of the lower hydrogen content or because the film is already more ordered because it contains a higher content of sp^2 bonding.

For 400°C<T_a<600°C the DLC film (V_b=50V) shows an increase in its spin concentration (N_V) with increasing T_a. This is most likely due to the loss of hydrogen from this film. The film in the transition region from DLC to GLHC (V_b=100V) also shows an increase in its spin concentration (N_V) with increasing T_a but it is less dramatic, probably due to the lower hydrogen content of this film compared to the DLC film. The films with a greater GLHC character (V_b=400 and 540V), show no increase in N_V with increasing T_a, in the range of temperatures 400°C to 600°C. This may be due to the fact that in the hydrogen content is already low in these films before annealing. Finally for all the films N_V falls with increasing T_a, for T_a>600°C, presumably due to the onset of graphitization and the reduction of defects within the structure of the films.

The DLC (V_b=50V) film and the film in the transition region from DLC to GLHC (V_b=100V) show a fall in ΔB_{pp} with increasing T_a, for 200°C<T_a≤500°C. This fall is not observed in our other two films (V_b=400 and 540V). The most likely explanation is that, for the first two films (V_b=50 and 100V) with initially a low sp^2 content, the sp^2 content in these films increases with increasing T_a. This increase in the sp^2 content within these films allows the unpaired electrons to become more delocalised and increasing the exchange narrowing of ΔB_{pp}. The last two films (V_b=400 and 540V) display no change in ΔB_{pp} with increasing T_a, for $T_a \leq$ 400°C.

This lack of change indicates that the sp^2 content in these films remains constant up to 400°C; this is reasonable because these films started initially with a much higher sp^2 content than the previous two films (V_b=50 and 100V).

For three of these films (V_b=100, 400 and 540V) ΔB_{pp} increased with increasing annealing temperature (T_a) when T_a was raised above ≈500°C. This may be due to an increased interaction between the unpaired π-electrons and conduction electrons due to the onset of graphitization. However measurements made of the T_1 (spin-lattice) and T_2 (spin-spin) relaxation times as a function of T_a for the GLHC film (V_b = 400V) suggest that T_1 increases while T_2 decreases with increasing T_a. This differs with the suggestion by Austen et al. (1958) that T_1 shortens with increasing T_a ,for T_a >550°C when carbonising sugars and coal. We found that the annealing behaviour of the a-C:H depends strongly upon the initial structure of the a-C:H film.

4.6 References

Abragam, A. (1996). Principles of Nuclear Magnetism, p. 126. Clarendon press, Oxford.

Austen, D. E. G., Ingram, D. J. E. and Tapley J. G. (1958). Transactions of The Faraday Society, **54**, 400.

Bounouh, Y., Th⬟ye, M. L. Dehbi-Alaoui, A., Matthews, A. and Stoquert, J. P. (1995). Physical Review B, **51**, 9597.

Carrington, A. and McLachlan. (1967). Introduction to Magnetic Resonance. Harper and Row, New York.

Chhowalla, M., Robertson, J., Chen, C. W., Silva, S. R. P., Davis, C. A. and Amaratunga, G. A. J. (1997). Journal of Applied Physics, **81**, 139.

Conway, N. M. J., Ilie, A., Robertson, J., Milne, W. I. And Tagliaferro, A. (1998). Applied Physics Letters, **73**, 2456

Dawson, J. C. and Adkins, C. J. (1995). Journal of Physics: Condensed Matter, **7**, 6297.

Fink, J., M✧ller-Heinzerling, Th., Pfl✧ger, J., Scheerer, B., Dischler, B., Koidl, P., Bubenzer, A. and Sah, R. E. (1984). Physical Review B, **30**, 4713.

Giorgis, F., Tagliaferro, A. and Fanciulli, M. (1998).In Amorphous Carbon: State Of The Art, (ed. S. R. P. Silva, J. Robertson, W. I. Milne and G. A. J. Amaratunga), p. 143.World Scientific, Singapore.

Goldsborough, J. P., Mandel, M. and Pake, G.E. (1960). Physical Review Letters, **4**, 13.González-Hernández, J., Asomoza, R. and Reyes-Mena, A. (1988). Solid State Communications, **67**, 1085.

Hoinkis, M. Tober, E. D., White, R. L. and Crowder, M. S. (1992). Applied Physics Letters, **61**, 2653.

Ilie, A. Conway, N. M. J., Kleinsorge, B., Robertson, J. and Milne, W. I. (1998). Journal of Applied Physics, **84**, 5575.

Kleber, R., Jung, K., Ehrhardt, H., M✦hling, I., Breuer, K., Metz, H. and Engelke, F. (1991). This Solid Films, **205**, 274.

Kon'kov, O. I., Kapitonov, I. N., Trapenznikova, I. N. and Terukov, E. I. (1997). Technical Physics Letters, **23**, 9.

Malhotra, M. and Kumar, S. (1997). Diamond and Related Materials, **6**, 1830.

McClintock, I. S. and Orr, J. C. (1968). Physica Status Solidi, **29**, K157.

Miller, D. J. and McKenzie, D. R. (1983). Thin Solid Films, **108**, 257.

Orzeszko, S., Bala, W., Fabisiak, K. and Rozploch F. (1984). Physica Status Solidi, **81**, 579.

Pastor, R. C. and Hoskins, R. H. (1960). Journal of Chemical Physics, **32**, 264.

Poole, C. P. (1983). Electron Spin Resonance, A Comprehensive Treatise On Experimental Techniques, (2nd edn). Wiley, New York.

Ristein, J., Sch·fer, J. and Ley, L. (1995). Diamond and Related Materials, **4**, 508.

Robertson, J and O'Reilly, E. P. (1987). Physical Review B, **35**, 2946.

Robertson, J. (1986). Advances in Physics, **35**, 317.

Robertson, J. (1996). Journal of Non-Crystalline Solids, **198-200**, 615.

Robertson, J. (1998). In Amorphous Carbon: State Of The Art, (ed. S. R. P. Silva, J. Robertson, W. I. Milne and G. A. J. Amaratunga), p. 32. World Scientific, Singapore.

Sadki, A., Bounouh, Y., Theye, M. L., Von Bardeleben, J., Cernogora, J. and Fave, J. L. (1996).Diamond and Related Materials, **5**, 439.

Sattel, S., Robertson, J. and Ehrhardt, H. (1997). Journal of Applied Physics, **82**, 4566.

Sch✧tte, S., Will, S., Mell, H. and Fuhs, W. (1993). Diamond and Related Materials, **2**, 1360.

Seidel, H. and Wolf, H. C. (1968). Physics of Color Centers, (ed. W. Fowler), p. 557. Academic press, New York.

Silva, S. R. P., Robertson, J., Rusli, Amaratunga, G. A. J. and Schwan, J. (1996). Philosophical Magazine B, **74**, 369.

Slichter, C. P. (1992). Principles of Magnetic Resonance, Springer-Verlag, Berlin.

Stoneham, A. M. (1972). Journal of Physics D: Applied Physics, **5**, 670.

Sullivan, J. P. and Friedmann, T. A. (1998). In Amorphous Carbon: State Of The Art, (ed. S. R. P. Silva, J. Robertson, W. I. Milne and G. A. J. Amaratunga), p. 281. World Scientific, Singapore.

Tamor, M. A., Vassell, W. C. and Carduner, K. R. (1991). Applied Physics Letters, **58**, 592.

Tsai, H. and Bogy, D. B. (1987). Journal of Vacuum Science Technology A, **5**, 3287.

Weiler, M., Sattel, Giessen, T. S., Jung, K., Ehrhardt, H., Veerasamy, V. S. and Robertson, J. (1996). Physical Review B, **53,** 1594.

Weinberger, B. R., Ehrefreund, E., Pron, A., Heeger, A. J. and MacDiarmid, A. G. (1980). Journal of Chemical Physics, **72**, 4749.

Wertz, J. E. and Bolton, J. R. (1972). Electron Spin Resonance: Elementary Theory and Practical Applications. McGraw-Hill, New York.

Chapter 5:

EPR study of nitrogenated diamond-like a-C:H

5.1 Introduction

Because of its high emission current, nitrogenated diamond a-C:H is a promising material for use as the cathode material in field-emission displays (Amaratunga and Silva 1996). In the semiconductor industry electronic doping of intrinsic semiconductor materials is very important. Because of this attempts have been made to dope a-C:H and ta-C films with nitrogen (Amir and Kalish 1991; Silva et al. 1997; Schwan et al. 1998; Veerasamy et al. 1993). Whether changes in conductivity, reported by the above groups caused by the addition of nitrogen originates from actual electronic doping or from changes in the structures of these films is still unknown. Therefore it is the aim the measurements reported in this chapter to identify the defects present in nitrogenated diamond-like a-C:H films grown by PECVD. We will examine the defects present using the technique of electron paramagnetic resonance (EPR).

We shall study the defects present in these diamond-like a-C:H,N films as a function of nitrogen content and annealing temperature. The results of the corresponding study of polymeric nitrogenated a-C:H films is given in chapter 3

5.2 Diamond-like a-C:H,N of variable nitrogen content

In this section of the chapter we examine what effect changing the amount of nitrogen present has on the defects present in diamond-like a-C:H,N films. We shall use the technique of electron paramagnetic resonance (EPR) to examine the paramagnetic defects present in a range of a-C:H,N films produced with different N contents. At low temperatures ,electrons from nitrogen in a doping configuration may remain at their nitrogen atoms; this would give rise to nitrogen dangling bond defects, such as those found by Hoinkis et al. (1991) in diamond-like a-C:H. Their presence would be evidence supporting the idea that doping is taking place. We shall record an EPR spectrum at low temperature (≈10K) to examine if nitrogen dangling bond defects are present in our a-C:H,N films.

5.2.1 Sample preparation.

In order to examine the effect of adding nitrogen we examine a set of nitrogenated diamond-like a-C:H films containing various amounts of nitrogen.

The samples used in this study, as in section 3.2.1, were produced in radio frequency (13.56MHz) driven plasma enhanced chemical vapour deposition reactor. The only difference being that for these samples the plasma is confined using a hollow cylindrical permanent Nd-B-Fe magnet, the details of the reactor are dealt with in chapter 2 (Silva et al. 1996; Silva et al. 1997). These samples were produced at the Engineering Department of the University of Cambridge by Dr. S. R. P. Silva. The preparation conditions for these films are listed below in table 5.1.

Name	N_2 flow rate [sccm]	Thickness [nm]	At.% of nitrogen (from Silva et al. 1997)	At.% of hydrogen (from Silva et al. 1997)
Mu3He	0	240	0	21
Mu3He0.5	0.5	220	3	20.8
Mu3He1.5	1.5	97	5.7	20.8
Mu3He2.5	2.5	95	7	20.6
Mu3He5	5	250	11	20.4
Mu3He10	10	430	14	13

Table 5.1 : Thickness, H and N content of nitrogenated a-C:H film produced with: Negative self bias-voltage (V_b) : 60V, Plasma gases: 5sccm CH_4 and 45sccm He, Pressure: 100mTorr, Substrate at room temperature.

The films produced with V_b=60V and magnetic confinement of the plasma are diamond like a-C:H films (DLC) (Weiler et al. 1996; Robertson 1993, 1994) with a low sp^2 and hydrogen content. The bias voltage in a PECVD reactor with magnetic confinement is lower, for ions with the same energy, than the V_b produced in a PECVD reactor without magnetic confinement, i.e. V_b=60V with magnetic confinement might be equivalent to V_b ~100V without magnetic confinement.

For our a-C:H films grown by PECVD without magnetic confinement we reported ,in chapter 4, for sample P5 and P2 the following

Sample P5: V_b(without confinement)=50V, $N_V=4.91\times10^{19}cm^{-3}$, ΔB_{pp}=1.42mT, 63% sp^2 content and 25 at.% H

Sample P2: V_b(without confinement)=100V, $N_V=1.5\times10^{20}cm^{-3}$, ΔB_{pp}=1.23mT, 54% sp^2 content and 13 at.% H

These films are close to DLC.

As mentioned earlier films produced with V_b=60V and magnetic confinement may be similar to those grown with $V_b\approx$100V without magnetic confinement. Therefore, based upon this and the hydrogen content (21at.%) of our a-C:H film containing no nitrogen (table 5.1), it is reasonable to assume that the Mu3He is DLC and contains ≈60% sp^2 bonded carbon.

5.2.2 EPR measurements of a-C:H,N

Figure 5.1 shows some of the spectra for ours a-C:H,N films as a function of nitrogen content. We can see that the linewidth (ΔB_{pp}) remains roughly constant with increasing nitrogen for the a-C:H,N films. The spin concentration (N_V) shows a dramatic fall with increasing nitrogen content unlike the case of adding nitrogen to polymeric a-C:H films which we discussed in chapter 3

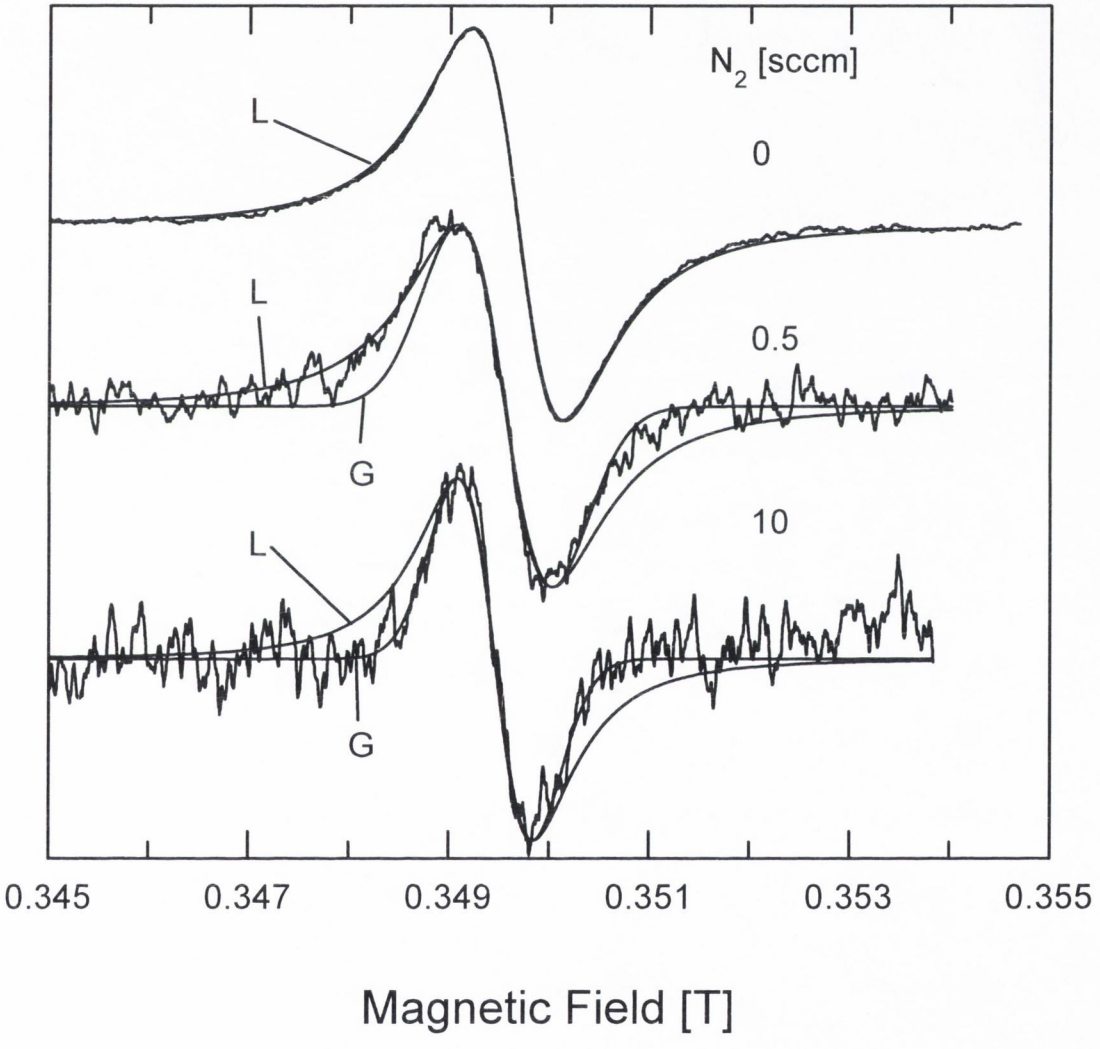

Figure 5.1 (ν = 9.8GHz) : EPR spectra for a-C:H,N as a function of nitrogen content with fits superimposed.

Figure 5.2 shows how the cross-over g_0-value, the linewidth (ΔB_{pp}) and the spin concentration (N_V) varies with the N_2 flow rate used during deposition of the a-C:H,N films. Initially changing the amount of nitrogen in the a-C:H films from 0at.%

to 3at.% (i.e. from 0 to 0.5sccm N_2) causes g_0 to jump from ≈2.0025 to ≈2.0031; a further increase in the nitrogen content has little effect upon the g_0-value which remains at ≈2.0032 up to 14at%. nitrogen (a flow rate of 10sccm N_2). The linewidth (ΔB_{pp}) remains roughly constant with increasing nitrogen for the a-C:H,N films. There may been a small decrease from ≈1mT to ≈0.8mT but it is impossible to be sure due to the noise in the spectra. Figure 5.2 N_V falls from $\approx 6\times10^{19}cm^{-3}$ to $\approx 1.5\times10^{18}cm^{-3}$ when the nitrogen flow rate increases from 0 (0at.% N) to 10sccm (14at.% N).

Figure 5.1 also displays fits superimposed upon these spectra, 'L' denotes a Lorentzian fit and 'G' a Gaussian. We can see in this figure that the lineshape of the N free a-C:H is very close to a Lorentzian. The lineshape remains symmetrical with increasing nitrogen content. The lineshape is somewhere between that of a Lorentzian and a Gaussian when nitrogen is added to the a-C:H films. The lineshape is very close to a Gaussian for the a-C:H,N films with the highest nitrogen content (N_2 flow rate 10sccm).

It may be possible at low temperatures to observe unpaired electrons at nitrogen atoms, i.e. a nitrogen dangling bond. As this may cause unpaired electrons to remain at nitrogen sites and not be ionised by thermal energy. Our a-C:H,N films (table 5.1) are deposited upon n-type Si substrate which will yield a signal from the donors in the substrate when the temperature is lowered down to ≈10K. Therefore an EPR spectrum was recorded for an a-C:H,N film grown without magnetic confinement deposited upon a p-type Si substrate with a flow rate of 1sccm nitrogen at a temperature of ≈10K. One nitrogen centre in diamond films grown microwave-assisted CVD (chemical vapour deposition) has g=2.0023 with two hyperfine lines ≈3mT (for a spectrum collected at 9.75GHz) each side of the central line due to splitting caused by nuclear spin of the nitrogen nucleus (Hoinkins et al. 1991). We found no sign of that this centre in our a-C:H,N film.

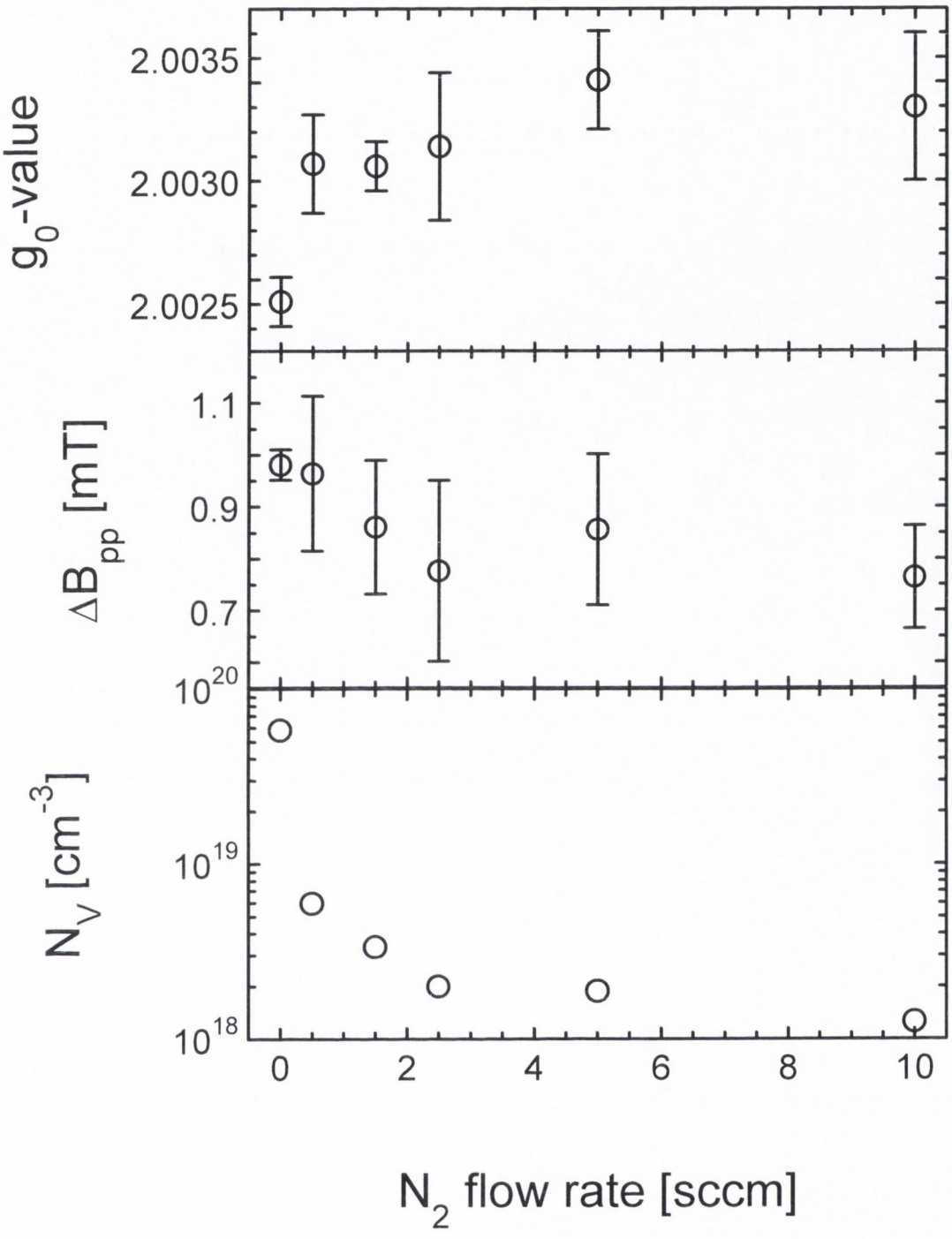

Figure 5.2 : EPR data for our a-C:H,N films as a function of nitrogen flow rate.

5.2.3 Discussion

We will begin our discussion of the effect on the defects of the addition of nitrogen by comparing our results with the results reported by others.

Lin et al. (1991) report an EPR signal with g_0=2.0028 and $\Delta B_{pp}\approx$1mT for a-C:H,N grown by PECVD with CH_4 and N_2 plasma gases and g_0 = 2.0032 for a-C:H. We in fact find the opposite. Our cross over g_0-value increases from ≈2.0025 to ≈2.0032 when nitrogen is added to the film. N_V falls by a factor of ≈30 when nitrogen is added to the film and this is in rough agreement with the results found by Lin et al. (1991) and Viehland et al. (1991). Viehland et al. (1991) found g_0 = 2.0030 and ΔB_{pp} = 1.5mT for their high nitrogen content a-C:H,N film grown by PECVD with CH_4 and N_2 as the plasma gases. Our g_0-value of ≈2.0032 and $\Delta B_{pp}\approx$1mT for our diamond-like a-C:H,N films grown with magnetic confinement agrees very well these values.

We can see that there is a range of reported g_0-values. We cannot explain why Lin et al. (1991) find that g_0 decreases while we find it increases when nitrogen is added to these a-C:H films. However the changes in g_0 are small and this indicates that changes in the nature of the defects present in these a-C:H,N films are also small. We believe as do others (Lin et al. 1991; Viehland et al. 1991) that the paramagnetic defects present are associated with unpaired π-electrons on conjugated chains of carbon atoms; the conjugation of the double bonds is either olefinic or aromatic in nature. These defects are the same as those present in a-C:H although the nitrogen may change the surrounding environment.

We will now discuss how nitrogen may be incorporated into the a-C:H,N films. This may allow us to explain the fall in the spin concentration (N_V) when nitrogen is added to the a-C:H films. It is possible that nitrogen may be bonded in the a-C:H lattice with a variety of different configurations. Figure 5.3 (taken from Silva et al. 1997) shows some of these possible configurations. Nitrogen usually has three or five valence electrons. Electronic doping of the a-C:H,N film only occurs if the nitrogen enters the a-C:H film with four bonds and has a valency of five. This makes the fifth unpaired electron available for doping.

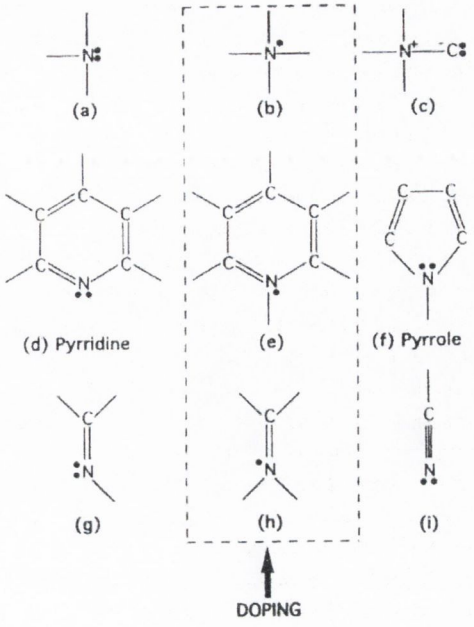

Figure 5.3 : Some bonding configurations of nitrogen in a-C:H,N.

(b), (e) and (h) of figure 5.3 show the configurations of nitrogen with four bonds which allow doping. The exception to this is (c) where nitrogen has four bonds but its excess electron is lost to a neighbouring carbon site which contains an unpaired electron and so doping does not take place. This is one possible explanation for the rapid drop in N_V we observed when nitrogen was added to a-C:H. More generally, any unpaired electrons on carbon atoms might combine with the doping electrons supplied by the nitrogen (figure 5.3 (b),(e) and (h)) and this would destroy the paramagnetic defects and reduce N_V. Some of the unpaired π-electrons on carbon atoms might be unable to combine with the doping electrons. This might occur if the carbon sites are physically separated from the doping electrons by sp^3 bonded regions, i.e. there was no path of conjugated sp^2 bonds between the unpaired and doping electrons. This would leave behind, after the addition of nitrogen, a residual spin concentration (N_V). This indeed appears to have be the case for our a-C:H,N films because N_V remained roughly constant for a nitrogen content of $\geq$7at.% (2.5sccm N_2). Silva et al. (1997) believe that 7at.% N is a crucial composition of their a-C:H,N films. They believe that at this nitrogen content, acceptor-like defects in the film are completely compensated by the N donor electrons, i.e. the a-C:H,N films begins as p-type material and becomes n-type with increasing N content. The transition between these two types of materials occurs at a composition of $\approx$7at.% N. Schwan et al. (1998) and Silva et al. (1997) found a maximum in the optical band gaps (E_{04} and

Tauc respectively) for their a-C:H,N films at 6 to 7at.% N. The idea of a critical composition is supported by the fact that N_V reached begins to level off at this composition and fall much slower as the nitrogen content is increased further. At higher N content it is supposed that the donor electrons contribute to the conductivity of the film (making the film n-type). Nitrogen is probably an inefficient dopant atom because as seen in figure 5.3 only a few configurations would allow doping. In our spectra collected at ≈10K we found no evidence that nitrogen atom with unpaired electrons are present in our a-C:H,N films. Such centres would correspond to doping configurations of (b), (e) and (h) in figure 5.3. The EPR measurements therefore provide no support to the idea that electronic doping by nitrogen does takes place in these films. Also Viehland et al. (1991) did not find this type of centre in their films and believed that the nitrogen dangling bond in a-C:H,N is below the top of the valence band and therefore contains a lone pair of electrons and is therefore not paramagnetic.

As already mentioned the lineshape for the a-C:H,N films is somewhere between that of a Lorentzian and a Gaussian but further analysis was made impractical due to the noise level of these spectra.

5.3 Annealing of a-C:H,N films

Annealing is important in the processing of semiconductor devices. Annealing is commonly used to remove damage and defects or to activate ions which may have been implanted (Sze 1985, p. 417). Other high temperature processes may also be used after deposition in the fabrication of devices. Therefore it is the aim of the measurements given in this section of the chapter to examine the effect of annealing on the defects present in a-C:H,N. In order to examine the effect annealing has over a range of a-C:H,N films, we chose to anneal films which have a range of nitrogen contents. We also study the effect annealing has on a control a-C:H film (Mu3He). We step anneal each sample in an Ar over-pressure for 10min at each annealing temperature. This process was described earlier in chapter 3. The EPR measurements are all at room temperature.

The films we annealed are Mu3He (0at.% N, 0sccm N_2), Mu3He0.5 (3at.% N, 0.5sccm N_2), Mu3He1.5 (5.7at.% N, 1.5sccm N_2) and Mu3He10 (14at.% N, 10sccm N_2).

5.3.1 EPR results of annealing diamond-like a-C:H

For clarity we shall break our results and discussion into two sections. The first deals with the a-C:H film (Mu3He) and the second with the a-C:H,N films.

In this section of the chapter we examine the EPR results of annealing our control a-C:H film, i.e. Mu3He (0at.% N, 0sccm N_2). We will also analyse the lineshape of the EPR spectra we record as a function of T_a.

Figures 5.4 shows some of the spectra and fits, as a function of annealing temperature (T_a), for sample Mu3He (a-C:H: 0at.% N, 0sccm N_2). As already noted in figure 5.1 the lineshape begins as a Lorentzian and it remains symmetrical with increasing annealing temperature (T_a). In the temperature range 300 to 400°C the lineshapes are somewhere between that of a Lorentzian and a Gaussian. We can see this in figure 5.4 for the spectrum for T_a=400°C. We see that the spectrum cannot be fitted by a single Gaussian (denoted by 'G') or a single Lorentzian (denoted by 'L'). As mentioned previously such a lineshape may be fitted by a Voigt profile or a superimposition of a Gaussian and a Lorentzian line. We see in figure 5.4 that these

two possible fits, (denoted by 'V' and 'L+G'), match the experimental spectrum very well. The lineshape becomes very close to a Lorentzian at T_a = 550°C. For T_a ≥600°C the line drops off more slowly in the wings than that of a Lorentzian.

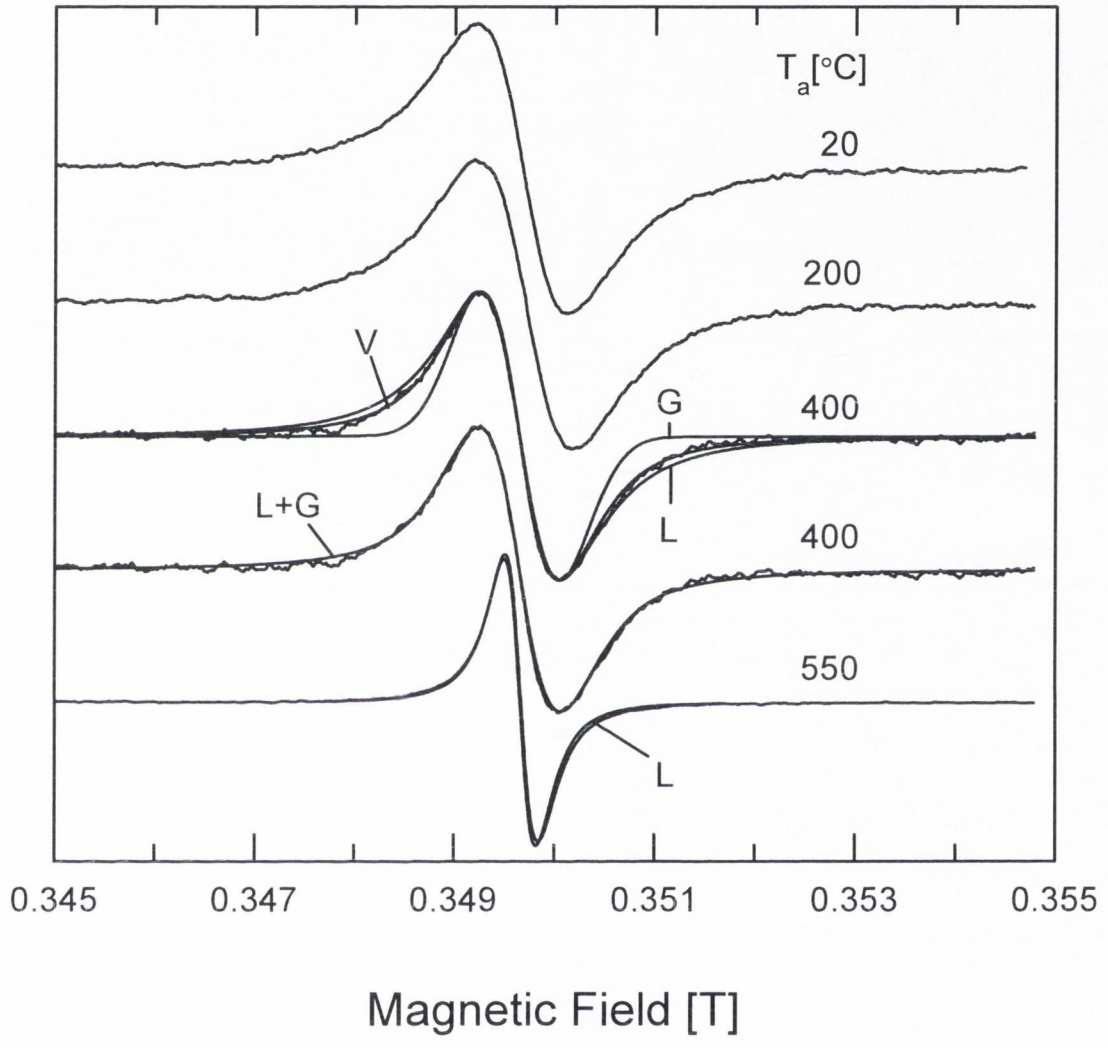

Figure 5.4 (ν = 9.8GHz) : EPR spectra and fits, as a function of T_a, for our control a-C:H film (Mu3He).

Figure 5.5 shows how the EPR parameters change with increasing T_a for this sample (a-C:H: 0at.% N, 0sccm N_2). As shown in this figure the g_0 value remains at ≈2.0025 over the entire range of annealing temperatures (T_a). The linewidth (ΔB_{pp}) remains constant at ≈1mT up to about 350°C, then it decreases with increasing T_a reaching a value of ≈0.33mT at T_a=550°C. Above this temperature ΔB_{pp} increases with increasing T_a until a temperature of 800°C is reached at which no signal is observed. The spin concentration (N_V) remains constant at $\approx 6\times10^{19}cm^{-3}$ until 200°C

is reached after which it falls to $\approx 2.5\times10^{19}cm^{-3}$ at T_a=450°C; above this temperature N_V rises to $\approx 6\times10^{19}cm^{-3}$ at 600°C. It again falls to less than $7\times10^{18}cm^{-3}$ when the sample is annealed at 800°C.

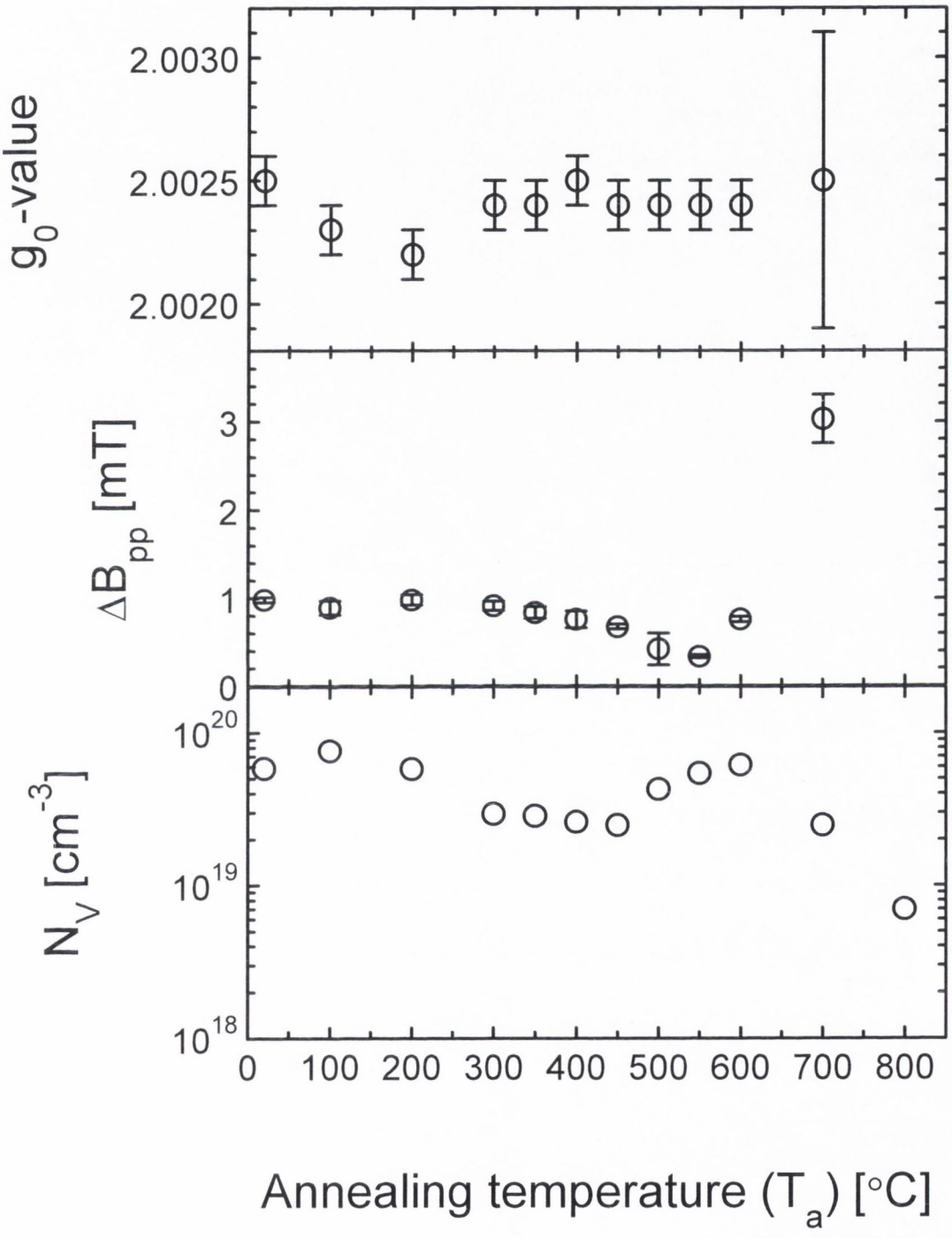

Figure 5.5 : EPR data for our control a-C:H film (Mu3He)as a function of T_a.

As mention earlier the lineshapes, particularly in the range of temperatures 300 to 400°C, are neither Gaussian or Lorentzian. We will now attempt to fit our spectra with either a Voigt or a two-line Gaussian and Lorentzian superposition.

First we shall deal with the possibility that the lineshape is a Voigt profile. We can determine parameters such as the width of the Lorentzian (${}^{L}\Delta B_{pp}$) component and the width of the Gaussian component (${}^{G}\Delta B_{pp}$) by fitting these spectra with Voigt profiles.

Figure 5.6 shows how these parameters change with increasing annealing temperature for this a-C:H film (Mu3He). For T_a<300°C the Lorentzian component (${}^{L}\Delta B_{pp}$) is wider than the Gaussian component (${}^{G}\Delta B_{pp}$) of the Voigt profile, i.e. the lineshape is predominately a Lorentzian. The ${}^{G}\Delta B_{pp}$ values for T_a<300°C may be as unreliable as ±0.25mT. The linewidth of the Lorentzian component (${}^{L}\Delta B_{pp}$) falls with increasing T_a while the Gaussian component (${}^{G}\Delta B_{pp}$) remains roughly constant from 300 to 450°C. Here we can easily see (figure 5.4) that the lineshape is between a Gaussian and Lorentzian. ${}^{G}\Delta B_{pp}$ falls for T_a>400°C. At 500°C ${}^{L}\Delta B_{pp}$ is much larger than ${}^{G}\Delta B_{pp}$ (this value has an error of ±0.1mT) as the lineshape becomes almost Lorentzian. Indeed the lineshape at 550°C is indistinguishable from a Lorentzian.

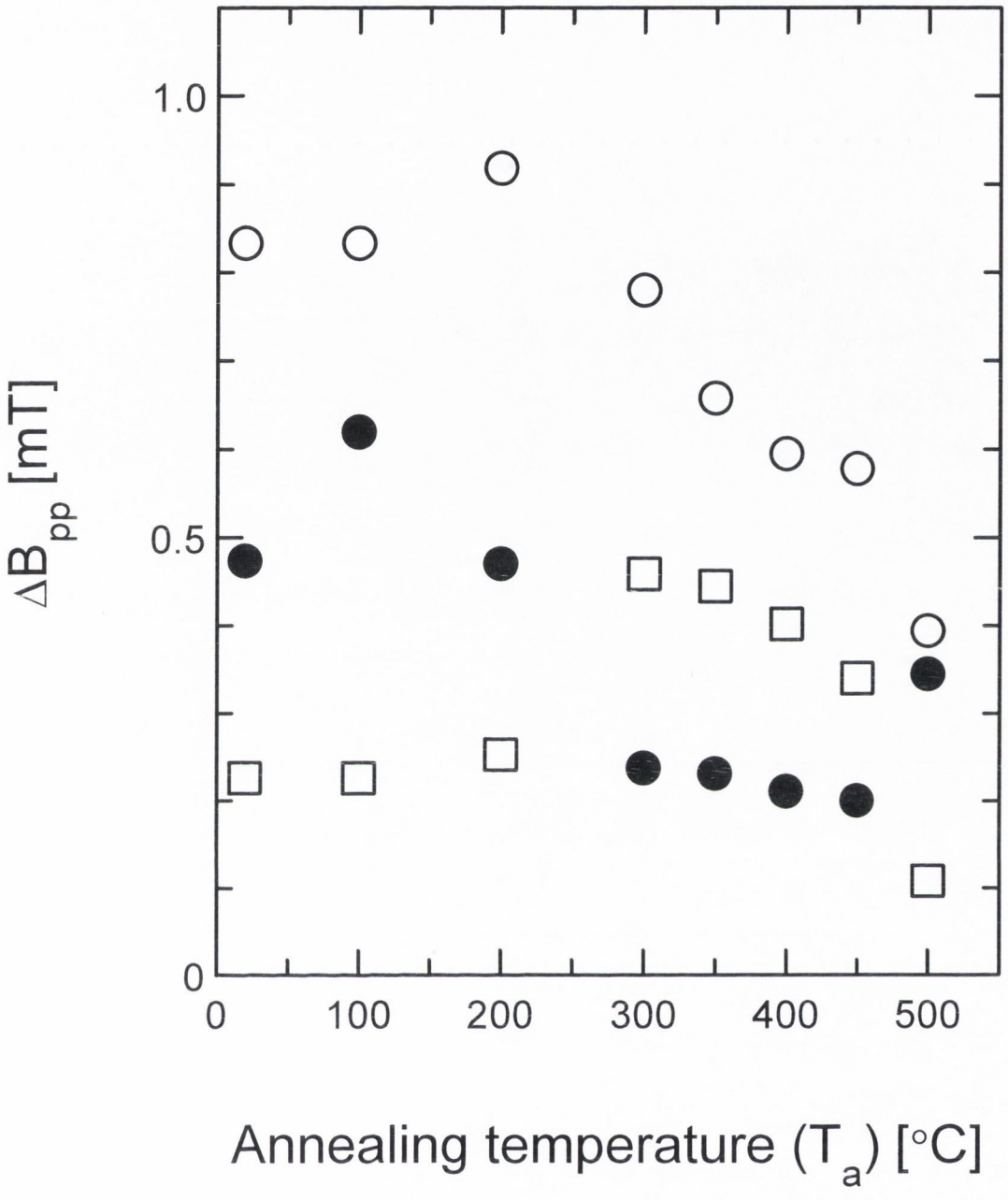

Figure 5.6 : Voigt parameters for a-C:H (Mu3He) as a function of T_a.

□ : ${}^{G}\Delta B_{pp}$.

O : ${}^{L}\Delta B_{pp}$.

● : ΔB_{pp} : *Calculated dipolar broadening (calculated from N_V and eq. 4.14).*

We will now deal with the other possibility, that the spectra are a superposition of a Gaussian and a Lorentzian. As already seen in figure 5.4 for T_a=400°C such a two-line fit is very close to the experimental spectrum. Table 5.2 lists the parameters we determine by fitting the lineshape with such a two-line fit as a function of T_a.

1^{st} lineshape = Lorentzian				2^{nd} lineshape = Gaussian		
Annealing temperature (T_a) [°C]	1^{st} g-value	1^{st} ΔB_{pp} [mT]	1^{st} N_V [$10^{19}cm^{-3}$]	2^{nd} g-value	2^{nd} ΔB_{pp} [mT]	2^{nd} N_V [$10^{19}cm^{-3}$]
20	2.0025	0.989	5.55	2.0025	1.00	0.28
100	2.0023	0.976	7.26	2.0023	0.989	0.37
200	2.0022	0.976	5.51	2.0022	0.989	0.28
300	2.0024	0.976	2.68	2.0024	0.989	0.25
350	2.0024	0.886	2.6	2.0024	0.886	0.25
400	2.0025	0.801	2.33	2.0025	0.886	0.27
450	2.0024	0.739	2.24	2.0024	0.764	0.23

Table 5.2 : Two-line fit parameters determined for the a-C:H (Mu3He) film as a function of T_a.

In table 5.2 the linewidth (ΔB_{pp}) of both the Lorentzian and Gaussian lines remain at ≈0.98mT until T_a = 300°C after which they both fall to ≈0.75mT for T_a=450°C. This does not follow the fall in the calculated dipolar broadening for T_a>100°C (figure 5.6). The g-values of both lines remain at ≈2.0024. Figure 5.7 shows how N_V varied for each line with increasing T_a. N_V for the Lorentzian line decreases with increasing T_a while N_V the Gaussian line remains approximately constant.

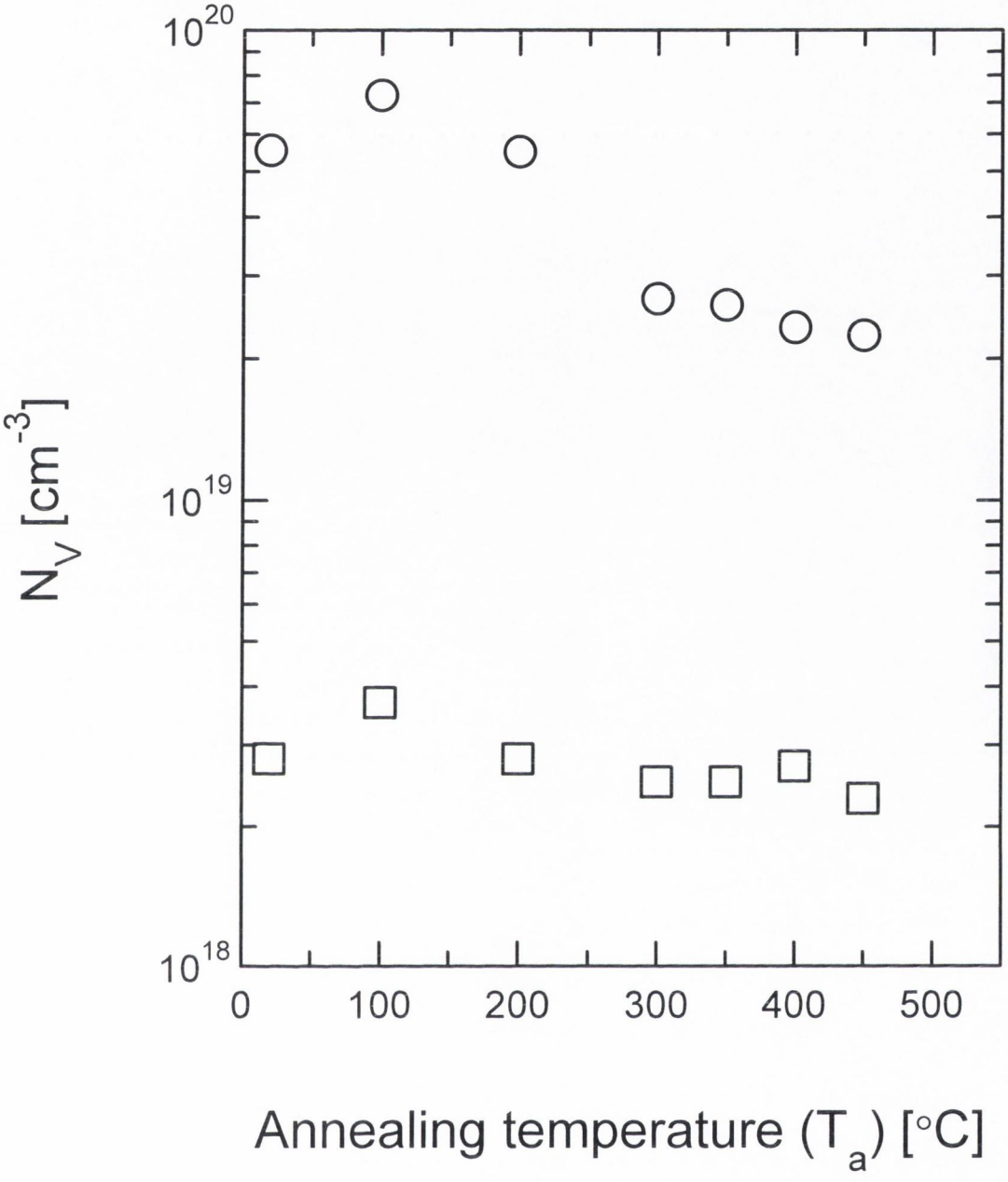

Figure 5.7 : Spin concentration of each component of the two-line fit for a-C:H (Mu3He) as a function of T_a.

□ : *N_V for the Gaussian line.*

O : *N_V for the Lorentzian line.*

5.3.2 Discussion

In this section we discuss the results and analysis of the effect annealing has on our control a-C:H film (Mu3He).

Sample Mu3He (0at.% N, 21at.% H, 0sccm N_2) is a a-C:H film which is produced under similar conditions to those of samples P5 and P2 (V_b=50 and 100V without magnetic confinement). In chapter 4 we examined the effect annealing had upon the defects present in two diamond-like a-C:H films (P5 and P2). It is interesting to compare the EPR parameters, as a function of T_a, of the a-C:H film produced with magnetic confinement (Mu3He), i.e. figure 5.5, with those obtained for the two a-C:H films (P5 and P2) produced without magnetic confinement, i.e. figures 4.12 and 4.13 in chapter 4. It can be seen by this comparison that annealing has very similar effects upon g_0, ΔB_{pp} and N_V for PECVD diamond-like a-C:H films produced with or without magnetic confinement. We can also compare how the lineshape changes, as a function of T_a, for diamond-like a-C:H films produced with and without magnetic confinement. The Voigt parameters for sample Mu3He (figure 5.6) change in a very similar way to those observed for sample P2 (figure 4.17). It is reasonable to assume that the defects present in PECVD diamond-like a-C:H produced with magnetic confinement are the same as those found in diamond-like a-C:H produced without magnetic confinement. Therefore the explanations of the changes in g_0, ΔB_{pp} N_V and the Voigt parameters are the same as those already given in chapter 4. In figure 5.6 the changes in $^L\Delta B_{pp}$, as a function of T_a, are similar to those in the linewidth predicted by dipolar broadening (from N_V and equation 4.14). This suggests that dipolar broadening may be mostly responsible for the Lorentzian component of the Voigt fits. It is possible that the spins are clustered together because $^L\Delta B_{pp}$ is larger than that predicted by dipolar broadening but absolute N_V values can be out by up to a factor of 2 which also could explains this difference.

We shall now discuss the possibility that the lineshape is due to a superposition of a Gaussian and a Lorentzian line.

If the EPR signal in this film is due to a superposition of a Gaussian and a Lorentzian then this indicates that there are defects present in two distinct environments. Looking at figure 5.7 we see that N_V the Gaussian line remains

constant up to 450°C. This may indicate that the spins giving rise to the Gaussian line are stable up to T_a = 450°C. The lineshape of this component is probably due to unresolved hyperfine splitting caused by the hydrogen present. Also the linewidth of the Gaussian line remains roughly constant which again, if we assume that its linewidth was due to unresolved hyperfine splitting due to hydrogen, may indicate that the hydrogen content remains relatively constant up to $T_a \approx 450$°C. The number of defects giving rise to the Lorentzian line fall with increasing T_a, up to T_a=450°C. This fall may be due to weakly bound hydrogen being thermally activated and diffusing to defect sites and pacifying them or possibly that the disorder in the structure of the film reduces.

Of course from the fits alone it is unclear whether the lineshape is a Voigt or a superposition of a Gaussian and a Lorentzian. In figure 5.6 we see that the linewidth due to dipolar broadening (calculated from N_V and equation 4.14) follows the changes in ${}^{L}\Delta B_{pp}$ from the Voigt fits. The linewidth of the Lorentzian component (table 5.2) of the two-line fit on the other hand does not follow the changes predicted by dipolar broadening. This supports the idea that the lineshape is a Voigt due to defects present in a single environment.

5.3.3 EPR results of annealed a-C:H,N

In this section of the chapter we present the EPR measurements on annealed a-C:H,N films. We will also analyse the lineshapes of the EPR spectra we record for these films, as a function of T_a.

The a-C:H,N films we annealed are Mu3He0.5 (3at.% N, 0.5sccm N_2), Mu3He1.5 (5.7at.% N, 1.5sccm N_2) and Mu3He10 (14at.% N, 10sccm N_2).

Figures 5.8 to 5.10 show selected spectra and fits, as a function of annealing temperature (T_a), for these three samples. The fits shown in these figures are Lorentzian, denoted by 'L', Gaussian, denoted by 'G' and Voigt, denoted by 'V'.

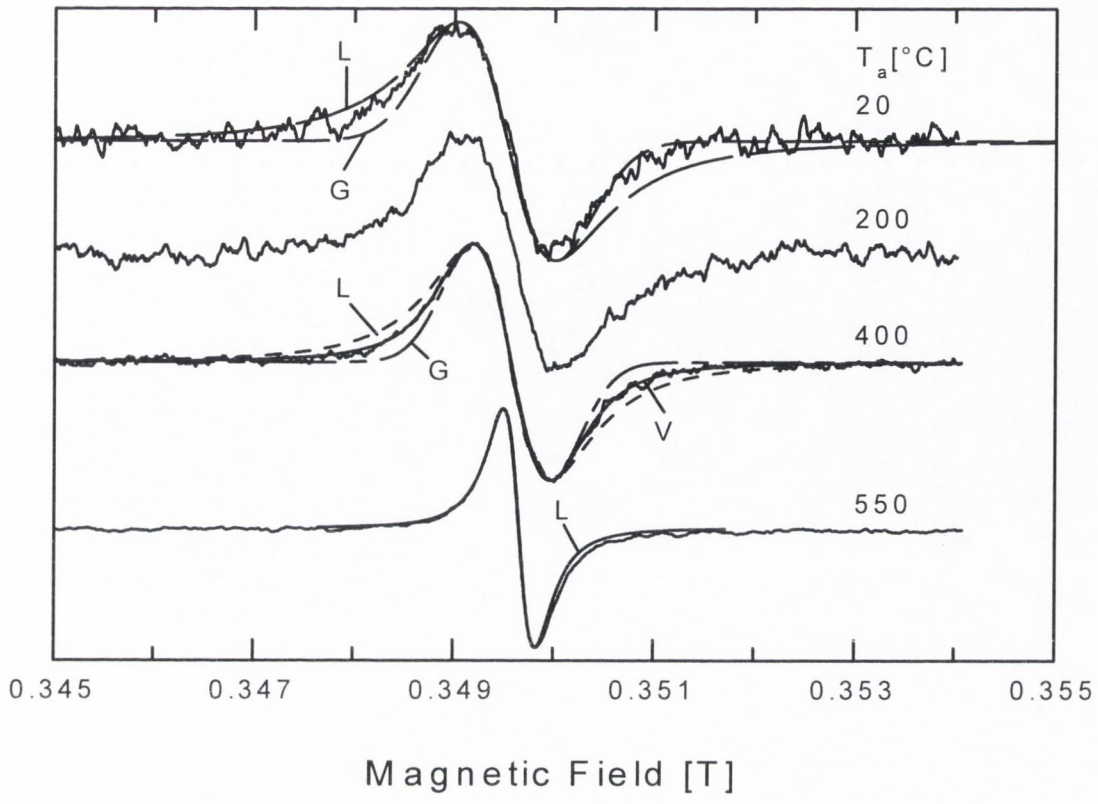

Figure 5.8 : EPR spectra as a function of T_a for the a-C:H,N film Mu3He0.5 (3at.% N, 0.5sccm N_2).

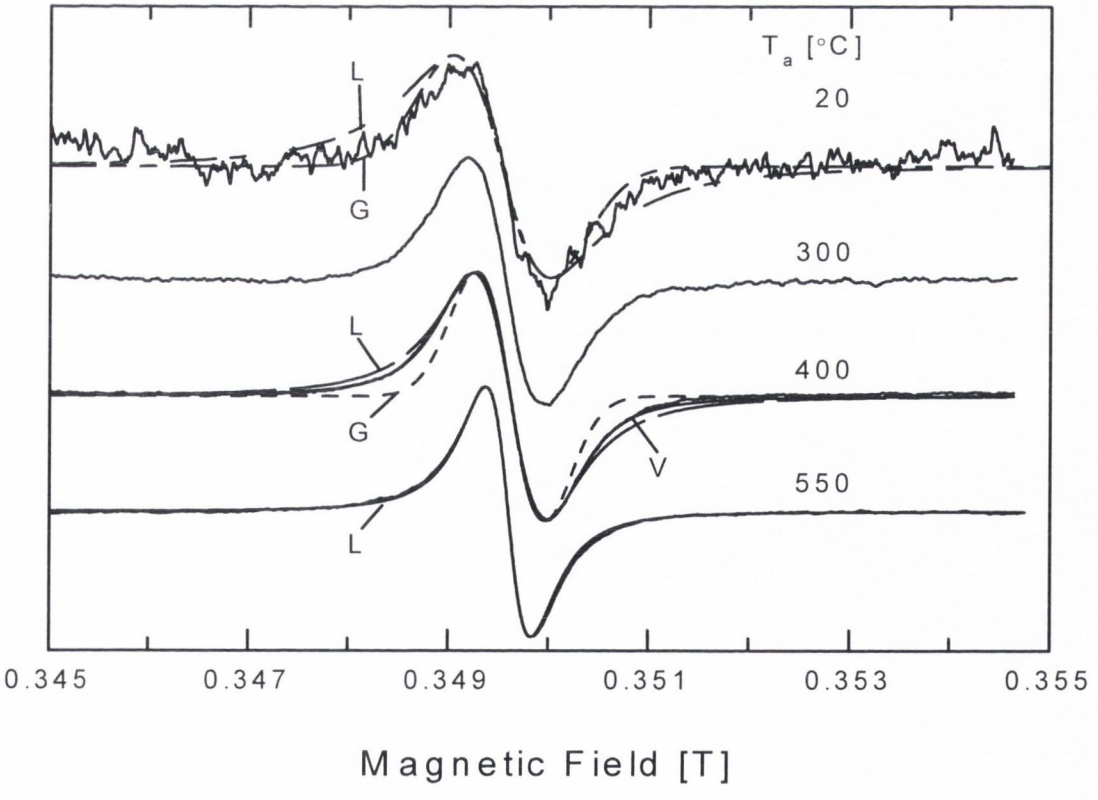

Figure 5.9 : EPR spectra as a function of T_a for the a-C:H,N film Mu3He1.5 (5.7at.% N, 1.5sccm N_2).

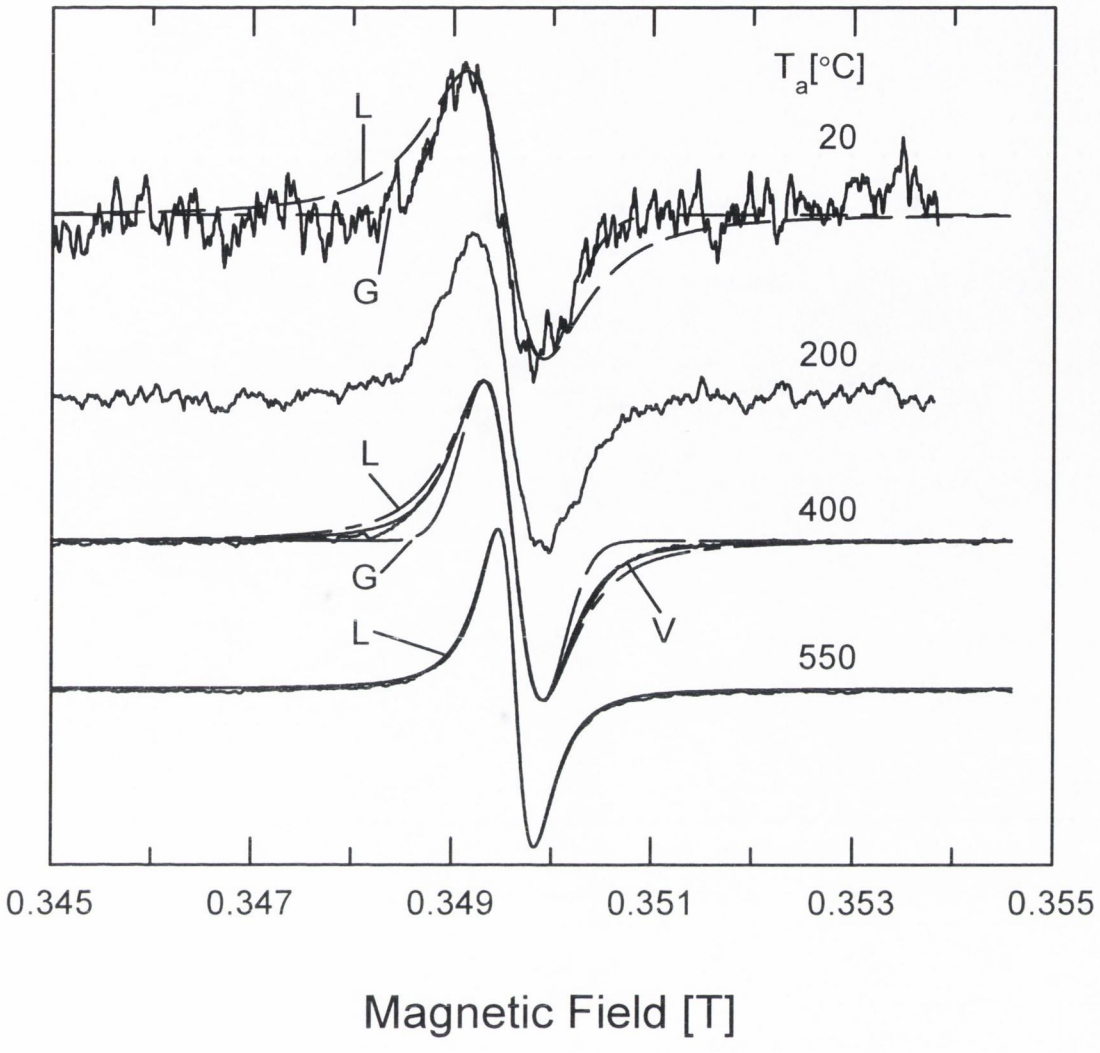

Figure 5.10 : EPR spectra as a function of T_a for the a-C:H,N film Mu3He10 (14at.% N, 10sccm N_2).

The spectra in figure 5.8 to 5.10 all show very similar changes as a function of annealing temperature (T_a). We can see that ΔB_{pp}, for the three a-C:H,N films we annealed, falls as a function of T_a, up to 550°C. We see that the lineshape, for each a-C:H,N film at T_a=20°C, is close to a Gaussian. As T_a increases above 200°C the lineshape can be seen to be between a Gaussian and a Lorentzian (see spectra for T_a=400°C in figures 5.8-5.10). Indeed the lineshape in the temperature range 300 to 450°C can be fitted to Voigt lineshapes (denoted by 'V' in figures 5.8-5.10). Also as mentioned before these spectra can also be equally well fitted by two-line fits created by a superposition of Gaussian and Lorentzian lines. At 550°C we can see that the spectra for these three a-C:H,N films become Lorentzian. For $T_a \geq$600°C the line drops off more slowly in the wings than that of a Lorentzian. The shape and widths

of the spectra at 550°C and above are very similar to the spectra we found earlier for our control a-C:H film.

Figures 5.11 shows plots of the EPR parameters for the three a-C:H,N films we annealed. The error bars on the values of ΔB_{pp} and g_0 are excluded from this figure for the sake of clarity.

We can see in this figure that the values of g_0, ΔB_{pp} and N_V behave in an almost identical way, as a function of T_a, for all three a-C:H,N films. It can be seen in this figure that the g_0-values fall with increasing annealing temperature (T_a) from $\approx$2.0031 to $\approx$2.0025 at T_a=550°C. Above 550°C the g_0-values are quite uncertain due to noise in the spectra. The linewidths (ΔB_{pp}) fall from $\approx$1mT with increasing T_a reaching a value of $\approx$0.4mT at T_a = 550°C, above this temperature ΔB_{pp} increases with increasing T_a until a temperature of 700°C is reached at which no signal is observed. The spin concentrations (N_V) increase with T_a up to $\approx 5\times10^{19}cm^{-3}$ at 550°C after which they fall. The values of g_0, ΔB_{pp} and N_V at and above 550°C for these three a-C:H,N films are very close to those found for our control a-C:H film for $T_a \geq 550$°C.

Next we examine the parameters determined by fitting the spectra. As we can see in figures 5.8 to 5.10 the lineshapes below T_a=550°C are somewhere between a Gaussian and a Lorentzian. Initially the spectra are very close to a Gaussian lineshape. As T_a increases they become somewhere between a Gaussian and a Lorentzian. Finally they become Lorentzians at 550°C. All these spectra can be fitted to Voigt profiles or they may equally well be fitted by two-line fits composed of a superposition of Gaussian and Lorentzian lines. We will examine how the fitting parameters change as a function of T_a.

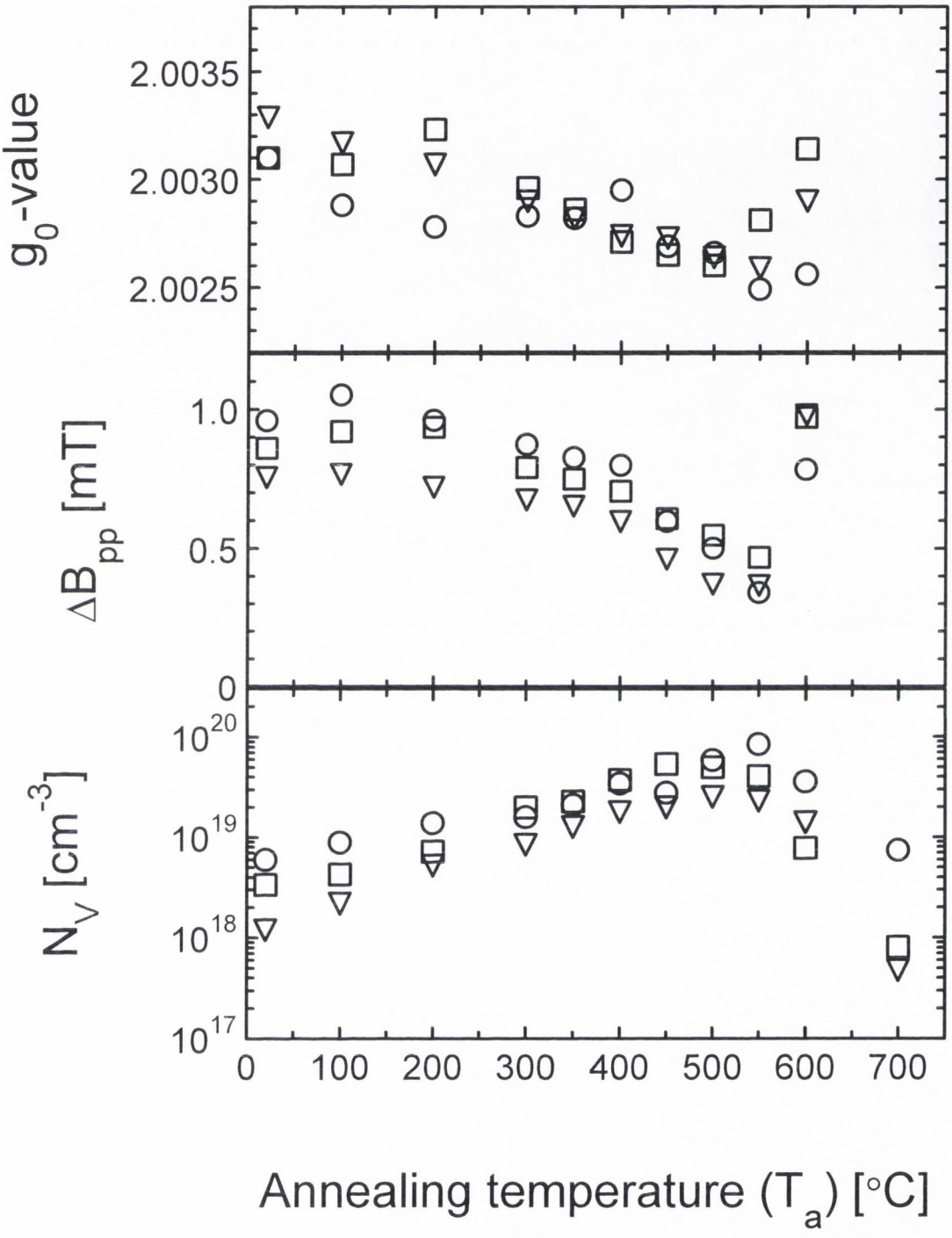

Figure 5.11 : EPR data for three a-C:H,N films as a function of T_a.

O : Film Mu3He0.5 (3at.% N, 0.5sccm N_2),

□ : Film Mu3HeN1.5 (5.7at.% N, 1.5sccm N_2),

∇ : Film Mu3HeN10 (14at.% N, 10sccm N_2).

We first deal with the possibility that the lineshapes, as a function of T_a, for our three a-C:H,N films are Voigt profiles. Figure 5.12 to 5.14 show how the parameters determined by fitting the spectra to Voigt profiles change as T_a increases. The uncertainty in the $^{L}\Delta B_{pp}$ values for $T_a \leq 200°C$ is ~50% and is about 50% for the $^{G}\Delta B_{pp}$ values for $T_a \geq 450°C$.

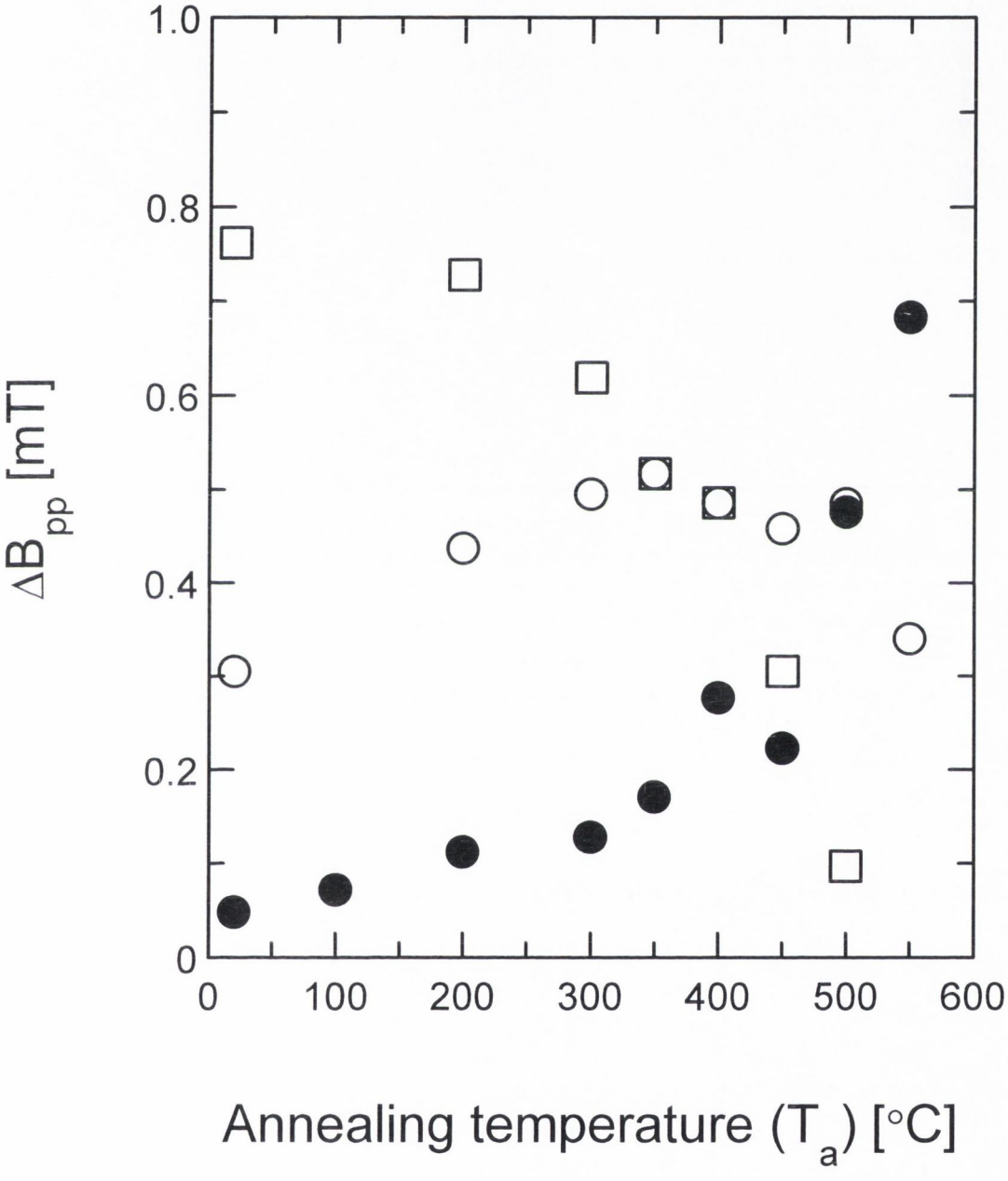

Figure 5.12 : Voigt parameters as a function of T_a for a-C:H,N film Mu3HeN0.5 (3at.% N, 0.5sccm N_2).

□ : $^{G}\Delta B_{pp}$,
O : $^{L}\Delta B_{pp}$,

● : ΔB_{pp} : *Calculated dipolar broadening (calculated from N_V and eq. 4.14).*

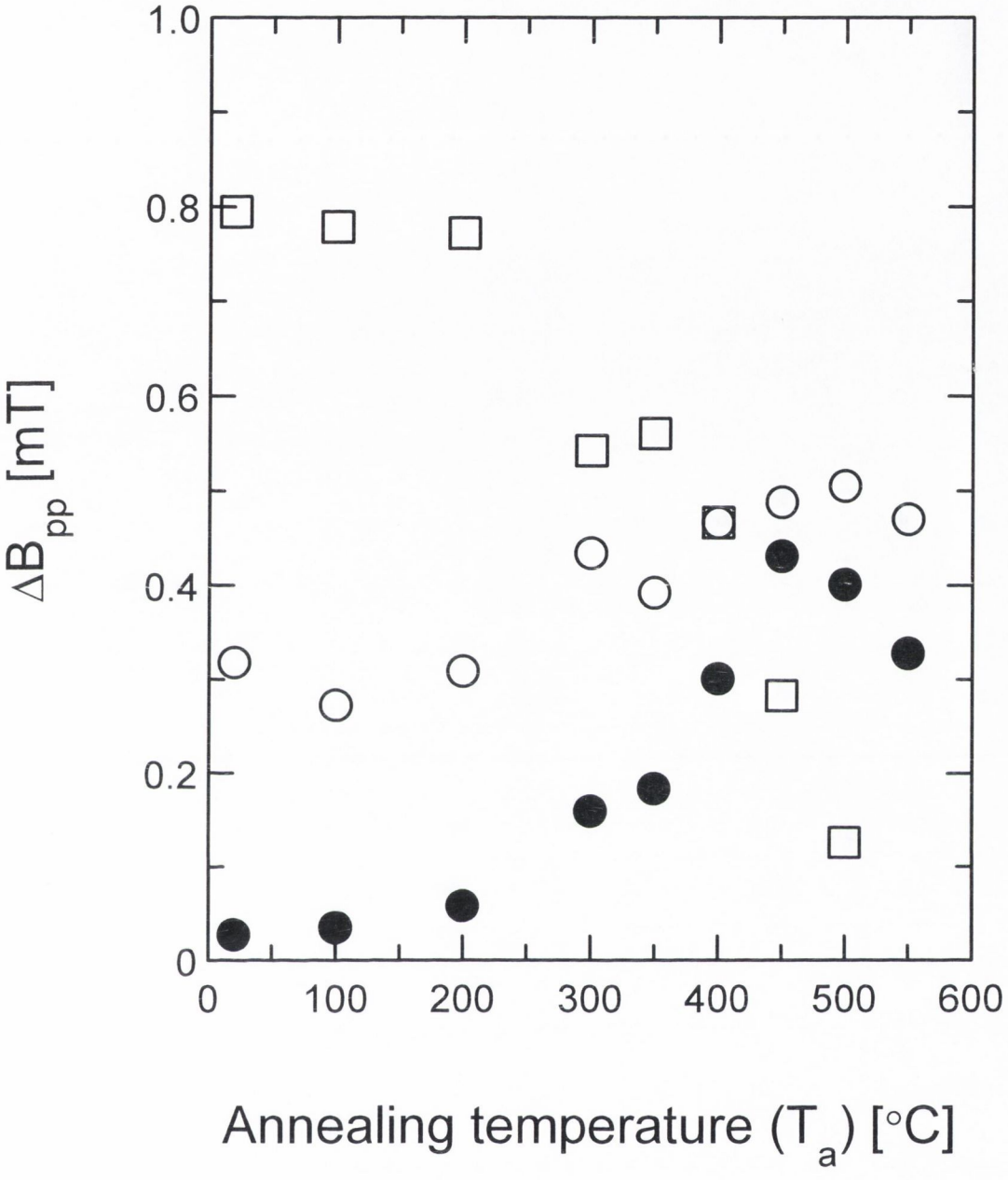

Figure 5.13 : Voigt parameters as a function of T_a for a-C:H,N film Mu3HeN1.5 (5.7at.% N, 1.5sccm N_2).

□ : ${}^{G}\Delta B_{pp}$,

O : ${}^{L}\Delta B_{pp}$,

● : ΔB_{pp} : *Calculated dipolar broadening (calculated from N_V and eq. 4.14).*

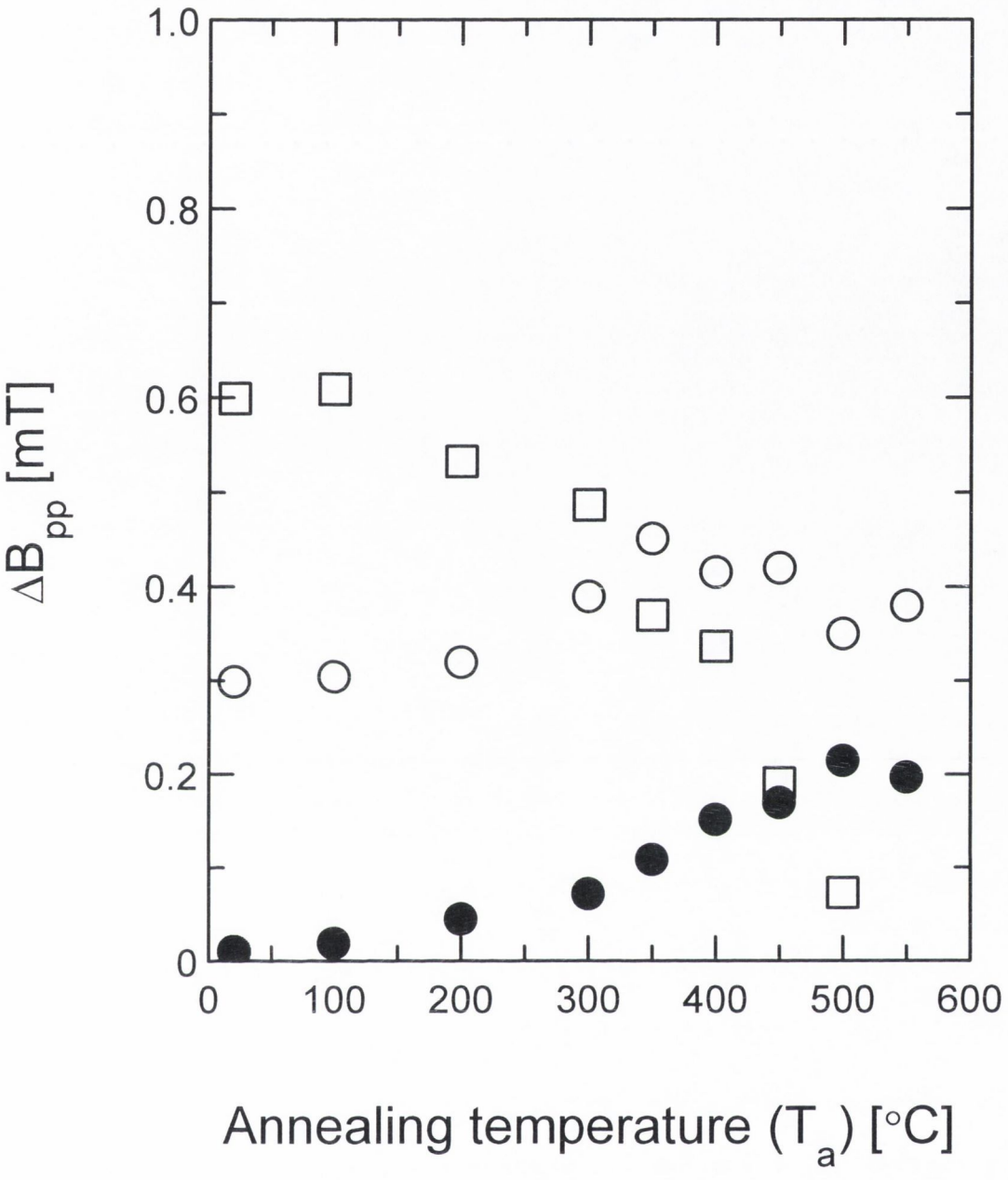

Figure 5.14 : Voigt parameters as a function of T_a for a-C:H,N film Mu3HeN10 (14at.% N, 10sccm N_2).

□ : ${}^{G}\Delta B_{pp}$,

O : ${}^{L}\Delta B_{pp}$,

● : ΔB_{pp} : *Calculated dipolar broadening (calculated from N_V and eq. 4.14).*

Figures 5.14 to 5.16 show how the Voigt parameters, for our three a-C:H,N films, change with increasing annealing temperature. We can see that the linewidths of the Gaussian component (${}^{G}\Delta B_{pp}$) are wider than the linewidths of the Lorentzian

component ($^{L}\Delta B_{pp}$) at room temperature. This increase in $^{G}\Delta B_{pp}$ compared to the a-C:H sample (Mu3He) may be because there is a contribution from nitrogen as well as hydrogen to the unresolved hyperfine splittings. $^{G}\Delta B_{pp}$ decreases with increasing (for $T_a > 200°C$) temperature which possibly indicated that either hydrogen and/or nitrogen began to evolve from the film when the temperature was greater than 200°C.

The values of $^{L}\Delta B_{pp}$ on the other hand increase with increasing T_a up to 350-450°C and this is matched by an increase in the calculated dipolar broadening. The magnitude of these two sets of values, at T_a=20°C are out by factors ranging from ≈5 to ≈18 depending upon the amount of nitrogen initially in the films. This difference falls as T_a increases. This difference is too large to be explained by experimental error as N_V values are usually only out by up to a factor of ≈2. The difference may be explained by the presence of spin clustering. For the a-C:H,N film containing 3at.% N (Mu3He) (figure 5.12), $^{L}\Delta B_{pp}$ above 350°C falls while the calculated dipolar broadening continues to increase. This may arise if the exchange narrowing in this film becomes stronger above 350°C. The increasing exchange narrowing may be due to greater delocalisation of the π-unpaired electrons due the to increasing sp^2 content of this film.

Now we will examine the possibility that the lineshapes, for our three a-C:H,N films, are produced by a superposition of a Gaussian and a Lorentzian line. In this case there exists defects in two distinct environments, one producing the Gaussian line while the other producing the Lorentzian. Figure 5.15 to 5.17 show how the parameters determined by fitting with such two-line fits change as T_a increases.

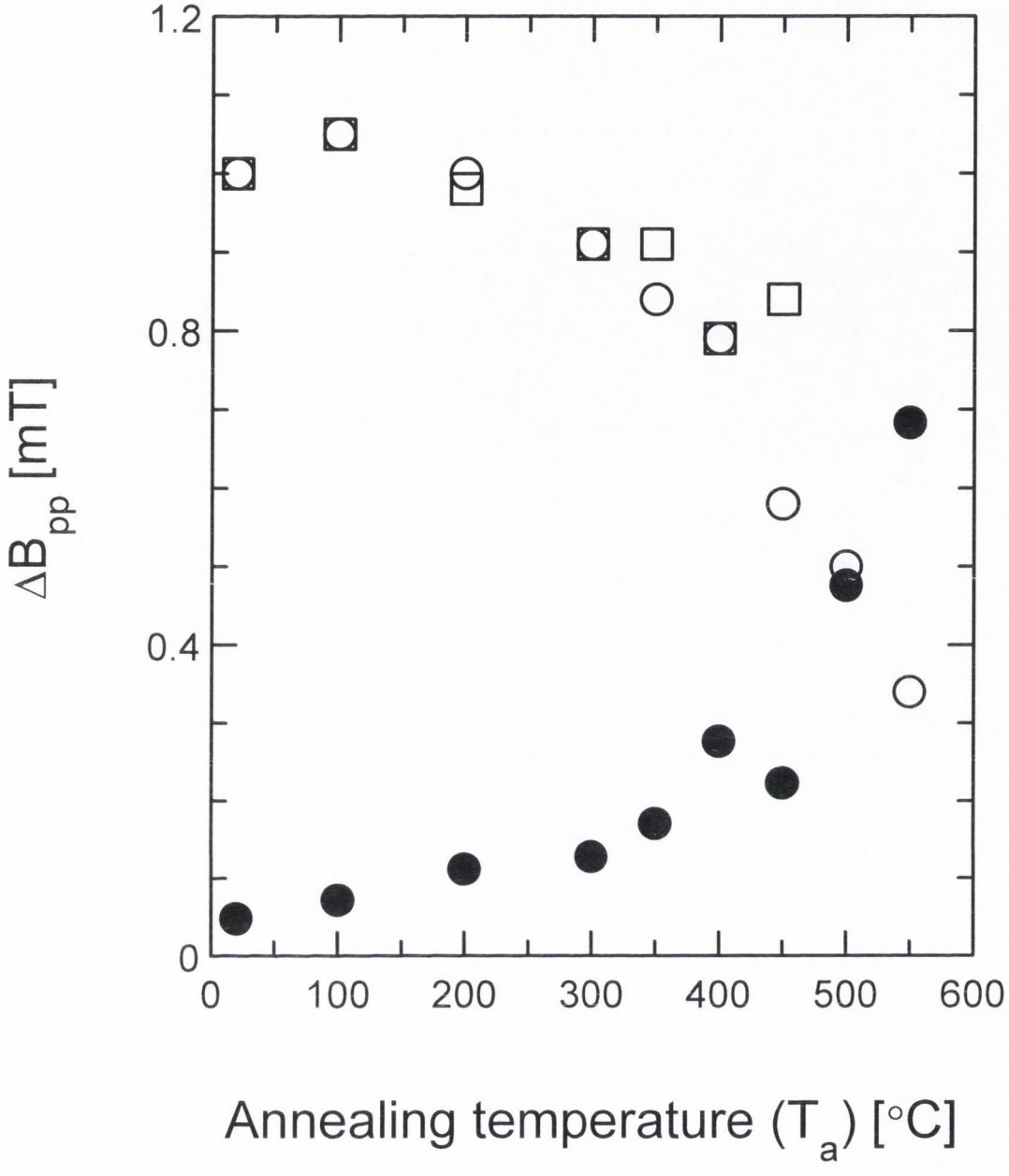

Figure 5.15 : The two linewidths of the two-fit as a function of T_a for a-C:H,N film Mu3HeN0.5 (3at.% N, 0.5sccm N_2).

□ : ΔB_{pp} for the Gaussian line,

O : ΔB_{pp} for the Lorentzian line,

● : ΔB_{pp} : Calculated dipolar broadening (calculated from N_V and eq. 4.14).

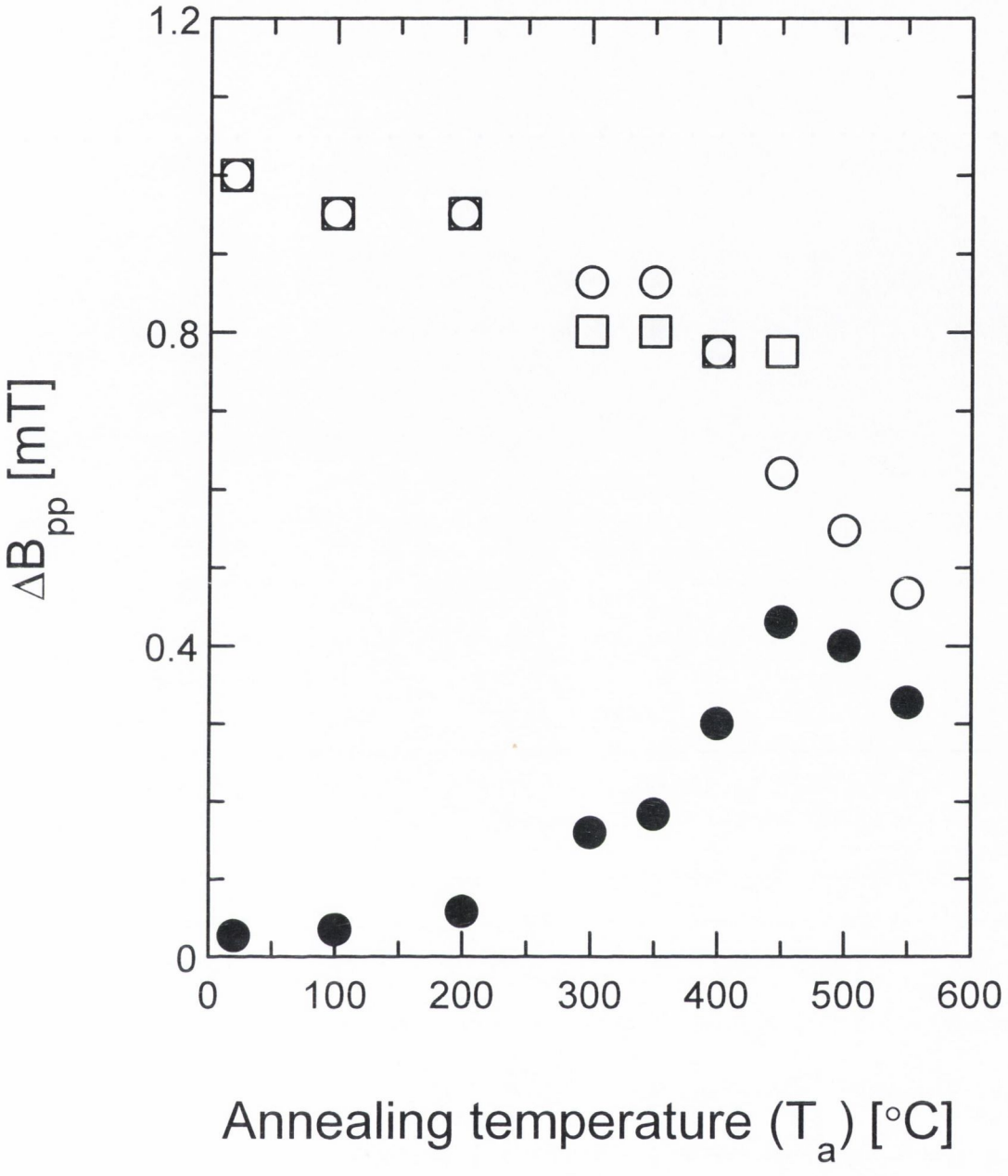

Figure 5.16 : The two linewidths of the two-fit as a function of T_a for a-C:H,N film Mu3HeN1.5 (5.7at.% N, 1.5sccm N_2).

□ : ΔB_{pp} for the Gaussian line,

O : ΔB_{pp} for the Lorentzian line,

● : ΔB_{pp} : Calculated dipolar broadening (calculated from N_V and eq. 4.14).

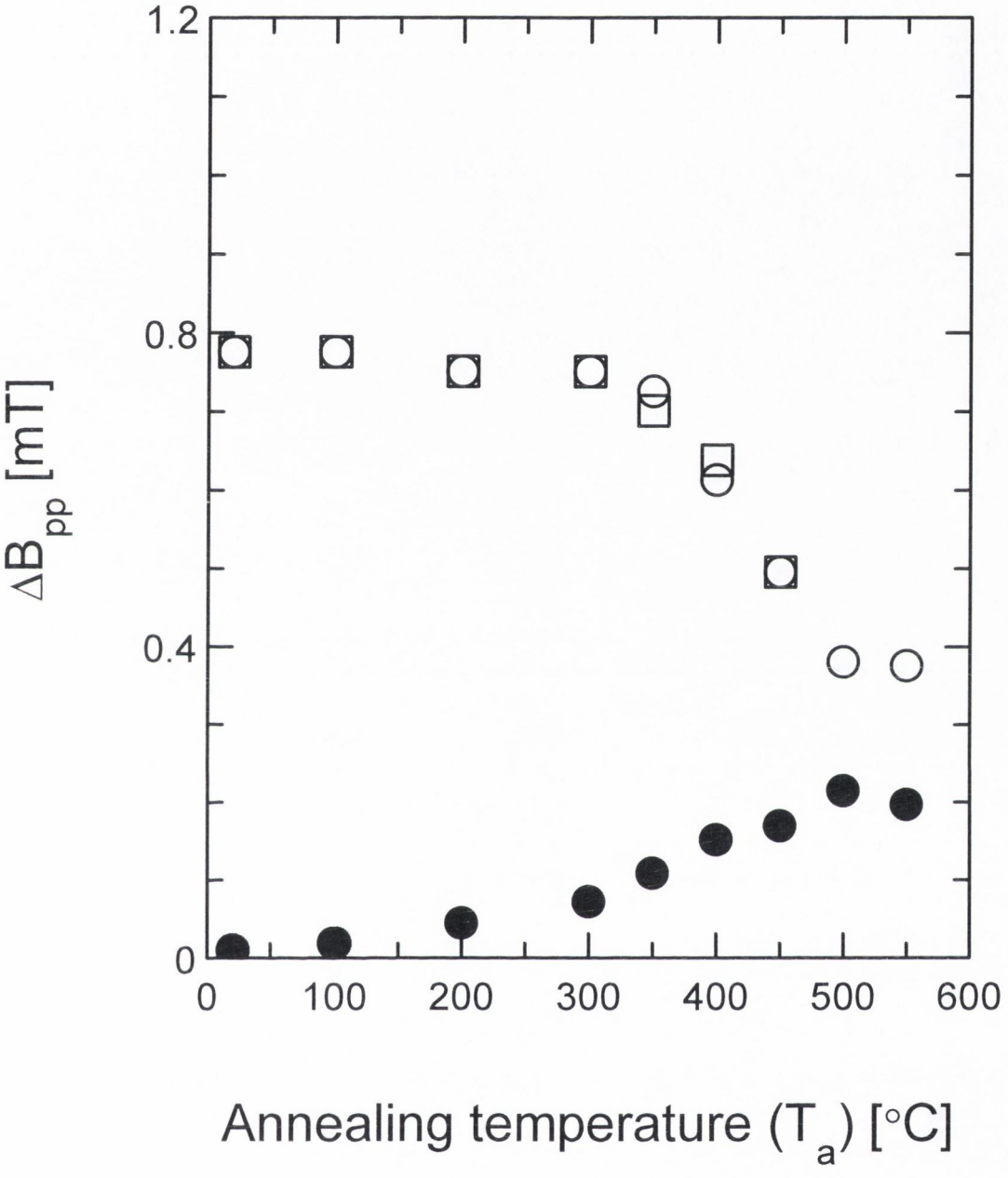

Figure 5.17 : The two linewidths of the two-fit as a function of T_a for a-C:H,N film Mu3HeN10 (14at.% N, 10sccm N_2).

□ : ΔB_{pp} for the Gaussian line,

O : ΔB_{pp} for the Lorentzian line,

● : ΔB_{pp} : Calculated dipolar broadening (calculated from N_V and eq. 4.14).

The g-values of both lines in the two-line fit are the same. These g-values fall from ≈2.0030 to ≈2.0025 as T_a increases, just as the g_0-values do (figure 5.11). N_V

for the Lorentzian lines increase with increasing T_a while N_V for the Gaussian line is smaller and does not change much. Figures 5.15 to 5.17 show that the changes in the linewidths of the component lines behave very similarly for all three a-C:H,N films. In figures 5.15 to 5.17 we can see that the linewidth of the Lorentzian line falls with increasing T_a for all three a-C:H,N films. The linewidth of the Gaussian line approximately equals that of the Lorentzian line and it too falls with increasing T_a.

These figures also show the linewidths, as a function of T_a, predicted by dipolar broadening. Figures 5.15 to 5.17 show that at T_a=20°C the magnitude of ΔB_{pp} of the Lorentzian lines is much larger than that predicted by dipolar broadening by a factor ranging from 20 to 80. For dipolar broadening to account the linewidths it would therefore require a very high degree of clustering of the unpaired spins to produce the necessarily higher local spin concentrations. Also the predicted dipolar broadening increases as T_a increases, for T_a<450°C, while ΔB_{pp} of the Lorentzian lines fall. These two facts suggest that the idea that there are defects present in two distinct environments is wrong, i.e. that the two-line fit is incorrect.

Therefore we rule out the idea that the EPR signal from a-C:H,N is due to a superposition of a Gaussian and a Lorentzian line. This leaves us with the idea that the lineshape of EPR signals for T_a<550°C is a Voigt due to defects present in a single environment.

5.3.4 Discussion

We will now discuss further our EPR results for the annealed a-C:H,N samples. We will discuss why g_0 and N_V changes as T_a increases. We also discuss how the lineshape and width change as a function of the annealing temperature (T_a).

We believe that the paramagnetic defects present in the a-C:H,N films are unpaired π-electrons.

In figure 5.11 we see that the g_0-value, ΔB_{pp} and N_V behave in a very similar manner for the three a-C:H,N films which we annealed. The g_0-values fall from ≈2.0031 to ≈2.0026 as T_a increases from 20 to 550°C. ΔB_{pp} falls from ≈0.9 to 0.4mT over the same range of temperatures. We can also see in this figure that N_V for the three films rises from $<10^{19}cm^{-3}$ to $\approx 4\times10^{19}cm^{-3}$. At 550°C the g_0, ΔB_{pp} and N_V values of the a-C:H,N films are very close to those we find for the control a-C:H film

after it was annealed at 550°C. Also the lineshape at 550°C for both the a-C:H and a-C:H,N films are Lorentzian. This is a very strong indication that after annealing at 550°C the defects present in the a-C:H,N films are identical to those in the a-C:H film. So it is likely that the structure of a-C:H,N films is the same as the structure of diamond-like a-C:H after annealing at 550°C. We believe that the majority of the nitrogen initially present is emitted from the a-C:H,N films below 550°C. This explains the fall in the g_0-values, shown in figure 5.11, because as the nitrogen diffuses out of the a-C:H,N films the g_0-values become close to that found for the a-C:H film. We see in figure 5.2 that the addition of nitrogen into diamond-like a-C:H reduces N_V. Therefore the increase in N_V up to T_a=550°C in the a-C:H,N films may be due to the release of nitrogen combined with the release of hydrogen. Finally, the fall in N_V for annealing temperatures above 600°C is likely to have be due to the onset of graphitization.

We rule out the possibility that the lineshapes for a-C:H,N (for T_a<550°C) are a superposition of two lines and consider them to be Voigt profiles. The values of ${}^{L}\Delta B_{pp}$ at low annealing temperatures are much higher than the linewidths expected for dipolar broadening. We believed that clustering together of the spins give rise to a higher local spin concentration (N_V) (initially $\approx 4\times10^{19}cm^{-3}$) which means that we underestimate the dipolar broadening. This may explain why the experimental ${}^{L}\Delta B_{pp}$ and the calculated linewidth (dipolar) are different.

The increase in the values of ${}^{L}\Delta B_{pp}$ (figures 5.12 to 5.14), as T_a increases up to ≈450°C, is most likely due to an increase in the dipolar broadening of linewidth. We can see in these figures that the calculated dipolar broadening also increases. Between ≈450°C and 550°C the ${}^{L}\Delta B_{pp}$ values (or ΔB_{pp} when the line is a single Lorentzian) fall with increasing T_a. This is probably due to an increase in the sp^2 content of the film which allows greater delocalisation of the π-electrons and thus increases the exchange narrowing of the line. Also there is a fall in the predicted dipolar broadening in figures 5.13 and 5.14. So these two effects reduce the ${}^{L}\Delta B_{pp}$ values (or ΔB_{pp} in the case of a Lorentzian).

The increase in ΔB_{pp} (figure 5.11) above 550°C we attribute to line broadening due to the interaction of the unpaired electrons with conduction electrons in the film.

$^{G}\Delta B_{pp}$ for the a-C:H,N films (figures 5.12 to 5.14) is initially larger than $^{L}\Delta B_{pp}$. In comparison $^{G}\Delta B_{pp}$ for the a-C:H film (figure 5.6) is initially smaller than $^{L}\Delta B_{pp}$. For the a-C:H film we explained the width of $^{G}\Delta B_{pp}$ as being due to the presence of unresolved hyperfine splitting caused by the hydrogen present. The increase in the width of $^{G}\Delta B_{pp}$ for the a-C:H,N films may be due to the presence of unresolved hyperfine splitting caused by the presence of both hydrogen and nitrogen. Values of $^{G}\Delta B_{pp}$ for the a-C:H,N films fall as T_a increases. This may be due to the emission of both nitrogen and hydrogen from these films. This is further evidence that nitrogen and hydrogen are emitted from the a-C:H,N films. It is also evidence that the a-C:H,N films become the same as the diamond-like a-C:H film after annealing at 550°C.

Now we discuss in further detail the possible clustering of the spins in the a-C:H,N films. Such a clustering gives rise to a higher local N_V value and thus a higher than expected dipolar broadening of the EPR spectra.

The factor by which the local spin concentration (N_V) would need to be higher that the average N_V value would equal the ratio of $^{L}\Delta B_{pp}$ to the calculated dipolar linewidth (ΔB_{pp}(Dipolar)). It must be remembered that as N_V may be out by a factor of ≈2 and thus so too can this ratio. We now examine how this ratio varies in our three a-C:H,N films and our control a-C:H film, at both high and low annealing temperatures (T_a). For the low temperature region, as the signal is noisy, we take the average of this ratio for T_a=100 and 200°C. While for the high T_a region we calculate this ratio for T_a = 550°C. Table 5.3 lists the results of our calculations.

Name	N at.%	H at.%	Average $^{L}\Delta B_{pp}/\Delta B_{pp}$(Dipolar) for T_a 100 to 200°C	$^{L}\Delta B_{pp}/\Delta B_{pp}$(Dipolar) for T_a = 550°C
Mu3He	0	21	≈1.6	≈1.2
Mu3He0.5	3	20.8	≈4.8	≈1
Mu3He1.5	5.7	20.8	≈6.3	≈1.3
Mu3He10	14	13	≈9.8	≈1.6

Table 5.3 : Ratio of the linewidth of the Lorentzian comonent of the Voigt to the predicted dipolar broadening.

For the low temperature region where the samples are close to their as grown states we can see that this ratio increases as the nitrogen content increases. For the

first three samples in table 5.3 where the hydrogen content is quite constant we can see that this ratio appears to depend upon the nitrogen content of the film. The fourth film in table 5.3 also shows an increase in this ratio with increasing nitrogen content even though the hydrogen content of this film has fallen. So it seems that this ratio (average of T_a=100 and 200°C) depends only upon the nitrogen content of the film. Figure 5.18 shows how these ratios vary with increasing nitrogen content. We can see that the average ratios calculated for T_a=100 and 200°C increase roughly linearly with increasing nitrogen content. So it appears that the addition of nitrogen into a-C:H films while reducing the average spin concentration still leaves behind regions in the a-C:H,N films where the spins are probably highly clustered together. $^{L}\Delta B_{pp}$ for the three a-C:H,N films, averaged over T_a=100 to 200°C, remains almost constant at ≈0.3mT, i.e. the reason the $^{L}\Delta B_{pp}/\Delta B_{pp}$(Dipolar) ratio increases, as the N content increases is due to a fall in ΔB_{pp}(Dipolar) because N_V falls. So it appears that while the addition of nitrogen reduces the average value of N_V, it leaves unaffected pockets of clustered spins which maintain a constant local value of N_V. This local N_V value would have to be $\approx 4\times10^{19}cm^{-3}$ spins.

The ratio $^{L}\Delta B_{pp}/\Delta B_{pp}$(Dipolar) calculated for the a-C:H,(N) films annealed at 550°C remain approximately constant in figure 5.18. This gives further support to the idea that all the nitrogen has evolved from the a-C:H,N films at 550°C, because the ratio is the same as the a-C:H film.

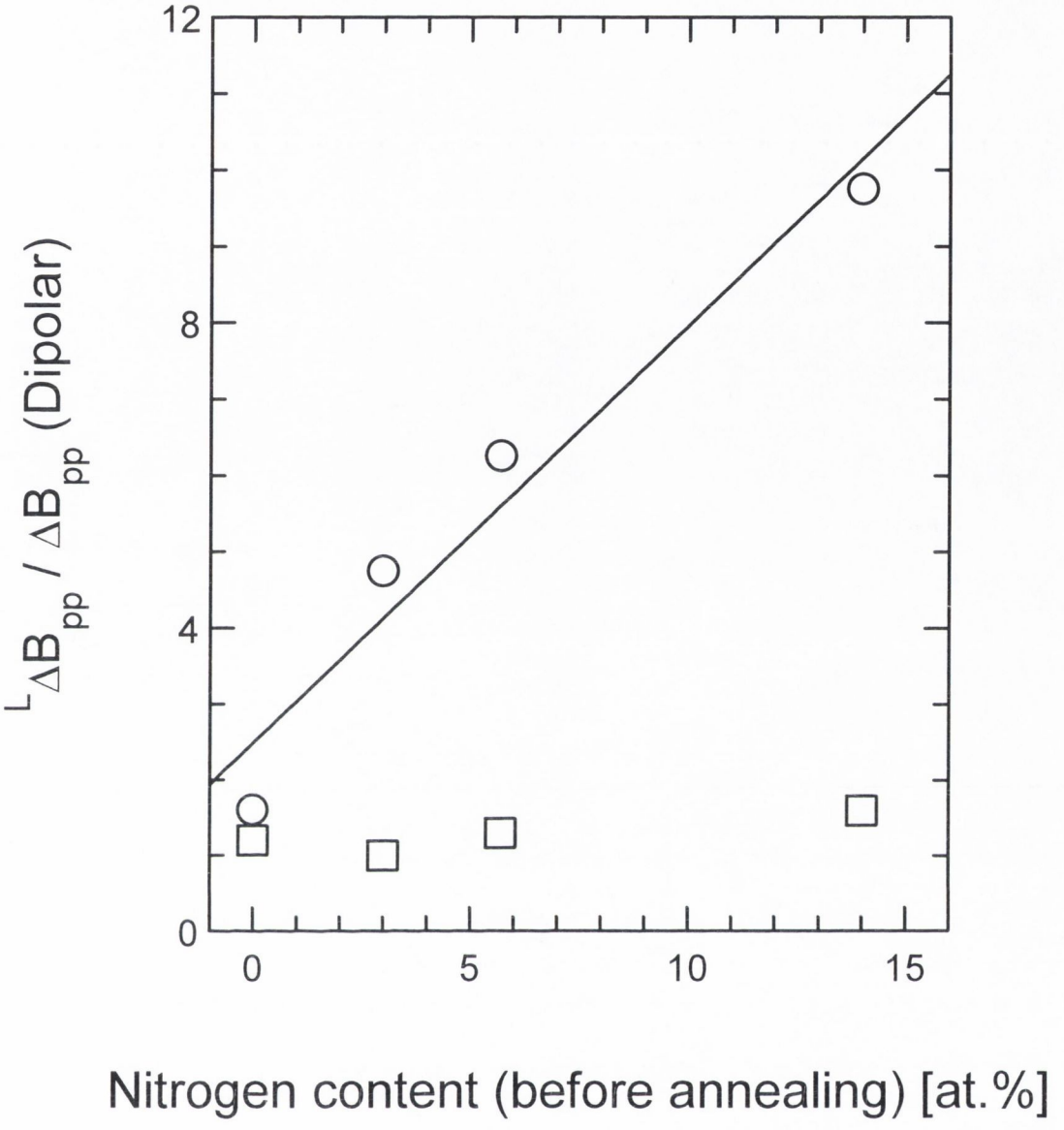

Figure 5.18 : Ratios of $^{L}\Delta B_{pp}/\Delta B_{pp}$(Dipolar) as a function of nitrogen content before annealing.

□ : *$^{L}\Delta B_{pp}/\Delta B_{pp}$(Dipolar) for T_a = 550°C.*

O : *$^{L}\Delta B_{pp}/\Delta B_{pp}$(Dipolar) averaged over T_a=100 and 200°C.*

From figure 5.18 we find an empirical relationship between the $^{L}\Delta B_{pp}/\Delta B_{pp}$(Dipolar) ratio, averaged over T_a=100 and 200°C, and the initial nitrogen content of the films. This relationship is,

$$^{L}\Delta B_{pp}/\Delta B_{pp}(\text{Dipolar}) = 0.548\times(\text{Nitrogen content [at.\%]}) + 2.48 \qquad (5.1)$$

By rearranging this equation and using equation 4.14 we get the following,

$$\text{Nitrogen content [at.\%]} = ({}^{L}\Delta B_{pp}/(8.12\times10^{-21}\times N_V) - 2.48) / .548 \qquad (5.2)$$

Where N_V is in units of cm^{-3} and ${}^{L}\Delta B_{pp}$ is in units of mT.

Such an empirical relationship could be used to estimate the nitrogen content in a-C:H,N films. Caution must be exercised when using this equation because the initial a-C:H films before the addition of nitrogen are diamond-like a-C:H so the relationship may change, or not even exist, for other forms of nitrogenated a-C:H films. Table 5.4 shows the estimated nitrogen contents for our films based upon this empirical relationship. Since the slope of this relationship is calculated from the average value of the ${}^{L}\Delta B_{pp}/\Delta B_{pp}$(Dipolar) ratio, for T_a=100 and 200°C, our estimates of the nitrogen content use the average values of N_V and ${}^{L}\Delta B_{pp}$ for T_a=100 and 200°C. This was done because the noise level in the EPR spectra of a-C:H,N films before annealing was very high and we hope that an average of the values at two lower annealing temperatures (100°C and 200°C) would give better estimates because the films remain relatively unchanged up to T_a=200°C. It would be better to carry out this estimation and calibration of the empirical relationship between the nitrogen content and the ${}^{L}\Delta B_{pp}/\Delta B_{pp}$(Dipolar) ratio at T_a=room temperature, but the noise levels in the spectra inhibit us. As can be seen in table 5.4 the estimated nitrogen content is correct to within ≈35%.

Name	Average N_V (for T_a=100 & 200°C) [$10^{19}cm^{-3}$]	Average ${}^{L}\Delta B_{pp}$ (for T_a=100 & 200°C) [mT]	Estimated at.% N (from eq. 5.2)	At.% N (from Silva et al. 1997)
MueH3	6.42	0.861	0*	0
Mu3HeN0.5	0.95	0.371	4.1	3
Mu3HeN1.5	0.49	0.300	6.9	5.7
Mu3HeN10	0.30	0.308	13.3	14

*Table 5.4 : Comparison of the estimated nitrogen content of the a-C:H,(N) films with those reported by Silva et al. (1997). *This estimate is a negative value which is unrealistic.*

5.4 Conclusions

We have examined how the addition of nitrogen to DLC a-C:H effects the paramagnetic defects present. We observed that the addition of nitrogen causes the number of unpaired spins (N_V) to drop quite considerably. This we believe is due mainly to nitrogen supplying doping electrons into the a-C:H,N film which were free to move and combine with unpaired π-electrons of the defects. This causes these defects to become diamagnetic and therefore undetectable to EPR. At low temperatures we did not observe paramagnetic N centres. We did not find any evidence to support the idea that nitrogen electronically dopes the diamond-like a-C:H films.

In order to further our understanding of these films we annealed them in Ar. A set of films with different nitrogen contents was examined. Annealing at $T_a \approx 550°C$ causes the a-C:H,N films to exhibit EPR features very similar to DLC a-C:H annealed at $T_a \approx 550°C$. Such similarities in the EPR spectra lead us to believe that the structure of both these a-C:H,N films and DLC a-C:H, after being annealed at $\approx 550°C$, are very similar. This possibly means that the majority of the nitrogen and hydrogen has been emitted from the a-C:H,N films by this temperature. We also believe that the experimental evidence supports the idea that the lineshape for the EPR spectra of the a-C:H,N films are Voigt profiles and not a two-line superposition of a Gaussian and a Lorentzian. This may mean that the unpaired electrons exist in only one environment and not two. We believe that the spins are due to unpaired π-electrons residing in systems of conjugated double bonds, both olefinic and aromatic. We found possible evidence that after the addition of nitrogen into the DLC a-C:H the residual spins are clustered together, i.e. that the local spin concentration (N_V) around the remaining unpaired spins is higher than the average N_V.

5.5 References

Amaratunga, G. A. J. and Silva, S. R. P. (1996). Applied Physics Letters, **68**, 2529.

Amir, O. and Kalish, R (1991). Journal of Applied Physics, **70**, 4958.

Hoinkins, M., Weber, E. R., Landstrass, M. I., Plano, M. A., Han, S. and Kania, D. R. (1991). Applied Physics Letters, **59**, 1870.

Lin, S., Noonan, K., Feldman, B. J., Min, D. and Jones, M. T. (1991). Solid State Communications, **80**, 101.

Robertson, J. (1993). Diamond and Related Materials, **2,** 984.

Robertson, J. (1994). Diamond and Related Materials, **3,** 361.

Schwan, J., Batori, V., Ulrich, S., Ehrhardt, H. and Silva S. R. P. (1998). Journal of Applied Physics, **84**, 2071.

Silva, S. R. P., Robertson, J., Rusli, Amaratunga, G. A. J. and Schwan, J. (1996). Philosophical Magazine B, **74**, 369.

Silva, S. R. P., Robertson, J., Amaratunga, G. A. J., Rafferty, B., Brown, L. M., Schwan, J., Franceschini, D. F. and Mariotto, G. (1997). Journal of Applied Physics, **81**, 2626.

Sze, S. M. (1985). Semiconductor Devices: Physics and Technology. Wiley, New York.

Veerasamy, V. S., Yuan, J. Amaratunga, G. A. J., Milne, W. I. Gilkes, K. W. R., Weiler, M. Brown, L. M. (1993). Physical Review B, **48**, 17954.

Viehland, J., Lin, S., Feldman, B. J., Kilgore, K. and Jones, M. T. (1991). Solid State Communications, **80**, 597.

Weiler, M., Sattel, Giessen, T. S., Jung, K., Ehrhardt, H., Veerasamy, V. S. and Robertson, J. (1996). Physical Review B, **53,** 1594.

Chapter 6:

EPR study of defects induced in 6H-SiC by ion implantation

6.1 Introduction

Silicon carbide (SiC) has electrical properties excellently suited for use in semiconductor devices, such as a high electron saturation velocity and a high electron mobility comparable to silicon (Si) (Sugli 1994). But SiC is unlikely to replace Si as the major raw material for semiconductor devices due to difficulties in manufacture and in growing large bulk SiC crystals. Where SiC comes into its own is in the possible production of semiconductor devices designed for use at high temperatures. SiC is a high-strength structural ceramic capable of retaining its excellent mechanical properties in both reactive chemical environments and in temperatures in excess of 1000°C. SiC is a wide band gap material (Sugli 1994) which means for a given temperature the amount of intrinsic electrons and holes is lower than Si. This allows SiC electronic devices to retain their extrinsic dopant populations at relatively elevated temperatures compared to Si. This means the characteristics of a SiC device remains stable at higher temperatures relative to Si devices. This wide band gap also makes such devices radiation hard. All the above properties show that SiC may be a useful material in producing superior semiconductor devices for use in such hostile conditions.

SiC can be grown by CVD (chemical vapour deposition), LPE (liquid phase epitaxy), MBE (molecular beam epitaxy) or ion-beam deposition (Sugli 1994). An important issue in the processing of SiC is that of doping. Conventional doping of SiC may be achieved by including the required dopant during growth of the bulk crystal or epitaxial layer. With this procedure it is impossible to produce laterally confined doped regions and/or buried dopant layers. The above diffusion based doping techniques require high temperature annealing (>1800°C) due to the very low diffusivities of dopants in SiC (Vodakov and Mokhov 1973). This high temperature

causes thermal degradation on the SiC surface. Ion implantation of dopants on the other hand allows the dopants to be confined to a desired area and allows for the production of buried dopant layers. Ion implantation means that the low diffusivities of dopants in SiC are no longer a concern. There have been several reports on ion implantation in to SiC (Spitznagel et al. 1986; Hirano and Inada 1995; Rao et al. 1995). But ion implantation creates damage and point defects. Therefore it is the aim of the work carried out in this chapter to identify and characterise, using EPR, the types of paramagnetic defects produced in silicon carbide (6H-SiC) by Ge^{+} as a function of implantation dose. It is of interest to see how thermally stable these defects are and if they can be removed by annealing. Therefore this work also aims to examine using EPR these defects, produced by ion implantation, as a function of annealing temperature (T_a).

6.2 Defects present in 6H-SiC as a function of dose

In this section of the chapter we examine what effect changing the implantation dose of Germanium ions has upon the paramagnetic defects created by implantation in 6H-SiC. As we are only interested in the damage produced by ion implantation into SiC. Therefore 6H-SiC is implanted with Germanium ions because it will not dope the SiC. 6H-SiC is a crystalline allotrope of silicon carbide, figure 6.1 shows the lattice structure of 6H-SiC (Balona and Loubser 1970).

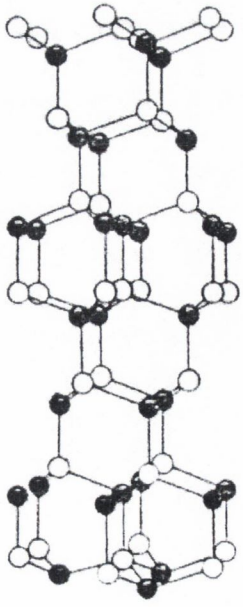

Figure 6.1 : Lattice structure of 6H-SiC.

6.2.1 Sample preparation

In order to examine the effect ion implantation dose has on defects produced in 6H-SiC, we examine samples implanted with various doses of Ge^+ ions. The 6H-SiC wafers are n-type (0001) crystals. They were obtained from Cree Research Incorporated, North Carolina, U.S.A. The implantation into these 6H-SiC wafers of 200keV Ge^+ ions was carried out by Y. Pacaud and W. Skorupa in the Forschungszentrum Rossendorf eV, Dresden, Germany. The preparation condition used are listed below in table 6.1 The Ge^+ ions were implanted into the 6H-SiC wafers at 7° to the wafer normal, i.e. 7° to the normal of plane (0001). This was done to avoid ion channelling in the 6H-SiC wafers (Sze 1985).

Name	Implantation dose (φ) [cm^{-2}]	Current [μA] (on 14.8cm^2)	Time for implantation [s]
EU8 (Virgin)	0	0	0
EU1	1×10^{12}	0.02	32
EU2	3×10^{12}	0.02	100
EU3	1×10^{13}	0.2	34
EU4	3×10^{13}	0.2	92
EU5	1×10^{14}	4	80
EU6	3×10^{14}	4	217
EU7	1×10^{15}	4	10

Table 6.1 : Ion implantation conditions.

6.2.2 EPR results of varying the Ge^+ ion dose.

In this section of the chapter we examine the EPR results varying dose of Ge^+ ions dose used during implantation. We also study, as a control, the defects present in a virgin 6H-SiC wafer without ion implantation (EU8). In this section we will also analyse our EPR results as a function of dose.

Figure 6.2 shows selected EPR spectra for the various implantation doses used. These EPR spectra were collected by Dr. L. Sealy. Also show in this figure are single Lorentzian line fits, denoted by 'L', for some of the spectra.

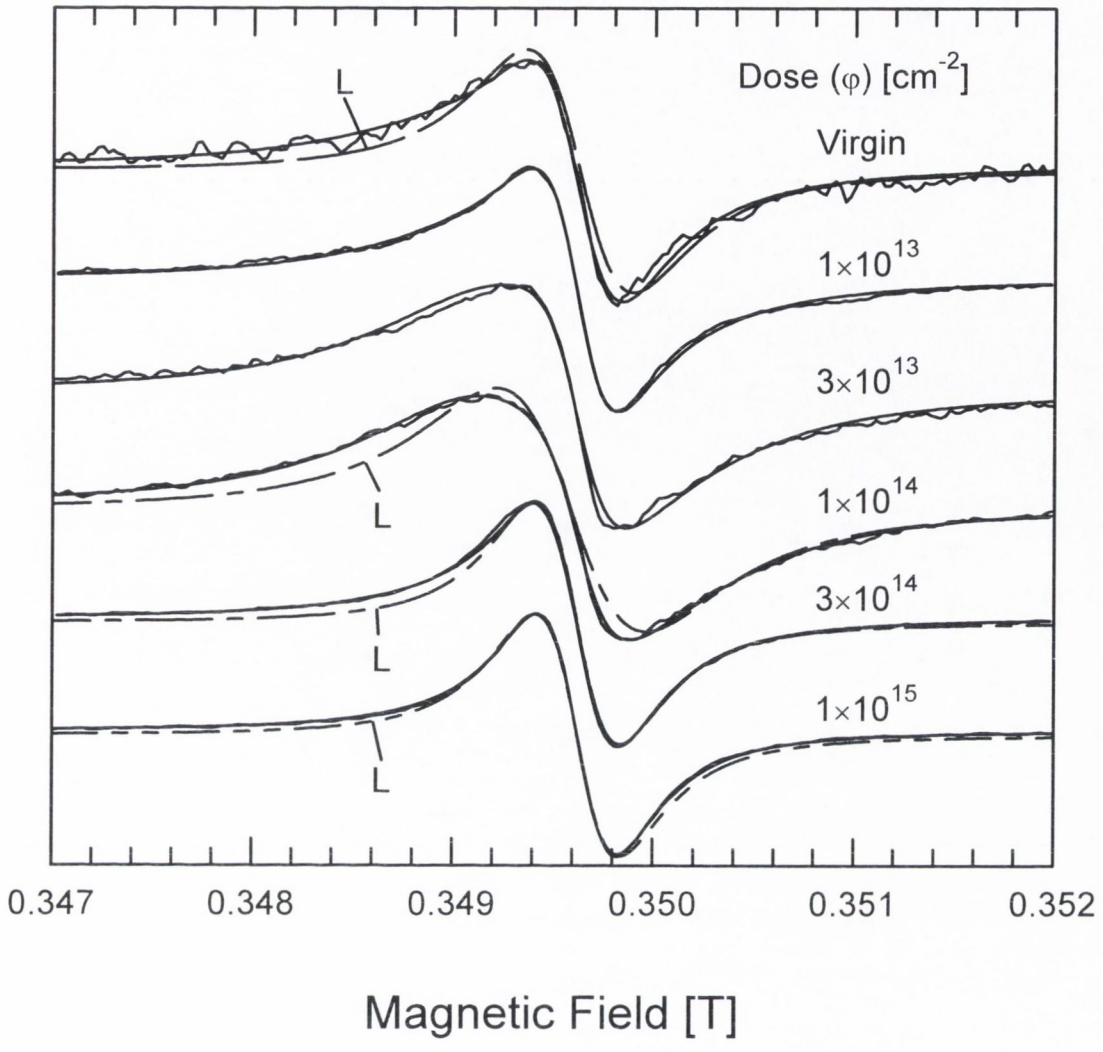

Figure 6.2 (ν=9.8GHz) : EPR spectra and fits for Ge^+ implanted 6H-SiC as a function of dose (φ).

We can see in figure 6.2 that none of the spectra from the virgin 6H-SiC (Eu8) to the 6H-SiC implanted with $\varphi=1\times10^{15}cm^{-2}$ can be fitted with a single Lorentzian line. The spectrum of the virgin sample is close to a Lorentzian. As φ increases the lineshape becomes quite asymmetrical and is not a Lorentzian, especially in the range of doses $3\times10^{13}cm^{-2}$ to $1\times10^{14}cm^{-2}$. Above $\varphi=1\times10^{14}cm^{-2}$ the lineshape becomes closer to a Lorentzian again. The linewidth (ΔB_{pp}) of the spectra increases as φ increases from 0 to $1\times10^{14}cm^{-2}$ after which it falls.

Figure 6.3 is a plot of the EPR data as a function of ion dose for these samples (table 6.1).

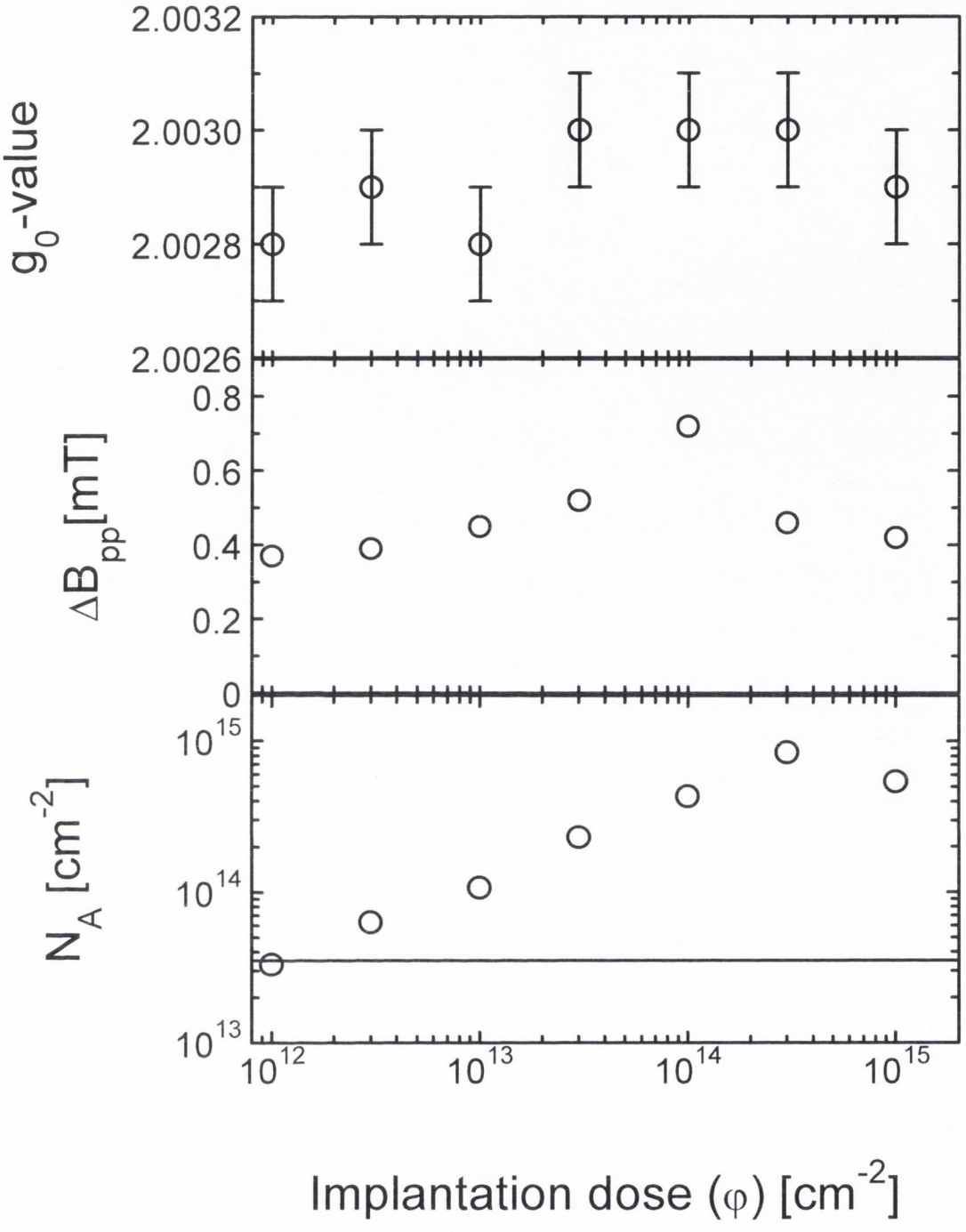

Figure 6.3 : EPR data for 6H-SiC as a function of Ge^+ implantation dose.
(Error estimates for ΔB_{pp} and N_A are within the symbol size)

The values of the EPR data for the virgin, i.e. non-implanted, 6H-SiC wafer are g_0=2.0029±0.0002, ΔB_{pp}=0.47±0.02mT and N_A=3.5×$10^{13}$$cm^{-2}$. The value of N_A for the virgin 6H-SiC sample is shown in figure 6.3 as a solid horizontal line. We can see in figure 6.3 that the sample implanted with 1×$10^{12}$$cm^{-2}$ Ge^+ ions has similar EPR data as the virgin sample.

In figure 6.3 the g_0-values remain at ≈2.0029 over the entire range of implantation doses. We can also see that ΔB_{pp} increases from ≈0.4mT to ≈0.8mT as the implantation dose (φ) increases from 1×10^{12} to $1\times10^{14}cm^{-2}$, above $\varphi=1\times10^{14}cm^{-2}$ this value ΔB_{pp} falls to ≈0.4mT. The areal spin population (N_A) increases above the virgin level as φ increases, up to $N_A\approx9\times10^{14}cm^{-2}$ at a dose of $\varphi\approx3\times10^{14}cm^{-2}$ after which it falls to $N_A\approx5\times10^{14}cm^{-2}$ at a dose of $\varphi\approx1\times10^{15}cm^{-2}$.

In figure 6.2 for $\varphi=3\times10^{13}cm^{-2}$ to $1\times10^{14}cm^{-2}$ the spectra are quite asymmetrical. In this section of the chapter we examine what may be producing such lineshapes.

One possible explanation for this is that two separate EPR lines are superimposed upon each other. Shimizu et al. (1981) found for amorphous SiC a Lorentzian line with g=2.0028 and ΔB_{pp}=0.51mT. Also Brodsky and Title (1969) found a Lorentzian line with g≈2.003 and ΔB_{pp}=0.6mT for amorphous SiC at 77K. The signal arising from amorphous SiC is due to dangling carbon bonds and not unpaired electrons on Si atoms (Ishii et al. 1982). We can see that indeed the g-value of this line is very close to the g-values we report in previous chapters for dangling bonds in a-C:H. The spectrum for amorphous SiC is similar to the spectra we find for $\varphi\leq1\times10^{13}cm^{-2}$ and for $\varphi\geq3\times10^{14}cm^{-2}$. It is possible that at these two extremes of implantation dose that the defects are the same as those found in amorphous SiC (Shimizu et al. 1980). Therefore when we carried out a two-line fit of the spectra, composing of two Lorentzian lines superimposed upon each other, one of the line we used had parameters close to the spectrum of amorphous SiC, i.e. g≈2.0028, $\Delta B_{pp}\approx0.4$mT.

We visually fitted the spectra as a function of dose (φ). In figure 6.2 superimposed upon the experimental spectra are the two-line fits we generated, these can be seen as smooth lines. These two-line fits are composed of two Lorentzian lines superimposed upon each other. The two-line fit for the virgin sample gives values of $N_A=1.06\times10^{13}cm^{-2}$ for a line with g≈2.0028 and $N_A=2.44\times10^{13}cm^{-2}$ for the a line with g≈2.0036. Since we are particularly interested in the defects produced by ion implantation, we can subtract these values of N_A from each of the component lines in our two-line fits. Table 6.2 displays the parameters we determined by fitting the spectra to two-line fits. For each of the areal spin population values (N_A) listed we

subtracted the virgin population of each line. These values of N_A are the populations induced by ion implantation only.

1^{st} lineshape = Lorentzian : 'Narrow' line					2^{nd} lineshape = Lorentzian : 'Broad' line		
Name	Dose φ [cm^{-2}]	1^{st} g-value	1^{st} ΔB_{pp} [mT]	1^{st} N_A [$10^{13}cm^{-2}$]	2^{nd} g-value	2^{nd} ΔB_{pp} [mT]	2^{nd} N_A [$10^{13}cm^{-2}$]
EU2	3×10^{12}	2.0028	0.385	1.98	2.0037	0.987	0.82
EU3	1×10^{13}	2.0027	0.385	2.29	2.0035	0.987	4.91
EU4	3×10^{13}	2.0030	0.395	1.84	2.0036	0.987	17.8
EU5	1×10^{14}	2.0027	0.395	2.52	2.0034	0.987	37.3
EU6	3×10^{14}	2.0031	0.405	50.9	2.0043	0.938	30.3
EU7	1×10^{15}	2.0028	0.395	38.8	2.0040	0.987	11.9

Table 6.2 : Two-line fit parameters determined for 6H-SiC as a function of φ.

In order to how good these two-line fits are, we compare in figure 6.4 the linewidth of the experimental spectra with the total linewidth peak-to-peak of the two-line fits. As can be seen in this figure that the total ΔB_{pp} of the two-line fits agree well with the measured ΔB_{pp} from the spectra.

Therefore we believe that two EPR lines are indeed present in our 6H-SiC samples implanted with 200keV Ge+ ions. The two lines are Lorentzian, one line has g≈2.0028 ΔBpp≈0.40mT and the second has g≈2.0036 ΔBpp≈1.00mT. We shall refer, from now on, to these two lines as the 'narrow' and 'broad' line respectfully.

Figure 6.5 shows the areal spin population (N_A) for implantation induced paramagnetic defects. This figure shows the total N_A and the N_A values of the 'broad' and 'narrow' lines as a function of implantation dose (φ). We can see in this figure that the total, implantation induced, areal spin population (N_A) grows approximately linearly with dose (φ) before dropping slightly at the highest dose ($10^{15}cm^{-2}$). The N_A values for the 'narrow' line (g≈2.0028, ΔB_{pp}≈0.4mT) is initially higher than those of the 'broad' line (≈2.0036 ΔB_{pp}≈1.00mT). These remain approximately constant with increasing dose (φ) up to $\varphi=1\times10^{14}cm^{-2}$ becoming smaller than those of the 'broad' line. Above $\varphi=1\times10^{14}cm^{-2}$ N_A for this line shows a very sharp rise in N_A, jumping from $N_A\approx2\times10^{13}cm^{-2}$ to $N_A\approx5\times10^{14}cm^{-2}$ becoming once again larger than N_A of the 'broad' line. N_A for the 'broad' line increases with increasing φ, up to $\varphi=1\times10^{14}cm^{-2}$ after which the N_A values fall with increasing φ.

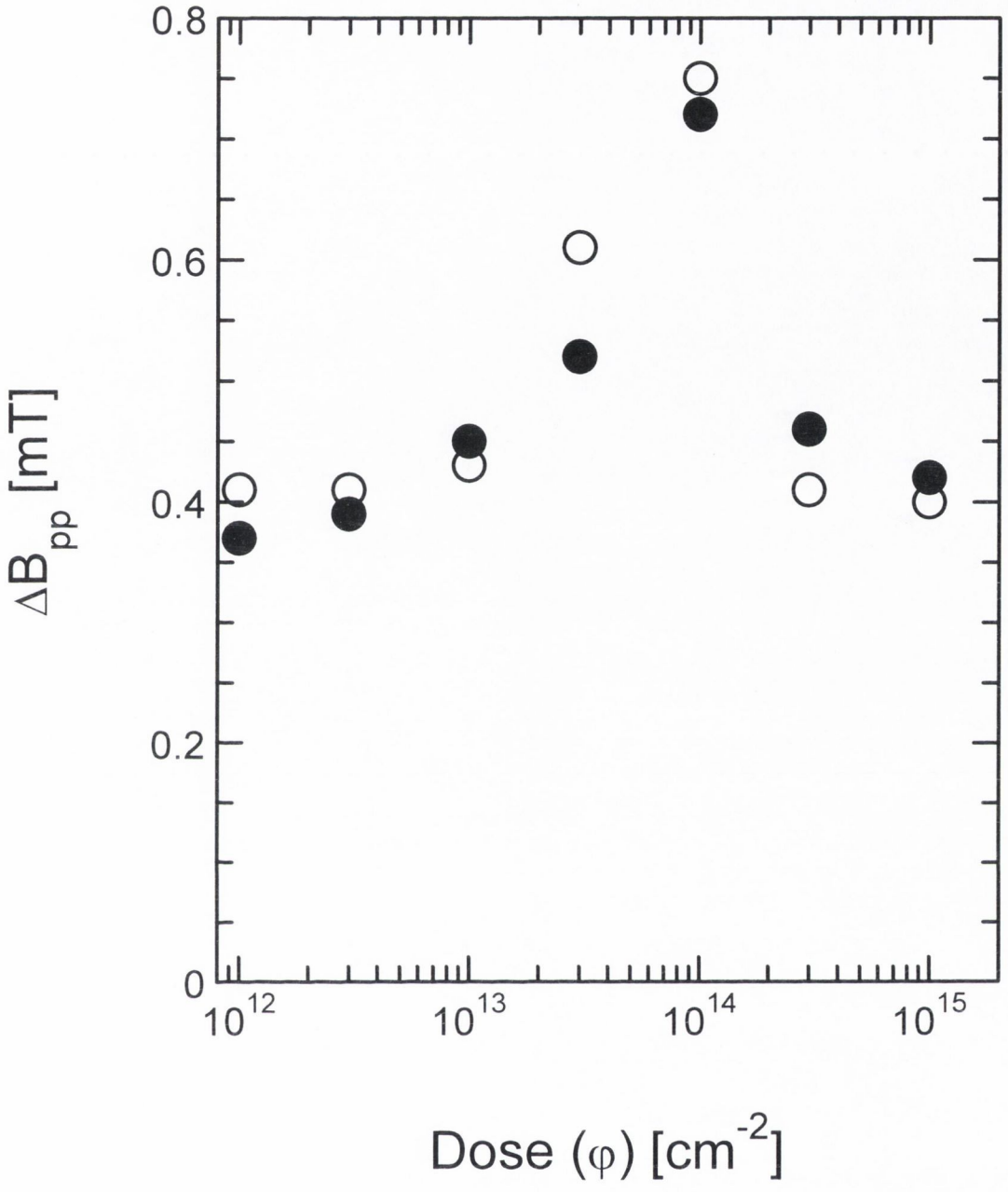

Figure 6.4 : ΔB_{pp} as a function of dose (φ).

O : *ΔB_{pp} of the two-line fits.*

● : *ΔB_{pp} of the experimental spectra.*

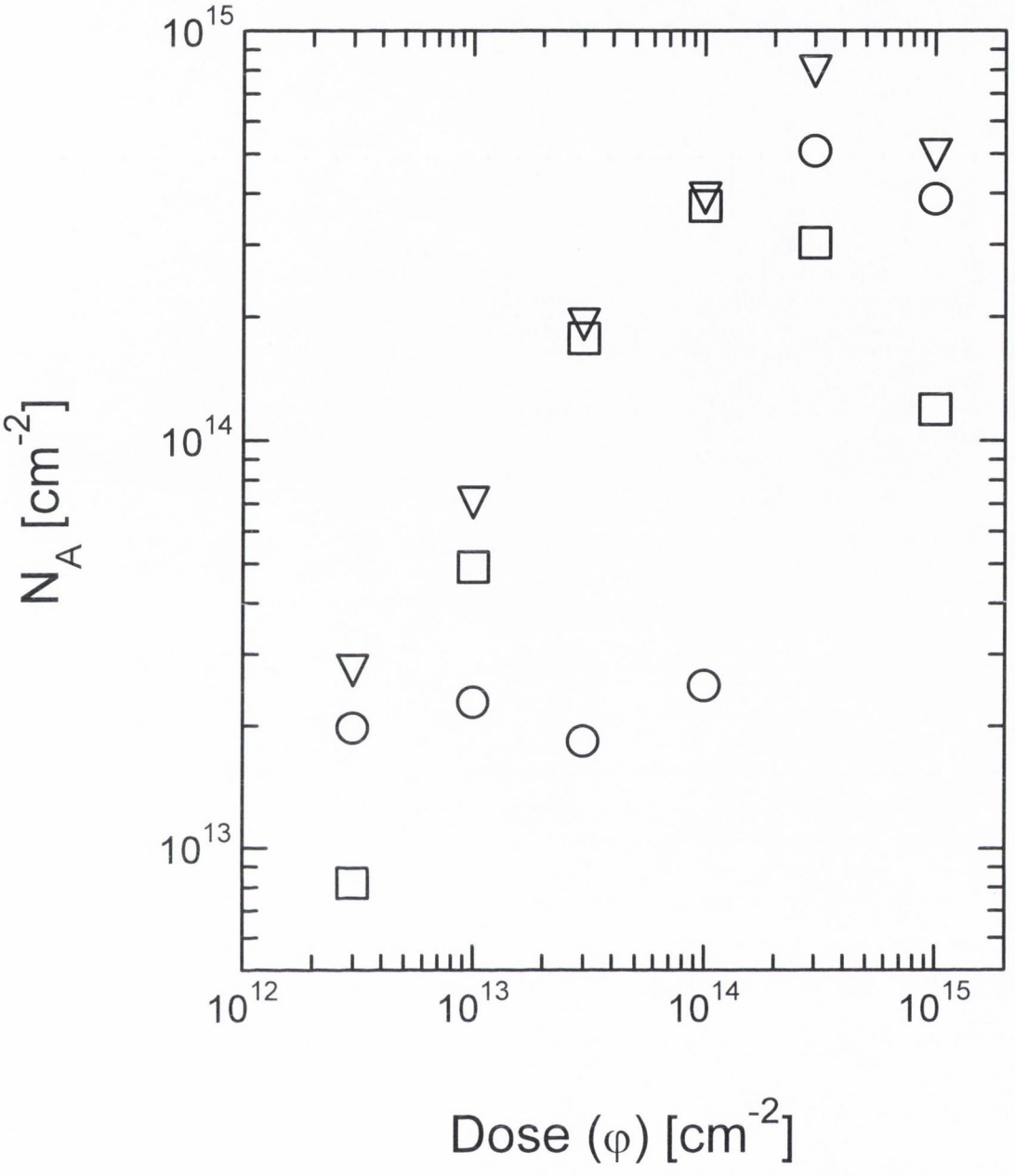

Figure 6.5 : N_A of implantation induced defects as a function of dose (φ).

∇ : Total areal population (N_A).

O : N_A for the 'narrow' line. g≈2.0028.

□ : N_A for the 'broad' line. g≈2.0036.

6.2.3 Discussion

In this section we discuss the results and analysis of the effect the implantation dose has upon the defects present in 6H-SiC.

We found that two types of defects are present in the 6H-SiC wafers, even before implantation. These two distinct paramagnetic defects give rise to a 'narrow' EPR line which has $g \approx 2.0028$ and $\Delta B_{pp} \approx 0.4$mT and a 'broad' EPR line which has $g \approx 2.0036$ and $\Delta B_{pp} \approx 1.00$mT. First we consider the source of the 'narrow' EPR line.

The paramagnetic defects in amorphous SiC reported by Shimizu et al. (1981) ($g=2.0028$ $\Delta B_{pp}=0.51$mT) and Brodsky and Title (1969) ($g \approx 2.003$, $\Delta B_{pp}=0.6$mT) are very similar to the defects which give rise to our 'narrow' line. Such defects are carbon dangling bonds in amorphous SiC (Ishii et al. 1982). We believe that the 'narrow' line is due to such defects.

Before we consider what effect ion implantation dose has upon the number and nature of these defects we will examine results obtained by others using different techniques on our samples and use them to help us understand our EPR results.

There exists a buried continuous amorphous SiC (a-SiC) layer, which is revealed by Cross-sectional Transmission Electron Microscopy (XTEM) (Heera et al. 1995), for doses $\geq 3\times10^{14}$cm^{-2} but no continuous layer is found for dose $\leq 1\times10^{14}$cm^{-2}. This is confirmed by Rutherford Backscattering Spectrometry (RBS) (Heera et al. 1995) which shows that the channelling yield reaches the random level for $\varphi \geq 3\times10^{14}$cm^{-2} indicating the presence of a continuous amorphous layer. Positron annihilation (PA) results also confirm the presence of a buried amorphous SiC layer (Brauer et al. 1996). Raman spectroscopy (RS) (Pérez-Rodriguez et al. 1996) of these samples show that when the dose (φ) increases from $\varphi=1\times10^{14}$cm^{-2} to $\varphi=3\times10^{14}$cm^{-2} there is an increase in the C-C and Si-Si bonds relative to the Si-C bonds. This may be due to the formation of a continuous a-SiC layer.

These XTEM, PA and RBS measurements found the thickness of the continuous amorphous layer to be 89, 124 and 166nm (mean=110nm), respectively and 143, 133 and 135nm (mean=137nm) respectively for the 6H-SiC wafers implanted with 3×10^{14} and 1×10^{15}cm^{-2} Ge^+ ions respectfully.

The EPR 'narrow' line signal shows a very large increase in N_A (figure 6.5) when φ increases above 1×10^{14}cm^{-2}. This we may now explain as being due to the

formation of a buried continuous a-SiC layer, as we believe these defects are due to carbon dangling bonds in a-SiC. These defects are present even in the virgin sample, it is possible that in this sample these defects are associated with surface damage. For $\varphi \leq 1\times10^{14}cm^{-2}$ we see a slight increase in these 'narrow' line defects with increasing φ. This may be due to the creation of small regions of amorphous SiC by the impinging ions.

Thus we believe that the 'narrow' EPR line is due to carbon dangling bonds in a-SiC. Initially these exist in small a-SiC regions inside the bulk of the 6H-SiC, but for doses (φ) $3\times10^{14}cm^{-2}$ and above a continuous a-SiC layer forms and majority of the carbon dangling bonds exist in this layer. The thickness of these layers are 110 and 137nm for $\varphi=3\times10^{14}$ and $\varphi=1\times10^{15}cm^{-2}$ respectfully. If we assume all the 'narrow' line spins are in these layers we get spin concentration (N_V) values of between $0.5\times10^{20}cm^{-3}$ to $0.3\times10^{20}cm^{-3}$ for doses of 3×10^{14} and $1\times10^{15}cm^{-2}$ respectfully. This is close to the spin concentration values of $\sim10^{20}cm^{-3}$ for a-SiC defects reported by Shimizu et al. (1981) and Brodsky and Title (1969). Positron annihilation in a-SiC layer may occur largely in vacancy clusters containing six vacancies (Brauer et al. 1996). Therefore it may be possible that the formation of the continuous buried a-SiC layer is accompanied by a clustering together of vacancies, the average concentration of these clusters may be $\sim10^{20}cm^{-3}$, from our average N_V over the a-SiC layer.

We now examine the nature of the defects giving rise to the 'broad' EPR line. Because of the differing g and ΔB_{pp} values, the defect producing the 'broad' EPR line does not arise from amorphous SiC. The g-value of the 'broad' line ($g=2.0036\pm0.0003$) does not correspond to the T1 defect ($g=2.0029\pm0.0001$), an isolated silicon vacancy, produced by electron or proton irradiation of 3C-SiC (Itoh et al.1989a; Itoh et al. 1989b; Iwanoto et al. 1988; Itoh et al. 1992).

However a signal with g=2.0032 has been reported for defects similar to the T1 centre, i.e. an isolated silicon vacancy, in electron and neutron irradiated 6H-SiC by Balona and Loubser (1970), they labelled the spectrum F. They also found other EPR spectra in electron and neutron irradiated 6H-SiC. Such as those they label B($g_{\|}=2.0032$, $g_{\perp}=2.0051$), D ($g=2.0026$), E_1 ($g=2.0034$) and E_2 ($g_{\|}=2.0033$, $g_{\perp}=2.0028$). Balona and Loubser (1970) attribute the defects producing spectrum B to the negative change state of a carbon vacancy, V_c^-, and the spectra E_1 and E_2 to the

positive charged state of a carbon vacancy , V_c^+. The mean of the g-values of all these spectra is 2.0034 with a spread in g of ±0.0021, which for spectra collected at ≈9.8GHz, as ours are, is only a spread in the magnetic field of ±0.2mT. While spectra B and E_2 are powder patterns and thus anisotropic, it is possible that if these defects exists in a number of possible local environments, then the their lineshape may be smeared out to become a featureless isotropic lineshape. A combination of such defects may be responsible for the 'broad' EPR line we observe. Also the g-value of a Si dangling bond surrounded by 12 carbons atoms has been calculated to be 2.0037 (Ishii et al. 1982). Therefore there may also be a contribution of defects such as $C_3{\equiv}Si\bullet$ ($\bullet$ represents an unpaired electron).

Therefore our 'broad' EPR line may be due to a combination of silicon (e.g. the T1 like centre) and carbon (e.g.the V_c^- and V_c^+ centres) mono and di-vacancies, i.e. a variety of Si and C dangling bonds.

In figure 6.5 we see that the areal spin population (N_A) for this ensemble of defects (the 'broad' line) increases, almost linearly, with increasing dose (φ), up to $1{\times}10^{14}cm^{-2}$. For $\varphi{>}3{\times}10^{14}cm^{-2}$ N_A falls with increasing dose (φ). This may be due to the formation of a continuous a-SiC layer, which while producing the 'narrow' line defects, may destroy the defects giving rise to the 'broad' line. The relative population of each of these possible defects, giving rise to the 'broad line', may change as a function of dose (φ), this may explain the changing g-values for the 'broad' line as the dose (φ) increases (table 6.2).

6.3 Effect of annealing on the implantation induced defects

It is of interest to study the thermal stability of defects present in ion implanted SiC. Also in device fabrication it is usually necessary to reduce the number of defects present, it may be done by annealing. Therefore in this section of the chapter we examine the effect annealing has on the paramagnetic defects produced by the implantation of 200keV Ge^+ ions into 6H-SiC.

6.3.1 Sample preparation

As mentioned in the previous section 6H-SiC implanted with $\varphi \geq 3\times10^{14}cm^{-2}$ ions contain a continuous buried a-SiC layer. Therefore in order to examine the effect of annealing on the defects induced by Ge^+ irradiation, we choose two levels of dose for annealing. The doses $1\times10^{14}cm^{-2}$ and $1\times10^{15}cm^{-2}$ are used, because a dose of $1\times10^{14}cm^{-2}$ produces no continuous amorphous layer in 6H-SiC while a dose of $1\times10^{15}cm^{-2}$ does. Samples EU10 ($\varphi=1\times10^{14}cm^{-2}$) and EU20 ($\varphi=1\times10^{15}cm^{-2}$) were step annealed, in Argon, (see chapter 3) at 100, 200, 300, 400, 500, 600, 700, 800 and 900°C.

Samples EU11, EU12, EU13 ($\varphi=1\times10^{14}cm^{-2}$) and EU21, EU22, EU23 ($\varphi=1\times10^{15}cm^{-2}$) were isochronally annealed. Samples EU11 to EU13 were implanted with a beam current of 1.2μA for 420s. Samples EU21 to EU23 were implanted with a beam current of 1.5μA for 2820s. These six samples were all annealed at a single temperature for 10 minutes in Argon. Table 6.3 gives the annealing temperatures (T_a) used for these samples.

Name	Dose φ [cm^{-2}]	Annealing temperature (T_a) [°C]
EU11	1×10^{14}	500
EU12	1×10^{14}	950
EU13	1×10^{14}	1500
EU21	1×10^{15}	500
EU22	1×10^{15}	950
EU23	1×10^{15}	1500

Table 6.3 : T_a and φ for isochronally annealed 6H-SiC samples.

6.3.2 EPR results of annealing

In this section we examine the EPR results of annealing 6H-SiC implanted with the two doses ($\times 10^{14}cm^{-2}$ and $1\times 10^{15}cm^{-2}$). We shall also analyse these results.

First we deal with the effect annealing has upon the defects present in 6H-SiC implanted with $\varphi=1\times 10^{15}cm^{-2}$. Figure 6.6 displays some of the spectra of the step annealed sample for this dose (φ) as a function of T_a. Superimposed upon these spectra are single Lorentzian line fits. The spectra for the isochronally annealed samples were collected by Dr. B. Holm.

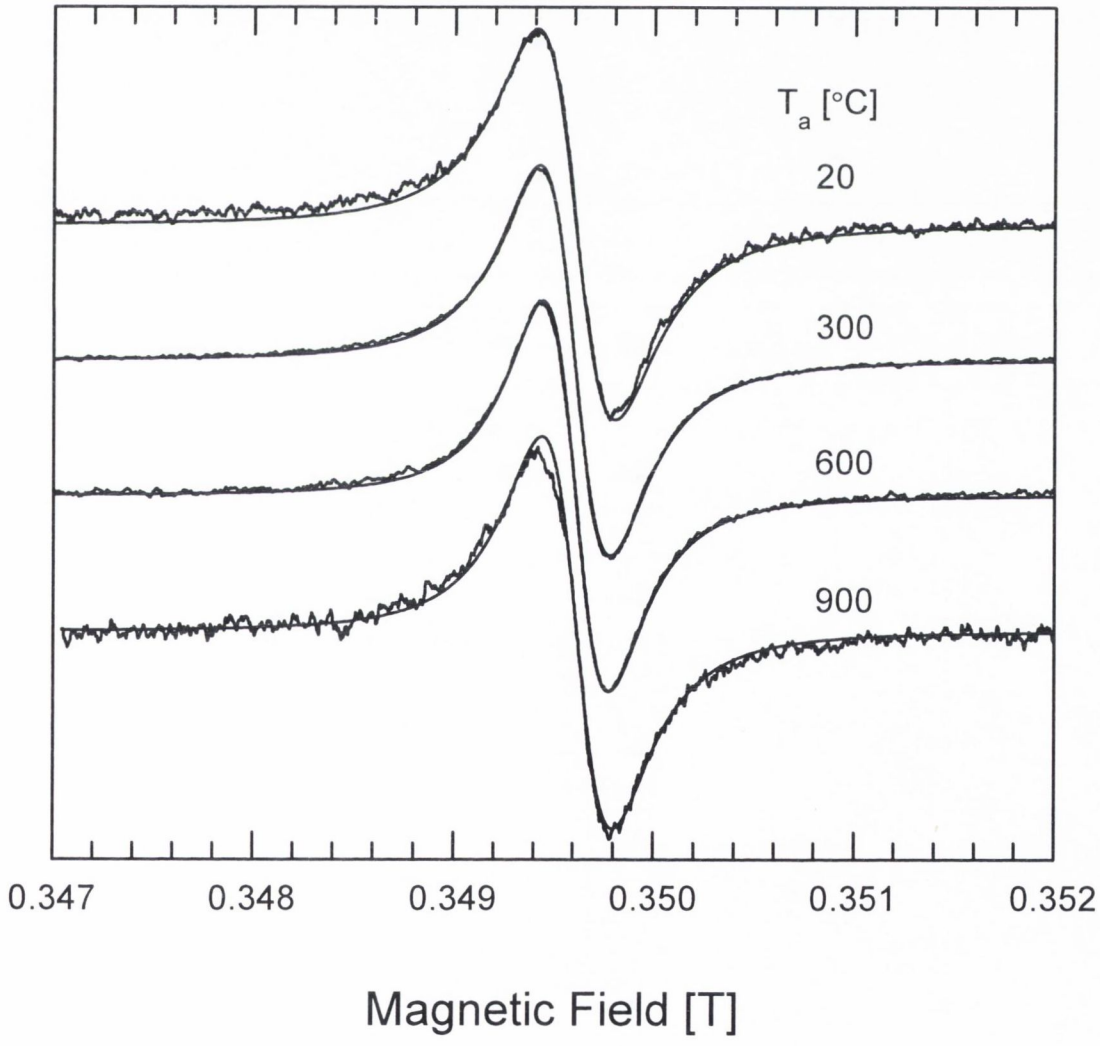

Figure 6.6 (ν=9.8GHz): EPR spectra as a function of T_a for 6H-SiC implanted with $\varphi=1\times 10^{15}cm^{-2}$ (Eu20).

We can see in figure 6.6 that the annealing temperature (T_a) has no major effect on linewidth, ΔB_{pp}=0.38±0.03mT, the lineshape, which remains Lorentzian, or the g_0-value, g_0=2.0028±0.0001. The only effect annealing has, for $\varphi=1\times10^{15}cm^{-2}$, is that the signal intensity, i.e. N_A and N_V in the a-SiC layer, falls with increasing T_a. The same is true of the isochronally annealed samples with $\varphi=1\times10^{15}cm^{-2}$.

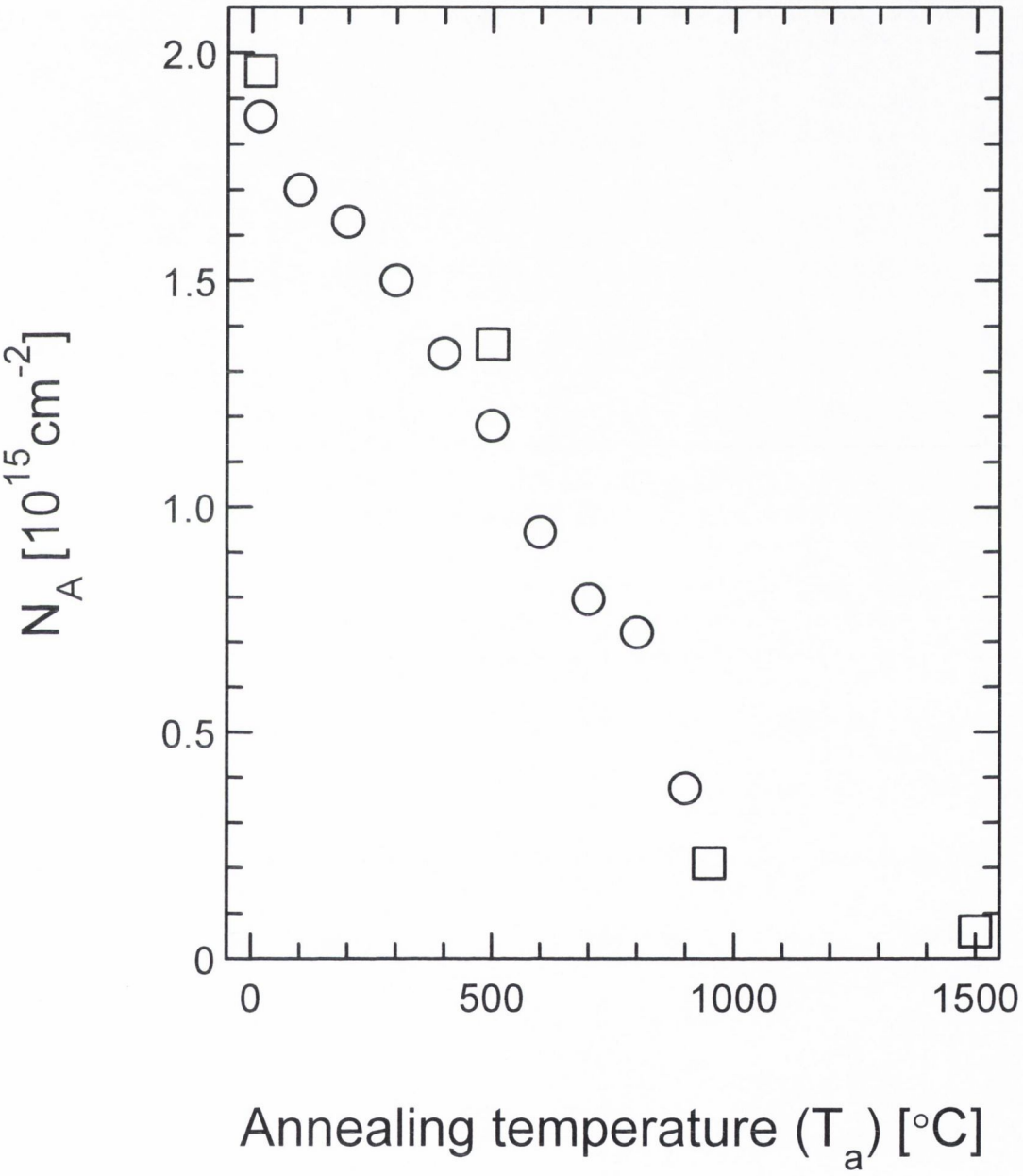

Figure 6.7 : N_A as a function of T_a for $\varphi=1\times10^{15}cm^{-2}$.

O : N_A for the step annealed sample (Eu20).

□ : N_A for the isochronally annealed samples (Eu21, Eu22 & Eu23).

Figure 6.7 displays the areal population (N_A) for the annealed 6H-SiC wafers implanted with $\varphi=1\times10^{15}cm^{-2}$ as a function of T_a. We can see in this figure that it makes little difference whether the 6H-SiC wafers are step or isochronally annealed. We can see in this figure that N_A decreases almost linearly with increasing T_a, up to 950°C after which it falls at a slower rate.

Next we look at the result of annealing the 6H-SiC wafers implanted with $\varphi=1\times10^{14}cm^{-2}$. Figure 6.8 shows selected spectra of sample Eu10 ($\varphi=1\times10^{14}cm^{-2}$), which we step annealed as a function of T_a.

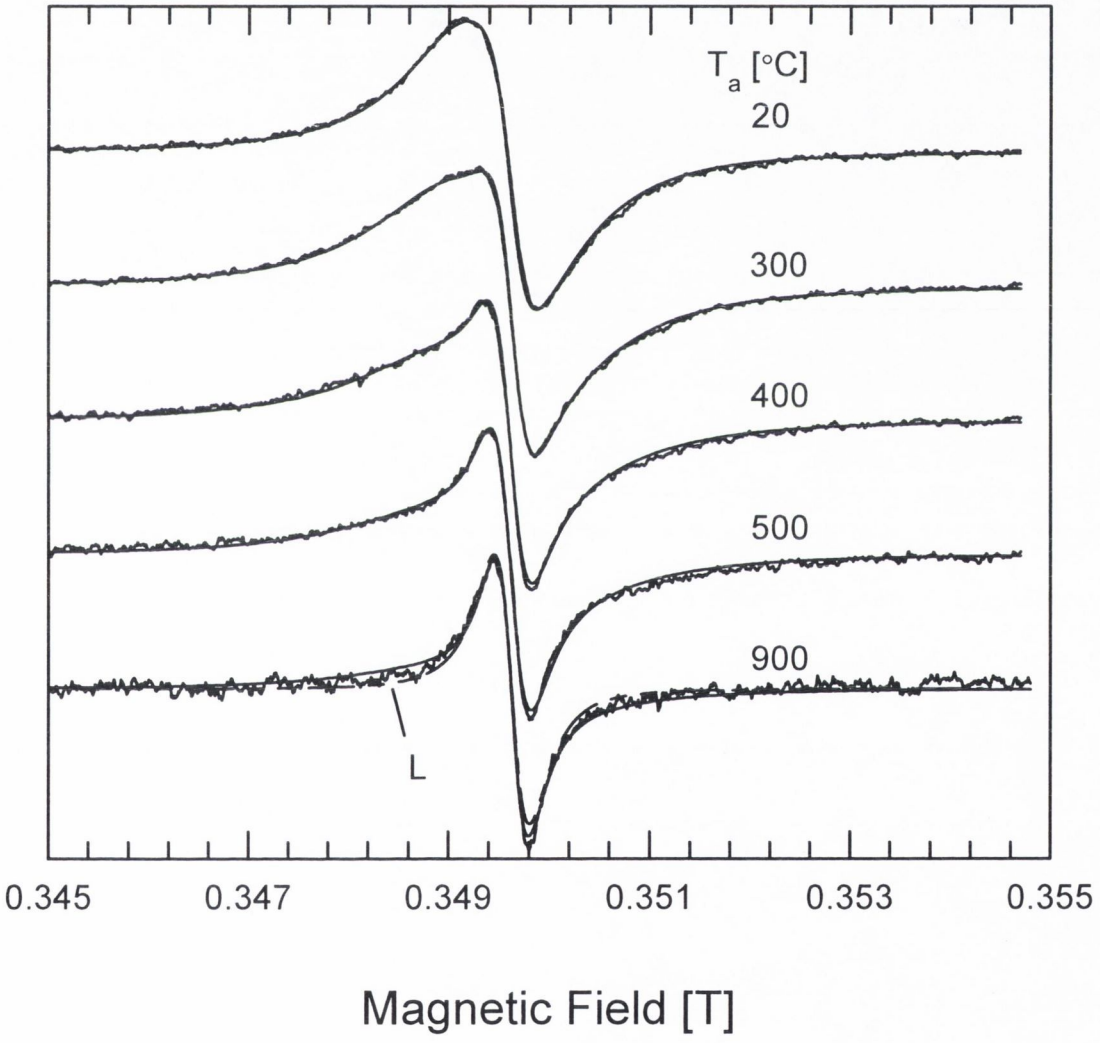

Figure 6.8 (ν=9.8GHz): EPR spectra as a function of T_a for 6H-SiC implanted with $\varphi=1\times10^{14}cm^{-2}$ (Eu10).

In figure 6.8 we see that, unlike the previous sample (Eu20, $\varphi=1\times10^{15}cm^{-2}$), the linewidth, shape and cross-over g_0-value change quite considerably with increasing T_a

for the samples implanted with $\varphi=1\times10^{14}cm^{-2}$. The spectra for the isochronally annealed samples show a very similar effect as T_a increases.

We can see that the lineshape of the spectra up to 500°C are asymmetrical. At T_a=900°C the lineshape becomes close to a Lorentzian, denoted by 'L' in figure 6.8. At 900°C ΔB_{pp}=0.33mT and g_0=2.0027 are very close to values we find in the samples implanted with $\varphi=1\times10^{15}cm^{-2}$, i.e. that the signal is due to dangling carbon bonds in small a-SiC regions. It is possible that the changes in ΔB_{pp}, g_0 and N_A, as T_a increases, are due to the fact that two EPR lines are present, i.e. a 'broad' and a 'narrow' line. Therefore we fitted these spectra with the 'broad' and 'narrow' Lorentzian lines. Figure 6.8 shows these two-line fits superimposed upon the experimental spectra. We can see that such two-line fits agree well with the experimental spectra. The parameters determined by fitting these spectra are given in table 6.4.

1st lineshape = Lorentzian : 'Narrow' line				2nd lineshape = Lorentzian : 'Broad' line		
Annealing temperature (T_a) [°C]	1st g-value ±0.0001	1st ΔB_{pp} [mT] ±0.02	1st N_A [10^{14} cm^{-2}]	2nd g-value ±0.0001	2nd ΔB_{pp} [mT] ±0.02	2nd N_A [10^{14} cm^{-2}]
Step annealed.						
20	2.0028	0.40	1.67	2.0033	1.00	15.3
100	2.0027	0.40	1.39	2.0034	1.00	14.4
200	2.0027	0.40	1.29	2.0033	1.00	13.9
300	2.0026	0.40	1.29	2.0036	1.25	10.5
400	2.0027	0.40	1.32	2.0039	1.40	7.36
500	2.0027	0.39	0.836	2.0039	1.50	3.32
600	2.0027	0.37	0.714	2.0041	1.50	2.58
700	2.0027	0.37	0.697	2.0037	1.50	1.80
800	2.0026	0.35	0.510	2.0040	1.50	1.25
900	2.0026	0.33	0.251	2.0038	1.50	0.639
Isochronally annealed.						
20	2.0027	0.41	1.50	2.0034	1.00	13.7
500	2.0028	0.37	1.13	2.0039	1.48	5.4
950	2.0027	0.33	0.615	2.0043	1.23	1.01
1500	2.0027	0.32	0.111	2.0035	1.48	0.183

Table 6.4 : Two-line fitting parameters, as a function of T_a, for 6H-SiC implanted with $\varphi=1\times10^{14}cm^{-2}$.

The 'narrow' line has g=2.0027. This line has ΔB_{pp}=0.40mT at low T_a and falls slightly to 0.35mT as T_a increases. The 'broad' line has g≈2.0033 and ΔB_{pp}=1.00mT which increases with increasing T_a to become g≈2.0039 and

ΔB_{pp}=1.50mT for $T_a \geq 500°C$. Figure 6.9 shows how the N_A values for these two EPR lines change as a function of T_a.

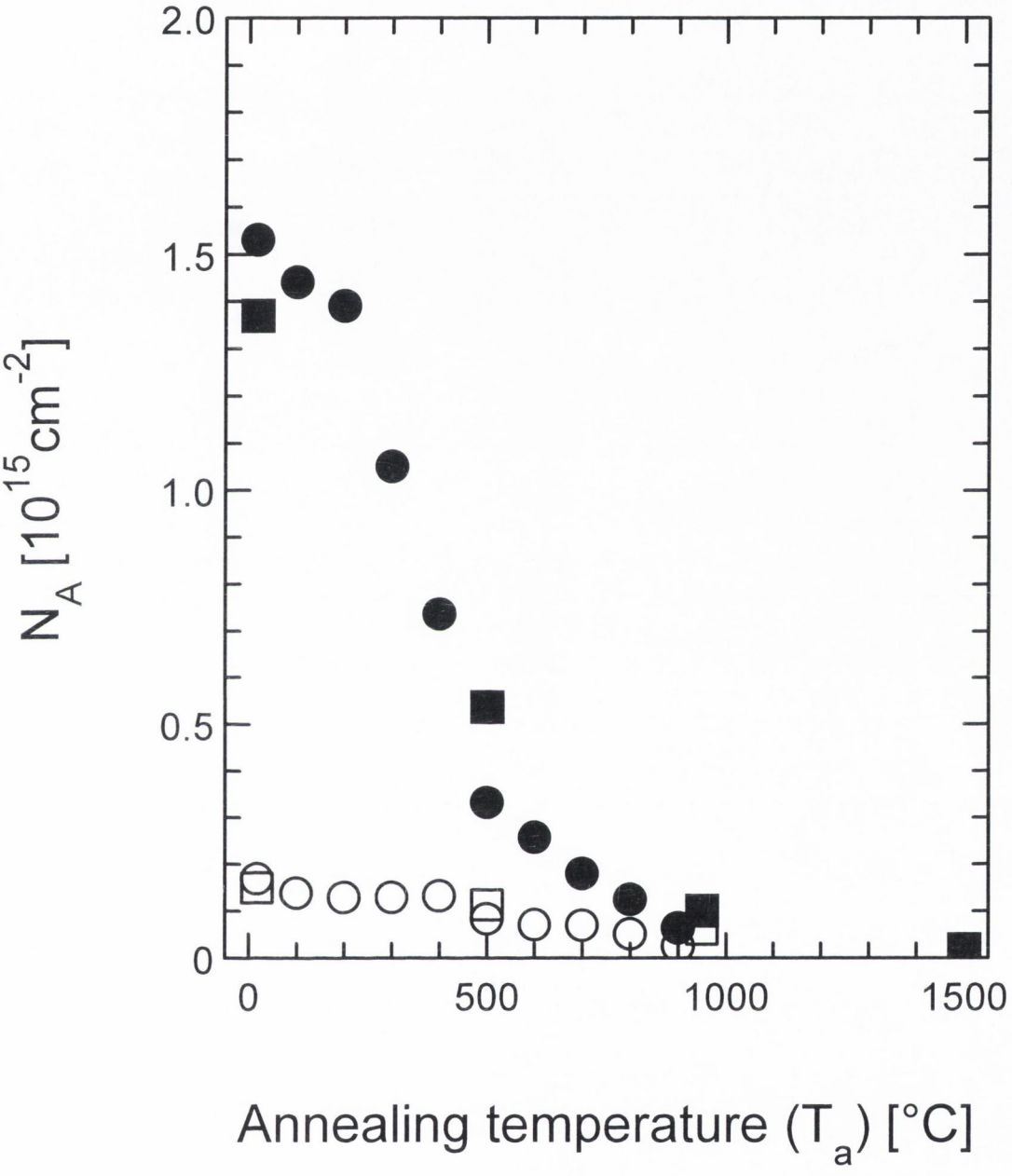

Figure 6.9 : N_A as a function of T_a for 6H-SiC wafers implanted with $\varphi=1\times10^{14}cm^{-2}$.

O : *N_A for the 'broad' line of the step annealed sample (table 6.4).*

□ : *N_A for the 'broad' line of the isochronally annealed samples (table 6.4).*

● : *N_A for the 'narrow' line of the step annealed sample (table 6.4).*

∝ : *N_A for the 'narrow' line of the isochronally annealed samples (table 6.4).*

In figure 6.9 we can see that the defects contributing to the 'broad' EPR line anneal out at a much faster rate with increasing temperature, than the defects contributing to the 'narrow' line, especially when T_a<500°C.

Finally it should be noted that N_A for the as-implanted $\varphi=1\times10^{14}cm^{-2}$ used in both the step and isochronal annealing studies (table 6.3) are $N_A=15\times10^{14}cm^{-2}$ and $N_A=17\times10^{14}cm^{-2}$ compared to $N_A=4\times10^{14}cm^{-2}$ for the $\varphi=1\times10^{14}cm^{-2}$ used in the variable dose set. Similarly, for the as-implanted $\varphi=1\times10^{15}cm^{-2}$, the corresponding N_A values are 20 and $19\times10^{14}cm^{-2}$ for the annealing samples (T_a=20°C) and only $5\times10^{14}cm^{-2}$ in the variable dose set. It is not clear why the spin concentration is lower in the later set of samples, but the relative concentrations of the defects at these two doses is about the same for all three sets.

6.3.3 Discussion

In this section we discuss the effect annealing has upon implantation induced defects present in 6H-SiC. We will begin by examining the effect of annealing upon the defects present in the $\varphi=1\times10^{15}cm^{-2}$ samples.

We see in figure 6.6 that the nature of the defects remains unchanged by annealing, i.e. the defects present for $\varphi=1\times10^{15}cm^{-2}$ are carbon dangling bonds in the buried a-SiC layer or small a-SiC regions. Figure 6.7 shows a gradual decrease in the number of these defects as T_a increases. This gradual decrease suggests that there is a spread in the activation energies required to anneal these defects.

The thickness of the buried continuous a-SiC layer, found by XTEM and RBS measurements (Heera et al. 1995), does not vary with increasing T_a for the isochronally annealed samples. As the thickness of this a-SiC layer does not fall, then the fall in N_A, as T_a increases, is not due to epitaxial re-growth of 6H-SiC into the a-SiC layer. The reduction of the carbon dangling bonds in a-SiC layer may result because of some relaxation within the a-SiC layer.

We now discuss the effect annealing has upon the defects present in implanted 6H-SiC with $\varphi=1\times10^{14}cm^{-2}$. In these samples we found two EPR lines, a 'broad' and a 'narrow' line. We have already discussed the possible defects which may give rise to these lines. We believe the 'narrow' line is due to carbon dangling bonds in small

a-SiC regions within the bulk 6H-SiC. Such defects may have a similar behaviour, as a function of T_a, to those found in the a-SiC layer in the samples implanted with $\varphi=1\times10^{14}cm^{-2}$. In order to compare these two behaviours we can normalise the defects present (N_A) to a value of ≈1 at room temperature. Figure 6.10 displays normalised N_A values for the carbon dangling bonds in a-SiC for $\varphi=1\times10^{14}cm^{-2}$ (i.e. the N_A for the 'narrow' line only) and $\varphi=1\times10^{15}cm^{-2}$ (i.e. the total N_A). We can see in this figure that the annealing rate of these two defects are very similar, giving support to the idea that they are both carbon dangling bonds in a-SiC. Again the gradual fall in the carbon dangling bonds in the a-SiC regions may result because of some relaxation within the a-SiC regions.

The 'broad' EPR line, for $\varphi=\times10^{14}cm^{-2}$, we believe is due to a collection of defects due to C and Si dangling bonds in a variety of mono- and di-vacancies. We can see in figure 6.9 that these defects anneal at a quicker rate than those we associate with a-SiC. The gradual fall in N_A for the 'broad' line we attribute to a spread in activation energies required for annealing. In table 6.4, ΔB_{pp} and the g-value increases with T_a. This may indicate that the defects giving rise to the 'broad' line are indeed an assortment of defects, with differing g-values and linewidths, which anneal out at different rates. This may explain the changes in the 'broad' line ΔB_{pp} and g-value as T_a increases.

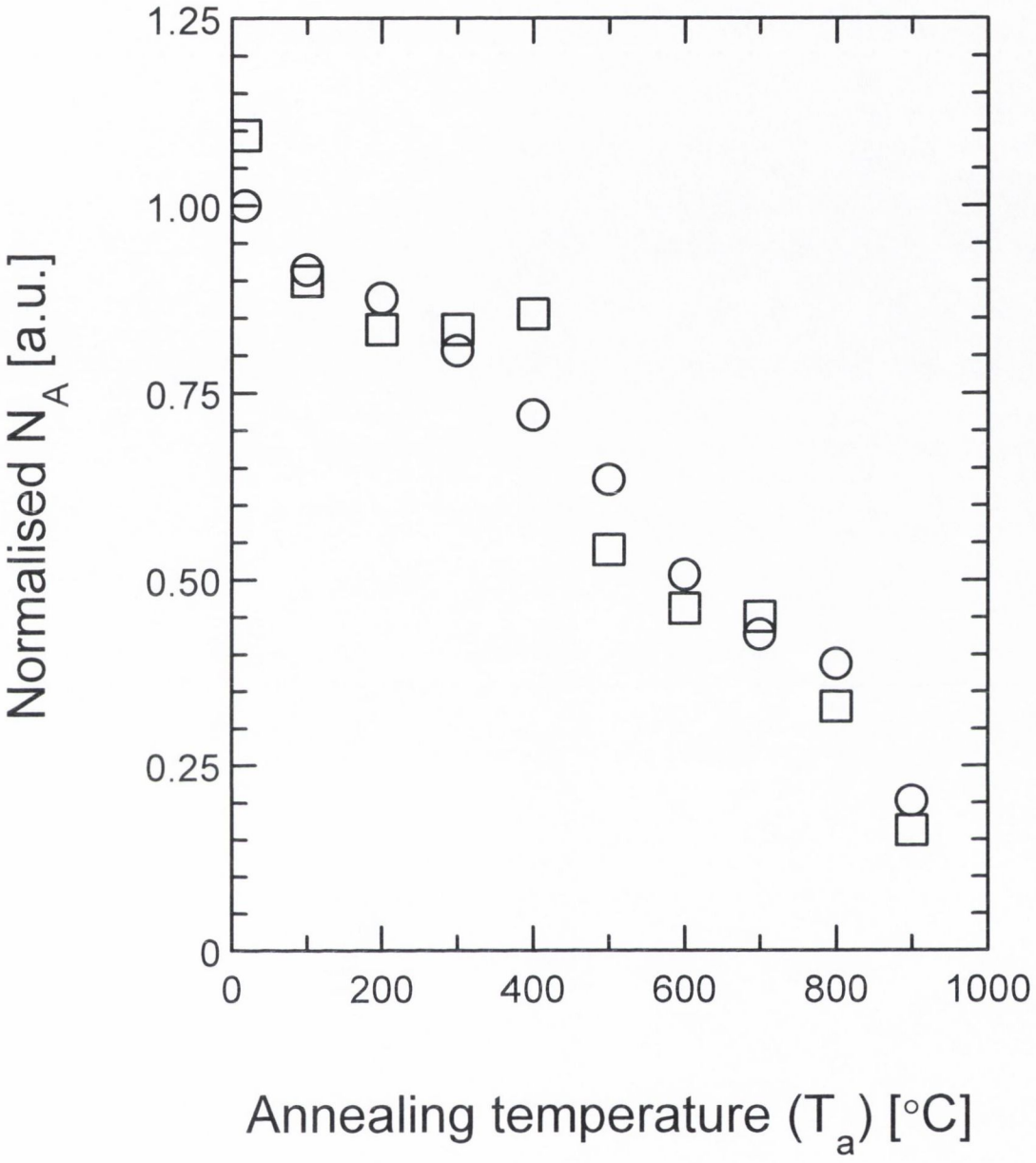

Figure 6.10 : Normalised N_A values as a function of T_a.

O : Normalised total N_A for $\varphi=1\times10^{15}cm^{-2}$ (Eu20).

□ : Normalised N_A, for the 'narrow' line only, for $\varphi=1\times10^{14}cm^{-2}$ (Eu10).

6.4 Conclusions.

200keV Ge^+ ion irradiation of bulk 6H-SiC produces a continuous buried amorphous layer for implantation doses $\geq 3\times10^{14}cm^{-2}$. For doses $\leq 1\times10^{14}cm^{-2}$ at least two types of defect are detected in 6H-SiC. A narrow EPR line defect (g=2.0028, $\Delta B_{pp}\approx 0.40mT$) and a wide EPR line defect ($g\approx 2.0037$, $\Delta B_{pp}\approx 1.0mT$). For doses $\geq 3\times10^{14}cm^{-2}$ a line very close to a single Lorentzian exists, having g=2.0028, $\Delta B_{pp}\approx 0.38mT$, most likely arising from defects similar to those producing the 'narrow' line.

The 'narrow' EPR line may be due to carbon dangling bonds in clusters of amorphous SiC. The spin population of these clusters remains roughly constant over the range of doses $1\times10^{12}cm^{-2}$ to $1\times10^{14}cm^{-2}$, until the formation of a continuous buried amorphous layer for doses of $3\times10^{14}cm^{-2}$ to $1\times10^{15}cm^{-2}$, where the number of defects increases dramatically. For doses $\geq 3\times10^{14}cm^{-2}$ most of the defects reside in the continuous a-SiC layer.

The nature of the defect(s) giving rise to the 'broad' EPR signal, for $\varphi<3\times10^{14}cm^{-2}$, is not as clear. This signal is not due to amorphous SiC. We believe that there is a collection of defects giving rise to this signal. It is possible that these defects are a collection of mono and di-vacancies containing carbon and silicon dangling bonds.

Annealing of samples implanted with $1\times10^{15}cm^{-2}$ ions shows that the number of defects falls gradually. This indicates a spread in the activation energies required to anneal out the carbon dangling bonds in the a-SiC layer.

A very similar behaviour was found for the 'narrow' line, for $\varphi=1\times10^{14}cm^{-2}$, which may support the idea that the 'narrow' line is due to similar defects in a-SiC regions before the creation of a continuous a-SiC layer. The defects producing the 'broad' EPR line anneal at a faster rate than the 'narrow' line defects. They also anneal out gradually, indicating that these too have a spread in annealing activation energies.

6.5 References

Balona, L. A. de S. and Loubser, J. H. N. (1970). Journal of Physics C: Solid State Physics, **3**, 2344.

Brauer, G., Anwand, W., Coleman, P. G., Knights, A. P., Plazola, F., Pacaud, Y., Skorupa, W., St★rmer, J. and Willutzki, P. (1996). Physical Review B, **54**, 3084.

Brodsky, M. H. and Title, R. S. (1969). Physical Review Letters, **23**, 581.

Heera, V., Stoemenos, J., K★gler, R. and Skorupa, W. (1995). Journal of Applied Physics, **77**, 2999.

Hirano, Y. and Inada, T. (1995). Journal of Applied Physics, **77**, 1020.

Ishii, N., Kumeda, M. and Shimizu, T. (1982). Solid State Communications, **41**, 143.

Itoh, H., Hayakawa, N., Nashiyama, I. and Sakuma, E. (1989a). Journal of Applied Physics, **66**, 4529.

Itoh, H., Hayakawa, N., Nashiyama, I. and Sakuma, E. (1989b). Japan Atomic Energy Research Institute Report, **M89-094**.

Itoh, H., Yoshikawa, M., Nashiyama, I., Misawa, S., Okumura, H. and Yoshida, S. (1992). Journal of Electronic Materials, **21**, 707.

Iwamoto, N. Makino, Y. and Matsunami, N. (1988). Nuclear Instrumentation and Methods B, **32**, 37.

Pérez-Rodrigues, A., Pacaud, Y., Calvo-Brrio, L., Serre, C., Skorupa, W. and Morante, J. R. (1996). Journal of Electronic Materials, **25**, 541.

Rao, M. V., Griffiths, P., Holland, O. W., Kelner, G., Freitas, J. A., Simons, D. S., Chi, P. H. and Ghezzo, M. (1995). Journal of Applied Physics, **77**, 2479.

Shimizu, T., Kumeda, M. and Kiriyama, Y. (1981). Solid State Communications, **37**, 699.

Spitznagel, J. A., Wood, S., Choyke, W. J., Doyle, N. J., Bradshaw, J. and Fishman, S. G. (1986). Nuclear Instrumentation and Methods B, **16**, 237.

Sugli, T. (1994). In Advances in Silicon and Semiconducting Silicon-Alloy based Materials and Devices, (ed. J. F. A. Nijs), p. 283. IOP Publishing, Bristol.

Sze, S. M. (1985). Semiconductor Devices: Physics and Technology, p. 412. Wiley, New York.

Vodakov, Y. A. and Mokhov, E. N. (1973). In Silicon Carbide, (ed. R. C. Marshall, J. W. Faust , Jr. and C. E. Ryan), p. 508. University of South Carolina Press, Columbia.

Chapter 7:

Conclusions

In polymeric a-C:H films grown by PECVD on Si substrates we found that two defect are present. One due to carbon dangling bonds uniformly distributed though the film and a defect from the Si substrate and possibly at the C/Si interface. The unpaired electrons in the film are most likely π-electrons and they probably reside in chains of conjugated double bonds, consisting of olefinic chains and possibly aromatic clusters. Annealing the a-C:H films produces an increase in the defect density probably due to the loss of hydrogen. This emission of hydrogen occurs mainly over the temperature range of ≈100°C to ≈500°C. ΔB_{pp} falls with increasing T_a, we believe that this is due to ratio of sp^2 hybridised bonds to sp^3 bonds on the carbon atoms increasing with annealing temperature, which may allow greater delocalisation and increase the exchange narrowing of the line. The substrate temperature during deposition is found to have a similar effect on polymeric a-C:H films as post-deposition annealing temperature.

The addition of nitrogen into polymeric a-C:H films seems to have very little effect on the paramagnetic defects present. This indicates that the nitrogen is a poor dopant in polymeric a-C:H. Annealing affects the defects present in polymeric a-C:H,N in the same way as it does those in a-C:H. The EPR signal is possibly as Voigt for 400 to 500°C. This leads us to believe that the lineshape, in this range of temperatures arises from dipolar interaction and unresolved hyper-fine splitting due to the presence of hydrogen and nitrogen. Implantation into polymeric a-C:H gives rise to two types of defects; one in the a-C:H films which we again believe are unpaired π-electrons on conjugated olefinic chains or on aromatic clusters with an odd number of fused rings, the other due to dangling bonds produced in the Si substrate. Whether the ion used was B, N or C had very little effect on the paramagnetic defects that were produced. Loss of hydrogen is probably a significant factor in producing defects in the a-C:H film when the implantation dose is 2×10^{16} B cm^{-2}.

The bias voltage (V_b) has a major effect on the defects present in the a-C:H films. All the unpaired electrons in all our samples are attributed to π unpaired electrons and not σ unpaired electrons. At low bias voltages we believe that the lineshape and linewidth are likely to be due to the presence of both dipolar broadening and unresolved hyperfine splitting caused by hydrogen, here the film is polymeric a-C:H. As the bias voltage increased and the film becomes DLC we explained the linewidth as due to dipolar broadening alone. As the bias is increases still further and the films become GLHC, we believe from the fall in ΔB_{pp} and the spin relaxation measurements (T_1 and T_2) that exchange narrowing is increasing. We believe that this increase in exchange interaction is due to an increase in the sp^2 content of the films.

We annealed this range of a-C:H films whose structures ranged from diamond like carbon (DLC) to graphite like hydrogenated carbon (GLHC). We found that annealing a-C:H had different effects which depended upon the initial structure of the film. The DLC film and the film in the transition region from DLC to GLHC (V_b=50 and 100V) show initially a reduction in the number of unpaired spins (N_V), which may be due to the passivation of unpaired spins by hydrogen. Another possibly is that the film became more ordered which remove the π-unpaired electrons. For the films with a more GLHC character (V_b=400 and 540V), i.e. higher sp^2 and low hydrogen content this initial drop in N_V is not observed probably because of the lower hydrogen content or because the film may be more ordered because it contains a higher content of sp^2 bonding. For 400°C<T_a<600°C the DLC film (V_b=50V) shows an increase in its spin concentration (N_V) with increasing T_a. This is may be due to a loss of hydrogen from this film. The film in the transition region from DLC to GLHC (V_b=100V) also shows an increase in its spin concentration (N_V) with increasing T_a but it is less dramatic, probably due to the lower initial hydrogen content of this film compared to the DLC film. The films with a greater GLHC character (V_b=400 and 540V), show no increase in N_V with increasing T_a, in the range of temperatures 400°C to 600°C. This may be due to the fact that in the hydrogen content is already low in these films before annealing. Finally for all the films N_V falls with increasing T_a, for T_a>600°C, presumably due to the onset of graphitization and the reduction of defects within the structure of the films.

For three films (V_b=100, 400 and 540V) ΔB_{pp} increased with increasing annealing temperature (T_a) when T_a was raised above ≈500°C. This may be due to an increased interaction between the unpaired π-electrons and conduction electrons due to the onset of graphitization. However measurements made of the T_1 (spin-lattice) and T_2 (spin-spin) relaxation times as a function of T_a for the GLHC film (V_b = 400V) suggest that T_1 increases while T_2 decreases with increasing T_a. This differs with the suggestion by Austen et al. (1958) that T_1 shortens with increasing T_a ,for T_a >550°C when carbonising sugars and coal. We found that the annealing behaviour of the a-C:H depends strongly upon the initial structure of the a-C:H film

We have examined how the addition of nitrogen to diamond-like a-C:H effects the paramagnetic defects present. The addition of nitrogen causes the number of spins (N_V) to drop quite significantly. This we believe is due mainly to nitrogen supplying doping electrons into the a-C:H,N film which were free to move and combine with unpaired π-electrons of the defects. At low temperatures we did not observe paramagnetic N centres. Thus we found no evidence to support the idea that nitrogen electronically dopes the diamond-like a-C:H films. Annealing at T_a≈550°C causes the a-C:H,N films to exhibit EPR features very similar to DLC a-C:H annealed at T_a≈550°C. We believe that the structure of both these a-C:H,N films and DLC a-C:H, after being annealed at ≈550°C, are very similar. This may means that the most of the nitrogen and hydrogen has been released from the a-C:H,N films when this temperature is reached. We believe that the lineshape for the EPR spectra of the a-C:H,N films are Voigt profiles. We found possible evidence that after adding nitrogen into the diamond-like a-C:H film the spins are clustered together, i.e. that the local spin concentration (N_V) around the remaining unpaired spins is higher than the average concentration of unpaired spins.

We found two types of defect present in ion implanted 6H-SiC. A 'narrow' EPR line defect (g=2.0028, ΔB_{pp}≈0.40mT) and a 'broad' EPR line defect (g≈2.0037, ΔB_{pp}≈0.10mT). The 'narrow' EPR line may be due to carbon dangling bonds in clusters of amorphous SiC. The spin population of these clusters remains roughly constant over the range of doses $1\times10^{12}cm^{-2}$ to $1\times10^{14}cm^{-2}$, until the formation of a continuous buried amorphous layer for doses of $3\times10^{14}cm^{-2}$ to $1\times10^{15}cm^{-2}$, where the number of defects increases dramatically. This coincides with the formation of the

buried layer. For doses $\geq 3\times10^{14}cm^{-2}$ most of the defects reside in the continuous a-SiC layer.

The nature of the defect(s) giving rise to the 'broad' EPR signal, for $\varphi<3\times10^{14}cm^{-2}$, is not as clear. We believe that there is a collection of defects giving rise to this signal. It is possible that these defects are a collection of mono and di-vacancies containing carbon and silicon dangling bonds.

Annealing of samples implanted with $1\times10^{14}cm^{-2}$ $1\times10^{15}cm^{-2}$ ions shows that the number of 'broad' and 'narrow' line defects fall gradually. This indicates a spread in the activation energies required to anneal these defects.